Investigating Simultaneous Microwave Dielectric and Structural Characterisation of Heterogeneous Gas Sorption Processes

Michael James Barter

Centre for High Frequency Engineering

Cardiff University

This thesis is submitted in candidature for the degree of

Doctor of Philosophy (PhD)

Cardiff School of Engineering 2019

DECLARATION

This work has not previously been accepted in substance for any degree and is not concurrently submitted in candidature for any degree.

Signed ______________________ Date ______________________

STATEMENT 1

This thesis is being submitted in partial fulfilment of the requirements for the degree of PhD.

Signed ______________________ Date ______________________

STATEMENT 2

This thesis is the result of my own independent work/investigation, except where otherwise stated. Other sources are acknowledged by explicit references. The views expressed are my own.

Signed ______________________ Date ______________________

STATEMENT 3

I confirm that the electronic copy is identical to the bound copy of the thesis.

Signed ______________________ Date ______________________

STATEMENT 4

I hereby give consent for my thesis, if accepted, to be available for photocopying and for inter-library loan, and for the title and summary to be made available to outside organisations.

Signed ______________________ Date ______________________

Abstract

The main aim of this thesis is to design, simulate, build, and conduct and interpret experiments using simultaneous microwave dielectric and structural measurements. These measurements will be used to characterise solid state materials during polar gas sorption processes. The gases reviewed in this thesis are ammonia and sulphur dioxide. Metal-organic frameworks are investigated for use as both ammonia and sulphur dioxide solid state storage materials. Metal halides are also investigated for absorption of ammonia. These sorption processes are investigated using microwave dielectric characterisation. This is combined with structural characterisation from either neutron or X-ray diffraction. The combination of these techniques is used to monitor changes in bulk material properties along with changes in molecular structure during the gas sorption processes.

A sample environment is designed for simultaneous neutron diffraction and microwave characterisation of materials at varying temperatures. The developed equipment uses heating coils to heat a flowing gas, which is used to heat the sample. A cylindrical cavity is designed and constructed for this experimental rig with a thinned section of cavity wall to minimise neutron scattering from the sample environment. This equipment is tested by successfully monitoring the activation of a MOF sample at 150 °C to remove water present in the sample. A hairpin style resonator is also developed for use with simultaneous dielectric characterisation and X-ray diffraction. The open structure of the hairpin geometry of this resonator allows the X-ray beam to be unimpeded by the resonator, maximising the resolution or X-ray data. This is used to investigate the absorption of ammonia by halides salts.

Also in this thesis, a new method for correcting for changes in frequency caused by changes in temperature is developed for cylindrical microwave cavities. Temperature correction is often required during microwave characterisation where changes in temperature caused by changes in ambient conditions, exothermic/endothermic reactions, or while examining dielectric properties over a range of temperatures. TM_{m10} modes consist of two symmetrical mode patterns with identical resonant frequencies. This technique uses a strategically placed sample to split the frequencies of these degenerate modes. The higher frequency, unperturbed mode is used as a local reference and the lower frequency, perturbed mode as the measurement mode. The effectiveness of this technique is proved by heating water sample from 20 ℃ to 60 ℃, calculating its permittivity and comparing against literature values.

Acknowledgements

Firstly, I would like to thank Adrian Porch for convincing me it was a good idea to pursue this PhD, then for his continued support, guidance, and expertise throughout the last few years. I would also like to thank Martin Owen Jones for coming up with “borderline impossible” experiments that somehow always worked and for always walking me through the chemistry behind them.

I would like to acknowledge the funding for this work from the Science and Technology Facilities Council as well as the Engineering and Physical Sciences Research Council.

My thanks to Ron Smith for his help with all things neutron on Polaris, Chris Goodway and the ISIS Pressure and Furnaces team for their support with sample environments and gas flow, and Phil Chater for his expertise on i15-1 at Diamond Light Source.

This work would not have been possible without the support of everyone in the Centre of High Frequency Engineering. Special mentions must got to Jon Hartley for all his preliminary work and for getting me started on the right track, Sam Partridge for his collaboration and for being my coding guru, and of course Nyle Parker for, well... being Nyle.

I would also like to thank my collaborators; Ross Forgan (Glasgow University) for his help with the work on ammonia absorption in MOFs. Sihai Yang (Manchester University) for his collaboration with sulphur dioxide absorption in MFM-170 and Gemma Smith (Manchester University) for making all this work happen.

Thanks to Andrew Rankmore and his team in the mechanical workshop for microwave resonator construction.

Finally I would like to thank my Mum, Dad and Sister who I will be forever grateful for in their unending support in everything I strive for, and Sian for all of the commas and putting up with me while I write this thesis!

Contents

List of Figures

List of Tables

Nomenclature

Abbreviations

CAD	Computer Aided Design
DOE	Department of Energy
FTIR	Fourier Transform Infrared (spectroscopy)
ID	Inner Diameter
IL	Insertion Loss
MCR	Microwave Cavity Resonator
MOF	Metal Organic Framework (Metal-Organic Framework)
NPD	Neutron Powder Diffraction
OD	Outer Diameter
PCA	Principal Component Analysis
PDF	Pair Distribution Function
PID	Proportional Integral Derivative
PTFE	Polytetrafluoroethylene (Teflon)
RF	Radio Frequency
RLC	Resistance Inductance Capacitance
RMS	Root Mean Square

RTD	Resistance Temperature Detector
RTP	Room Temperature and Pressure
SCC	Stress Corrosion Cracking
sccm	Standard Cubic Centimeters Per Minute
SCR	Selective Catalytic Reduction
SMA	SubMiniature Version A
STFC	Science and Technology Facilities Council
TE	Transverse Electric
TEM	Transverse Electric Magnetic
TGA	Thermal Gravimetric Analysis
TM	Transverse Magnetic
TOF	Time Of Flight
VNA	Vector Network Analyser
XPDF	X-ray Pair Distribution Function

Chapter 1

Introduction and Thesis Overview

1.1 Motivation

For many years there has been an initiative from the scientific community, industry, and governments worldwide to develop an energy source that does not contribute to climate change through the release of CO_2. Linked to this is the need for a suitable means of energy storage. This has a major significance in the automotive industry as a replacement for petrol and diesel combustion engines.

Hydrogen has been at the forefront of much of this research in this field due to its high gravimetric energy content of 123 MJ/kg compared to 47.2 MJ/kg for petrol for example [1]. Hydrogen can be used in a modified internal combustion engine or alternatively used in a hydrogen fuel cell. Although the majority of hydrogen produced worldwide uses fossil fuels, it is possible for it to be produced CO_2-free by electrolysis of water using sustainably produced electricity [2, 3]. The problem with use of hydrogen as an energy vector is its storage. As a gas at 0 °C and 1 bar hydrogen has a density of only 0.089886 $\mathrm{kgm^{-3}}$[4]. Due to this, a method of storing hydrogen at high pressure or low temperature is commonly used to greatly increase the volumetric density. High pressure systems can not only be large and heavy but also provide a safety concern. Low temperature systems have the issue of hydrogen boil-off. Due to the large amounts of energy required to cool hydrogen and its continued boil-off, storing hydrogen as a liquid at low temperature can be very expensive. A different solution to this problem is to find an indirect hydrogen storage material.

The use of ammonia as a potential hydrogen storage material has been widely suggested [2, 5–7]. This is largely due to its high gravimetric (17.8 wt% H_2) and volumetric (121 kg H_2 m^{-3} in the liquid form) H_2 density [8]. Its usefulness as a potential energy vector is emphasised by the current network for production and distribution, supplying 120 M tonnes worldwide annually, predominantly for the industrial and agricultural industries. The major issue with the use of ammonia for energy storage is its toxicity. In order to alleviate this problem, a way to safely and efficiently store ammonia must be developed. Several methods of storing ammonia have been suggested such as urea, metal-halides and MOFs [2, 6, 9, 10]. These methods all eliminate of the issues of toxicity. Before any method can be adopted the storage material must be fully characterised.

Sulphur dioxide is a toxic and corrosive gas which can cause irritation to eyes, skin and airways. Extended exposure can lead to permanent lung damage [11]. SO_2 gas is released naturally from volcanic eruptions [12]. It is also produced as a waste product in many industries, including during energy production from fossil fuels [13–15]. To reduce the amount of SO_2 released into the atmosphere from industrial processes, an absorbent material must be used to remove this toxic gas from the waste gas produced. Materials suggested for SO_2 absorption include weak base / polyethylene glycol binary systems [16], aqueous solutions [17, 18], ionic liquids supported on mesoporous molecular sieves [19], and metal organic frameworks [14, 15, 20–22]. It may also be possible to develop a SO_2 sensor to measure the concentration of SO_2 present, by measuring the properties of the storage material as it absorbs SO_2.

There are several methods commonly used to measure gas uptake in materials. These include; thermogravimetric analysis[23, 24], Raman spectroscopy[25, 26], neutron diffraction and X-ray diffraction[27, 28]. These techniques have the drawbacks of being invasive or destructive, not being able to perform in-situ analysis, or have a high cost associated with performing measurements. Microwave measurements provide an alternative for measuring polar gas absorption which is non-invasive, non-destructive, usable for in-situ analysis and can be performed at relatively low cost. The microwave cavity perturbation technique can be used to find the bulk dielectric properties of a material, which can be used to infer structural changes in the material as it absorbs or desorbes polar gases such as ammonia and sulphur dioxide.

1.2 Chapter Overview

Chapter 2 - Survey of Materials and Measurement Techniques: Presents a background information on the materials investigated as well as the measurement techniques used in this thesis. The materials focused on in this chapter are suitable for ammonia and/or sulphur dioxide absorption. These include halide salts and metal organic frameworks (MOFs). Measurement techniques described in this chapter and used throughout this thesis include; the microwave perturbation technique, neutron powder diffraction, and X-ray diffraction.

Chapter 3 - Experiment and Resonator Design: Documents the design, simulation, construction and preliminary testing of two experiments and microwave resonators. For the first experiment, a cavity type resonator is designed for use in simultaneous microwave characterisation and neutron powder diffraction of gas sorption processes at elevated temperatures. A new sample environment is created for this experiment, including cavity resonator and heating equipment. For the second experiment, a hairpin type resonator is designed for use in simultaneous characterisation and X-ray powder diffraction of gas sorption processes.

Chapter 4 - Simultaneous Neutron Diffraction and Microwave Measurement: The use of simultaneous NPD and microwave characterisation is used to investigate gas sorption systems. These techniques are combined for the first time to investigate ammonia absorption in a complex system, MOFs, to study their ammonia absorption processes. Absorption of SO_2 in the MOF MFM-170 is also investigated in this chapter. Finally the microwave cavity and heating equipment developed in Chapter 4 is tested by heating argon gas to 150 °C in order to remove water from the MOF. This equipment may be used in the future for experiments at elevated temperatures or when removal of water from the sample is key.

Chapter 5 - Simultaneous X-ray Diffraction and Microwave Measurement: Experiments using the hairpin type resonator developed in Chapter 4 are used for simultaneous X-ray diffraction and microwave characterisation for the first time. This equipment was used to investigate the absorption of ammonia by halide salts. The aim of these experiments was to differentiate between physisorbed and chemisorbed ammonia using these combined techniques.

Chapter 6 - Degenerate Mode Temperature Correction: A new method to correct for changes in frequency caused by changes in temperature in cylindrical cavities, using degenerate cavity modes is presented. This method uses a strategically placed sample perturbation to separate the frequencies of degenerate modes. The perturbed, lower frequency mode is used for sample measurement, and the unperturbed, higher frequency mode is used as a local reference for temperature correction. Using the developed method, there is no dependence on previously measured data of expansion coefficients, only simple instrumentation providing less than 100 MHz is required, and reduces error when compared to other temperature correction methods.

Chapter 7 - SO_2 Absorption in MFM-170: The absorption of SO_2 in MFM-170 is measured using microwave characterisation. Measurements taken using the cylindrical cavity resonator designed in Chapter 4 and are repeated where the sample is activated, partially hydrated and fully hydrated and the results compared. An additional experiment is carried out using the hairpin type resonator designed in Chapter 4. This geometry of resonator allowed simultaneous use of a thermal camera, to track the temperature of the sample during the exothermic absorption of SO_2 and endothermic desorption of SO_2.

1.3 Original Contributions

- The first use of simultaneous neutron diffraction and microwave characterisation on MOFs.

- The first use of simultaneous neutron diffraction and microwave characterisation at elevated temperatures, as well as the development of the microwave cavity resonator and heating equipment to conduct this experiment.
- The first use of simultaneous X-ray diffraction and microwave characterisation on a continuous gas flow system, as well as the development of a microwave hairpin type resonator to conduct this experiment.
- The development of a new method for temperature correction for cylindrical cavity perturbation measurements using degenerate modes.

1.4 Publications

M. Barter, J. Hartley, F. Yazigi, R. J. Marshall, R. S. Forgan, A. Porch, and M. O. Jones. Simultaneous neutron powder diffraction and microwave dielectric studies of ammonia absorption in metal-organic framework systems. Phys. Chem. Chem. Phys., 20(15):10460–10469, 2018.

M. Barter, S. Partridge, D. R. Slocombe, and A. Porch. Temperature Correction Using Degenerate Modes for Cylindrical Cavity Perturbation Measurements. IEEE T. Microw. Theory, 65(6):800–805, 2018.

Chapter 2

Survey of Materials and Measurement Techniques

2.1 Ammonia and Sulphur Dioxide

For differing purposes, there are needs to find effective solid state stores for the polar gases ammonia and sulphur dioxide. Ammonia requires a solid state absorption material for energy storage applications. The toxicity of sulphur dioxide means an absorption material is required for ambient absorption and sensing. The high polarity and dielectric loss associated with these gases makes their absorption by solid state materials suitable for measurement by microwave characterisation.

Energy production and storage is a major area of research, aimed at developing an energy source that does not contribute to climate change through the release of CO_2. Hydrogen has attracted much attention in this field due to its high gravimetric energy density, however storage of hydrogen has proved problematic. Ammonia has been suggested for use as an energy vector that is CO_2-free [5, 6, 29–32]. Since ammonia at RTP is gaseous and has a high gravimetric (17.8 wt% H_2) and volumetric (121 kg H_2 m^{-3} in the liquid form) H_2 density [8].

A disadvantage of ammonia as a possible energy vector is its toxicity [5, 8]. For these reasons it is necessary to store ammonia in a form where it is more viable as an energy carrier, as well as being non-toxic. Possible ammonia storage materials include; zeolites [33, 34], metal hydrides [23, 30, 35, 36], lithium fullerides [28], selective catalytic reduction (SCR) catalysts such as TiO_2 supported V_2O_5-WO_3 [37, 38], ammonia borane [2, 39], and metal-organic frameworks [25, 26, 40–42].

Sulphur dioxide is a toxic and corrosive gas. Upon contact with mucus membranes, sulphur dioxide forms sulphurous acid causing irritation to eyes, airways, and skin [43]. Extended exposure can lead to permanent effects on the respiratory system[11]. Sulphur dioxide is released both naturally, through volcanic activity[12], and is also produced as a by-product of energy production from fossil fuels [13–15], agriculture [44], industry [16] and other sources. Materials for absorption of sulphur dioxide from the air and for detection of SO_2 have been investigated. These include weak base / polyethylene glycol binary systems [16], aqueous solutions [17, 18], ionic liquids supported on mesoporous molecular sieves [19], and metal organic frameworks [14, 15, 20–22].

Microwave characterisation is a suitable technique for both of these gas sorption systems, due to the highly polar nature of the subject gases. Unlike most characterisation techniques, microwave perturbation can be used to directly measure the sample at the gas sorption interface.

2.2 Ammonia Storage Methods

Various methods of storing ammonia to solve this have been suggested. As well as energy content and non-toxicity, other factors must be considered, such as percentage hydrogen content, cost, and operating temperature. Before exploring some of the options of storage materials, targets must be set.

As a major use of ammonia storage would be for automotive use, any storage material should fulfil the US Department of Energy (DOE) 2015 guidelines [2, 45, 46]. Key DOE guidelines are shown below:

- Gravimetric energy density at least 3.0 kWh/kg
- Volumetric energy density at least 2.7 kWh/litre
- Gravimetric H_2 capacity of at least 9 %wt
- Maximum storage system (and fuel) cost of $67 per kg H_2
- Operating temperatures between -40 °C and +60 °C at a maximum pressure of 100 atm
- System fill time (for 5 kg) of under 2.5 minutes
- Loss of usable H_2 of under 0.05 g/h/kg
- Cycle life of 1500 cycles
- Fuel purity of at least 99.99% H_2

Complying to these targets would ensure the storage material used would be a viable candidate for use as an ammonia storage material.

2.2.1 Liquid Ammonia Storage

Storing ammonia as a liquid is one possible option which can be done with a pressure of only 8.88 bar (at 21 °C) or at -33.5 °C at atmospheric pressure [2, 47]. Ammonia is currently predominantly transported as a liquid for agricultural and industrial use, with over 120 M tonnes produced per year globally. Liquid ammonia meets the targets for energy densities and hydrogen content as well as being cost effective. Unlike storage of liquid hydrogen, with boil-off rates of over 2-3% per day [6], no such leakage is apparent in liquid ammonia vessels. Problems with storing ammonia as a liquid include: susceptibility of the container to stress corrosion cracking (SCC), reactivity with water, high coefficient of thermal expansion, high vapour pressure and the high level of toxicity of ammonia vapour [47]. To solve the issue with toxicity, some form of solid state storage must be found. Figure 2.1 shows possible methods for ammonia storage, as well as the high hydrogen densities possible using both liquid and solid state storage methods.

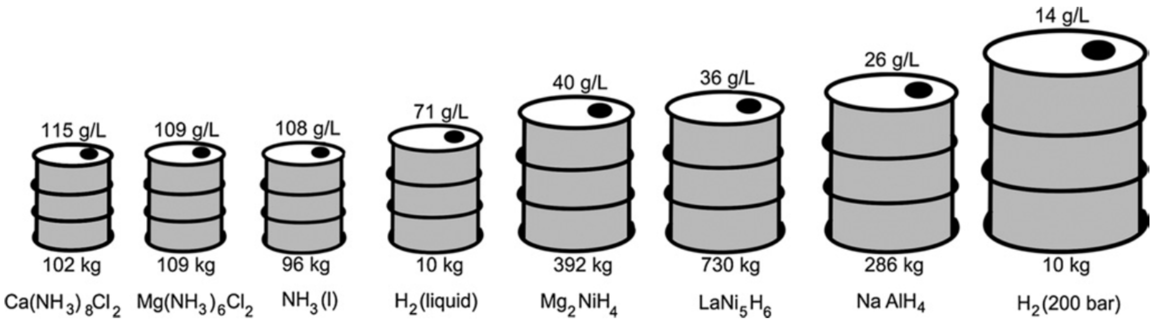

Figure 2.1: Mass and volume of 10 kg hydrogen stored reversibly by eight different methods, based on the best obtained reversible densities reported in the literature without considering the space or weight of the container. [6]

2.2.2 Solid State Ammonia Storage

Ammonia can also be stored within a solid state material, which can provide high gravimetric densities of ammonia. Solid state storage materials can also be made non-toxic, as shown in Figure 2.2, where a hexaamminemagnesium chloride sample containing approximately 0.62 g of NH_3 can safely be handled [5]. Ammonia within a solid can be stored in two different ways; weakly bound to the surfaces of the material (physisorbed), or strongly chemically bound to the material (chemisorbed).

2.3 Sulphur Dioxide Absorption and Removal Methods

Due to the corrosive and toxic nature of sulphur dioxide, materials for absorption and removal of this gas have been investigated. Removal of sulphur dioxide from exhaust gases is especially important for industries where SO_2 is released, such as energy production from fossil fuels. It would be highly desirable in the relevant industrial processes to have a gas-permeable material which is capable of capturing SO_2 but allowing non-harmful gases to pass, whilst also having a sensor for the amount of SO_2 absorbed.

Figure 2.2: Tablets of hexaamminemagnesium chloride (featuring the logo of the Technical University of Denmark) have been shown to effectively store ammonia and can be safely handled conveniently in the palm of a hand [5].

2.3.1 Liquid Sulphur Dioxide Absorption

A possible method for absorbing sulphur dioxide from the air is by using a liquid phase absorbent. Possible candidates for SO_2 absorption from the air include; ionic liquids [19, 48], distilled water [18], and sea water [49]. Sea water has also been found to be effective at desulphurisation for marine engine exhaust gases [50, 51]. Ionic liquids such as tetramethylguanidinium lactate supported on a mesoporous molecular sieve have been shown to absorb 0.682 mol SO_2/mol [19]. Repeated cycling of SO_2 absorption and desorption has shown that lower percentages of SO_2 loading have proven greater recycling ability.

2.3.2 Solid State Sulphur Dioxide Absorption

Solid state absorption materials have also been suggested for sulphur dioxide removal from the air. The predominant candidates for a solid state desulphurisation material are metal organic frameworks [15, 52]. This mesoporous series of materials has shown exceptionally high

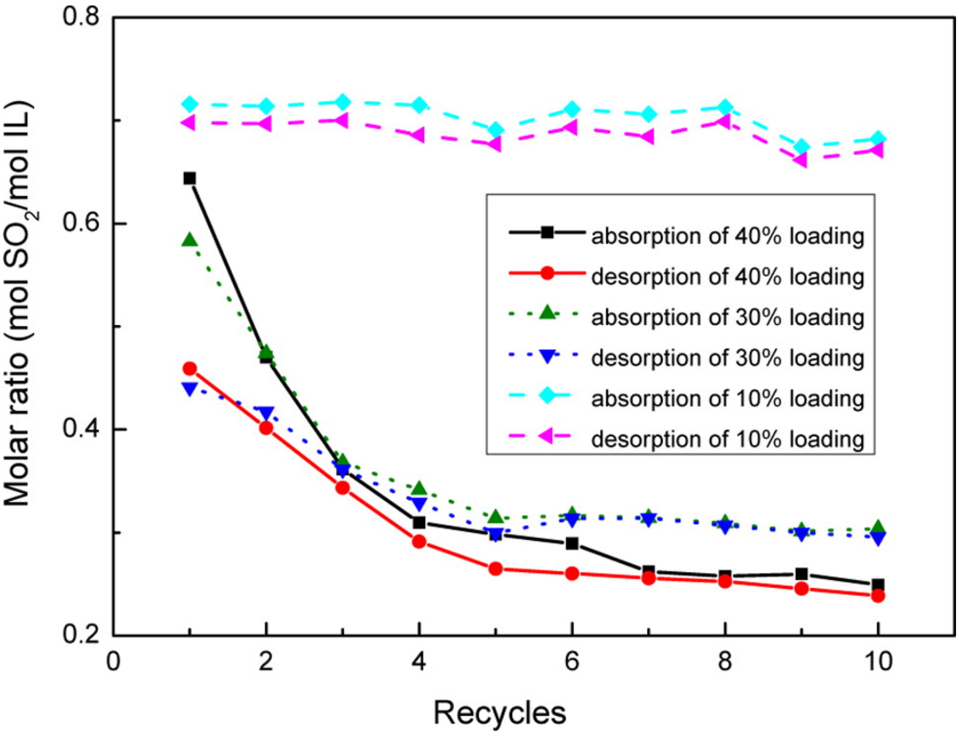

Figure 2.3: Comparisons of MCM-41-TMGL with SO_2 concentrations of ; 10%/30%/40% with ten cycles of loading [19].

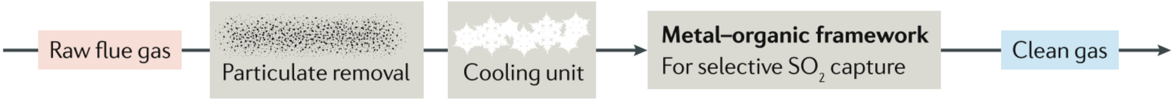

Figure 2.4: Flue gas desulphurisation for the selective capture of SO_2 by metal–organic frameworks [15].

porosity with incredibly high internal surface areas of up to 6000 m^2/g [53]. The flexible design and make up of MOFs can be used to create MOFs with high selectivity of gas absorption [21]. Metal organic frameworks can be used in conjunction with particulate removal and gas cooling, for use in flue gas desulphurisation, as seen in Figure 2.4.

2.4 Metal Organic Frameworks

Metal organic frameworks (MOFs) have been widely suggested as a possible ammonia storage and removal material [10, 25, 40]. They have also been suggested as SO_2 absorption materials

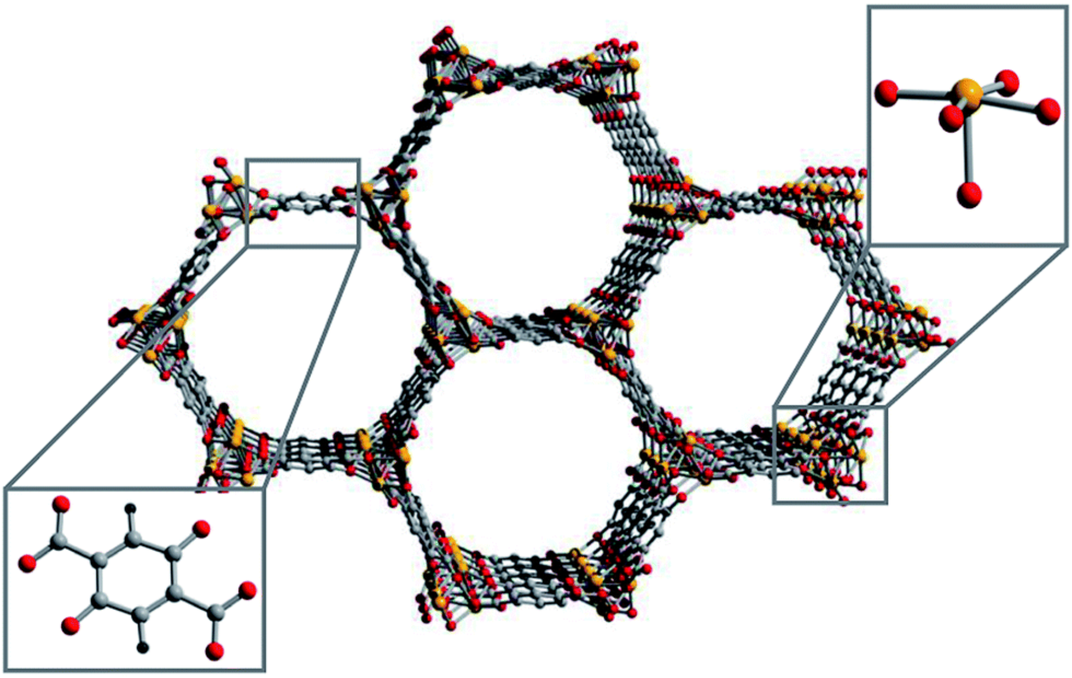

Figure 2.5: Ball and stick model of the M_2(dobdc) structure type showing the MO_5 polyhedron and (dobdc)$^{4-}$ linker. Orange, red, grey, and black spheres represent the metal, oxygen, carbon, and hydrogen atoms, respectively. [65]

[14, 15, 21, 22, 54]. MOFs consist of metal ions or clusters connected by organic linkers to form multidimensional structures, as shown in Figure 2.5 which regularly possess permanent porosity [53, 55, 56]. This high level of porosity in MOFs leads to incredibly large surface areas of over 1000 m^2g^{-1} lending them to a variety of uses, including effective gas storage materials. By appropriately selecting the metal and ligand combination, various uses can be achieved, such as chemical sensing [57], chemical separation [58, 59], catalysis [60], toxic gas adsorption [52, 61] and gas storage [62–64].

There have been many studies carried out showing the possibility of using MOFs to store gases such as hydrogen [1, 62] and carbon dioxide [59, 66]. Storage of ammonia and absorption of SO_2 in MOFs is much less studied. This is likely due to ammonia and sulphur dioxide being corrosive and having highly coordinative properties, causing it to degrade materials by breaking metal-ligand bonds. In the studies that have been carried out, a concern for the repeatability of toxic gas storage in these materials has been raised due to its corrosive nature. Gases are adsorbed both by physisorption in the pores of the MOF and by strongly binding to

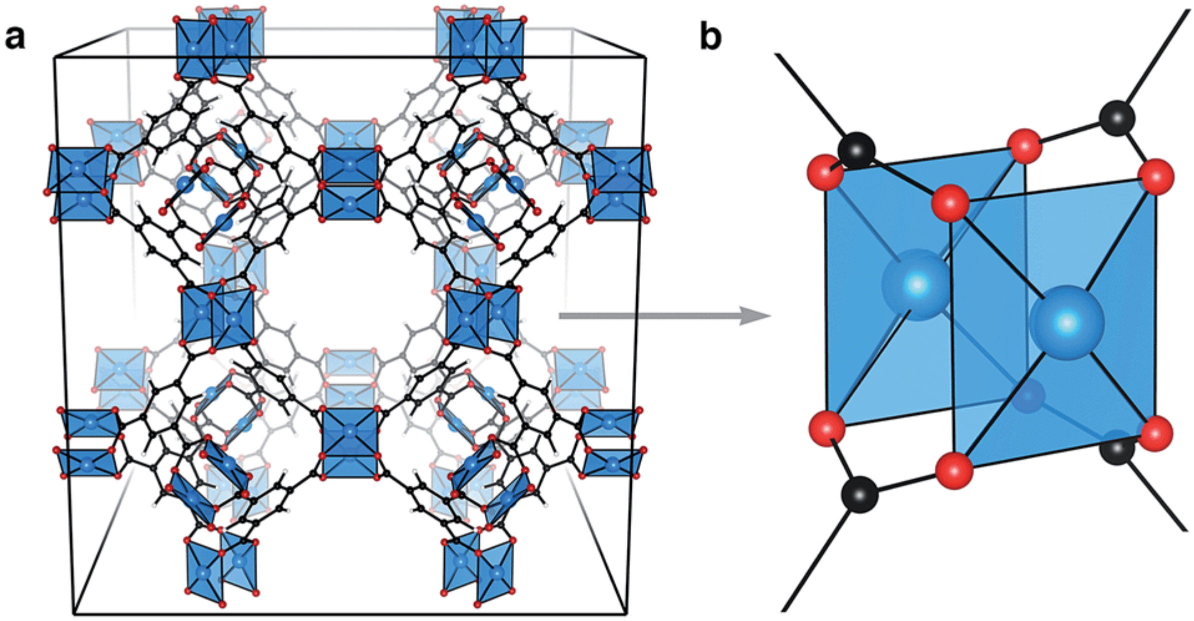

Figure 2.6: Crystal structure of HKUST-1 showing (a) crystallographic unit cell, and (b) copper paddlewheel structure[70].

the open metal sites.

In Zinc MOFs, initial studies showed that open metal sites and nucleophilic substituents improve ammonia uptake [52] but later work showed their decomposition during ammonia uptake measurements [26, 67, 68]. The copper MOF HKUST-1 was also found to be mostly stable during ammonia uptake, however it began to decompose when water was also present [41, 69]. The structure of HKUST-1 can be seen in Figure 2.6..

The absorption of ammonia in CPO-27 has been previously investigated [71, 72]. This material has shown promisingly high uptake of ammonia, predominantly due to its ability to store five coordinate Cu(II) species [40]. CPO-27(Ni) was shown to have slightly reduced ammonia capacity upon exposure to a humid environment but did not decompose. The structure of CPO-27 is shown in Figure 2.7. In this thesis the CPO-27-Co variant of this MOF is used.

The MOFs UiO-66 and UiO-67 have both been shown to be stable under ammonia absorption [42]. UiO-67 has also been shown to be a candidate for NO_2 absorption [15], methane absorption [64], and water vapour [74]. The decomposition during a TGA experiment demonstrated

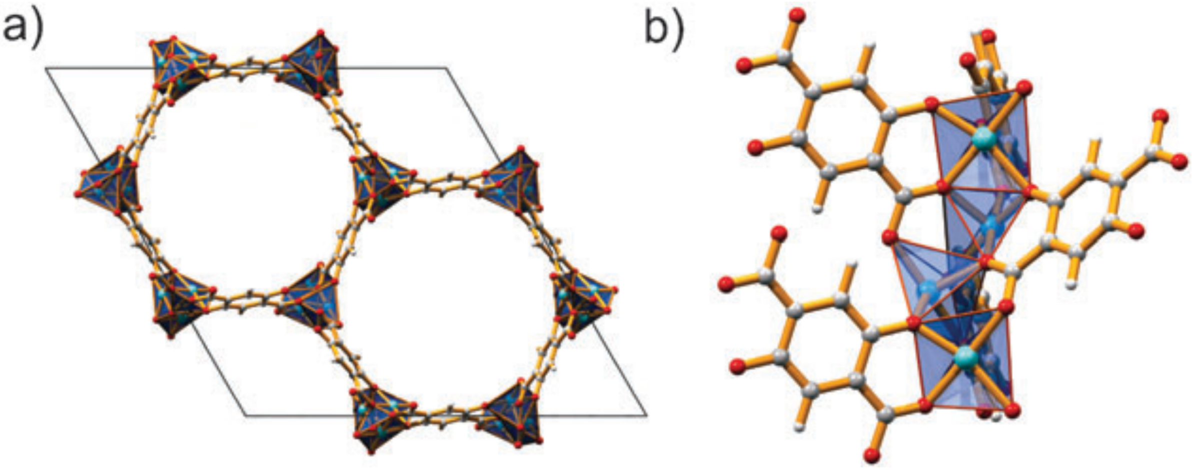

Figure 2.7: Crystal structure of the evacuated CPO-27 metal–organic framework: (a) viewed along the cylindrical channels, and (b) helical chain with accessible exposed metal coordination sites [73].

this MOF has also shown to be stable at elevated temperatures up to 540 °C [75]. The structure of UiO-67 is shown in Figure 2.8.

MFM-170 is a porous metal-organic framework with copper metal centres and carboxylate linkers. The void space in this MOF has three distinct cages ranging in size from 12 to 22 Å which alternate in a regular pattern. MFM-170 has a large surface area of approximately 2400 m^2g^{-1} due to the highly porous nature of the structure. Water on the metal centres can be removed by activation at 150 °C to open up metal sites for guest coordination. This MOF has shown to be thermally stable up to at least 330 °C. As SO_2 is a highly corrosive gas, few MOFs have shown reversible adsorption of SO_2. MFM-170 shows 42% higher SO_2 capacity than the current leading SO_2 absorption material - MFM-601, under ambient conditions. MFM-170 also shows no loss of absorption capacity after 50 cycles. Due to this high stability and SO_2 storage capacity, MFM-170 has shown its possible applications in SO_2 storage, sensing and separation. As this MOF has not yet been published, no structure can be shown in this thesis.

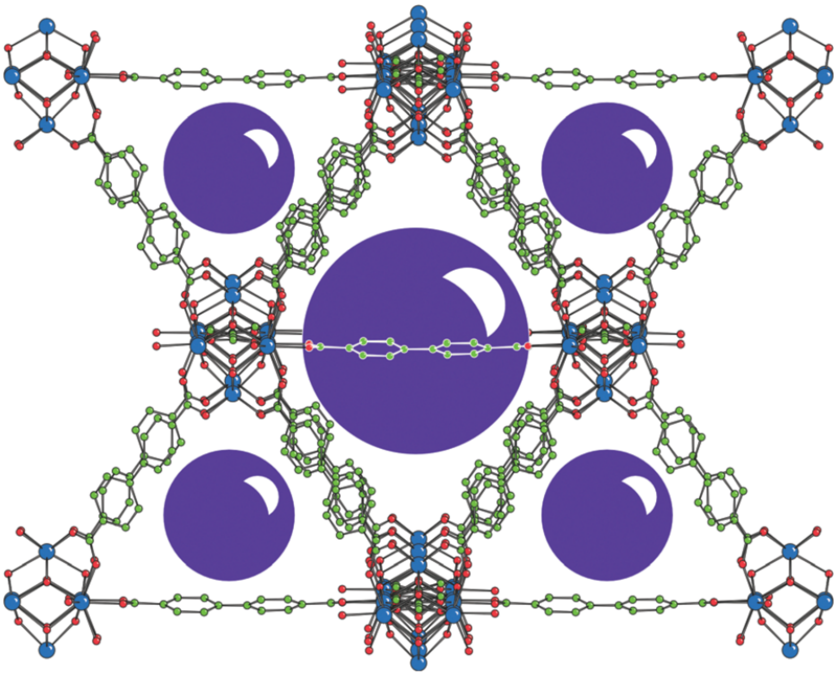

Figure 2.8: The structure of UiO-67 showing a single octahedral cage (large sphere). The face of each octahedral is shared with 8 smaller tetrahedral cages (small spheres) [71].

2.5 Metal Ammine Salts

Metal ammine salts have also been frequently suggested as a possible ammonia storage material to use for energy storage [2, 5, 27, 30, 31, 35, 45, 76]. Halide salts are simple compounds consisting of a metal atom and a halogen in the formula MX_2 where M is the metal atom and X is a halogen. These salts often form octahedral or rhomboid crystal structures around the metal centres. When ammonia is flowed through these materials, it is absorbed forming metal ammine salts. As ammonia is absorbed by the salt, the stoichiometry of the sample changes. For halide salts the stoichiometry takes the form $M(NH_3)_nX_2$ where n increases as ammonia is absorbed. Only certain stoichiometric states are valid for a given halide salt. For example magnesium chloride the stoichiometry goes from $MgCl_2$, to $Mg(NH_3)Cl_2$, then $Mg(NH_3)_2Cl_2$, and finally $Mg(NH_3)_6Cl_2$[31, 77].

The structure of $Mg(NH_3)_6Cl_2$ along with a photo of the ammoniated salt in pellet form can be seen in Figure 2.9.These materials have been shown to be capable of storing comparable volu-

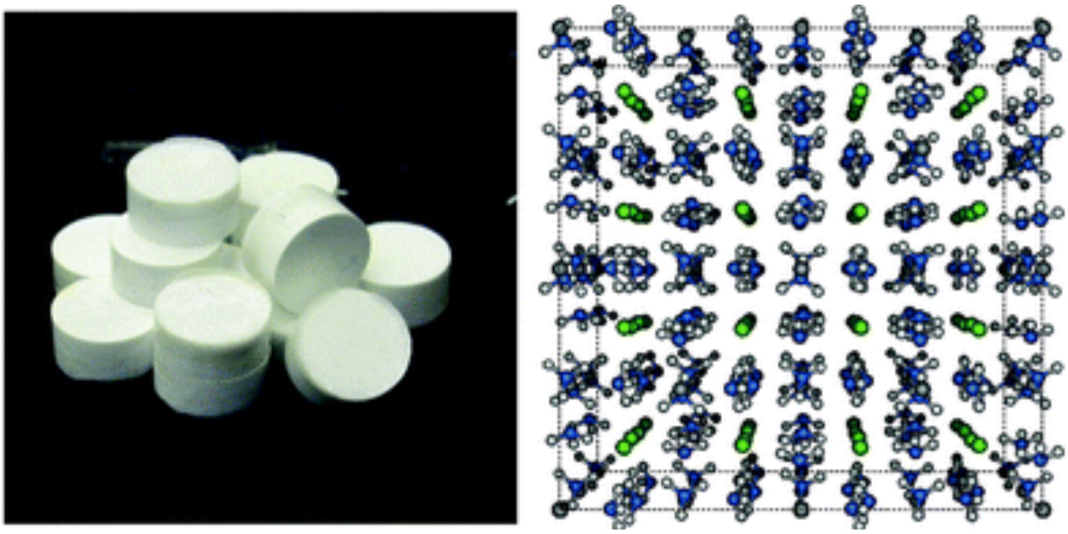

Figure 2.9: Pellets of $Mg(NH_3)_6Cl_2$ (left). The skeleton density is 1.25 g cm^{-3} and the pellets have a density within 5% of this. It crystallizes in a cubic unit cell with a lattice constant of 10.19 Å [79]. The atomic structure of the crystalline complex is shown to the right, as it comes out of an energy minimization using density functional theory calculations. Mg^{2+} is shown grey, Cl_2 is green, nitrogen blue, and hydrogen is white [29].

metric and gravimetric hydrogen densities as liquid ammonia storage methods [6]. Another benefit of storing ammonia in metal salts is that, due to their simple structure and synthesis, metal salts can be produced in a very large scale [78].

2.6 Neutron and X-ray Diffraction

Neutron or X-ray diffraction can be used to find the atomic and/or the magnetic structure of materials due to their wavelength being comparable to the distance between atoms, as will be discussed in Section 2.6.1. These methods can be used to characterise gases, liquids and amorphous solids and are especially useful for crystalline structures such as MOFs.

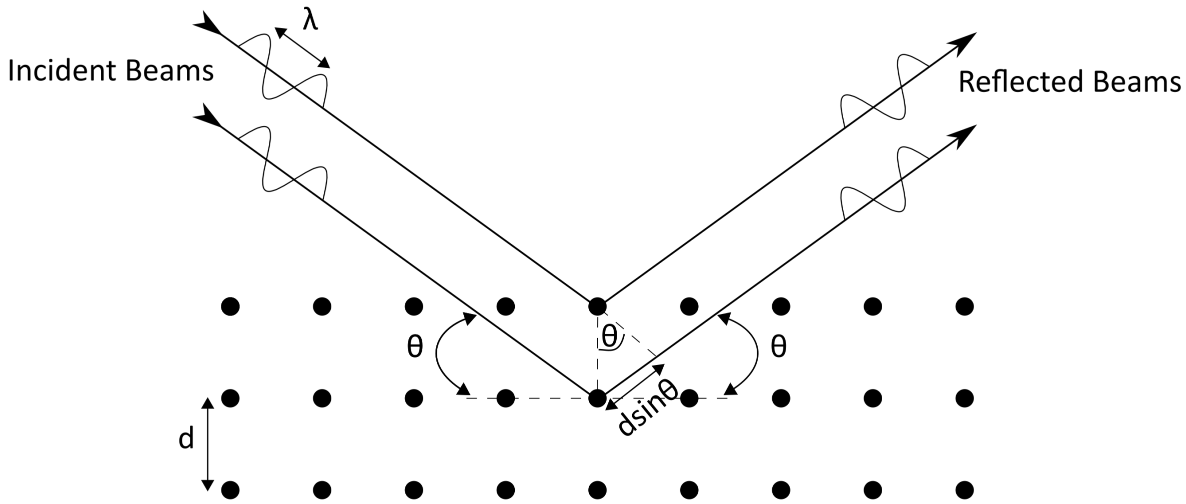

Figure 2.10: 2D representation of Bragg's Law showing incident and reflected beams with wavelength (λ) reflected by angle (θ) in a crystalline solid with interatomic distance (d)

2.6.1 Principles of Neutron and X-ray Scattering

Figure 2.10 shows how neutrons are diffracted in crystalline solids. In this figure, atoms are located distance d from each other, θ is the reflected angle and λ is the wavelength of the incident wave. Bragg's Law, defined in [80] and shown in Equation 2.1, is said to have been met when constructive interference occurs - where n is the integer number of wavelengths. The angle at which constructive interference occurs manifests itself in the Bragg diffraction data as a diffraction peak. This data is generally displayed with 2θ or d spacing along the x-axis and the intensity of neutrons at the corresponding angle on the y-axis. The location of this peak defines the distance between atoms in the sample via Equation 2.1.

$$n\lambda = 2dsin\theta \tag{2.1}$$

2.6.2 Differences Between Neutron and X-ray Diffraction

Neutrons have no net atomic charge with zero (or too small to be measurable) electric dipole moment. This means that neutrons react via nuclear forces as opposed to electrical forces.

These nuclear forces occur at a femtometer scale (10^{-15} m) with distances between nuclei of atoms over 100,000 times larger [81]. Due to this, solid matter is seemingly sparse for neutrons, leading to their high penetration depth when compared with charged particles. This allows neutron scattering techniques to be used on bulk solids. Alternatively, X-rays are part of the electromagnetic spectrum and are scattered by the electron cloud of an atom. This process works in the same way that visible light diffracts through a diffraction grating, however with X-rays it occurs on an atomic scale. As electron clouds are much larger than the nucleus of an atom, X-rays have much smaller penetration depths than neutrons.

The scattering length of X-rays increases as the atomic number of the element increases. As nuclei are seen as point scattering centres by an incident neutron beam, neutron scattering lengths show no angular dependence and therefore have seemingly random scattering lengths. Due to this, elements with similar atomic number or different isotopes of the same element are difficult to resolve using X-ray diffraction, but often appear very different by neutrons. Alternatively, elements with similar neutron scattering lengths can often be better resolved by X-ray diffraction. The scattering amplitudes for atomic weights for both neutron and X-ray diffraction can be seen in Figure 2.11.

2.6.3 Diffraction Techniques

Using a randomly oriented single crystal and arbitrary wavelength neutron or X-ray beam it is highly unlikely for diffraction to occur. In order to ensure Bragg's condition has been met there are three practical approaches.

Firstly a single crystal sample with a monochromatic radiation can be used to obtain the structure of the sample. This technique is often used to observe the structure of minerals and large organic molecules in crystalline form [83].

Another method is the "Laue method". This technique also involves a single crystal sample but this time uses a variety of wavelengths of radiation, often referred to as "white" radiation.

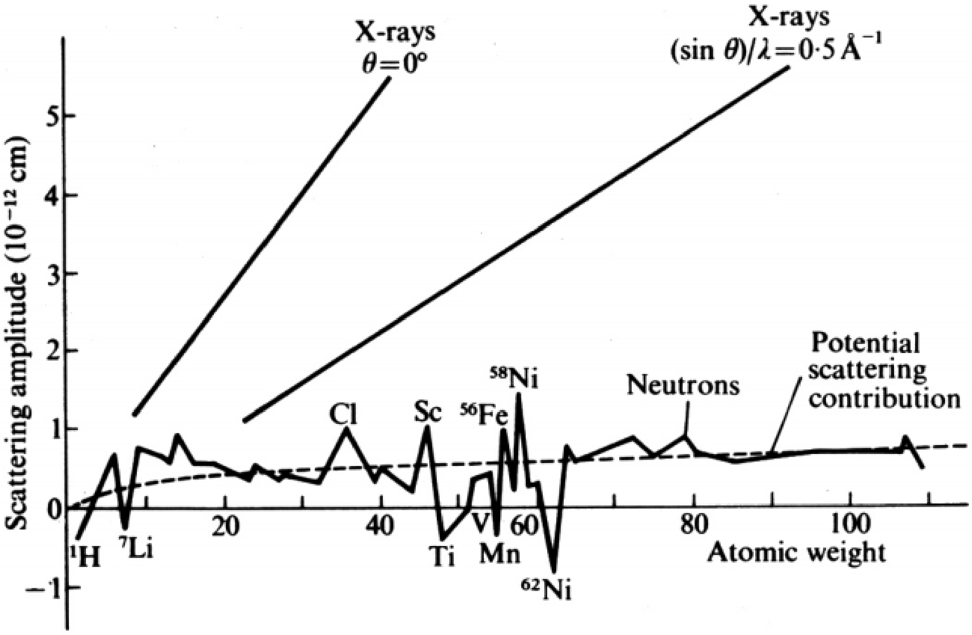

Figure 2.11: The variation of the scattering amplitude of atoms for neutrons as a function of their atomic weight. The irregular variation is contrasted with the linear variation for X-rays, which depends also on the angle of scattering [82].

This technique is most commonly used to find the orientation of a single crystal structure. The position of the sample and radiation source are kept stationary while a white neutron or X-ray beam is used. Some of the incident neutrons or X-rays are of the correct wavelength to meet Bragg's condition, meaning a certain interatomic distance present in the sample. The spots produced in a Laue diffraction pattern, indicated by the red circles in Figure 2.12 on a given radial row, can be from various combinations of wavelengths and crystal planes, making it difficult to evaluate these combinations [83]. It becomes especially difficult using this method to evaluate a sample with various crystal orientations.

Additionally, the "Debye–Scherrer" method can be used, which utilises a monochromatic radiation beam with a powdered or polycrystalline sample. As the crystals in the powder are randomly aligned, the vast majority of the planes are misoriented; however, in a powdered sample some crystals will be aligned for diffraction to occur. It is this principle which is used to achieve neutron powder diffraction [81]. Using this method neutrons are diffracted in a cone, as shown in Figure 2.13. These cones result in a diffraction pattern such as the

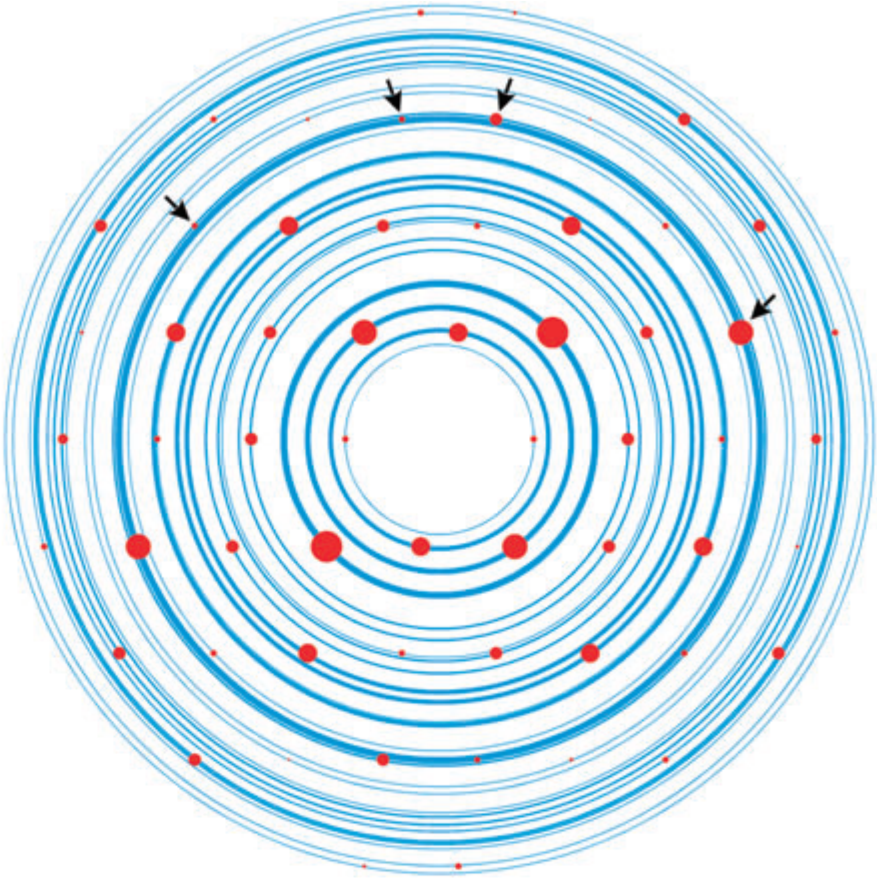

Figure 2.12: A single crystal diffraction pattern (red circles) overlaid on the corresponding powder diffraction pattern (blue rings). One group of four overlapping reflections is indicated with arrows. The diffraction angle 2θ increases radially from the centre of the diffraction pattern [84]

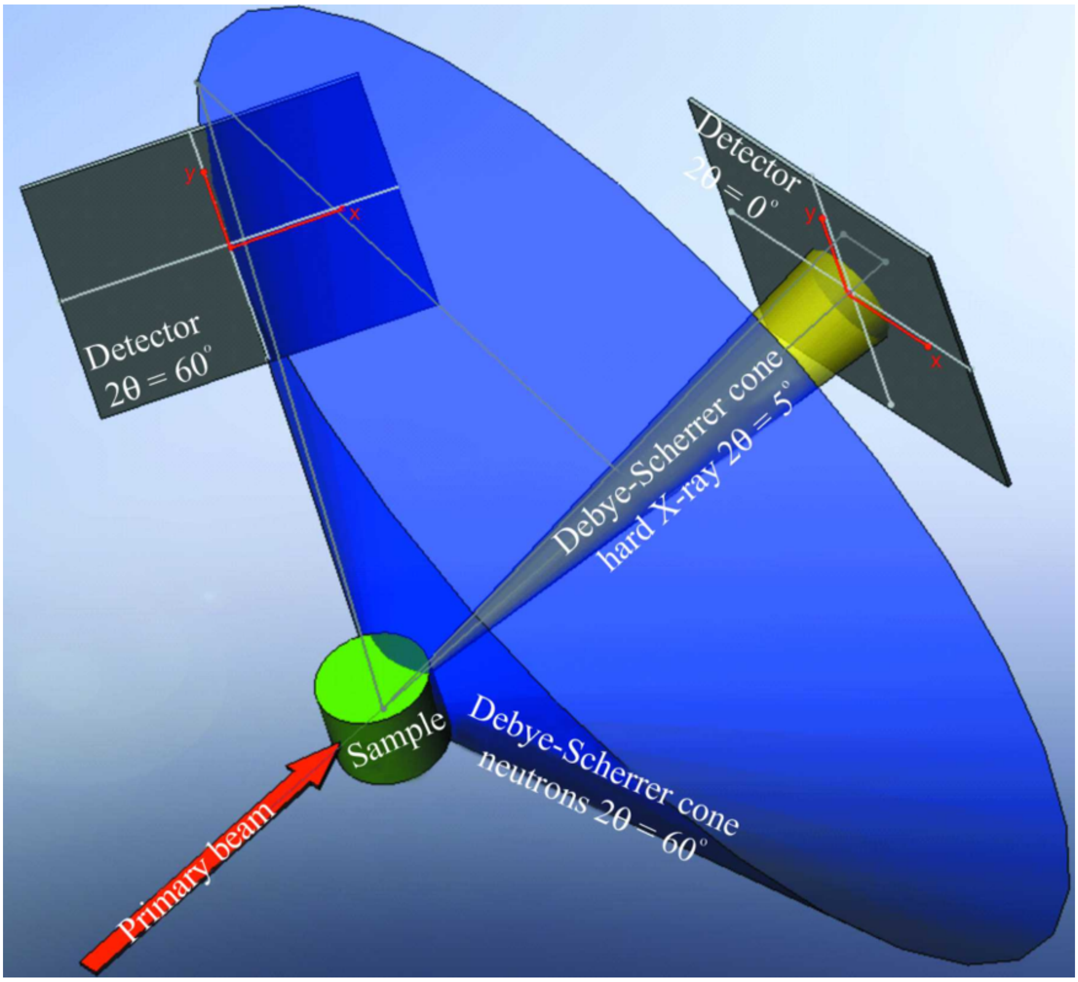

Figure 2.13: Schematic illustration of the standard detector position for neutron and hard X-ray texture measurements [85].

blue rings in Figure 2.12. The angles from which the neutrons or X-rays are diffracted from the sample to produce these rings are recorded and used to produce a series of Bragg peaks. The location of these Bragg peaks defines the interatomic distances present in the powdered sample. A typical powder diffraction pattern is shown in Figure 2.14.

Finally it is possible to use a polycrystalline or powdered sample with a white radiation source. Initially it seems that with variably aligned crystals and a variety of wavelengths of radiation, this method would cause Bragg peaks to occur at varying angles for the same d-spacing, without a way to resolve them. A way around this is to use a time-of-flight (TOF) diffractometer. By knowing the precise time the neutrons of a specific energy enter the sample chamber,

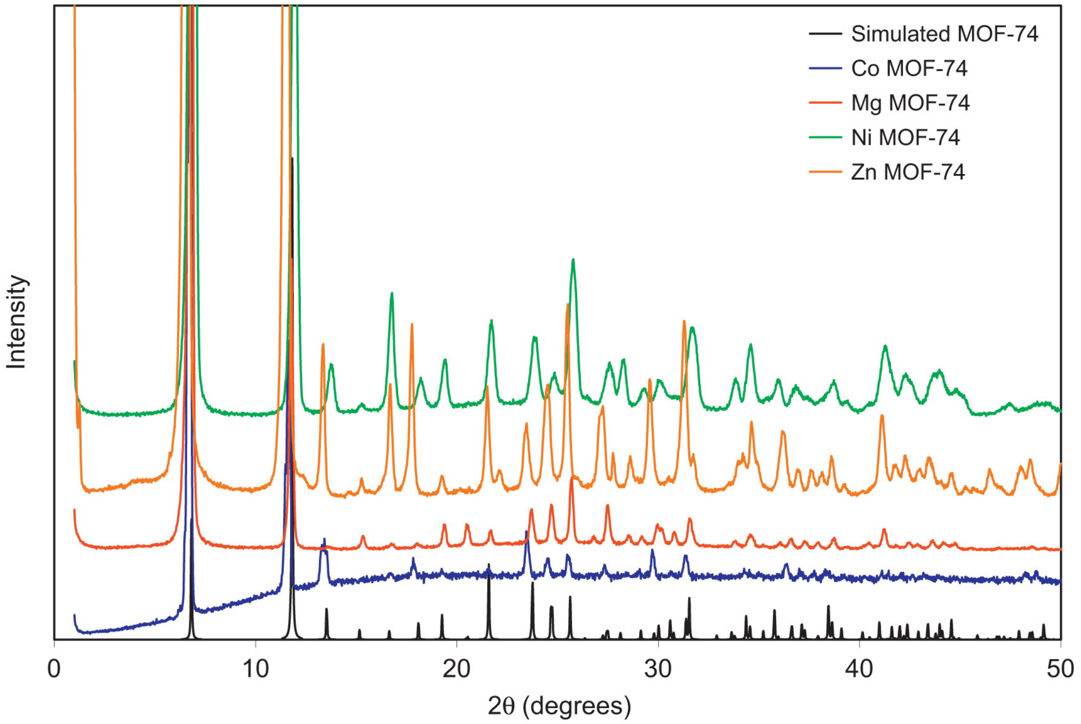

Figure 2.14: Powder X-ray diffraction patterns for MOF-74 analogues [61]

and the distance they must travel to pass through the sample and reach the measurement plane, it is possible to find the energy of the neutron. With the knowledge of the energy of the neutron and its angle of diffraction, the corresponding d-spacing can then be calculated. An example of a TOF diffractometer is Polaris at the ISIS neutron and muon source.

2.7 Microwave Measurements

Microwaves are a form of electromagnetic radiation from 1 GHz to 30 GHz with free space wavelengths from 30 cm down to 1 cm, respectively. As well as the conventional idea of microwave heating, microwaves are commonly used in wireless communications such as Wi-Fi, mobile communications and in satellite navigation systems. They can also be utilised to perform microwave measurements. Using microwave measurement techniques various properties can be measured, for example; polarity, dielectric loss, temperature, concentration and flow rates. Predominantly in this thesis they are used to measure dielectric properties of materials -

permittivity (ε) and permeability (μ).

2.7.1 Dielectric Properties

The electrical properties of a material can be expressed through its permittivity (ε) . The permittivity of a substance is its ability to store and dissipate electrical energy in an applied electric field. The complex permittivity of a material is expressed as $\varepsilon = \varepsilon_1 - j\varepsilon_2$. When a dielectric material is placed in an electric field this causes a polarisation of the material which creates a dipole moment to oppose the applied field [86]. This effect caused by the polarisation of the material is quantised by the real part of the permittivity, ε_1. The polarity of a molecule can be expressed as its electric dipole moment. For water this dipole moment is 1.85 D. The polar gases investigated in this thesis, ammonia and sulphur dioxide, have dipole moments of 1.47 D and 1.63 D respectively [87]. The imaginary part, ε_2, relates to the materials dielectric energy loss (lost as heat). This is caused by the dampening of vibrating dipole moments [86].

The magnetic property of a material can similarly be expressed in terms of its permeability (μ). Analogous to the electrical case, permeability can also be expressed in the complex form $\mu = \mu_1 - j\mu_2$. Applying a magnetic field to a sample causes magnetic dipole moments to align, leading to magnetic polarisation, commonly known as magnetisation and quantised as μ_1. The magnetic dampening is quantised through μ_2, which plays the same role in magnetic samples as ε_2 in dielectrics.

2.7.2 Microwave Cavity Perturbation Technique

The microwave cavity perturbation technique is a commonly used method to assess dielectric properties of materials. This approach involves introducing a sample with a small volume into a microwave cavity. It is assumed that the addition of this sample does not greatly change the fields from the empty cavity. Changes in the resonant frequency and bandwidth of the system can be related to the dielectric properties of the sample material. The numerical analysis of this can be achieved using the perturbation equation shown in Equation 2.2 derived from Maxwell's Equations [86, 88–90].

$$-\frac{\delta\omega}{\omega} = \frac{\int_{V_s} \varepsilon_0(\varepsilon_r - 1)\bar{E}_s \cdot \bar{E}_c^* + \mu_0(\mu_r - 1)\bar{H}_s \cdot \bar{H}_c^* dV}{\int_{V_c} \varepsilon_0 \bar{E}_c \cdot \bar{E}_c^* + \mu_0 \bar{H}_c \cdot \bar{H}_c^* dV} \tag{2.2}$$

where V_s and V_c are the volume of the sample and cavity, ε_r and μ_r are the complex relative permittivity and permeability, $\bar{E}_s$ and $\bar{H}_s$ are the electric and magnetic fields at the sample location, respectively, and $\bar{E}_c$ and $\bar{H}_c$ are the electric and magnetic fields in the unperturbed cavity, respectively. This shows that when a sample is placed into an electromagnetic field, the resonant frequency and bandwidth of the sample loaded cavity change in accordance to the material's permittivity and permeability. Equation 2.2 relies on two assumptions [90, 91]:

1. The field in the empty cavity is changed negligibly by the addition of the sample.
2. The sample is placed within a volume in which the field is uniform.

As this thesis focusses on electric properties of materials, when the sample is placed at the maximum of electric field Equation 2.2 can be simplified to Equation 2.3[90, 91].

$$-\frac{\delta\omega}{\omega} = \frac{(\varepsilon_r - 1)\int_{V_s} \bar{E}_s \cdot \bar{E}_c^* dV}{2\int_{V_c} |\bar{E}_c \cdot \bar{E}_c| dV} \tag{2.3}$$

The complex frequency can be separated into its real and imaginary parts as shown in Equation 2.4,

$$\frac{\delta\omega}{\omega} = \frac{(f_s - f_0)}{f_s} + \frac{j}{2}\left[\frac{1}{Q_s} - \frac{1}{Q_0}\right] \tag{2.4}$$

where f_0 and Q_0 are the resonant frequency and Q-factor of the empty cavity, respectively, and f_s and Q_s are the frequency and Q-factor with sample inserted. If the aforementioned assumptions are satisfied then $E = E_0$ and $H = H_0$. Equation 2.3 can then be integrated and rearranged to show that the real and imaginary parts of permittivity can be calculated using Equations 2.5 and 2.6 [90, 91].

$$\varepsilon_{1r} = \frac{(f_0 - f_s)}{2f_0}\frac{V_c}{V_s} + 1 \tag{2.5}$$

$$\varepsilon_{2r} = \frac{V_c}{V_s}\left(\frac{1}{Q_s} - \frac{1}{Q_0}\right) \tag{2.6}$$

2.7.3 Resonator Model

To measure the resonant frequency of a microwave resonator, microwave frequencies are swept and power is measured at each frequency by a Vector Network Analyser (VNA). For a one port network, the magnitude of the reflected power $|S_{11}|^2$ is measured close to resonance. In this case, at resonance, the minimum amount of power is reflected causing a minima in reflected power. Alternatively a two port measurement may be conducted. This setup can measure the transmitted power $|S_{21}|^2$. Transmitted power measurements will have a maxima in transmitted power at resonance. It is possible to model the impedance of the resonator using an RLC circuit.

A microwave resonator can be capacitively coupled with an open circuit transmission line coupling to the resonators electric field. Alternatively it may be coupled to inductively using coupling loops to couple to the magnetic field of the resonator. The equivalent circuit of a two port, inductively coupled microwave resonator can be seen in Figure 2.15. The coupling loops in this circuit have associated mutual inductances m_1 and m_2 located at resonator ports 1 and 2, respectively. The mutual inductances are related to the geometry of the loops such as the area of the loop, the orientation of the loop, and the position of the loop with respect to the microwave resonator. When coupling loops are identical they will have a single mutual inductance $m = m_1 = m_2$. Self inductances can be assumed to be negligible for this analysis since the loops are made small to ensure this factor can be neglected..

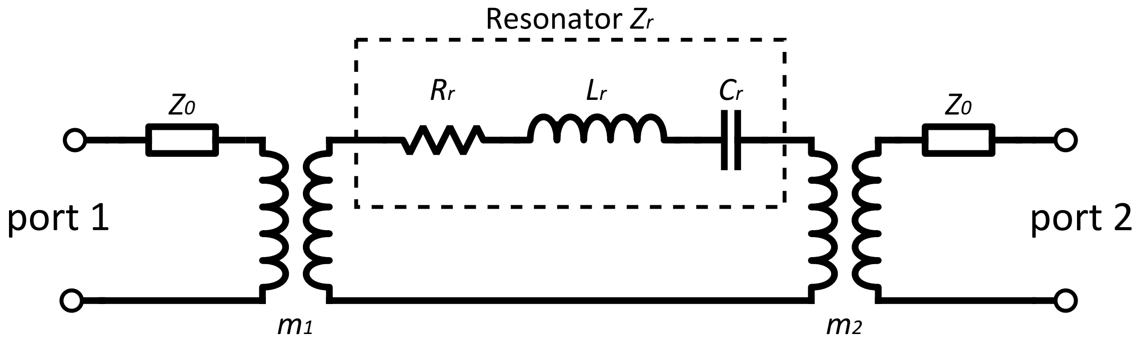

Figure 2.15: The equivalent circuit of a two port, loop-coupled resonator

As seen in Figure 2.15 the resonator's impedance Z_r can be separated into its resistance R_r, inductance L_r, and capacitance C_r. First consider an empty metal cavity. The resistive element is associated with the power losses in the cavity walls due to surface currents. The reactive components are associated with the electromagnetic energy stored in the resonator. The angular resonant frequency, impedance, and unloaded Q factor of this circuit are defined in Equations 2.7, 2.8, and 2.9, respectively. The input and output lines have their own characteristic impedance Z_0, typically 50 Ω.

$$\omega_0 = \frac{1}{\sqrt{L_r C_r}} \tag{2.7}$$

$$Z_r = R_r + j\omega L_r + \frac{1}{j\omega C_r} \tag{2.8}$$

$$Q_0 = \frac{\omega_0 L_r}{R_r} \tag{2.9}$$

As described in [92], for a high Q resonator the resonator impedance, close to its resonant frequency, can be approximated to:

$$Z_r \approx R\left[1 + j2Q_0\left(\frac{f - f_0}{f_0}\right)\right] \tag{2.10}$$

The dimensionless coupling coefficients are defined in Equations 2.11 and 2.12. Increasing the power transmission at resonance can be achieved by increasing m and therefore coupling strength, increasing Q_0 or by increasing both. In most cases it is convenient to have symmetrical coupling, such that $g = g_1 = g_2$.

$$g_1 = \frac{\omega_0^2 m_1^2}{Z_0 R_r} = \frac{\omega_0^2 m_1^2 Q_0}{L_r} \tag{2.11}$$

$$g_2 = \frac{\omega_0^2 m_2^2}{Z_0 R_r} = \frac{\omega_0^2 m_2^2 Q_0}{L_r} \tag{2.12}$$

The peak power at resonance P_0 and the loaded Q factor Q_L are given by Equations 2.13 and 2.14, respectively.

$$P_0 = \left(\frac{2g}{1+2g} \right)^2 \tag{2.13}$$

$$Q_L = Q_0 \left(1 - \sqrt{P_0} \right) \tag{2.14}$$

The loaded Q factor refers to the fact that the resonator is coupled to the outside world, and these coupling ports act as loss mechanisms. This means that the measured Q factor, known as the loaded Q factor, is lower than the unloaded Q factor (i.e. Q_0) due to the effects of coupling. In practice, Q_0 can be found in a straightforward way using the following analysis. Finally the power at a specific frequency can be calculated using Equation 2.15.

$$P(f) = \frac{P_0}{1 + 4Q_L^2 \left(\frac{f - f_0}{f_0} \right)^2} \tag{2.15}$$

Hence, the loaded Q factor (i.e. Q_L) is deduced by fitting the measured data for $P(f)$ to a Lorentzian curve (as implied by Equation 2.15), and the unloaded Q factor (i.e. Q_0) is calculated using the relationship in Equation 2.14.

2.7.4 Cavity Modes

At different resonant frequencies in a microwave cavity, different field patterns are produced. It is possible to take advantage of these various field patterns, called modes, for different applications. Microwave cavity measurement modes can be referred to as either a transverse magnetic (TM) where $H_z = 0$, or transverse electric (TE) where $E_z = 0$. Here, the cavity can be considered to be fully enclosed by a single metal surface, and for the associated waveguide modes that set up the cavity resonance, to be propagating along the z-axis. For cylindrical cavities used predominantly in this thesis, cavity modes are referred to as either TM_{mnp} or TE_{mnp} where m, n and p relate to the number of field nodes along the azimuthal, radial and axial variation respectively.

As described in [86], assuming all fields to be phasors with time-dependence described by $e^{j\omega t}$, the electric field amplitudes (E_r, E_ϕ) for TE_{mn} and TM_{mn} circular waveguide modes can be expressed as:

$$\bar{E}_t(r,\phi,z) = \bar{e}(r,\phi)(A^+e^{-j\beta_{mn}z} - Ae^{-j\beta_{mn}z}) \tag{2.16}$$

where $\bar{e}(r,\phi)$ represents the variation of the mode and A represents either the E or H field with the sign indicating the direction. The propagation constant β_{mn} for a TE_{mn} mode can be expressed as:

$$\beta_{mn} = \sqrt{(\omega\sqrt{\mu\varepsilon})^2 - (\frac{k'_{mn}}{a})^2} \tag{2.17}$$

Similarly the propagation constant β_{mn} for a TM_{mn} mode can be expressed as:

$$\beta_{mn} = \sqrt{(\omega\sqrt{\mu\varepsilon})^2 - (\frac{k_{mn}}{a})^2} \tag{2.18}$$

where k_{mn} and k'_{mn} are the n^{th} root of the m^{th} order Bessel functions $J_m(x)$ and $J'_m(x)$, respectively. Since $\bar{E}_t = 0$ at $z = 0$, values must be chosen such that $A^+ = -A^-$ and

$$\beta_{mn} l = p\pi \tag{2.19}$$

for $p = 0, 1, 2, 3....$ This suggests length p must be an integer of half wavelengths long. Taking this into account the resonant frequency for TE_{mnp} mode is:

$$f_{mnp} = \frac{c}{2\pi\sqrt{\mu_r\varepsilon_r}}\sqrt{(\frac{k'_{nm}}{a})^2 + (\frac{p\pi}{l})^2} \tag{2.20}$$

and the resonant frequency for TM_{mnp} mode is:

$$f_{mnp} = \frac{c}{2\pi\sqrt{\mu_r\varepsilon_r}}\sqrt{(\frac{k_{mn}}{a})^2 + (\frac{p\pi}{l})^2} \tag{2.21}$$

When measuring the bulk electric properties of materials, the measurement modes TM_{0n0} are predominantly used. This is due to the constant high electric field within the volume of the sample if placed along the cavity axis, with zero magnetic field occupying the same volume, as shown in Figure 2.16. The TM mode with the lowest frequency is is $\text{TM}_{010}$and is the most commonly used mode for this purpose and is shown in Figure 2.16. For all of these modes, as $p = 0$ the field is constant along the height of the cavity.

Similarly, for the measurement of bulk magnetic properties the modes TE_{0np}(where p is an integer greater than 0) are used. In this case, the sample again occupies the volume of high magnetic field along the axis of the cavity, where the electric field can be assumed to be zero. Again the lowest frequency mode for this is TE_{011}.

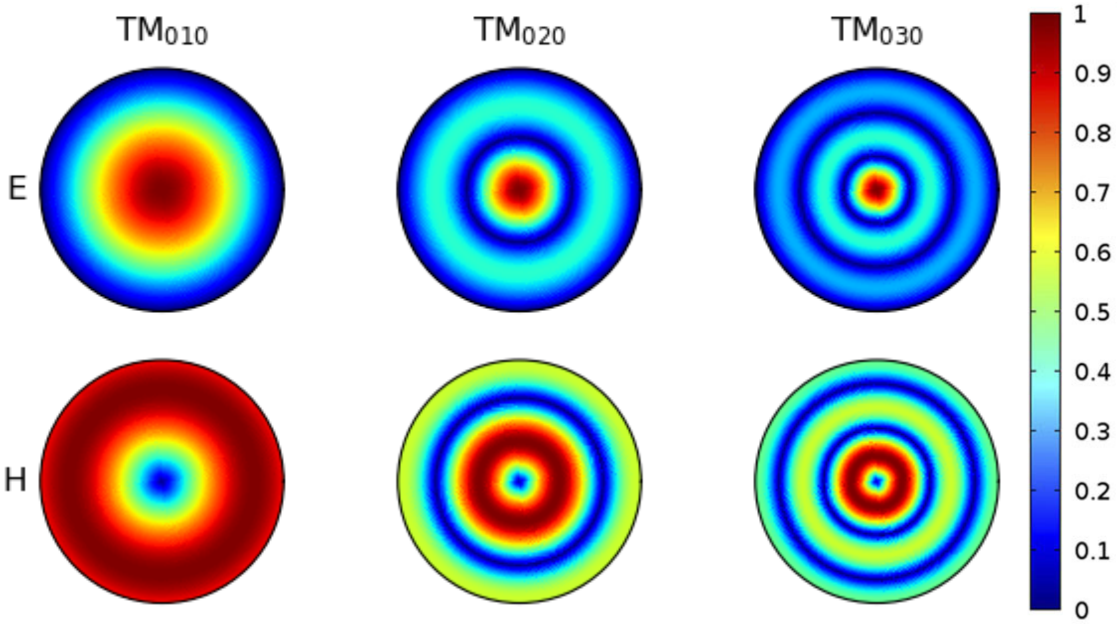

Figure 2.16: Electric field (E) and magnetic field (H) patterns for the degenerate TM_{010}, TM_{020}, and TM_{030} modes.

Other frequently used modes have a zero for both electric and magnetic field at their centre. These modes are commonly used for temperature correction as described in detail in Section 2.7.7, since they are not perturbed by the presence of a sample.

2.7.5 Coupling

Coupling of microwave fields into the resonant structures described in this thesis is provided in two different ways [93]. In order to couple into the electric field of a resonant structure, an antenna type coupling probe is used to capacitively couple to this field. This can be provided by a straight section of wire, the length and position of which can be adjusted to regulate the coupling strength. This type of coupling is used in the C1 and C2 cavities discussed in this thesis. This structure is shown in Figure 2.17(a). Alternatively, coupling can be provided by a coupling loop to inductively couple into the magnetic field of a resonant structure. Coupling strength of a loop can be adjusted by changing the size or shape of the loop, the number of

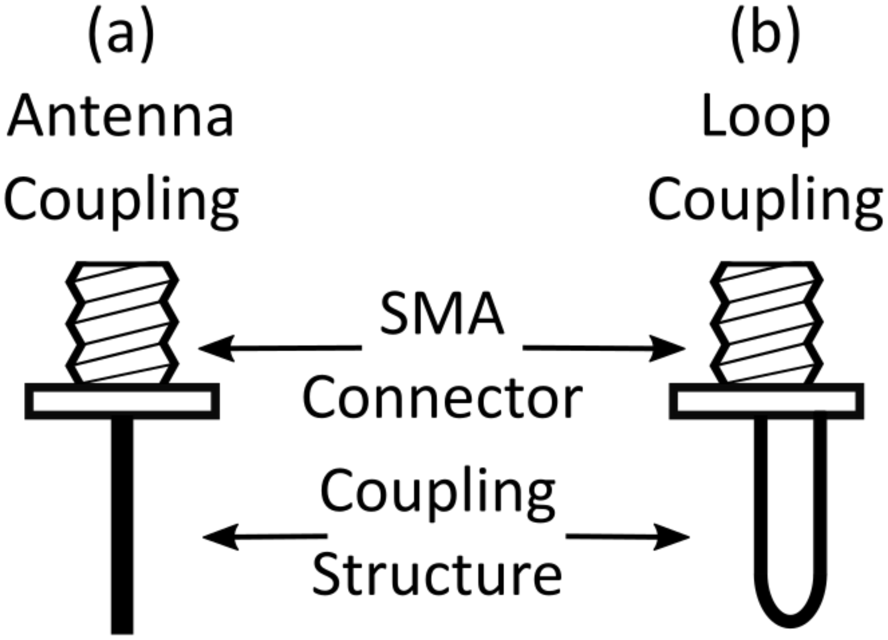

Figure 2.17: Schematic diagram of coaxial SMA connector jacks with (a) antenna probe coupling and (b) loop coupling

turns (although it is usually impractical to have more than one turn, without increasing the undesired self-inductance of the loop), or the angle at which it is inserted into the resonant structure. This type of coupling is used in the H1 hairpin type resonator discussed in this thesis. This coupling structure is shown in Figure 2.17(b).

2.7.6 Simulation

The simulations carried out in this thesis have been performed using COMSOL Multiphysics. COMSOL is a general purpose simulation software capable of simulating a wide range of physics. This includes; electromagnetics, structural mechanics and acoustics, fluid flow and heat transfer, and chemical engineering, as well as multi-purpose optimisation and the possibility to interface with popular CAD software. COMSOL is used in this work for simulation of electromagnetic waves, to observe field patterns of resonant structures, and to simulate heat transfer, to ensure heating equipment stays within operating temperatures during experiments [94].

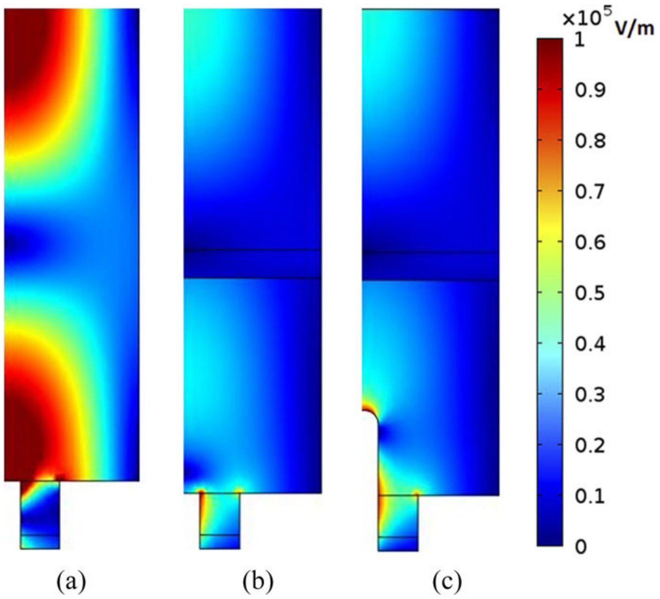

Figure 2.18: Electric field distribution (a) for an empty resonant cavity, (b) for an empty resonant cavity with a separation plate, (c) for an empty resonant cavity with a separation plate and an antenna insertion, the full field strength is still present in this structure with the auto-scaling of colour showing high field strength at the coupling structure [95].

COMSOL allows users to input the geometry of the system to be simulated, include materials and desired physics, create a mesh for refinement before computing the result. Resonator field simulations can be completed using a 3D simulation, Electromagnetic Waves - Frequency Domain physics, and Eigenfrequency study. This allows the software to compute the electromagnetic field pattern of a three dimensional resonant structure for a range of cavity resonant modes. An Eigenfrequency study is first used to quickly find resonant frequencies and field patterns of the desired resonant cavity modes. A frequency domain study, which would be very time consuming if run over all frequencies, can then be conducted only around the resonant frequencies found from the Eigenfrequency analysis. This can be used to ensure adequate frequency separation between cavity modes. An example of the field pattern generated from COMSOL for a resonant cavity can be seen in Figure 2.18 from [95]. Heating of structures over time can be completed using a 3D simulation, Heat Transfer with Surface-to-Surface Radiation, and Time Dependent study. This allows the software to compute the temperature of points in a structure as it is heated, including conduction, convection, and radiation. An example of the heat distribution in the human eye can be seen in Figure 2.19 from [96].

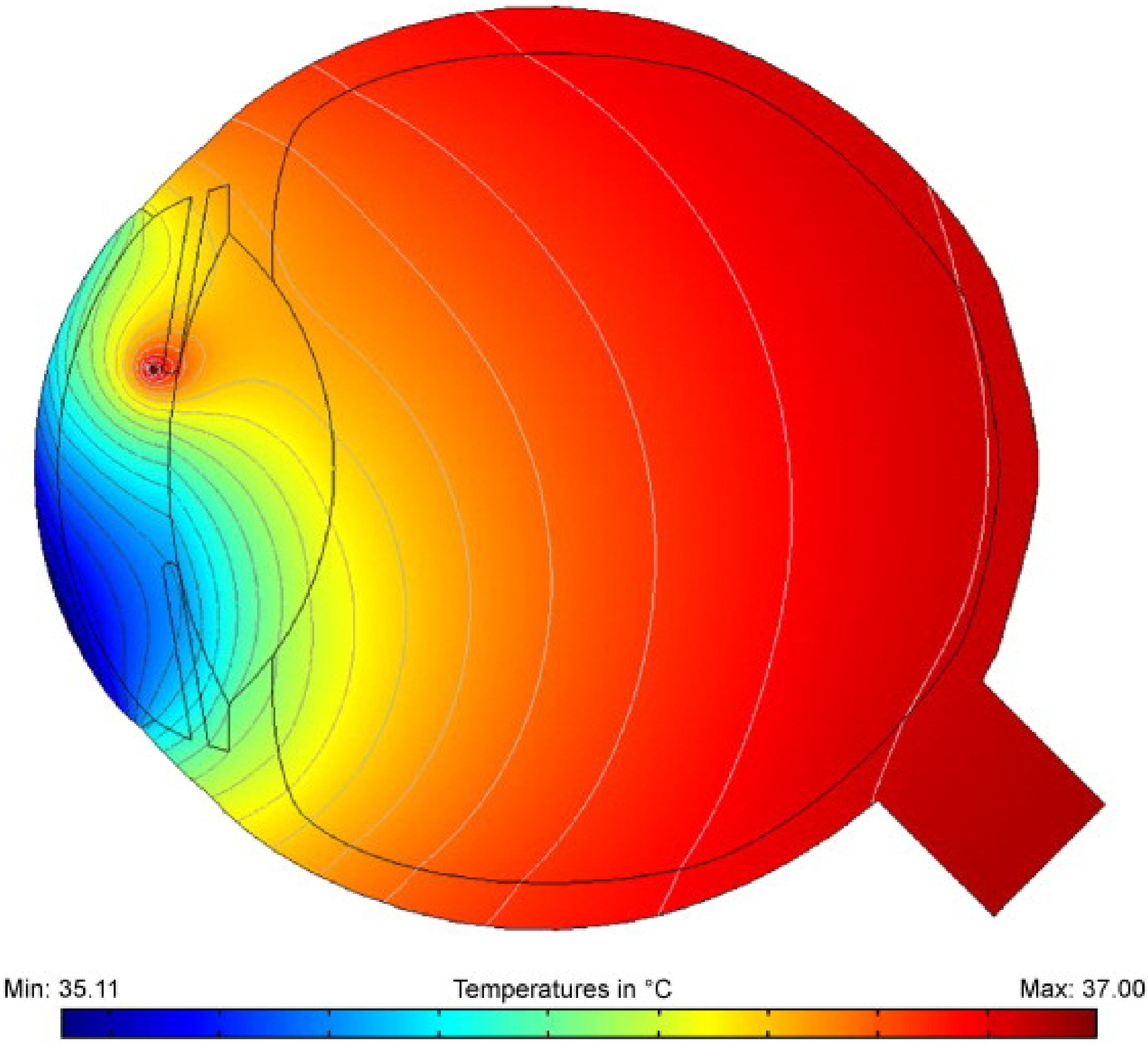

Figure 2.19: Temperature distribution of the eye with aqueous humor flow and artificial heat source in place at t = 50 s [96].

2.7.7 Temperature Correction

When using the microwave perturbation technique, changes in temperature must be taken into account. When a metal cavity experiences a change in temperature, this causes the cavity to expand or contract. Any changes in the geometry of the cavity, even changes as small as those caused by thermal expansion of the cavity, change its resonant frequency. Changes in resonant frequency per change in temperature can be found using Equation 2.26. This equation shows the change in frequency is only due to the temperature change and the linear thermal expansion coefficient of the metal from which the cavity is made. This means that changes in temperature could mistakenly be interpreted as a difference in the properties of the material being measured. This is particularly important for the experiments in this thesis, where real-time data are reported associated with small changes in resonant frequency, linked to the state of the sample. In order to account for this, either the cavity must be kept at a constant temperature or changes caused by temperature must be factored out.

Temperature is typically corrected for using two different modes, a measurement mode and a temperature correction mode. The measurement modes most commonly used for electric properties are the TM_{0n0} modes with an axially placed sample. These modes are chosen as the field can be assumed to be constant over the sample volume with a high electric field and no magnetic field in the location of the sample. The reference mode used for temperature correction is chosen which has zero electric or magnetic field at the sample location, generally TM_{m10} modes. The electric and magnetic field patterns for the TM_{110}, TM_{210}, TM_{310}, and TM_{410} modes are shown in Figure 2.20. This ensures that any change in frequency or bandwidth in this mode must be caused solely by changes in temperature of the cavity. These choices of modes allow the measurement mode to be sensitive to changes in electric properties of the sample, while the reference mode allows for temperature correction to be applied.

Using the microwave characterisation technique, the measured resonant frequency f_0 can be

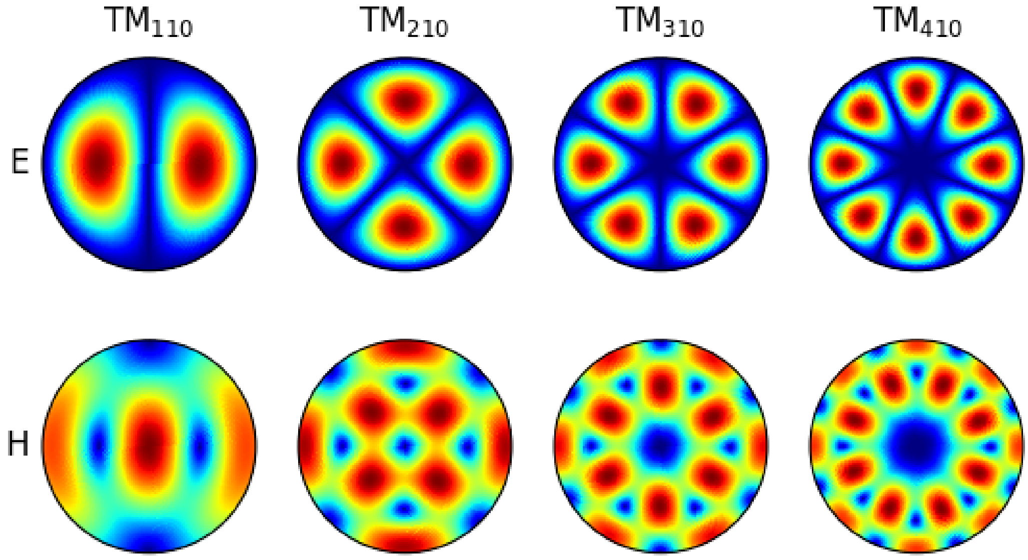

Figure 2.20: Electric field (E) and magnetic field (H) patterns for the degenerate TM_{110}, TM_{210}, TM_{310}, and TM_{410} modes.

calculated using Equation 2.22,

$$f_0 = \frac{c}{2\pi}\sqrt{\left(\frac{k_{mn}}{a(T)}\right)^2 + \left(\frac{p\pi}{l(T)}\right)^2} \tag{2.22}$$

where c is the speed of light, m,n, and p are the mode integers, k_{mn} is the n^{th} root of the m^{th} order Bessel function of the first kind and $a(T)$ and $l(T)$ are the temperature dependent radius and height of the cavity, respectively. As described in [97, 98], the temperature dependent dimensions of the cavity can be described using the first order, linear thermal expansion approximation,

$$a(T) \approx a_0(1+\alpha_c\Delta T) \tag{2.23}$$

$$l(T) \approx l_0(1+\alpha_c\Delta T) \tag{2.24}$$

where a_0 and l_0 are the initial dimension lengths, ΔT is the change in temperature, and α_c is the linear thermal expansion coefficient of the cavity material. First-order partial derivatives can be used to find the change in resonant frequency caused by a change in temperature, the result being given by,

$$\frac{\delta f_0}{\delta T} \approx \frac{\delta f}{\delta a}\frac{\delta a}{\delta T} + \frac{\delta f}{\delta l}\frac{\delta l}{\delta T} \approx \alpha_c \left(\frac{\delta f}{\delta a} a_0 + \frac{\delta f}{\delta l} l_0 \right). \tag{2.25}$$

By evaluating each partial derivative and taking discrete measurements of frequency and temperature the fractional frequency shift can be expressed as,

$$\frac{\Delta f_0}{f} \approx -\alpha_c \left(\frac{c}{2\pi f_0} \right)^2 \left(\frac{k_{nm}^2}{a_0^2} + \frac{p^2 \pi^2}{l_0^2} \right) \Delta T \approx -\alpha_c \Delta T. \tag{2.26}$$

This equation suggests that any change in temperature causes a proportional change in the resonant frequency of the cavity. This change in frequency has the same fractional shift for an ideal cavity regardless of cavity mode. The gradient of this frequency shift will be equal to $-\alpha_c f_0$. However this will only account for changes in the cavity geometry in an ideal system. In a real cavity system including coupling structures, mechanical joins, holes for sample and coupling etc. more sources of error are present. The negative sign simply means that an increase in temperature causes an increase in cavity size and so a decrease in resonant frequency.

As explained in [97], the resonant frequency of the sample measurement mode for a varying temperature has an error by a certain gradient. This gradient is dependent on the thermal expansion and temperature dependent resistivity of the cavity. This error in gradient must be removed.

Using $\mathrm{TM}_{\mathbf{010}}$ as the measurement mode and $\mathrm{TM}_{m\mathbf{10}}$ as the reference mode, the frequency shift with temperature for these two modes can be defined as,

$$\frac{\Delta f_{010}(T)}{f_{010}(0)} \approx \frac{\Delta f_k(T)}{f_k(0)} - (\alpha_c + \kappa_{010})\Delta T + \kappa_{err}(T) \tag{2.27}$$

$$\frac{\Delta f_{m10}(T)}{f_{m10}(0)} \approx -(\alpha_c + \kappa_{m10})\Delta T + \kappa_{err}(T) \tag{2.28}$$

where the fractional frequency shift denoted by k is caused by the perturbation from the sample, κ_{010} and κ_{m10} are the differences in gradient of the thermal expansion coefficient of the cavity material in the given mode, and κ_{err} is the systematic thermal expansion error in the experiment. To remove the fractional frequency shift caused by changes in temperature, Equation 2.29 can be used. This equation does not account for the errors in gradient however, as shown below:

$$\frac{\Delta f_{010}(T)}{f_{010}(0)} - \frac{\Delta f_{m10}(T)}{f_{m10}(0)} \approx \frac{\Delta f_k(T)}{f_k(0)} - (\kappa_{010} - \kappa_{m10})\Delta T \tag{2.29}$$

These errors in gradient can be removed by subtracting the unperturbed state of the system over the same temperature range using Equation 2.30,

$$\frac{\Delta f_s(T)}{f_s(0)} \approx \left[\frac{\Delta f_{010,s}(T)}{f_{010,s}(0)} - \frac{\Delta f_{m10,s}(T)}{f_{m10,s}(0)}\right] - \left[\frac{\Delta f_{010,u}(T)}{f_{010,u}(0)} - \frac{\Delta f_{m10,u}(T)}{f_{m10,u}(0)}\right] \tag{2.30}$$

where u represents the unperturbed cavity and s when the sample is present. With corrected frequency measurements, the values for real permittivity can then be calculated using Equation 2.31. Similarly, using corrected bandwidth or quality factor measurements, the imaginary part of permittivity can be found using Equation 2.32.

$$\varepsilon_1(T) \approx -2\left[\frac{f_s(T) - f_0(0)}{f_0(0)}\right]\frac{V_c}{V_s} + 1 \tag{2.31}$$

$$\varepsilon_2(T) \approx \left[\frac{1}{Q_s(T)} - \frac{1}{Q_0(0)}\right]\frac{V_c}{V_s} \tag{2.32}$$

As this method uses an inter-modal relationship between cavity modes, no previous measurements of expansion coefficients are required [97].

2.8 Practical Dielectric Measurement

Dielectric measurements conducted in this thesis have been performed using Vector Network Analysers (VNA). A VNA is capable of measuring both the magnitude and phase of microwave frequency signals - commonly Scattering Parameters (S-Parameters). Dielectric measurements in this thesis need only use scalar measurements, since the phase can be thought of as being embedded in the resonant frequency data. All measurements in this thesis are transmission measurements, or S_{21}measurements, (more accurately the transmitted power $|S_{21}|^2$). To perform these measurements, 2 ports are used. At port 1, the frequency is swept across a given span of frequencies with a power of 0 dBm (1 mW). The transmitted power is measured at port 2 for all input frequencies and is expressed as Insertion Loss (IL). The span of frequencies should be chosen such that the resonant frequency and -3 dB bandwidth can clearly be observed. The number of points measured can be set by the user. The greater the number of points, the greater the accuracy of measurement but this also increases the time taken to perform a frequency sweep. The need for a large number of points for precise measurement of resonant frequency is reduced by curve fitting. Non-linear, least-squares curve fitting to a Lorentzian response is used to determine frequencies, as shown in Equation 2.15, Q factors and peak power.

Figure 2.21 shows a representative resonant trace of an empty cavity in the TM_{010} mode at 2.5 GHz and a Q factor of 11,000. This high Q factor can be identified by the sharp resonant peak. After an empty quartz tube is inserted along the central axis of the cavity, the resonant frequency and Q factor are not greatly effected. These changes are exaggerated in Figure

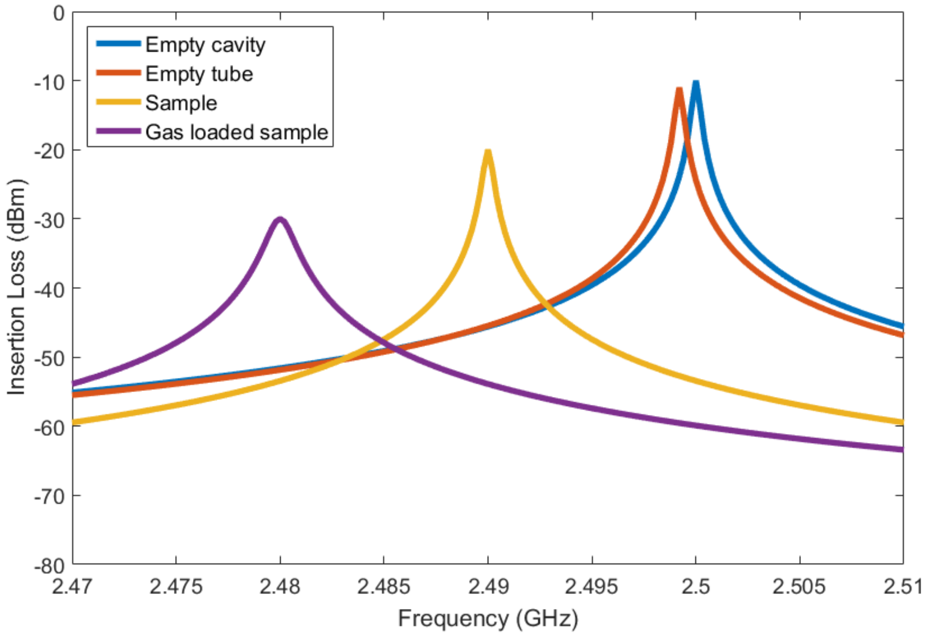

Figure 2.21: Resonant traces for an empty microwave cavity (blue), with empty quartz tube inserted (orange), with quartz tube plus sample (yellow), and with quartz tube plus gas loaded sample (purple.

2.21 in order to clearly identify the two traces. The addition of a solid state, powdered porous sample introduces a much larger change in frequency and Q factor due to the addition of material with an associated polarity and dielectric loss, respectively. As these are volumetric measurements, the addition of a larger volume of material into the electric field of the cavity will have a greater effect on both resonant frequency and Q factor, as shown in Equations 2.5 and 2.6, respectively. When a polar gas with high dielectric loss is passed through the powdered sample, the gas molecules are absorbed, either physisorbed in the pores of the material, or strongly bound to the solid state sorbent material. The gas loading of the sample causes further decreases in resonant frequency and Q factor.

Q factor can be calculated in two different ways. The first can be calculated from the Lorentzian fit of the resonant peak. The full width half maximum (or 3 dB) bandwidth can be found from the Lorentzian fit. Q factor can then be calculated by dividing the resonant frequency by the bandwidth, as seen in Equation 2.33.

$$Q_s = \frac{f_s}{BW_s} \tag{2.33}$$

where subscript s is used to denote when the sample is inserted. Alternatively, Q factor can be calculated from the Insertion loss using Equations 2.34,2.35 and 2.36.

$$Q_s = \frac{g_s}{k_e} \tag{2.34}$$

where subscript e is used to denote when the cavity is empty, k_e is defined by,

$$k_e = \frac{g_e}{Q_e} \tag{2.35}$$

and g is given by,

$$g = \frac{IL}{2(1-IL)} \tag{2.36}$$

To calculate Q factor from insertion loss, a reference Q factor value must be used indicated by Q_e. Using this initial value of Q factor, any changes in Q factor can then be calculated using the insertion loss. This method is the more reliable when Q is low, as resonances become distorted. During polar gas sorption experiments, a change in resonant frequency of the cavity is observed. To account for this change, the measurement window will be centred to the resonant frequency. If the Lorentzian response of the system is skewed, this movement of the measurement window can sometimes introduce a small change in the shape of the Lorentzian. This, in turn, can cause a small but sudden jump in Q factor. Resonant frequency and insertion loss do not experience this artefact. In this thesis, Q factor is calculated using the insertion loss method, so as not to introduce this artefact in changing Q factor values.

When using microwave characterisation techniques, either full width half maximum bandwidth or Quality factor can be used to express changes relating to the imaginary part of the permittivity. Q factor can be expressed as the stored energy divided by the power dissipated [86, 97, 99], as seen in Equation 2.37.

$$Q = 2\pi \frac{Energy\,stored\,per\,cycle}{Energy\,lost\,per\,cycle} \tag{2.37}$$

When measuring materials during absorption of a polar gas, the focus of the experiment are the power losses in the system. Due to this, it is not ideal to use Q factor to describe the losses in the system with power loss as the denominator. Use of $1/Q$, or indeed bandwidth, means power losses are the numerator, and therefore the subject, of the equation allowing dielectric loss to be properly displayed when plotting values under a dynamic flow system.

In this thesis, changes in dielectric parameters are plotted as $\Delta f/f$ and $\Delta(1/Q)$. As the electric field is parallel to the sample and the sample is small in comparison to the cavity volume, the full perturbation equations simplify to the following (where the powdered sample is assumed to be bulk sample):

$$\frac{\Delta f}{f_0} \approx k \Delta \varepsilon_1 \tag{2.38}$$

$$\Delta \left(\frac{1}{Q} \right) \approx 2k \Delta \varepsilon_2 \tag{2.39}$$

where $k = 0.5(V_s/V_{eff})$. Figure 2.22 shows the real and imaginary permittivity of water at 25 °C between 2 and 70 GHz. At 2.5 GHz, for example, ε_1 is 79 and ε_2 is 10. Substituting these values into Equations 2.38 and 2.39 gives a ratio of ε_1 to ε_2 of approximately 4:1. When observing changes in $\Delta f/f$ and $\Delta(1/Q)$ during absorption or desorption of water from a sample, it would be expected for there to be a four times larger shift in the $\Delta f/f$ response than the $\Delta(1/Q)$ response. Plotting changes in frequency and inverse Q factor in this way can show more information about the sample and its changes in real and imaginary permittivity than plotting changes in raw frequency and Q factor.

2.9 Previous Work on Microwave Characterisation of Solid State Ammonia Storage

The microwave characterisation technique has been used previously in collaboration between Cardiff University and STFC to study the absorption of ammonia in halide salts [9]. The schematic diagram for this experiment can be seen in Figure 2.23. Ammonia gas was flowed through the sample using a mass flow controller to control the flow. A mass spectrometer was used to measure the outgas. The microwave cavity operated at 2.5 GHz in the TM_{010} mode. The dielectric response of the sample material was tracked as ammonia was absorbed by the sample using a VNA. This experimental setup was used to investigate ammonia absorption in CaI_2.

Figure 2.24 shows resonant traces of the empty cavity, cavity with ammonia flow, sample under no gas flow, and sample saturated with ammonia. The empty cavity under argon flow shows a sharp Lorentzian peak, indicating a high Q factor, as expected for the empty cavity trace. Under an ammonia flow a small shift in frequency can be observed accompanied by a small change in Q factor. These changes are due to the polar and lossy nature of ammonia, respectively. The ammonia flow only causes minor changes as the ammonia is in a gaseous state and therefore only a small mass of ammonia is within the cavity. Once the sample is introduced, there is a greater change in frequency and Q factor, as expected when introducing a large sample of 1 g of CaI_2. Finally the ammoniated sample shows a further decrease in frequency and Q factor due to the additional presence of ammonia - a lossy, polar molecule. The addition of ammonia to the sample caused much larger changes to frequency and Q factor than the empty cavity with ammonia gas. This is because the sample is capable of storing significantly more ammonia than ammonia in a gaseous state at RTP.

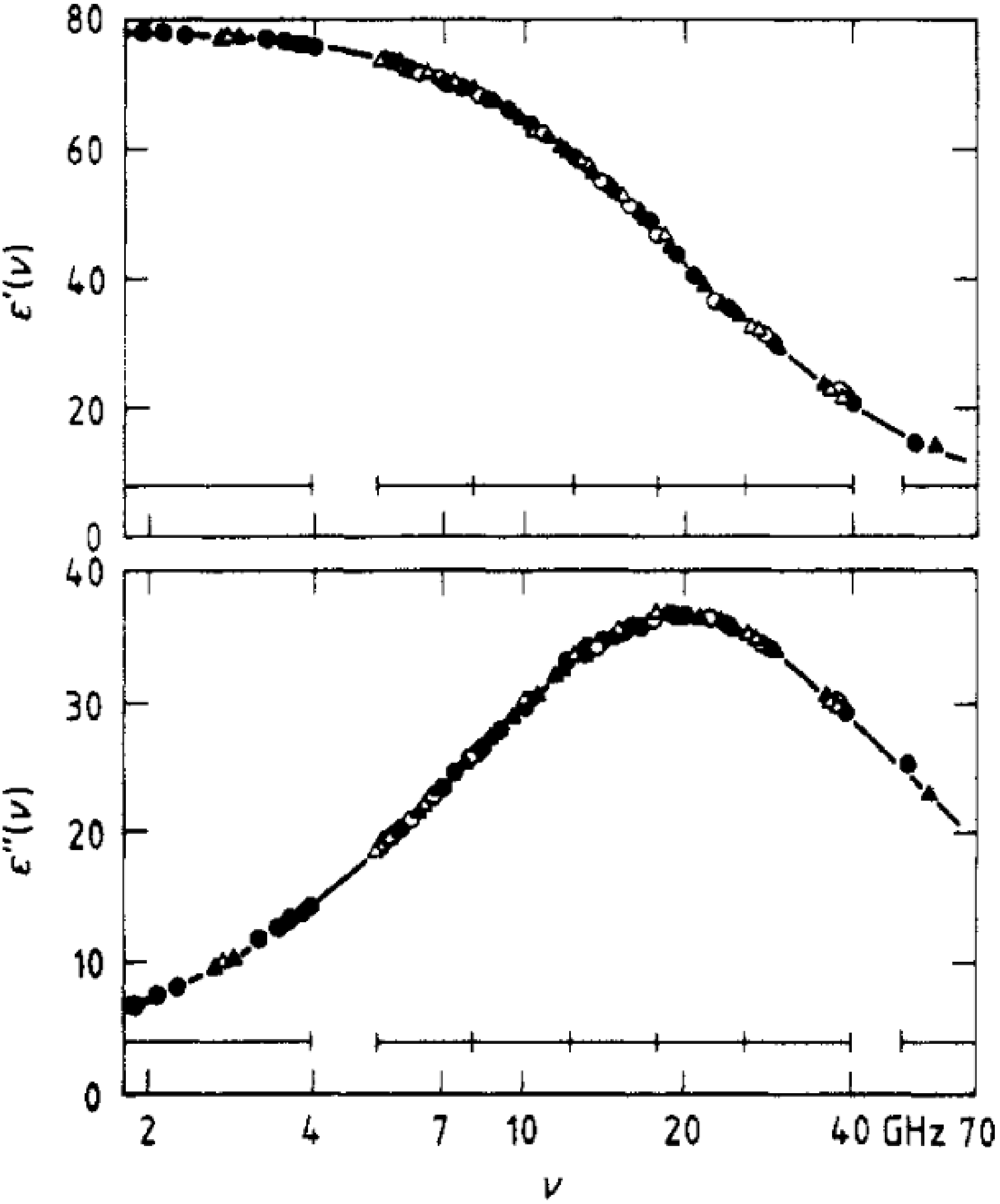

Figure 2.22: Real and imaginary parts of the complex permittivity of water at 25 °C as a function of frequency [100].

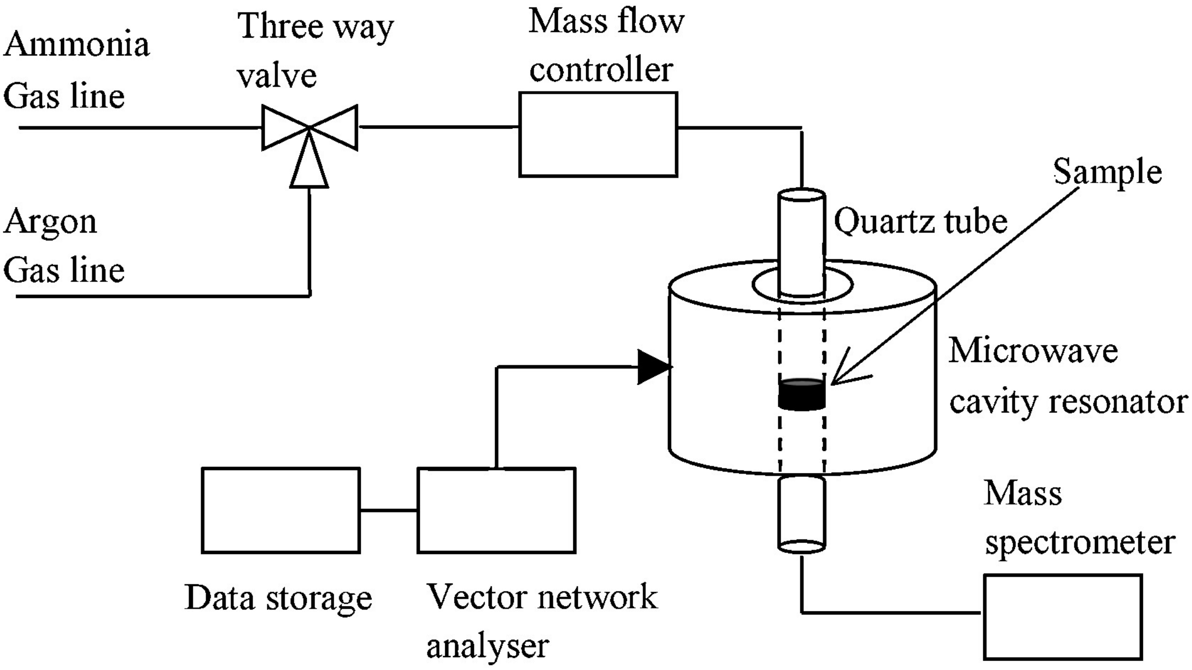

Figure 2.23: Schematic diagram showing the incorporation of the MCR into the gas flow and detection system [9].

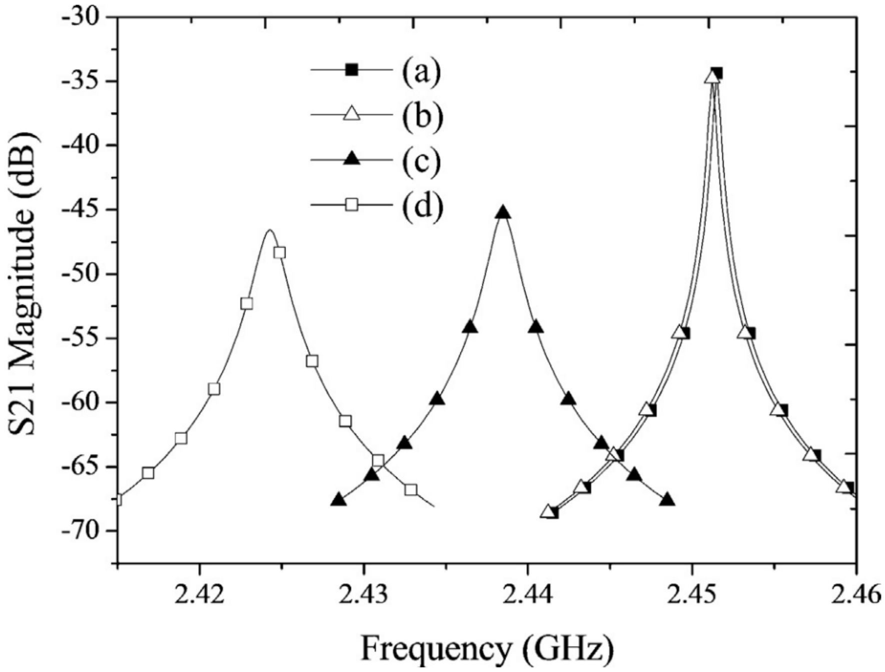

Figure 2.24: Resonant traces of the TM_{010} mode in the frequency domain, measured when the cavity is (a) empty under argon gas, (b) empty under ammonia gas, (c) filled with 1 g of unammoniated CaI_2, and (d) filled with 1 g of ammoniated CaI_2[9].

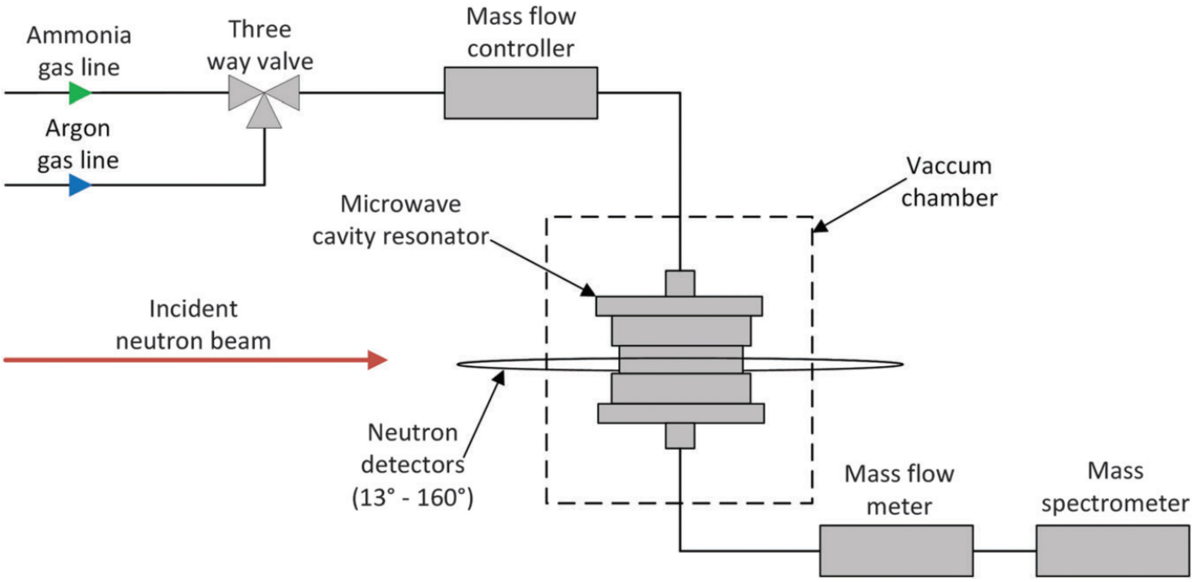

Figure 2.25: Schematic diagram of the simultaneous neutron diffraction measurement setup, showing neutron beam, gas lines, and measurement apparatus.

2.10 Microwave Characterisation of Solid State Ammonia Storage with Simultaneous Neutron Diffraction

The setup described in Section 2.9 has also been used with simultaneous neutron diffraction [27]. The schematic diagram for this experiment can be seen in Figure 2.23. The microwave cavity used for this experiment has a 20 mm high section of the cavity wall that has been thinned to 1 mm. This thin section in the cavity wall reduces the amount of neutrons that will be diffracted by the sample environment and ensures adequate resolution, as the majority of scattered neutrons are from the sample itself. Mass flow controllers are used to set the gas flow rates. The mass flow meter and mass spectrometer on the outgas can measure the flow through the sample and determine the gas present in this flow, respectively. This experiment was used to investigate ammonia absorption in Halide salts.

Figure 2.26 shows the results for ammonia absorption in $CaBr_2$. Scattering intensity from the n = 2 phase increased as ammonia was introduced until 2 hours. At this point the n = 2 phase decreased and a phase transition occurred to the n = 8 phase. The resonant frequency of the

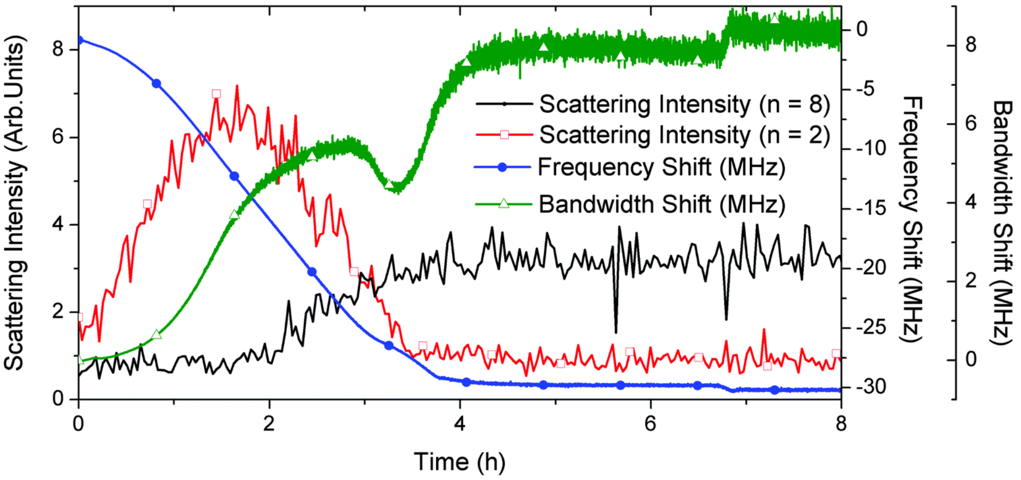

Figure 2.26: Plot of Bragg peak intensity for $Ca[NH_3]_2Br_2$ (3.11 Å) and $Ca[NH_3]_8Br_2$ (2.96 Å) peaks vs. frequency shift (MHz) and change in bandwidth for ammonia adsorption by $CaBr_2$. The dramatic change in dielectric properties is shown to commence with the increase in Bragg peak intensity. This change continues to increase until the Bragg peaks saturates in intensity (1.6 h) at which point the shift in frequency and change in bandwidth both also saturate. The dip in bandwidth and corresponding change in gradient of the frequency shift corresponds to the change in dipolar bond length as the n = 2 phase transforms into the n = 8 phase [27].

cavity resonator decreased as ammonia was absorbed by the sample. The bandwidth showed a general increase, as expected during the absorption of a lossy molecule, such as ammonia. Dielectric loss in a sample has been shown to be greatly effected by phase transitions [101]. The complex behaviour of bandwidth from 3-4 hours is caused by the change from the n = 2 to the n = 8 phase observed at this point. This work has shown the use of simultaneous dielectric measurement with neutron techniques implemented for the first time.

2.11 Variable Temperature Microwave Characterisation

Custom built equipment has previously been developed to conduct microwave characterisation experiments at elevated temperatures, a schematic diagram of this is shown in Figure 2.27. This system was developed to measure ammonia uptake in zeolites. The ammonia gas was flowed through the zeolite sample, supported by a silica frit inside a quartz tube. Quartz tubes are used to maximise the proportion of the dielectric loss coming from the sample. The ammonia gas and sample catalyst was heated by a spiral-shaped gas stream of hot air flowed around the sample tube. A double walled evacuation tube is included to minimise heat losses. This quartz tube setup is secured using a sealing mechanism. Thermocouples are used to monitor gas temperatures and the equipment can be used up to 300 °C. The microwave cavity is constructed from aluminium and designed to operate at 1.2 GHz in the TM_{010} mode. This resonant frequency allows the cavity to have an adequate diameter such that the holes made to insert the quartz tubes will not have a large effect on the Q factor of the cavity. Additional waveguide extensions, or chokes, also help reduce field escaping the cavity.

This equipment has been used to measure ammonia uptake in zeolites [34]. Figure 2.28(a) shows the amount of ammonia stored by the sample related to the sample mass. This value is calculated from the difference in ammonia concentrations measured upstream and downstream of the sample. The calculated values of real and imaginary permittivity from measured dielectric properties are shown in Figure 2.28(b). In this experiment, the sample was heated to 250 °C with a gas stream of 5% oxygen in nitrogen. At time t_1, ammonia was added to the gas stream at 500 ppm. Ammonia flow was stopped once ammonia was detected in the downstream gas at t_2, as the sample was fully saturated. The base gas flow continued until all weakly bound ammonia was removed from the powdered zeolite sample. At t_3, when no additional ammonia desorption is detected, 175 ppm of NO and NO_2 is added to the base gas. This converts the strongly bound ammonia to nitrogen and water. Figure 2.28 clearly shows the strong correlation between the mass of ammonia present in the sample and the change in both real and imaginary permittivity. This work has shown the use of dielectric measurement to observe gas sorption at elevated temperatures.

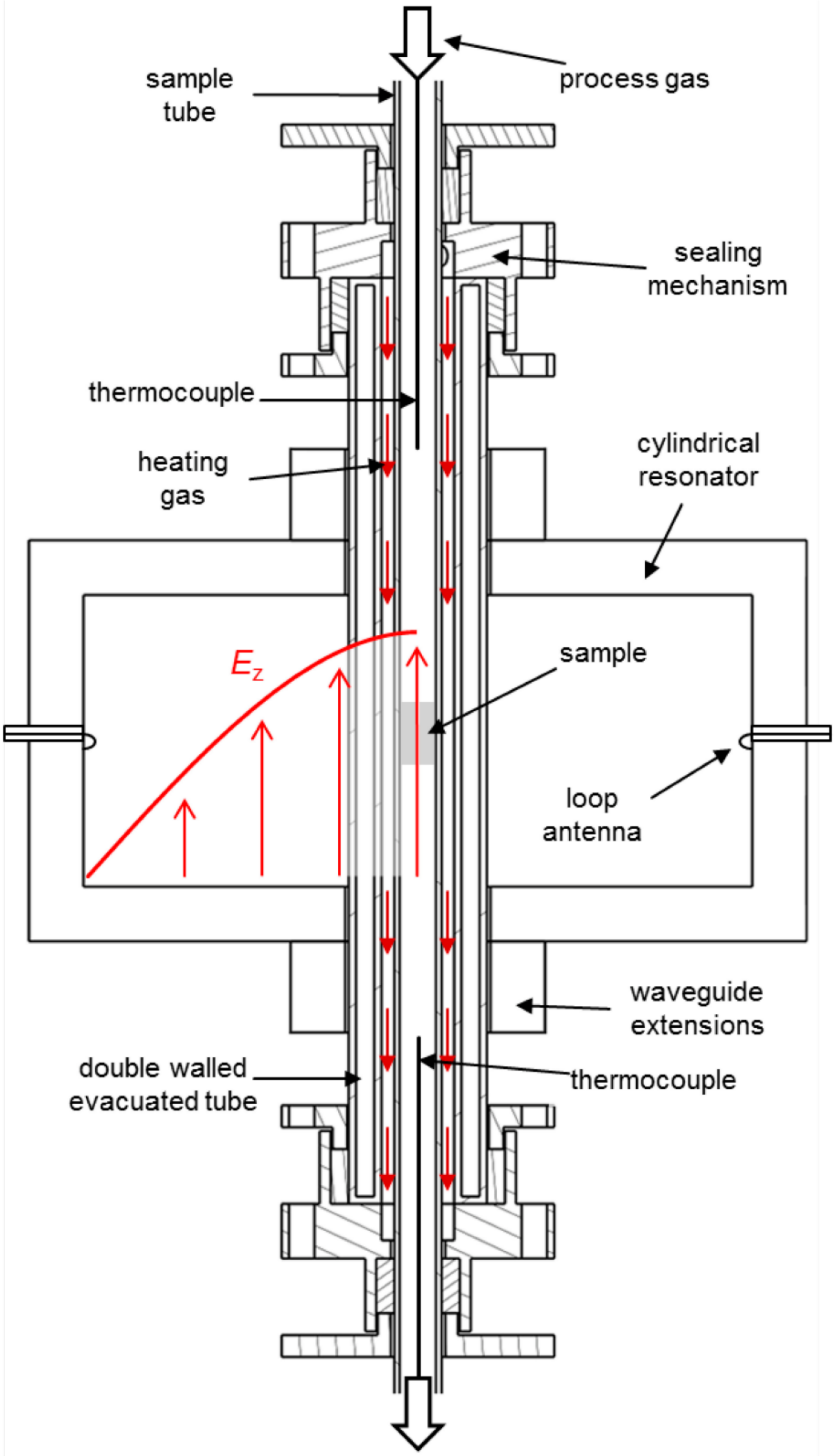

Figure 2.27: Schematic setup of the developed test bench including the sample tube, the double-walled and evacuated tube, the sealing mechanism, the resonator with waveguide extensions, loop antennas and two thermocouples. The gas heater, the Fourier transform infrared (FTIR) gas analyser and the network analyser (all external components) are not shown [102].

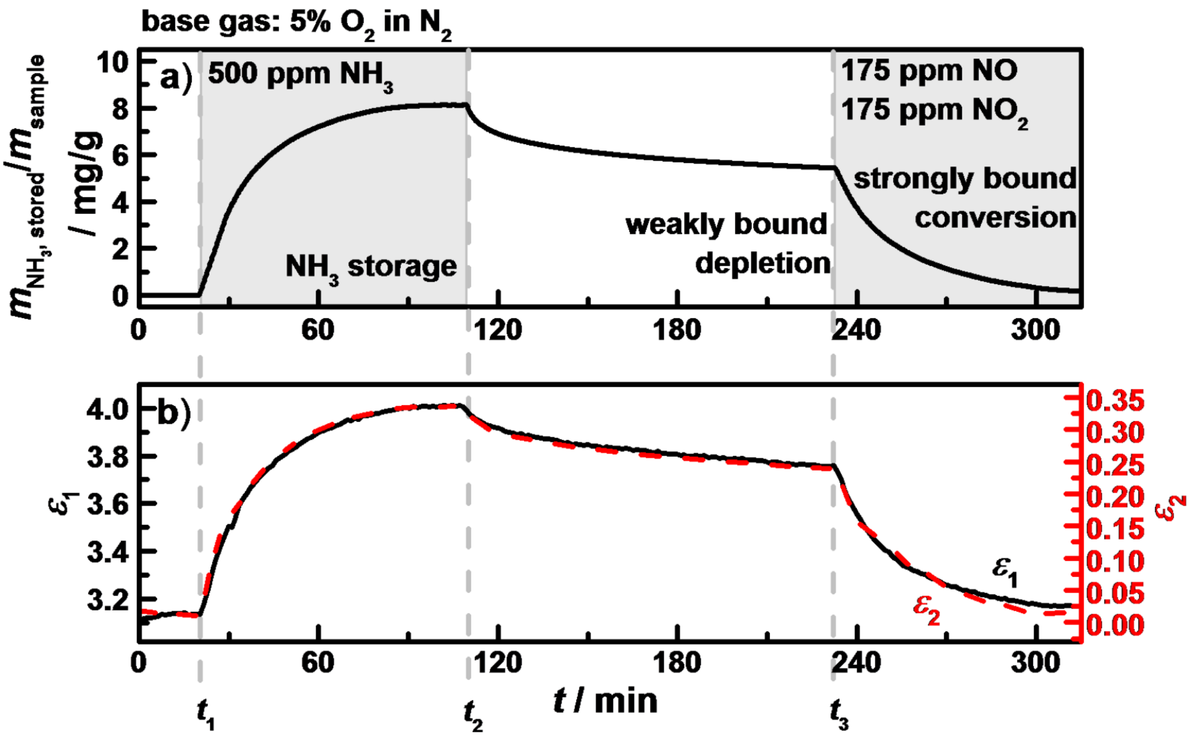

Figure 2.28: Experimental run for an H-ZSM-5 zeolite with a Si / Al ratio of 27 at 250 °C: (a) the stored amount of ammonia in the sample, and (b) the measured complex dielectric permittivity. [34].

Chapter 3

Degenerate Mode Temperature Correction

Work in this chapter was carried out in collaboration with Samuel Partridge, PhD student at Cardiff University. A method for temperature correction for cylindrical microwave cavities is detailed in Section 2.7.7. Temperature changes can be introduced during these measurements either intentionally or as a result of some other process. The microwave cavity itself also has a temperature dependent response which can affect the results. A common method to correct for this is to use another resonant mode separate to the measurement mode which is not affected by the sample. Instead of using independent modes, this chapter describes a method to use split degenerate TM$_{m10}$ modes of cylindrical cavities. TM$_{m10}$ consists of two modes with identical field patterns with a relative rotation between them and identical resonant frequencies. A strategically placed perturbation reduces the frequency of one of the TM$_{m10}$ modes and affects the coupling of both modes by reconfiguring the fields. This perturbation can be placed to suppress one of the two degenerate modes to allow a single, clean, Lorentzian response. Adding an off axis perturbation can also be used for temperature correction by placing a sample such that both modes are equally coupled. The lower frequency, perturbed mode is used as a measurement mode. The higher mode is used as a reference for temperature correction as it is unaffected by the sample. This technique was verified by measuring the permittivity of pure water using an aluminium microwave cavity resonator at 3.96 GHz. The temperature was swept between 20 ℃ and 60 ℃ and the results verified against the literature.

3.1 Degenerate Modes

All cylindrical cavities have modes that can be considered degenerate. In a rectangular cavity, such modes occur by geometric factors alone, when at least two of the internal dimensions are equal. By analogy, a cylindrical cavity will have some modes which are doubly degenerate, whilst a spherical cavity will have some which are triply degenerate (as in the case of a perfectly cubic cavity). Degenerate modes occur when two cavity modes have the same resonant frequency. Mode degeneracy can have two different causes. The roots of Bessel functions that define two different modes can force the frequencies to be equal, for example cylindrical modes TM_{111} and TE_{011} (since $J_0^{'}(x) = -J_1(x)$) [103]. Alternatively, degenerate modes can occur when rotational symmetry of the mode allows different possible orientations such as cylindrical modes TM_{m10} (where $m \geq 1$)[103].

Assuming a perfectly constructed microwave cavity, these degenerate modes would have exactly the same resonant frequency. In practice, inevitable small imperfections in the cavity construction can cause these modes to have slightly different resonant frequencies. By inserting a sample away from the central axis of the cavity, it is possible to separate the resonant frequencies of the modes. This is often referred to as a mode trap [104, 105]. Perturbing the cavity field causes the orientation of one of the possible modes to align with a local maximum at the sample. The other mode would have a local minimum. This sample can be placed at a location to suppress the degenerate mode by ensuring it is not coupled to. Alternatively, the sample can be placed at a location such that both orientations are coupled to equally. Due to this phenomena it is possible to use equally coupled, split degenerate modes to correct for changes in temperature during perturbation measurements. The main advantage of the proposed method is the much narrower bandwidth required for measurement compared with using a non-degenerate reference mode. This is described in Section 2.7.7, for example TM_{310}

at 6.62 GHz can be used as a reference for measurements using TM$_{010}$ at 2.50 GHz, leading to a wide bandwidth. This proposed method dramatically simplifies the instrumentation for dielectric sensor applications, where a measurement bandwidth of less than 100 MHz will suffice. A further advantage is the reduction in other systematic errors, such as variations in the coupling coefficients as a function of frequency.

3.2 Splitting the Degeneracy of TM$_{m10}$ Modes

TM$_{mnp}$ modes are described by the parameters m, n, and p where m is the azimuthal periodicity, n is the number of Bessel function maxima between the axis and circumference, and p is the number of nodes in the z direction. The axial electric field amplitude (E_z) is described by Equation 3.1 derived using [86]

$$E_z\left(r,\phi,z\right)=E_0J_m\left(\frac{\alpha_{mn}r}{a}\right)\cos\left(m\left(\phi+\theta\right)\right)\cos\left(\frac{p\pi z}{h}\right) \tag{3.1}$$

where a is the cavity radius, h is the cavity height, θ is the axial rotation (resulting in the TM$_{m10,\text{a}}$ and TM$_{m10,\text{b}}$ variants), and α_{mn} is the n^{th} root of the the m^{th} order Bessel function of the first kind. The field patterns of these modes are shown in Figure 3.1.

As well as introducing a frequency and Q factor shift, a perturbation of a microwave cavity can also reconfigure the resonant modes. This can be useful where multiple modes overlap, such as between TM and TE modes (since $J_0^{'}(x)=-J_1(x)$), or where a solution has finite azimuthal symmetry such as with the TM$_{m10}$ modes (where $m\geq 1$). The TM$_{m10}$ field pattern exists in two orientations simultaneously, which are seen in Figure 3.1.

In a perfectly cylindrical cavity, the TM$_{m10}$ modes are perfectly degenerate and so have exactly the same frequency. The case of coupling to the doubly-degenerate TM$_{110}$ mode is shown in Figure 3.2. Since both modes are equally probable, both are equally excited. Without any

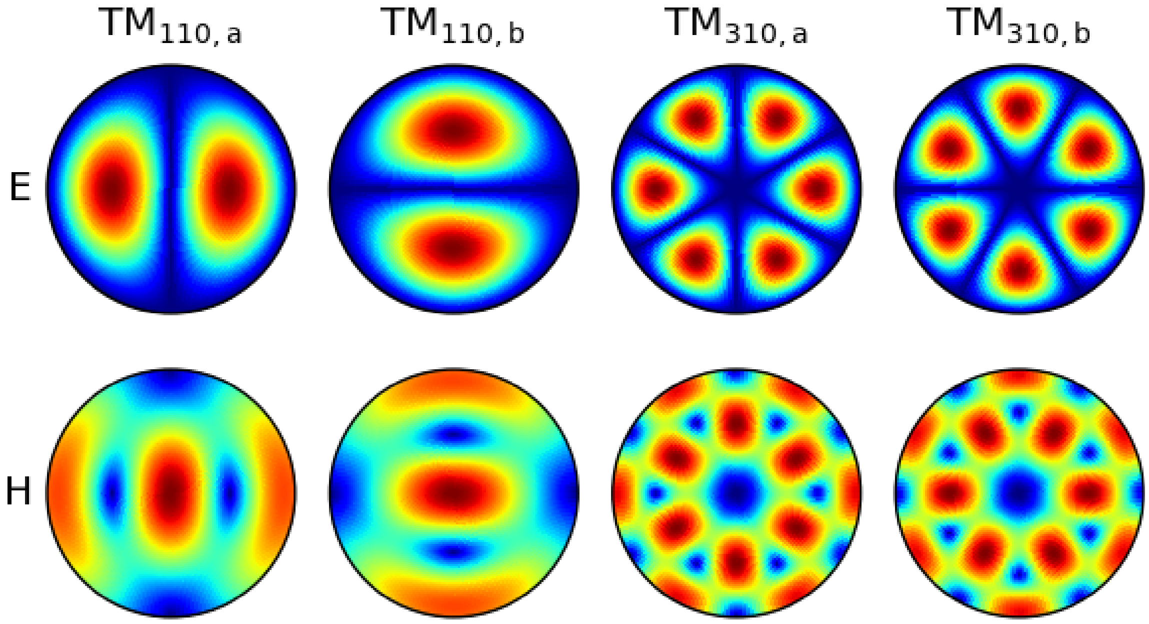

Figure 3.1: Electric field (E) and magnetic field (H) patterns for the degenerate $TM_{110,a}$, $TM_{110,b}$, $TM_{310,a}$, and $TM_{310,b}$ modes [106].

shape or material perturbation, these two modes coexist. This is equivalent to the mathematical process of Gram-Schmidt orthogonalisation process applied to degenerate eigenfunctions. Defining the electric fields of the $TM_{110,a}$ and $TM_{110,b}$ modes to be E_a and E_b, respectively, the net E-field is formed from the linear combination $E = (E_a + E_b)/\sqrt{2}$. The quantum interpretation of this result is that of the paradox of Schrödinger's cat. Both modes exist simultaneously and the degeneracy is only removed by an act of perturbation, which fixes the system in a particular eigenstate, with non-degenerate eigenvalue (i.e. in the case of a cavity resonator, a non-degenerate resonant frequency). This is what happens when a material sample is introduced, as in Figure 3.3.

Distortion of the Lorentzian response can occur when the frequencies are unequal. This can happen when the azimuthal symmetry of the cylindrical cavity is broken, such as with a split in the vertical plane, or where there are holes in the cavity. Holes in the microwave cavity are always present to allow the sample to be inserted into the cavity and also for cavity coupling. Additional holes may also be included to allow external stimulus - such as UV light, or complimentary measurement techniques - such as pyrometers. The ideal and practical scenarios

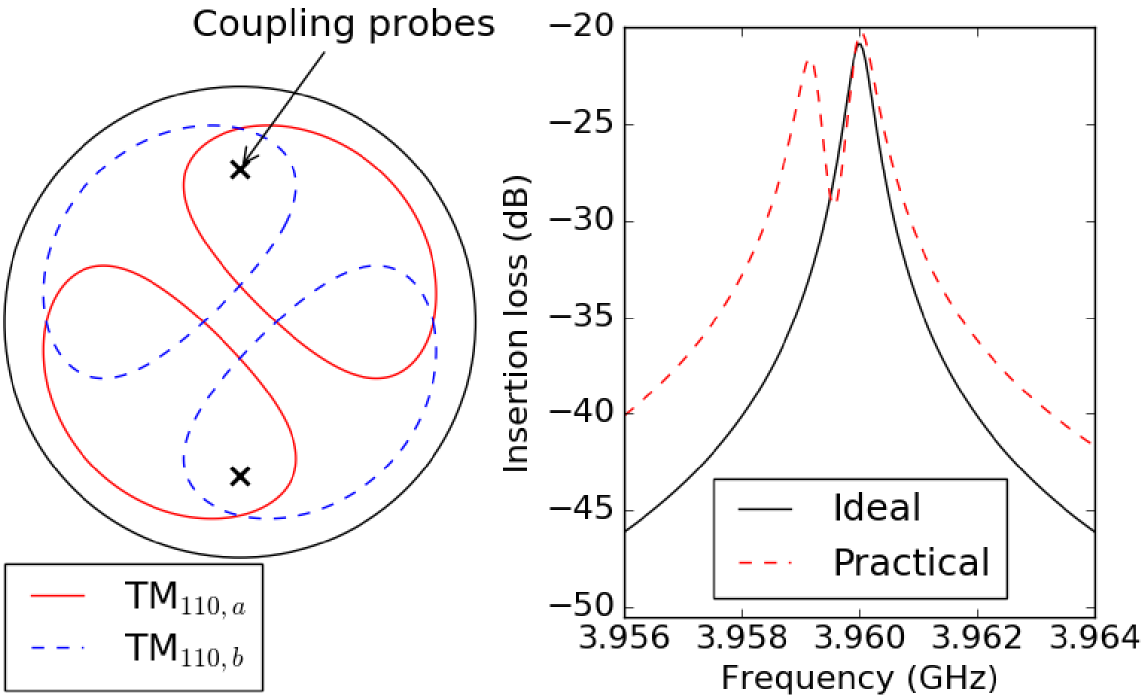

Figure 3.2: Schematic contour plot of the electric field magnitude for the TM$_{110}$ mode with capacitive (i.e. E field) coupling probes, located as shown for a transmission measurement (left). Measured transmitted power $|S_{21}|^2$ in the frequency domain of the TM$_{110}$ mode in a cavity split in the vertical plane in the ideal case (black solid) and in the practical case (red dashed) [106].

can be seen in Figure 3.2 along with the orientation of TM$_{110,a}$ and TM$_{110,b}$ modes.

To fix this distortion, a perturbation can be introduced in such a way to reconfigure the overlapping modes, such that only one is coupled [107]. This is illustrated in Figure 3.3 for the orthogonal TM$_{110}$ modes. The difference in frequency response between the original degenerate modes, with split resonant frequencies, and the perturbed modes where only one mode is coupled are shown in Figure 3.4. As only one mode is coupled to, a single, clean Lorentzian response can be seen. The reduced distortion of the Lorentzian response yields fewer errors when extracting mode parameters, such as frequency and Q factor. Using the resonant frequency obtained after mode suppression allows the use of the temperature correction technique discussed in Section 2.7.7. The resonant frequency obtained from the clean Lorentzian will give a substantially more accurate temperature corrected frequency. If the resonant

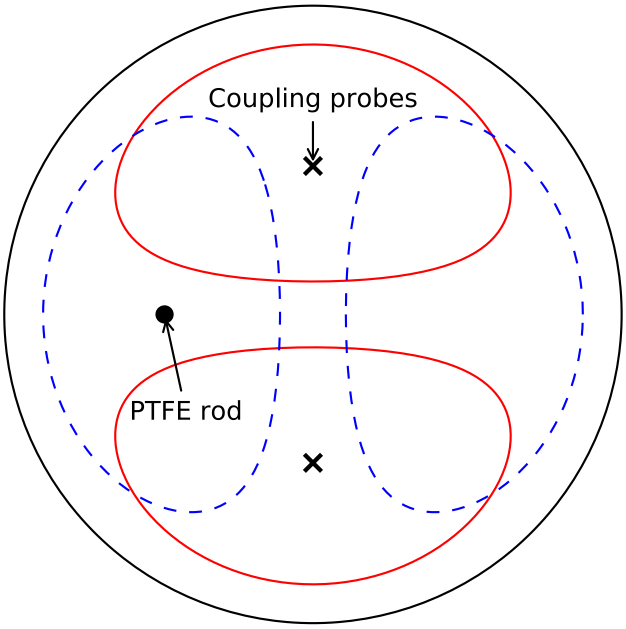

Figure 3.3: Schematic contour plot of the electric field magnitude for the TM_{110} mode with capacitive (i.e. E field) coupling probes, located as shown for a transmission measurement. Only one of the degenerate modes is coupled in this configuration, with the PTFE sample position shown.

frequency of the temperature correction mode is taken without mode suppression, the lack of clean Lorentzian response will lead to errors in temperature corrected frequency. There is even a chance of the measured resonant frequency jumping from the resonant frequency of the $TM_{m10,\mathrm{a}}$ and $TM_{m10,\mathrm{b}}$ modes during measurement. This is due to an error in the frequency tracking. If this were to happen, and temperature correction was carried out using these measurements, the corrected frequency would also incorrectly have jumps in frequency. Suppressing the lower frequency degenerate mode, so it is not coupled to, ensures this jump in frequency will not occur.

Alternatively a perturbation can be positioned to maintain equal coupling between the two modes, while also increasing separation between the $TM_{110,\mathrm{a}}$ and $TM_{110,\mathrm{b}}$ modes. If the perturbation is large enough to ensure sufficient separation, then the unperturbed TM_{110} mode can be used for temperature correction. This is discussed in Section 3.3.

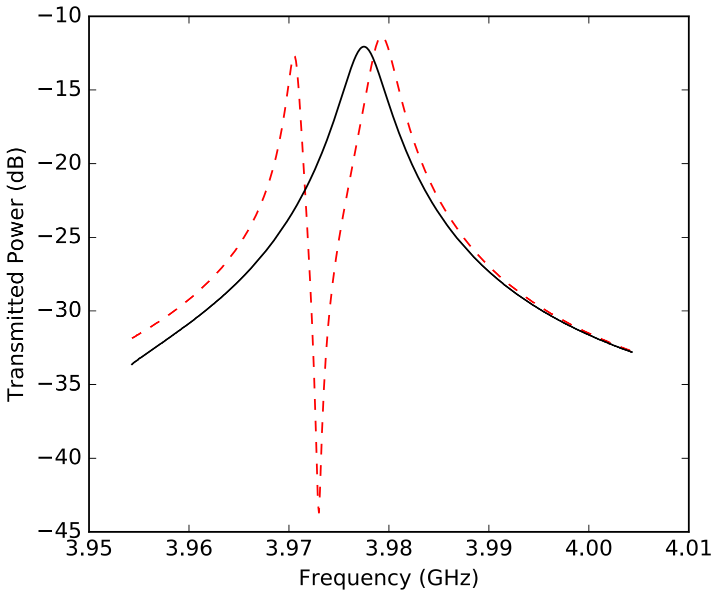

Figure 3.4: Measured transmitted power $|S_{21}|^2$ in the frequency domain of the TM_{110} mode in a cavity split in the vertical plane without a perturbation (red dashed) and with a perturbation (black solid).

3.3 Temperature Correction Using Split Degenerate Modes

Many microwave cavity perturbation measurements involve a change in temperature of the measurement cavity. For example, these can be unintentional changes due to room temperature fluctuations, or while measuring an exothermic/endothermic reaction. Alternatively, the change can be intentional while examining dielectric properties over a range of temperatures. Regardless of the reason behind it, a change in cavity temperature causes several changes to the host cavity that affect the frequency response of the system; change in cavity geometry, coupling geometry, and temperature dependent electrical conductivity of the cavity walls. These temperature changes during microwave perturbation measurements cause changes in measured frequency and Q factor. These must be accounted for so that any changes in the resonant frequency and Q factor are caused by changes in the sample.

3.4 Proposed method of temperature correction

Degenerate modes, as discussed in Section 3.2, can be used as an alternative method for correcting for temperature changes. When a sample is inserted into the cavity off-axis, this causes degenerate modes to split. The placement of the sample must be chosen to ensure both modes are coupled to equally. For modes TM_{110} and TM_{310} used in this experiment, the sample is inserted at an angle of 45° from the coupling structures, however this results in TM_{210} and TM_{410} being unusable. This is shown in Figure 3.5.

This perturbation locks the orientation of the modes. One of the modes will be perturbed by the sample and thus will have a lower frequency. This lower frequency mode becomes the measurement mode and is referred to as $\mathrm{TM}_{m10,\mathrm{a}}$. The higher frequency of the two modes will not be affected by the introduction of the perturbing sample. This unaffected mode becomes the reference mode and is used for temperature corrections. This mode is referred to as $\mathrm{TM}_{m10,\mathrm{b}}$.

Due to the geometry of the modes, not all of them could be coupled equally at once. Placing the sample at 45° from the coupling probes allows use of the TM_{110} and TM_{310} modes. TM_{210} and TM_{410} are unusable due to them only coupling the unperturbed and perturbed mode respectively. The technique used in Section 2.7.7 is utilised to correct for temperature, while replacing TM_{010} and TM_{m10} modes in Equation 2.30, with $\mathrm{TM}_{m10,\mathrm{a}}$ and $\mathrm{TM}_{m10,\mathrm{b}}$ modes, respectively.

Using this technique the sample is placed in the region of high electric field and notionally zero magnetic field of the measurement mode $\mathrm{TM}_{m10,\mathrm{a}}$. When considering the fields of the reference mode $\mathrm{TM}_{m10,\mathrm{b}}$ the sample is in a region of low electric field but high magnetic field. As described in Section 2.7.7, in order for this technique to work for any material the reference mode must have no magnetic or electric field at the sample location. Due to this, the degenerate mode temperature correction technique described may only be used on samples which are non-magnetic.

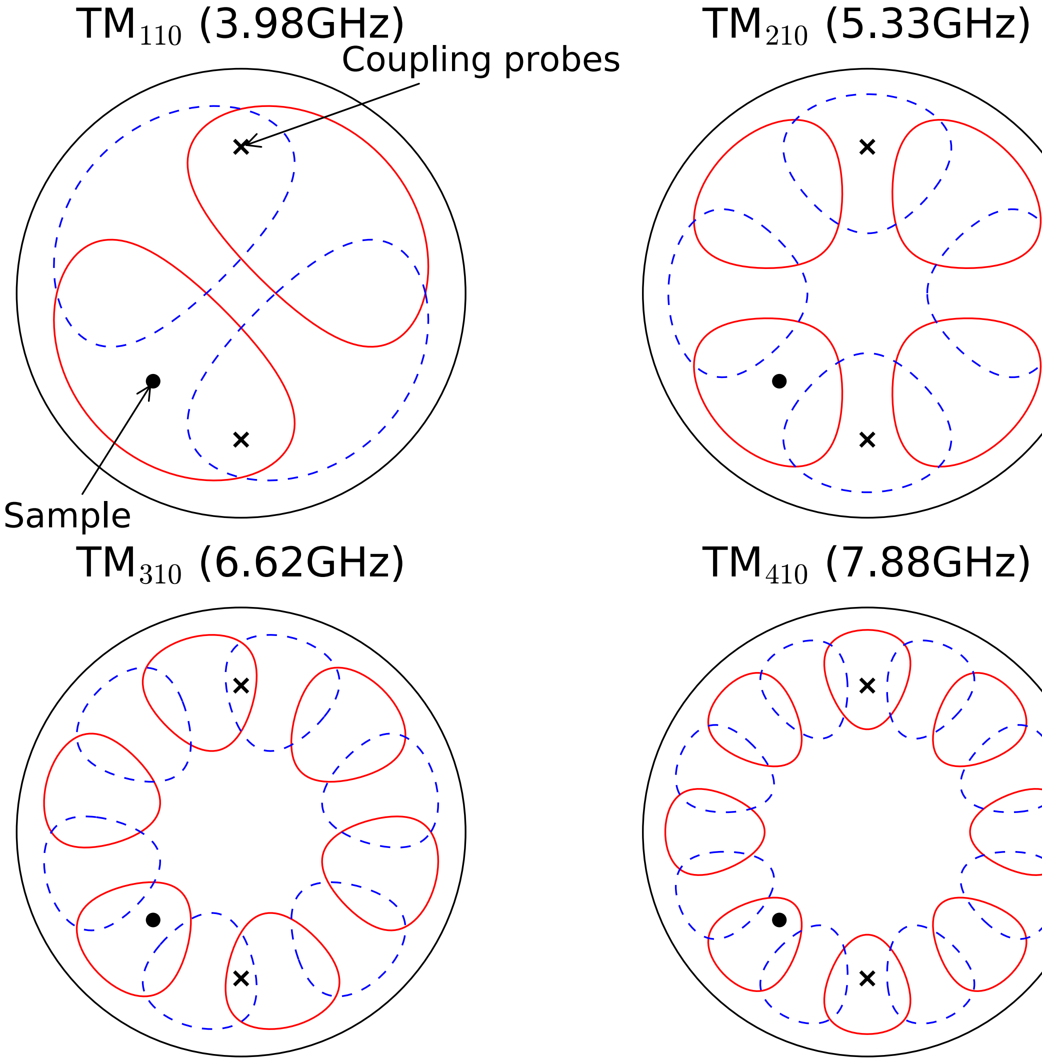

Figure 3.5: Contour plots of TM$_{m10}$ modes. TM$_{110}$ and TM$_{310}$ have equal coupling between the perturbed and unperturbed modes. Only the unperturbed TM$_{210}$ mode is coupled, and only the perturbed TM$_{410}$ mode is coupled [106].

3.5 Experimental Setup

These experiments were conducted using an aluminium microwave cavity resonator designed for TM measurements, with capacitive antenna coupling into the E-field. This cavity resonator will be referred to as the C3 cavity. Measurements were taken using the TM_{110} mode configuration shown in Figure 3.5. The TM_{310} mode was not used due to interference from another mode with similar resonant frequency.

The temperature was controlled by placing the resonant cavity in a Memmert IPP400 temperature controlled oven. The transmission (S_{21}) measurements were obtained using Keysight Technologies Vector Network Analyser (VNA) (PNA-L N5232A) with RF cables from Huber+Suhner. The VNA was connected to a PC running an in-house measurement acquisition program built with LabVIEW. The program also measures the temperature of the cavity using an Omega PT100 temperature sensor connected to a National Instruments (NI) cDAQ-9171. This is shown in Figure 3.6.

3.6 Proof of Method

In order to confirm this method, experiments were conducted using water as a sample and varying temperature then using the technique in Section 3.4 to correct for temperature. These results were then compared to the literature to confirm effectiveness of this method. The experiment consisted of two temperature ramp measurements, one with empty quartz tubes, and the other with the addition of a water sample. Two nested quartz tubes were used. The outer tube has an outer diameter of 4.0 mm and inner diameter of 2.0 mm. The inner tube has an outer diameter of 0.4 mm and inner diameter of 0.3 mm. The purpose of the outer tube was to split the high and low TM_{110} modes enough to treat them as separate modes and reliably extract the frequency and Q factor. The inner tube is used as a container for a small volume of water. The frequency response showing the separation of these modes can be seen with and without the water sample in Figure 3.7.

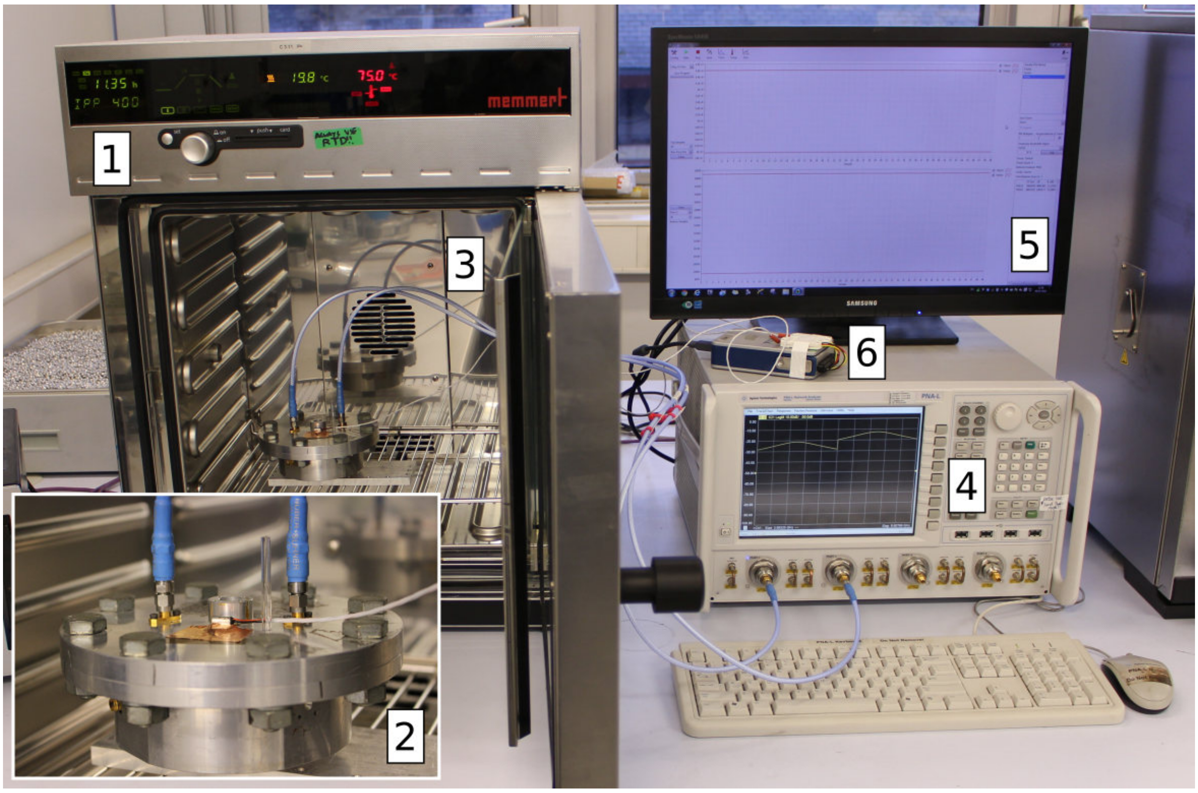

Figure 3.6: Experimental setup showing the temperature controlled oven (1) containing the microwave cavity resonator with inserted sample and attached temperature sensor (2). Coaxial cables (3) connect the cavity to the VNA (4) which is being driven by the LabVIEW measurement acquisition program (5). The temperature sensor is connected to the NI-DAQ (6), also controlled by the same program [106].

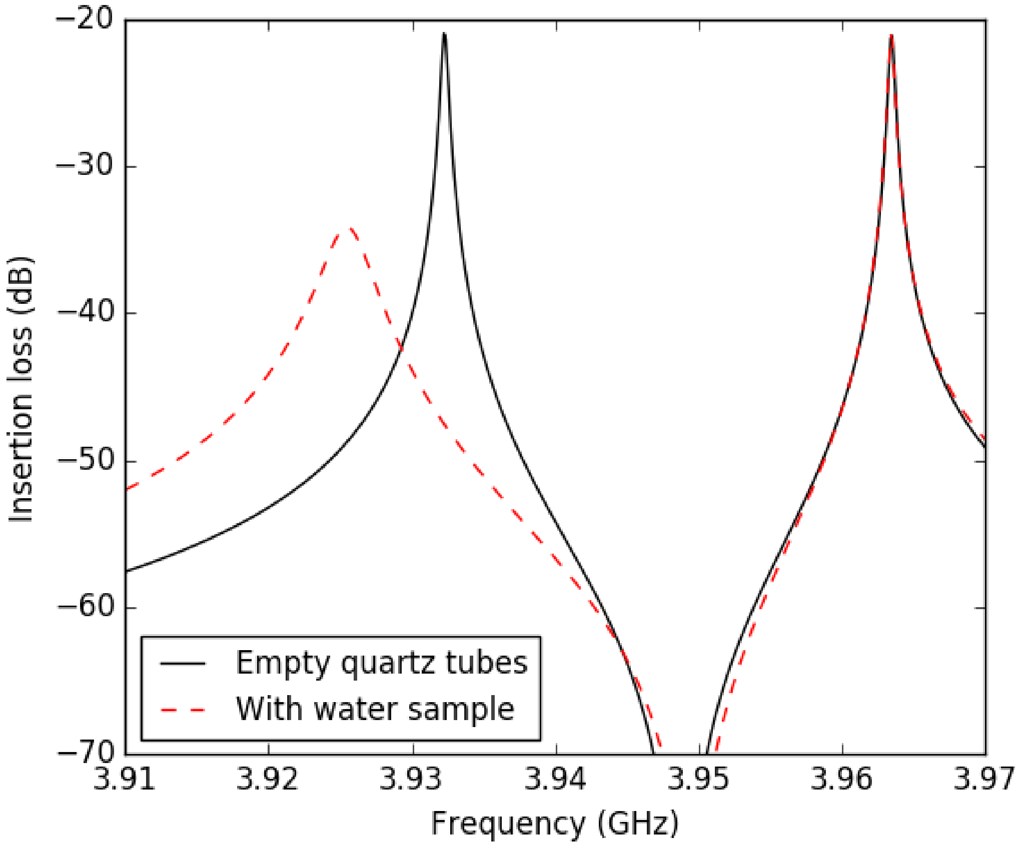

Figure 3.7: Measured transmitted power $|S_{21}|^2$ in the frequency domain of the TM_{110} mode when perturbed by the empty quartz tubes (black solid) and when a water sample is added (red dashed) [106].

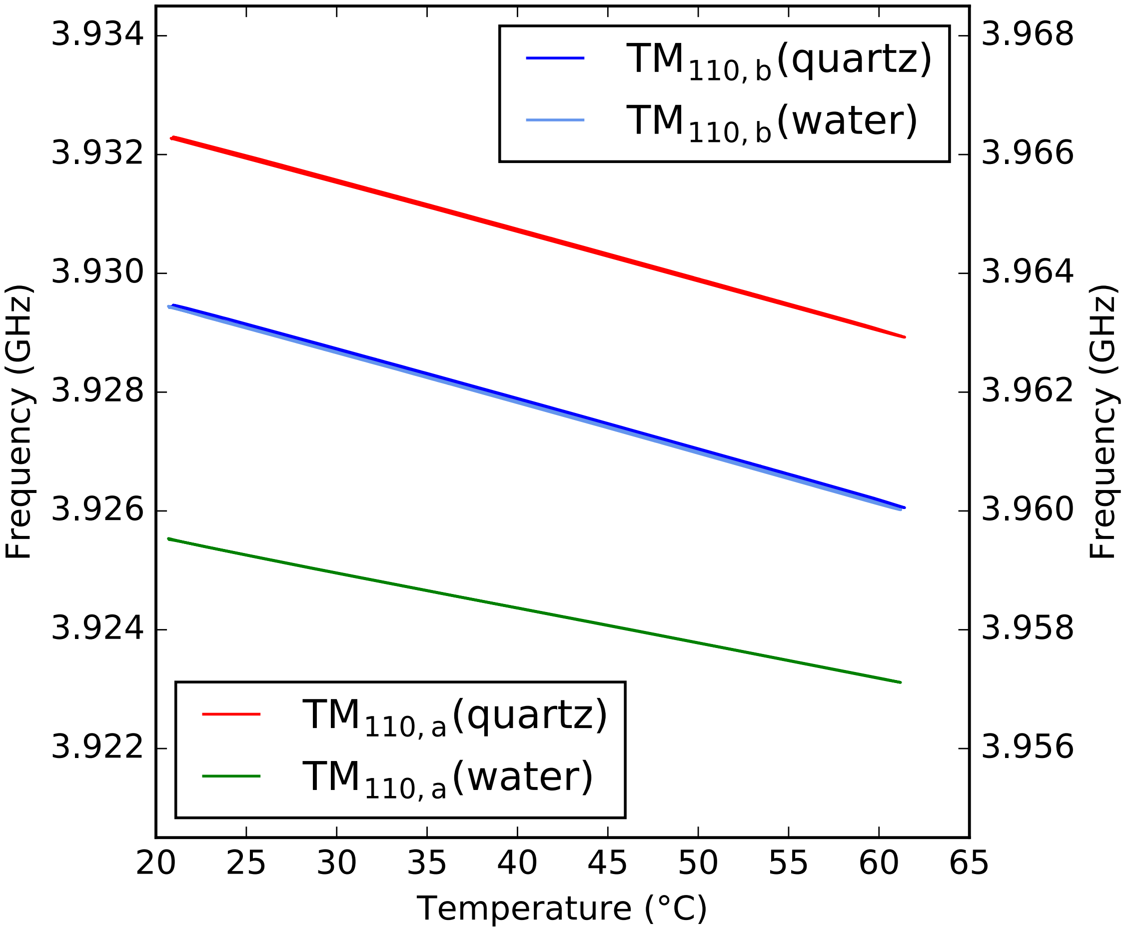

Figure 3.8: TM_{110} measured frequency versus temperature with measurement modes on the left axis and reference modes on the right axis [106].

The temperature ramps were performed from 20 °C to 60 °C over 8 hours, then returning to 20 °C at the same rate. Both the measurement mode $TM_{110,a}$ and reference mode $TM_{110,b}$ were measured for the empty and water ramps. The frequency results of these measurements are shown in Figure 3.8.

Frequency results show the reference mode $TM_{110,b}$ is not affected by presence of the sample, as described in Section 3.4. The measurements for the $TM_{110,a}$ mode have different resonant frequencies for water and quartz, due to the addition of water affecting the perturbation. These measurement modes also have different gradients. The gradient in the quartz tubes is caused predominantly by the change in cavity temperature, as the permittivity of quartz has very

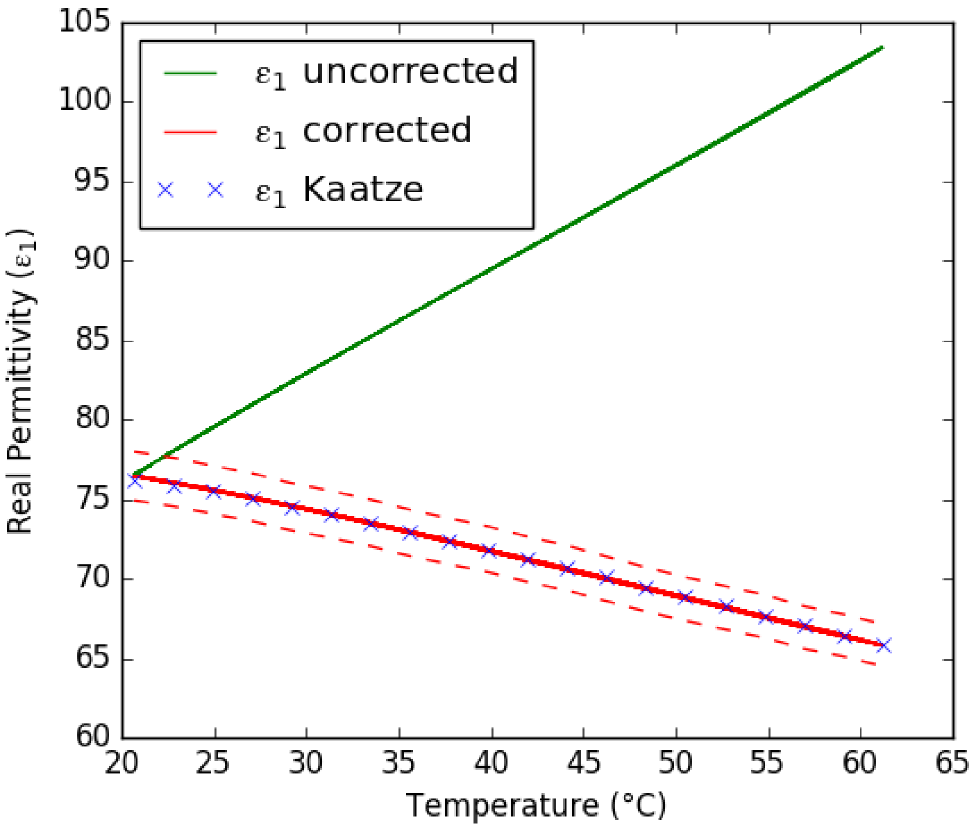

Figure 3.9: Corrected, uncorrected and literature values for real permittivity (ε_1) of water at 4 GHz versus temperature with 2% systematic error indicated by the dotted lines [106].

little temperature dependence. The gradient of the water containing sample has the same contribution from temperature change of the cavity and quartz, but also a contribution due to the temperature dependence of permittivity for water. Before temperature correction of the water sample, the frequency decreases as temperature increases. This trend is the opposite of the expected result. To resolve this, the temperature correction technique explained in Section 3.4 is used to remove the contributions from the cavity and quartz tubes, as well as reduce the errors present. This method ensures that after correcting these values, the only changes in observed frequency are due to changes in the permittivity of water. The real permittivity of water is calculated using Equation 2.31 before and after temperature correction of frequency has been carried out. This can be seen in Figure 3.9.

Table 3.1: Comparison of experimental measurements versus theoretical values of the permittivity of water.

T (°C)	$\varepsilon_{1,Kaatze}$	$\varepsilon_{1,measured}$	Percentage difference
25.0	75.46	75.54	0.11%
30.0	74.37	74.43	0.08%
35.0	73.14	73.04	-0.13%
40.0	71.82	71.67	-0.21%
45.0	70.44	70.27	-0.24%
50.0	69.03	68.91	-0.17%
55.0	67.60	67.49	-0.17%
60.0	66.18	66.18	0.01%

Real permittivity values shown in Figure 3.9 show that before temperature correction the graph suggests a rise in permittivity of the water sample as temperature increases. Once this data has been corrected, a decrease in real permittivity can be seen between 20°C and 60°C. This corrected negative gradient and corresponding ε_1 values now closely match the literature values calculated from the equations developed by Kaatze [100]. This also matches closely with the values seen in literature [108, 109]. The errors for these measurements were also calculated and compared with the theoretical values as shown in Table 3.1.

The main systematic errors accounted for include the permittivity and volume of the calibration quartz rod, and the volume of the water sample. These are approximately 2%. The random errors, introduced by the noise from the VNA, were negligible in comparison, less than 0.1%. As the table shows, the experimental results were well within the systematic error when compared against the literature permittivity values.

3.7 Conclusion

This chapter has shown how a perturbation can be used to suppress degenerate modes. Degenerate modes cause a splitting of the Lorentzian curves in the frequency response of microwave cavities. This distortion causes errors in measurement of frequency and Q factor of the cavity. The TM_{m10} modes are always degenerate due to their finite azimuthal symmetry. These TM_{m10}

modes can be used for temperature correction, however their degeneracy can cause problems when measuring them. To solve this issue, an appropriately placed, off axis perturbation can be introduced to suppress the lower frequency degenerate mode. This perturbation causes the frequency response to become a single Lorentzian. Frequency and Q factor measured from this mode can then be used reliably.

It has also been shown that degenerate modes can be used for temperature correction by splitting degenerate modes and using one as a robust and precise reference. The degenerate TM_{m10} modes can be reconfigured by perturbing the cavity. This is useful to prevent the interference between the higher and lower frequency TM_{m10} modes. The position of the mode relative to the cavity coupling structures determines how strongly that mode is coupled. The use of TM_{m10} modes is applied to the temperature correction technique developed by Cuenca et al. This technique is required due to the temperature dependent properties of the microwave cavity. The sample is placed in a position to ensure equal coupling of both TM_{m10} modes. The lower frequency perturbed mode is used to measure the sample and the higher mode is used as a reference, unaffected by the sample. To verify this technique, the temperature dependent properties of water were investigated. Before correction, the frequency response of the water sample appeared to be incorrect, due to the dominating temperature dependent properties of the microwave cavity. After temperature correction the values were verified against the literature and confirmed to be accurate.

Chapter 4

Experiment and Resonator Design

In this chapter the simulation, design and measurement of two types of microwave frequency resonators is discussed. One (cylindrical cavity type) resonator will be used for simultaneous NPD and MCR measurements and also incorporates a method of heating the sample using a high temperature gas flow. The equipment used for heating is also discussed. This equipment is designed to be able to activate a MOF sample in-situ. The second (hairpin type) resonator is designed to perform simultaneous X-ray PDF and dielectric characterisation. This hairpin geometry resonator will be used to observe the absorption of ammonia in halide salts. Both resonators designed have novel features to allow the entry of incident and diffracted beams.

4.1 Simultaneous NPD and MCR High Temperature Resonator Design

This section documents the design of experimental equipment in order to perform experiments combining simultaneous NPD and MCR measurement while flowing high temperature gases over a solid powdered sample. The ability to heat the sample during these measurements can have many applications, however, this experiment is specifically designed to allow activation of a powdered MOF sample. The method and results for combined MCR and NPD measurements are described later, in Section 4.1. The addition of gas heating to this set-up presents additional technological challenges. To do this a method of heating gases to a constant temperature whilst in a vacuum chamber for NPD is described in Section 4.1.1. To allow heating equipment as close to the sample as possible required a new microwave cavity, the design of which is documented in Section 4.1.2. The cylindrical microwave cavity resonator designed in this section will be referred to as the C1 cavity.

4.1.1 Heating Equipment

For this experiment a way of heating gases during NPD and MCR measurements must be formulated. Using the quartz tube shown in Figure 4.1 with a flow rate of 10 sccm (standard cubic centimetre per minute), a temperature of 150 °C of the flowing gas should be achieved. A method of heating gases for ammonia absorption measurements is described in [34, 102]. This method involves passing a heated gas through the outer layer of a double walled sample tube. For MCR measurements alone this method proves effective. However, in order to allow the neutron diffraction contrast to remain as high as possible, the neutrons must pass through as little material as possible on top the powdered sample.

Alternatively it is possible to heat the gas before it enters the quartz tube, using a circulation heater for example. One problem with this method is that there is a long section of quartz tube for the gas to flow through before reaching the sample. This gives a long period of time for the gas to cool before reaching the sample and could lead to inadequate heating of the sample. Another problem with this method is that there will be a temperature gradient across the sample height.

To resolve these problems, heating coils are chosen for gas heating for this experimental setup. This method allows heating coils to be placed out of the neutron beam path but close to the sample and also allows coils to be placed both above and below the sample location, decreasing the temperature gradient across the sample. Coils for this experiment were custom made

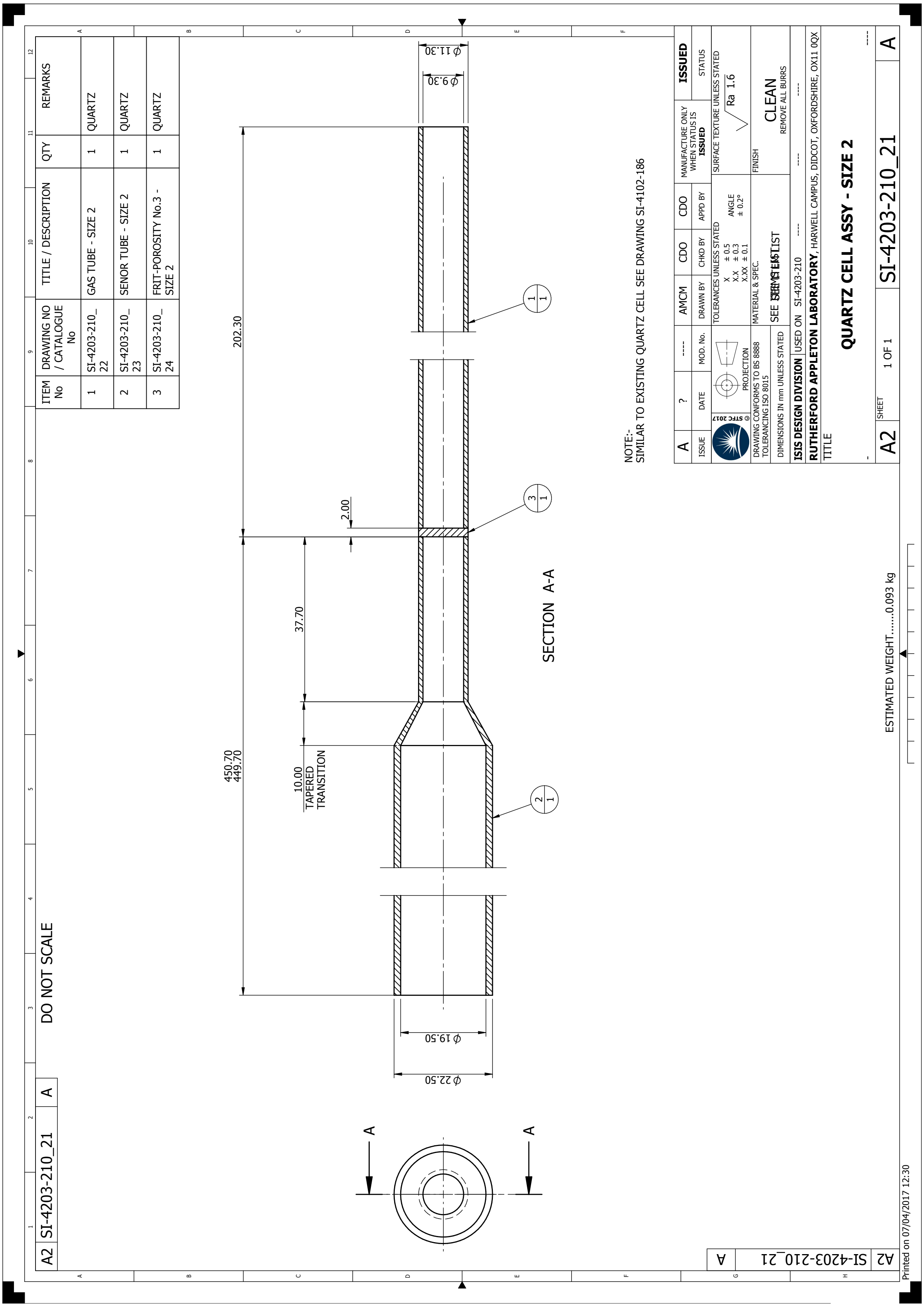

Figure 4.1: Quartz tube schematic drawing as provided by ISIS design division

Table 4.1: Specification of Coil heaters

	Top Coil	Bottom Coil
Location	Inside Quartz tube	Outside Quartz tube
RMS Voltage	110 V	230 V
RMS Power	500 W	125 W
Cable Diameter	1.57 cm	2.39 cm
Coil ID	0.953 cm	1.27 cm
Coil height	38.1 cm	3.81 cm

by Watlow. The coil specifications can be seen in Table 4.1.

The top coil is inserted into the quartz tube and is of appropriate height that the coil ends as close to the top of the cavity as possible without encroaching on the microwave fields or touching the taper of the quartz tube. This placement allows maximum thermal contact with the gas and ensures gas reaching the sample is as close as possible to the target temperature. Due to the reduced diameter of quartz tube below the sample, placing the bottom coil inside the tube is not an option. Because of this, the coil is placed on the outside of the quartz tube, as close to the bottom of the cavity as possible, without encroaching on electromagnetic fields. Thermocouples to read temperatures are placed at the end of the coils closest to the sample. The upper thermocouple is suspended in the gas flow above the microwave cavity. The lower thermocouple is taped to the outside of the quartz tube between the cavity and bottom heating coil. The locations of the heating coils and thermocouples can be seen n Figure 4.2. Both of these coils are controlled using Eurotherm 3504 temperature controllers.

4.1.2 Microwave Resonator Design

The microwave resonator design shown in this section is created to work with the heating equipment shown in Section 4.1.1. These pieces of equipment are designed to operate in tandem to provide dielectric measurements while passing a heated gas over the sample while simultaneous NPD measurements are taken. For NPD measurements a sample weight of approximately 1 g is used. The resonator chosen must be able to contain this sample with an

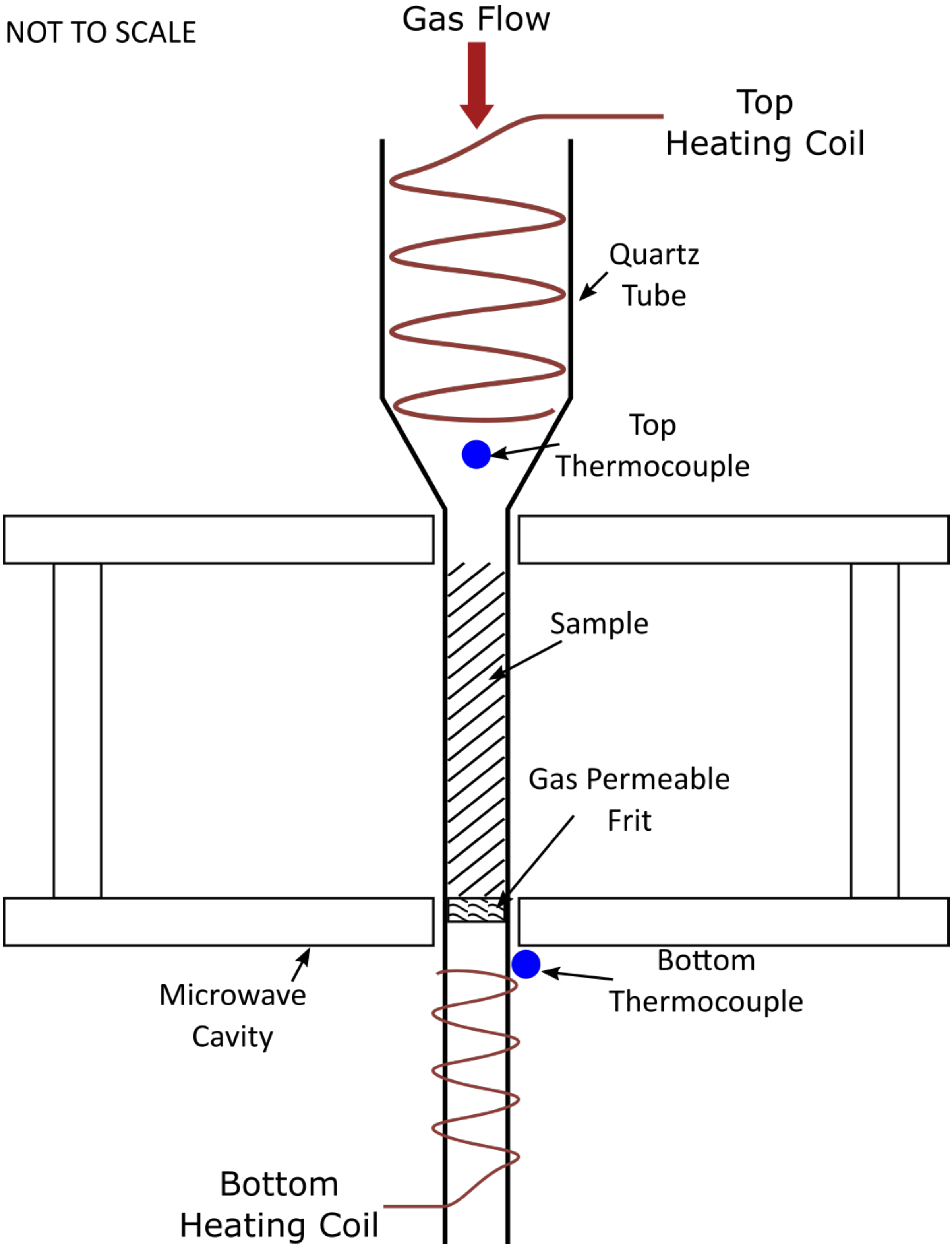

Figure 4.2: Schematic diagram showing the locations of top and bottom heating coils with associated thermocouples in relation to the cavity and sample.

appropriate filling factor. It must also have adequate dynamic range, for the measurement of transmitted microwave power, to be able to cope with a large and lossy sample. Design requirements for the resonator are shown below:

- Sample hole of over 12 mm to allow insertion of the sample tube.
- 20 mm high section thinned to 1 mm thick to minimise neutron scattering.
- Cavity height as small as possible to allow heating elements close to sample.
- A resonant frequency of approximately 2.5 GHz for the TM_{010} mode.
- A mode independent of ammonia absorption to allow temperature corrections.
- Appropriate balance between sensitivity and dynamic range.
- Maintain a maximum cavity temperature of below 100 °C.

The material chosen for construction of the resonator is aluminium which allows the the cavity to have a high Q factor due to its high electrical conductivity. Copper would be ideal for high Q factor due to its higher conductivity however copper has a much higher neutron scattering cross section. Generally vanadium sample environments are used for NPD experiments due to its low neutron scattering coefficients, however its electrical conductivity is too low to make it suitable for a microwave cavity. Aluminium also has adequately low coherent and incoherent neutron scattering cross section to minimise scattering from the resonator, especially considering the section of cavity in the neutron beam will be only 1 mm thick. A cylindrical shaped cavity is chosen as this geometry is suitable for measurement of samples of this size.

Heating elements must be placed as close to the sample as possible in order to stop the heated gas from cooling before it passes through the sample. To do this the resonator must have as shorter height (d) as possible. The Q factor of the cavity is approximately proportional to the height of the cavity (where $d < a$), as shown in Equation 4.1 (full derivation shown in Appendix A.1). The relationship between Q factor and the ratio of radius and height can also be seen in Figure 4.3.

$$Q = \frac{a/\delta}{1 + a/d} \tag{4.1}$$

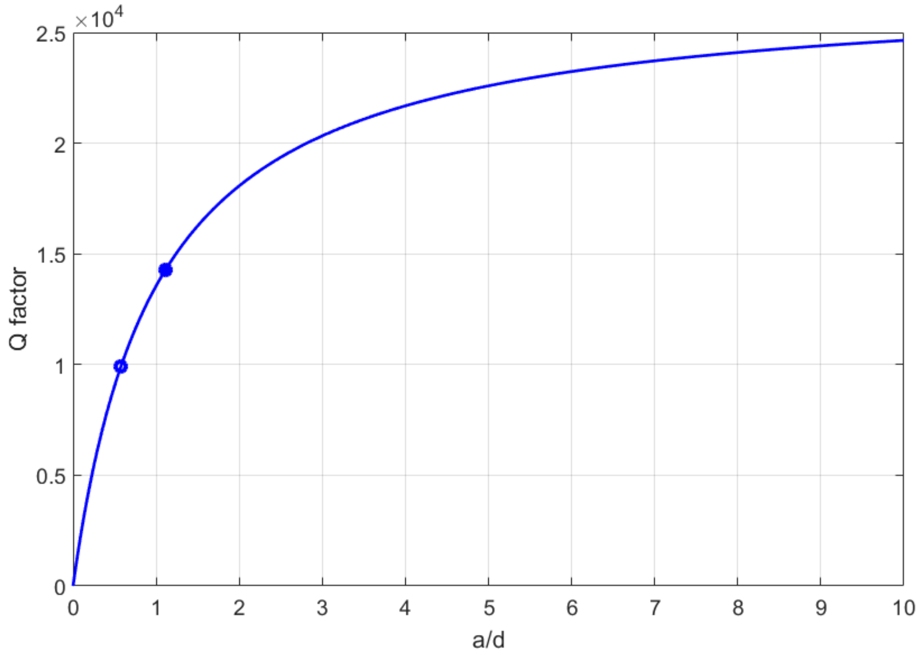

Figure 4.3: Q factor of the TM_{010} mode versus the ratio of cavity radius over cavity height. The point on the curve selected for the C1 cavity and for a typical microwave cavity (used for perturbation measurements without sample heating) are indicated by the open and filled circles, respectively.

where δ is the skin depth at the resonant frequency.

Neutron powder diffraction requires approximately 1 g of sample. This is to allow enough neutrons to be diffracted such that adequate resolution of Bragg data is obtained. As this sample may have a high dielectric loss the cavity should be as tall as possible to allow for a high intrinsic Q factor leading to a large dynamic range. Different cavity heights also change the resonant frequency of many cavity modes. In a comparatively short microwave cavity, the lowest frequency, dominant mode is the TM_{010} mode. As height increases the resonant frequency of the TE_{111} mode decreases until it becomes the dominant mode [86]. Selecting a height that allows any used mode to be spectrally far from other modes ensures the shape of the measurement peak remains a clean Lorentzian. In practice a balance of these factors must be considered when deciding the height of the cavity.

As mentioned previously, a 20 mm high section of cavity wall must be thinned to 1mm thickness. In order to create this MCR the cavity space is milled from two solid blocks of machine grade aluminium. This aluminium alloy allows ease of machining but negatively affects Q factor due to reduced conductivity. The milling process means the corners of the cavity space cannot have a 90° angle and must have a radius equal to the radius of the milling bit. The smallest radius possible for the radius of cavity used is 3 mm. With this taken into account the smallest possible height of the cavity $d = 26$ mm. Assuming a conductivity of 3.77×10^7 Sm^{-1} and using Equation 4.1, the theoretical maximum Q factor for this cavity is $Q = 9927$. When this value is simulated using COMSOL a value of $Q = 9874$ is given. This Quality factor is large enough to allow an adequate dynamic range and should allow the heating coils to be placed as close to the sample as possible so a cavity height of $d = 26$ mm is selected.

The cavity is milled to form two semi-cylinders and secured together by 4 bolts. The current path for the TM_{010} measurement mode is shown in Figure 4.4. The construction method used, with the cavity split in the vertical plane, ensures the current path for the TM_{010} measurement mode is not obstructed. A split in the horizontal plane would obstruct these current path, leading to a decrease in Quality factor. Microwave chokes around the 12 mm sample hole were considered to act as a waveguide to attenuate the electromagnetic fields and maintain the stored energy within the cavity. Upon simulating the effect of chokes using COMSOL, it was found that extended microwave chokes have little effect on the Q factor. Also extending the chokes would require the heating coils to be placed further from the sample which should be avoided. Due to this, 8 mm thick top and bottom plates for the cylinder are used with no extended choke. This thickness is appropriate from an electromagnetic standpoint but also allows adequate thickness to be used for mechanical connection of the two cavity sections as well as connection of the cavity to the rig.

To give a resonant frequency of the TM_{010} mode close to 2.5 GHz, a cavity diameter of 90 mm is used. The measured frequency response for the TM_{010} mode of this cavity can be seen in Figure 4.5. A cavity of 90 mm diameter and 26 mm height means TM_{010} has its nearest mode (TM_{110} at approximately 4 GHz), in terms of frequency, 1.5 GHz away . This allows TM_{010} to be effectively used as the measurement mode. The broadband frequency response of this

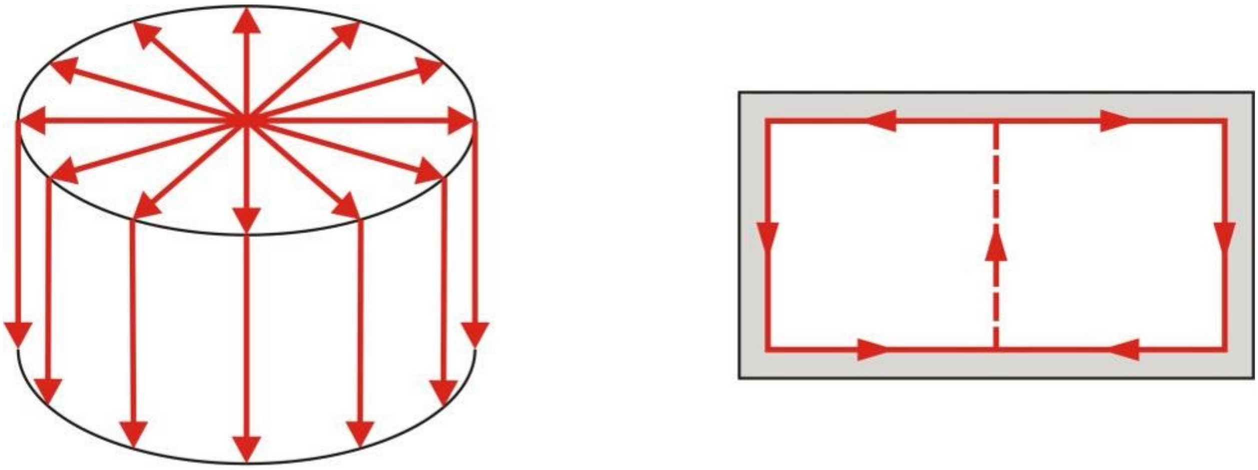

Figure 4.4: Surface currents for the TM_{010} mode in a cylindrical cavity.

cavity can be seen in Figure 4.6. Possible temperature correction modes TM_{110}, TM_{210}, and TM_{310}, as discussed in Section 2.7.7, also have adequate frequency spacing from other modes of at least 100 MHz. The coupling for this cavity is provided by two coupling antennas which capacitively couple into the electric field of the cavity, as shown in Figure 4.7. Antennas are constructed to give an insertion loss of approximately -30 dBm to provide an appropriate balance between dynamic range and sensitivity. A render of this cavity can be seen in Figure 4.8 and the electric field pattern can be seen in Figure 4.9.

Simulation of the heat distribution in the cavity, quartz tube and supports was carried out using COMSOL Multiphysics. The result of this simulation can be seen in Figure 4.10. The quartz tube was set to a temperature of 150 °C with no contact with the cavity or support structure. Of course in the physical system the support structure will be in contact with the structure holding the quartz tube. Also this simulation has a simplified version on components used (without coupling probe holes, tapered on quartz tube etc.) but should give a reasonable approximation of the heat within the system. Heating in this simulation was only through radiative heating, as it will be when used in the vacuum chamber of the POLARIS sample tank for the experiments. This simulation suggested a maximum cavity temperature of under 40 °C. This is well within the working range of the cavity.

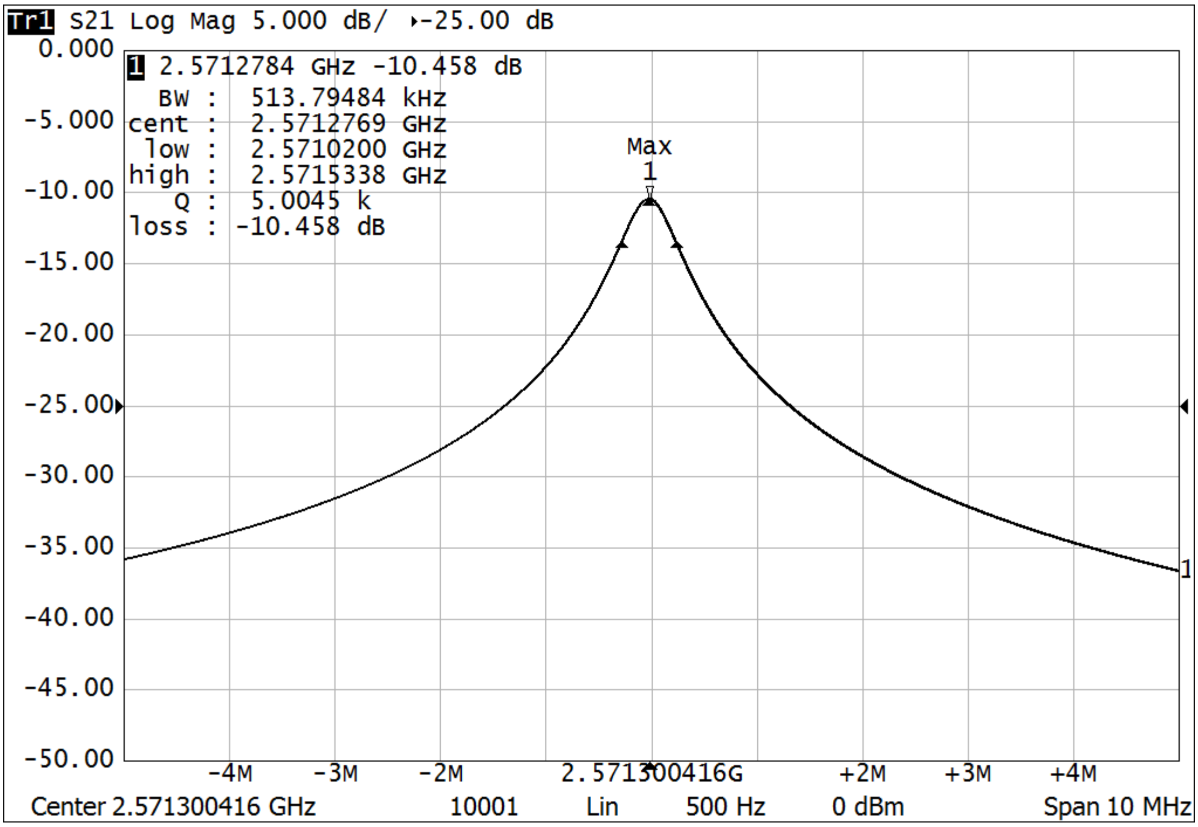

Figure 4.5: Frequency response of the C1 cavity TM_{010} mode showing resonant frequency, bandwidth, Q factor, and insertion loss as measured using a Copper Mountain S5085 VNA .

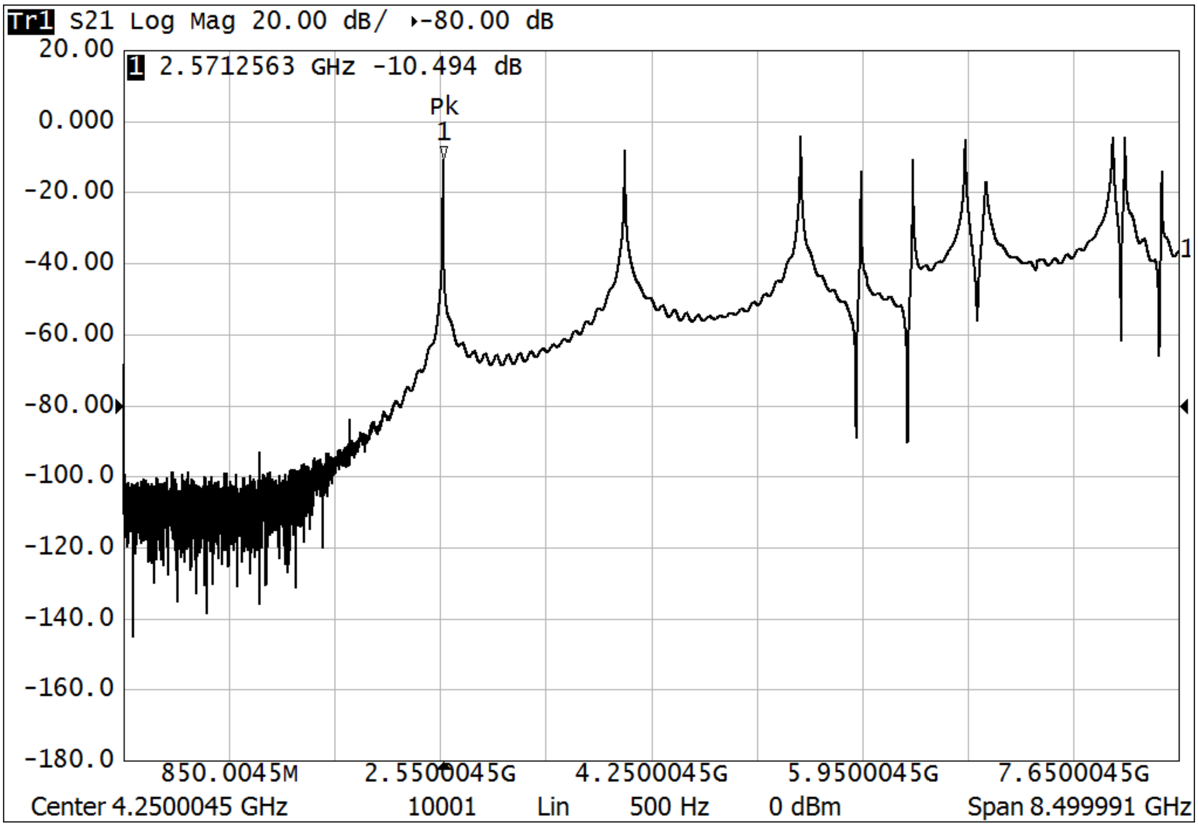

Figure 4.6: Broadband frequency response of the C1 cavity showing resonant frequency of the TM_{010} mode as measured using a Copper Mountain S5085 VNA.

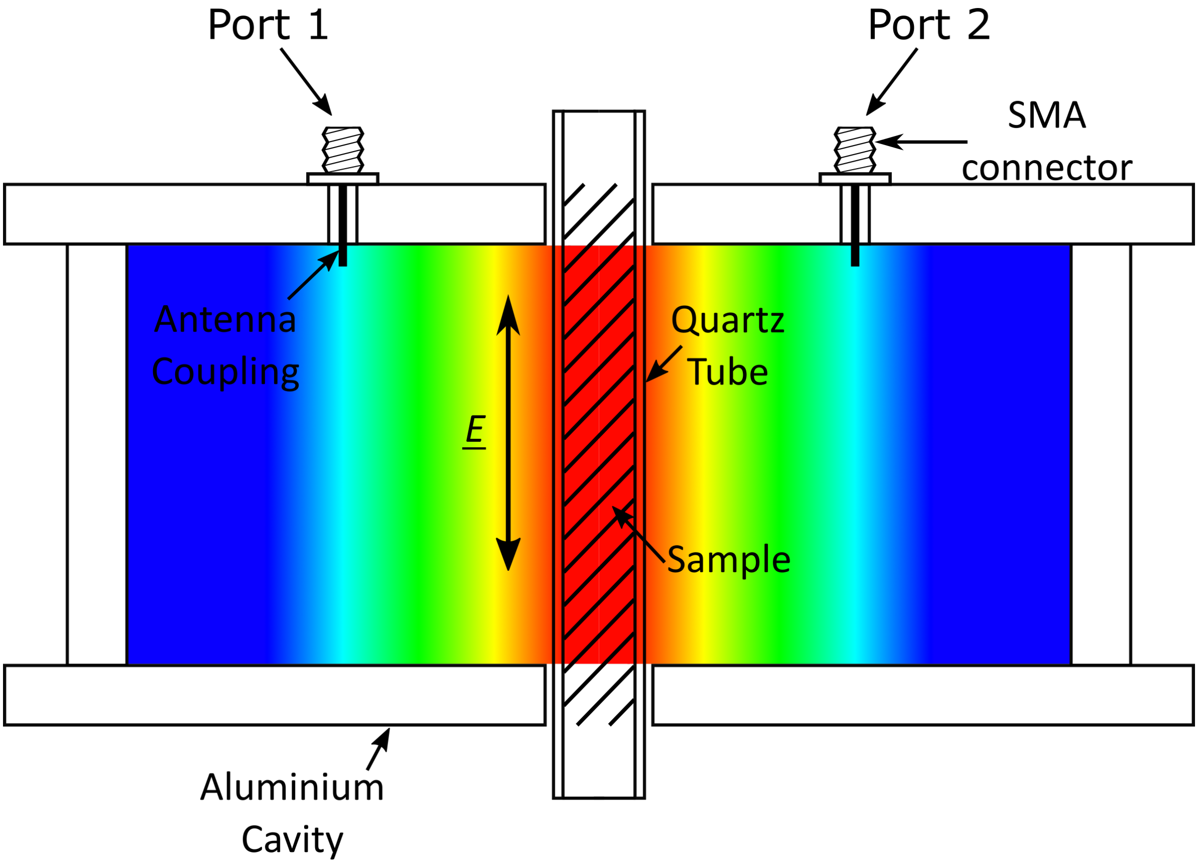

Figure 4.7: Schematic diagram of the microwave cavity showing the electric field of the TM_{010} mode, sample in quartz tube, SMA connectors and antenna coupling.

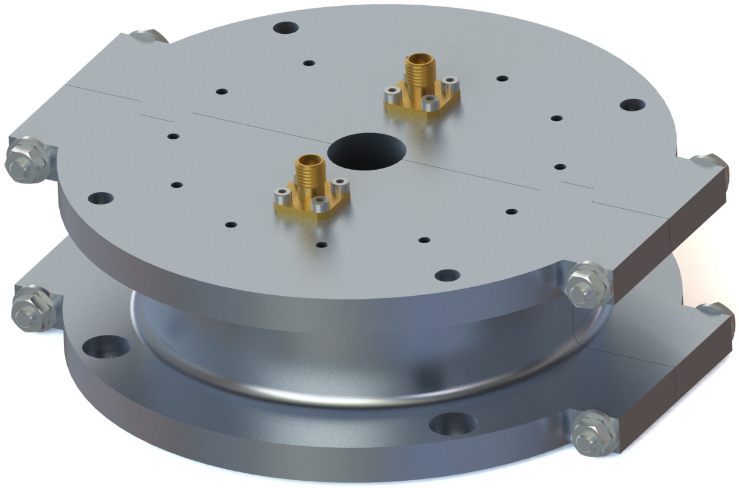

Figure 4.8: Render of cavity resonator showing aluminium cavity, steel construction bolts, SMA connectors, and construction holes to allow the cavity to be integrated into a experiment rig. The split between two halves of the cavity do not break any current paths for the TM_{010} mode.

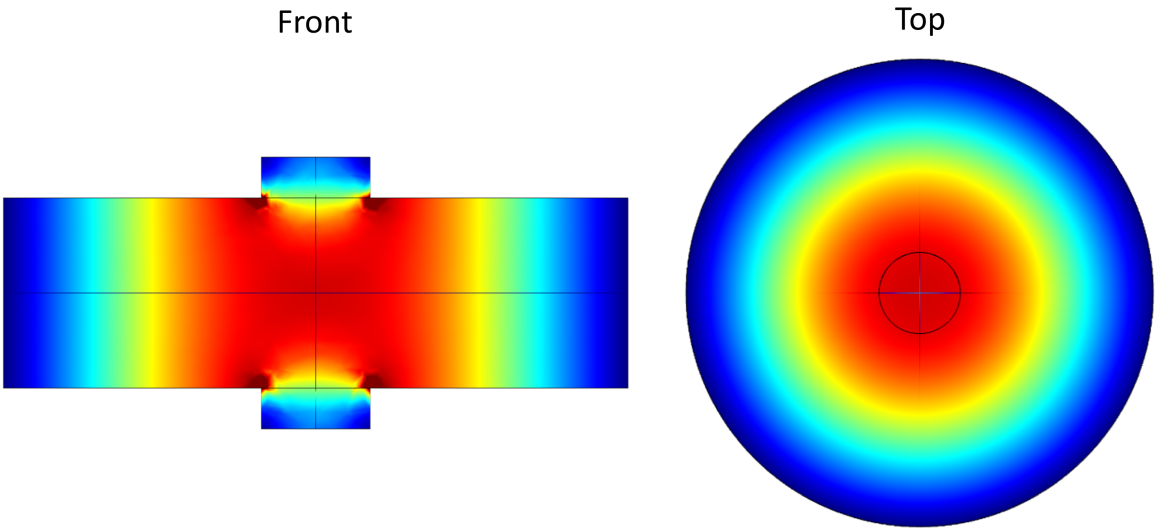

Figure 4.9: Front and top views of electric field within the cavity resonator.

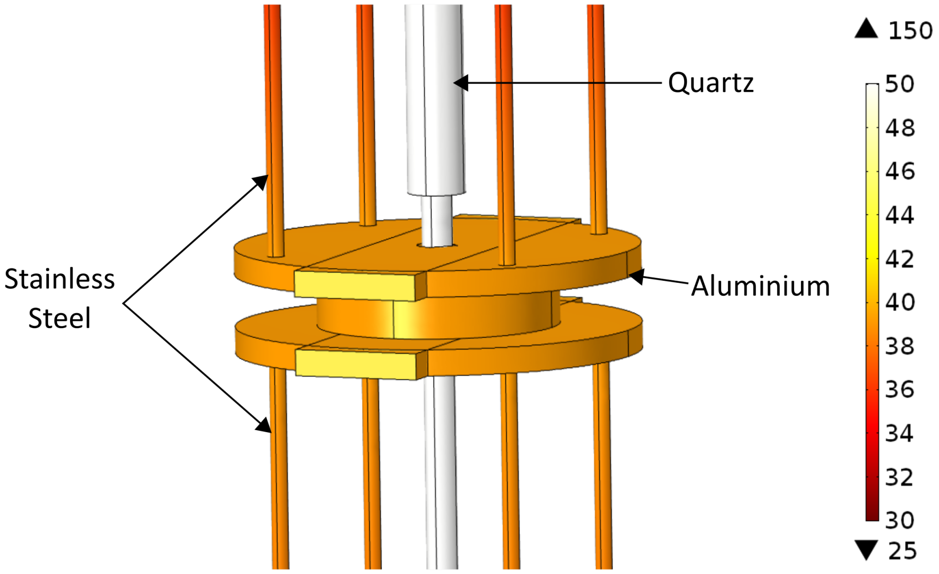

Figure 4.10: COMSOL simulation of the temperature distribution throughout the microwave cavity, quartz tube and supports at maximum temperature.

4.1.3 Heating Equipment Testing

Before using this equipment for simultaneous NPD and MCR measurements at elevated temperatures, it must be tested to ensure the target of 150 °C can be reached with a flowing gas. This temperature is selected as it is appropriate for activating MOF samples, as discussed further in Section 5.3. The NPD experiment occurs in the sample tank of POLARIS which contains a vacuum. As the quartz tube is not in contact with the cavity there is no heating of the cavity due to conduction. As the rig is located in a vacuum there is no heating through convection. This means any heating of the cavity must be through purely radiative heating, ensuring the cavity temperature will not reach the temperature of the gas flow. The increase in temperature of the microwave cavity should be quantified to observe its effect on the measurements. Heating of the cavity will cause changes to the resonant frequency and Q factor of the cavity. Being in a vacuum, the heating effect of the coils will perform differently to when performing the same experiment in an atmosphere due to increased loss of heat to the environment in air via conduction and convection. Due to this, the testing is carried out in the POLARIS sample tank while the neutron beam was off.

An argon gas flow was used with a mass flow controller to set a flow rate of 10 sccm. Heating coils were controlled with temperature controllers with thermocouples placed as close to the sample position as possible, however temperatures were not able to be recorded during this testing due to availability of equipment. Results from this testing can be seen in Figure 4.11. Heating coils were set to 150 °C at the start of this measurement. It can be seen that frequency and Q factor drop as the cavity is heated due to the increased temperature of gas flows. Gas temperature increased to the temperature set point within under 10 minutes. As the cavity temperature was increased only by radiative heating the dielectric data took much longer to stabilise - approximately 6 hours.

It was found that the cavity temperature started at 26 °C and stabilised at 48 °C, well within the operating temperatures of this equipment. The change in frequency during this time was approximately 1.5 MHz, compared to a theoretical change in frequency for this temperature change of 1.27 MHz. The change in temperature due to temperature change is considerably smaller than the expected change in frequency caused by the activation of the sample performed by this equipment in Section 5.3 and so is an acceptable value. This frequency shift may also be greatly reduced by employing the temperature correction technique discussed in Section 2.7.7 for the final experiments. Q factor shift during this time was approximately 300 - less then a 5% reduction. Again this is an acceptable amount as it is far less than the expected shift during activation of the MOF sample.

To further test the equipment the temperature of the heating coils is then increased to 200 °C with the same flow rate. This ensures the equipment is able to operate at above the maximum requirements of the experiments performed in Section 5.3. The final cavity temperature recorded is 59 °C. This temperature is still well within the operating temperatures of the cavity and proves the equipment will be able to perform the heating experiments it was designed for, detailed in Section 5.3. During this period of heating, again the gas temperature reaches its set point within under 10 minutes and cavity temperature only stabilises after approximately 4 hours. This increase in temperature came with an associated shift in frequency of approximately 0.75 MHz, compared to a theoretical change in frequency for this temperature change of

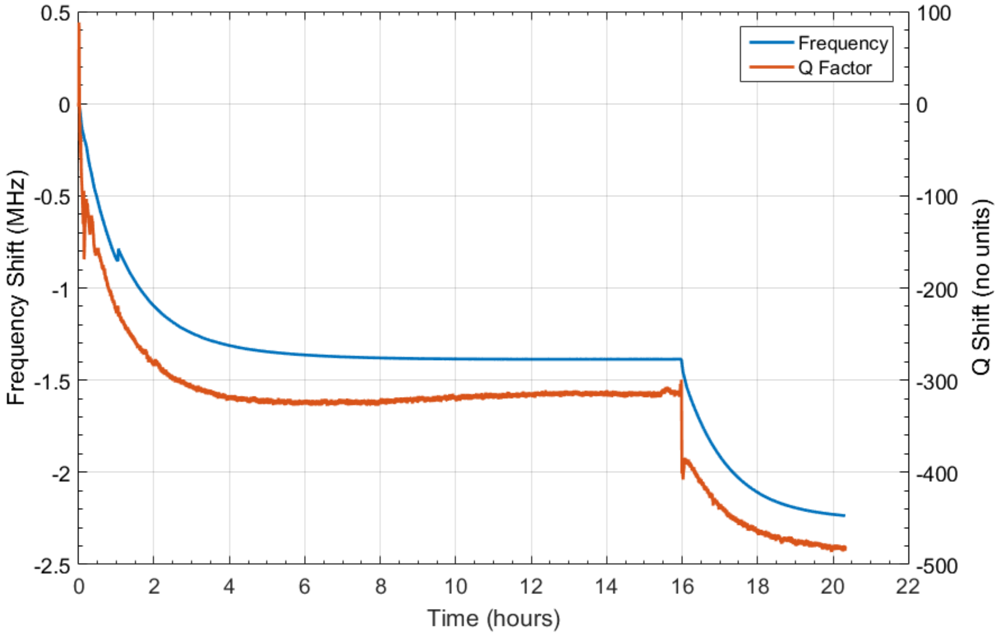

Figure 4.11: Frequency and Q factor shift of microwave cavity over time as gas is flowed through the sample tube and is heated to 150 °C at time = 0, and increased to 200 °C at time ≈ 16 hours

0.64 MHz. This change in frequency was accompanied by a shift in Q factor of approximately 150 - less then a 2.5% reduction. The dielectric response observed during this testing shows the equipment designed in this section will provide adequate heating during NPD experiments as well as be able to accurately track the dielectric response of the system during this heating.

The heating equipment and cylindrical cavity resonator designed in this section is used in Section 5 for simultaneous neutron powder diffraction and dielectric measurement.

4.2 Simultaneous XPDF and Dielectric Measurement Resonator Design

This section describes the design of a microwave resonator able to perform simultaneous dielectric and XPDF measurements of saline salts under a flow of ammonia gas. In order to maximise the resolution of X-ray scattering measurements, no material from the microwave resonator must be in the path of the X-ray beam or in the scattering path. The hairpin geometry microwave resonator designed in this section will be referred to as the H1 resonator.

4.2.1 Resonator Design

The design requirements of the resonator for this experiment are shown below:

- Sample hole of at least 4mm to allow insertion of sample tube.
- At least 1mm hole to allow X-ray beam to enter the cavity.
- An aperture of 60° in the vertical direction to allow scattered X-rays to pass unimpeded.
- An aperture of 30° in the horizontal direction to allow scattered X-rays to pass unimpeded.
- A resonant frequency of approximately 2.45 GHz for the measurement mode.
- Appropriate balance between sensitivity and dynamic range.

The first iteration of design for this resonator was a conventional microwave cavity. To resonate at approximately 2.5 GHz a diameter of 46 mm is used. In order for this cavity to have no material in the path of the X-ray beam a hole must be introduced to allow the beam to enter the cavity unimpeded. As the beam only has a 200 µm width, this hole could be made as small as a 1 mm diameter to allow extra room for easy alignment with the beam. A hole of this size located in the side wall of the cavity would have very little effect on the microwave fields or Q factor of a cavity. To allow an angle of 60° for scattered X-rays to pass through unimpeded by cavity material in the vertical direction, a cavity height 85 mm must be used with the X-ray beam passing through the sample a maximum of 4 mm above the bottom plate of the cavity. This cavity height pushes the TM_{010} mode closer in frequency to other resonant modes but still produces a clean Lorentzian response to be effectively measured. Expanding the height of the cavity also greatly increases the Q factor to a value of 18,200 using equation 4.1 and assuming a perfect cavity before any holes are introduced.

Taking a slice from the cavity wall of this cavity at an angle from the sample position and increasing the angle of the removed slice causes the Q factor to drop. The TM_{010} mode is still able to resonate as the current path is not interrupted. In order to allow scattered X-rays to pass unimpeded and be able to see a very small section of the Debye–Scherrer rings only a small slice of the cavity wall must be removed. However, to increase the resolution of these experiments to be suitable for XPDF measurements an angle of 30° is preferable. As the angle of this slice increases from 0° to the 30° required, the Q factor drops to approximately 200, as seen in Figure 4.12. Once the sample is inserted and a highly lossy gas such as ammonia is introduced, this would cause the Q factor to drop far lower. This Q factor is not adequate for dielectric measurement and would not be reliably measurable. Due to this a cavity resonator for use in these experiment is not viable and another microwave frequency resonating structure must be used.

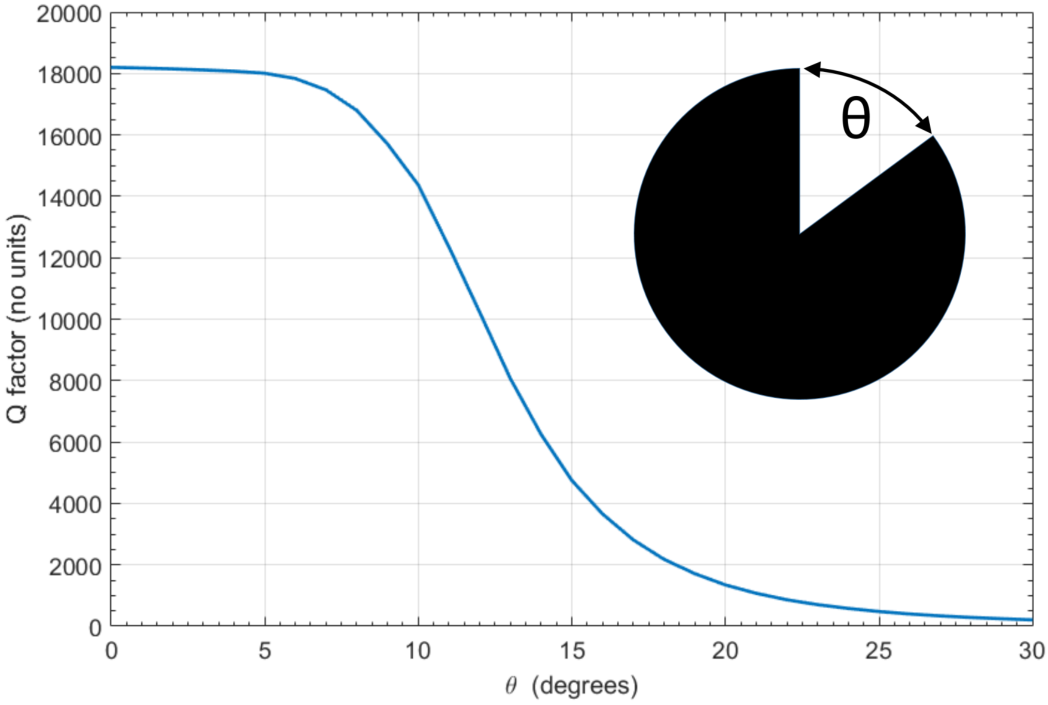

Figure 4.12: Q factor of the TM_{010} mode versus angle (θ) of slice removed from cavity side wall

A quarter wave hairpin style resonator is chosen as an alternate resonant geometry able to fulfil the specification. This geometry of resonator has previously been used for dielectric characterisation of carbon nanotubes [110]. The resonator was designed with a copper hairpin structure mounted on a PTFE base and surrounded by an aluminium shield. The hairpin is made from copper as this has a high electrical conductivity allowing for a high Q factor. The approximate resonant frequency of the dominant mode for a hairpin geometry resonator can be calculated using Equation 4.2,

$$f \approx \frac{c}{4l} \tag{4.2}$$

where l is the height of the hairpin [110]. In practice the resonant frequency is around 10% lower due to electric and magnetic field not being confined to within the resonant structure and spreading out above the hairpin ends. The correction factor shown in Equation 4.3 can be applied to account for this difference,

$$l_{eff} \approx l + \frac{d}{2} \tag{4.3}$$

where l_{eff} is the effective length and d is the separation of the hairpin ends [111]. The height of the hairpin is 27 mm with a width of 6 mm allowing it to resonate with a high electric field at the top of this hairpin structure, with a resonant frequency of approximately 2.45 GHz. The frequency response of the measurement mode can be seen in Figure 4.13. This measurement mode is adequately separated from other resonant modes by 0.9 GHz allowing this resonant mode to be used effectively for sample characterisation. The broadband frequency response for the H1 hairpin resonator can be seen in Figure 4.14. Nylon bolts connect the shield to the PTFE and copper hairpin. The metal shield is included to confine the field. There is no shield along one face to allow X-rays which have been scattered by the sample to pass unimpeded. A hole through the structure is situated in the centre of the resonator base allowing X-rays to pass though without being obstructed by the resonator which would adversely affect PDF resolution. The location of this hole does not effect the electromagnetic performance of the resonator.

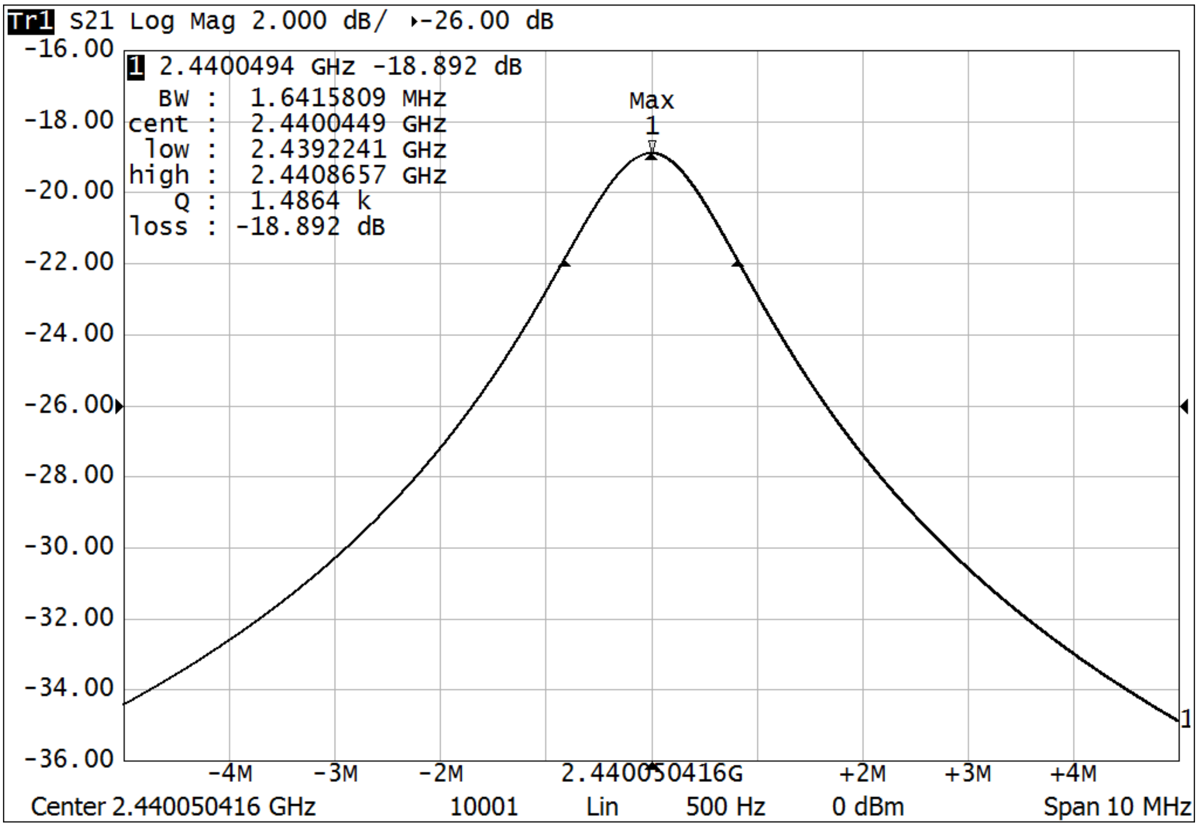

```
Tr1 S21 Log Mag 2.000 dB/ ▸-26.00 dB
1 2.4400494 GHz -18.892 dB
  BW :  1.6415809 MHz
cent :  2.4400449 GHz
 low :  2.4392241 GHz
high :  2.4408657 GHz
   Q :  1.4864 k
loss : -18.892 dB
Center 2.440050416 GHz    10001    Lin    500 Hz    0 dBm    Span 10 MHz
```

Figure 4.13: Frequency response of the H1 cavity measurement mode showing resonant frequency, bandwidth, Q factor, and insertion loss as measured using a Copper Mountain S5085 VNA.

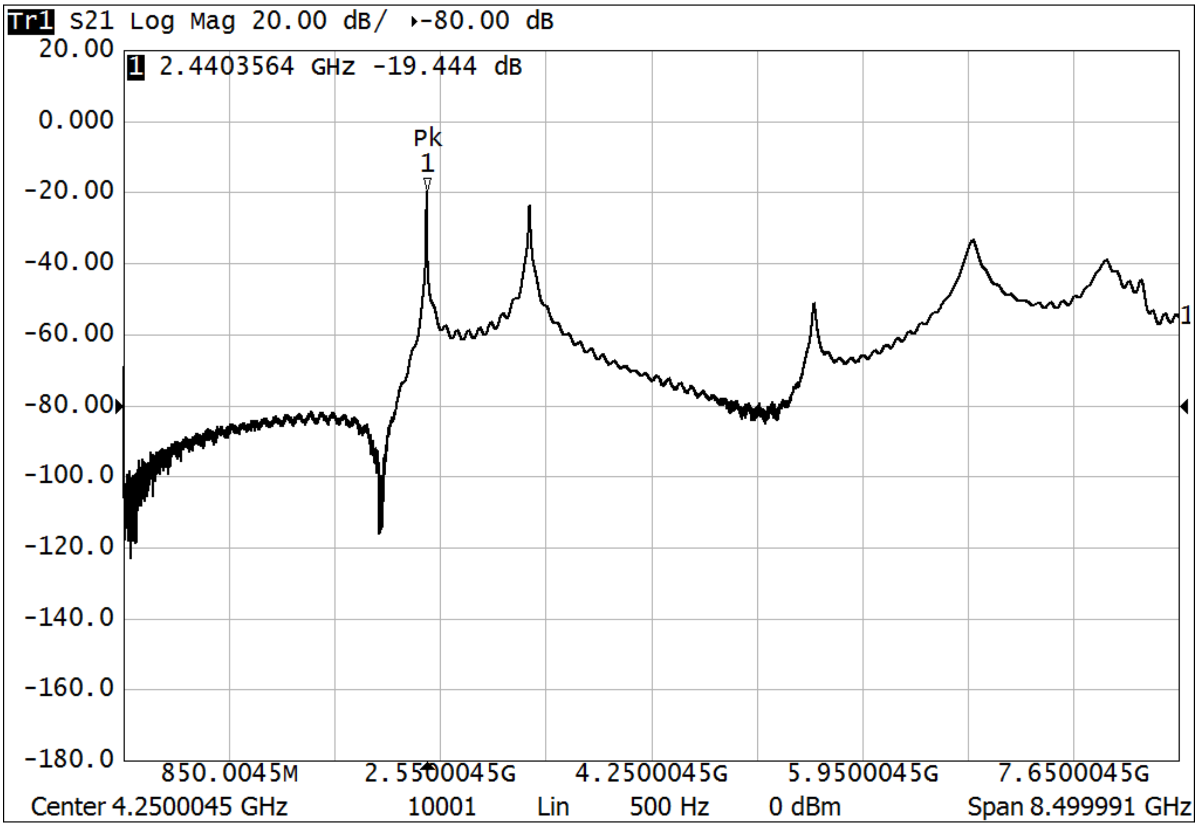

Figure 4.14: Broadband frequency response of the H1 cavity showing resonant frequency of the measurement mode as measured using a Copper Mountain S5085 VNA.

A rounded slot is cut into the shielding so that the sample tube can be inserted into the end of the hairpin resonating structure where the electric field is at its highest. The rounding of this slot ensures that when the sample is loaded the location is self-centred. This sample location has a approximately uniform electric field across the sample volume within the resonator. It also places the sample in line with the incident X-ray beam. Alignment of the sample places the sample tube perpendicular to the electric field. This desensitises the measurement to the introduction of a material with high dielectric loss, such as ammonia, and allows the continued measurement of the sample during the ammonia absorption process. Locating the sample at the hairpin end also places the sample in an area of very low magnetic field. This ensures the resonator is only sensitive to the electric properties of the sample. The resonator was excited using panel mounted SMA connector jacks with a coupling loop, providing inductive coupling to the magnetic field at the bottom of the hairpin structure. A render of this cavity can be seen in Figure 4.15 along with hairpin dimensions. The electric field pattern can be seen in Figure 4.16.

The hairpin resonator designed in this section is used in Section 6 for simultaneous X-ray diffraction and dielectric measurement.

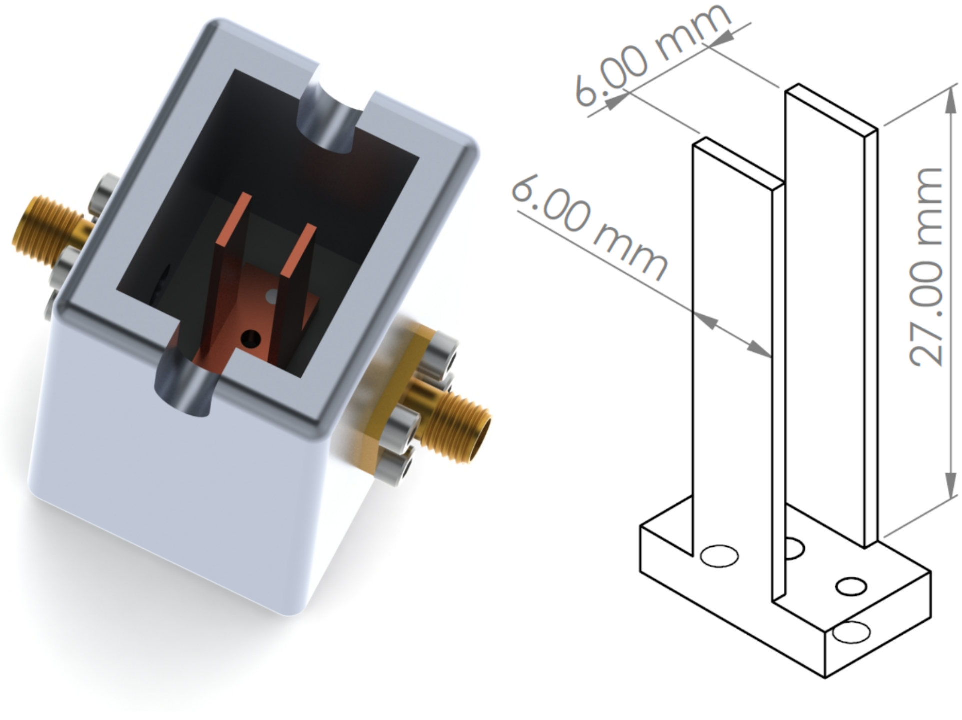

Figure 4.15: Render of hairpin resonator showing copper hairpin, PTFE base, aluminium shield, nylon bolts and SMA connectors (left). Dimensions of hairpin resonator (right).

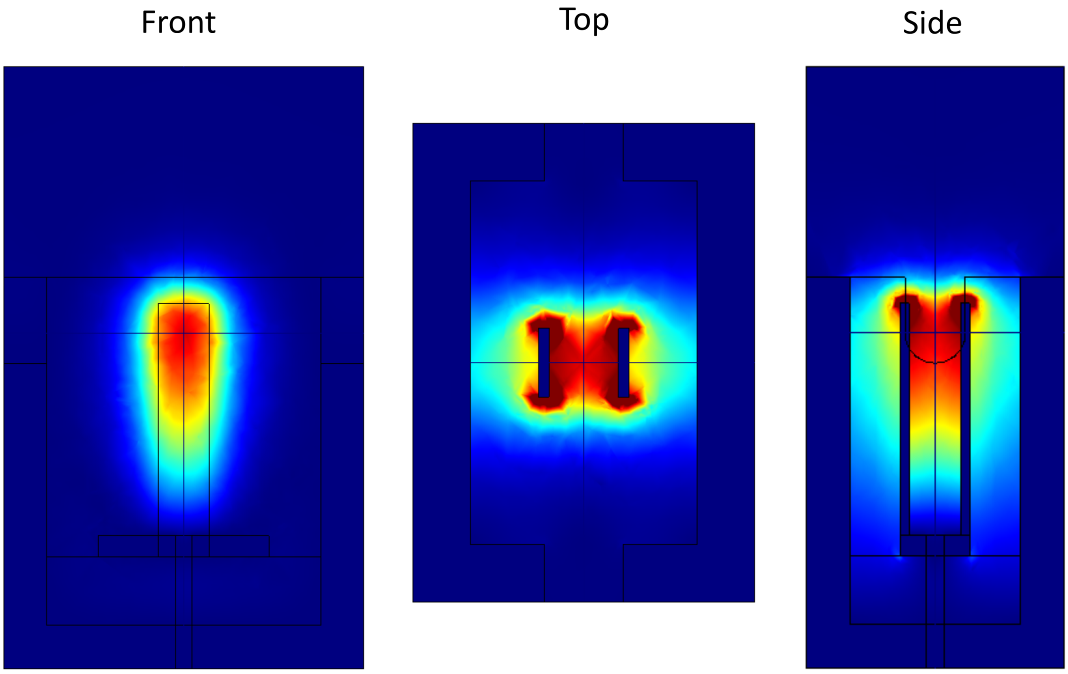

Figure 4.16: Front, top, and side views of electric field within the hairpin resonator with air space on top.

Chapter 5

Simultaneous Neutron Diffraction and Microwave Measurement

The combination of NPD and microwave dielectric techniques are used to investigate solid state materials during the absorption and desorption of polar species. The combination of these complimentary techniques monitors the structure of the material, as well as the changes in the sample's electromagnetic properties. The first series of experiments investigates the absorption of ammonia storage in a selection of metal-organic frameworks. These ammonia storage materials are investigated for use as a possible energy vector and/or air purification filters. The second series of experiments looks at the solid state absorption of SO_2 in MFM-170 to characterise this storage process. This material has shown promise as an appropriate sensor for SO_2. The changes in dielectric properties of MFM-170 during the absorption of SO_2 could be used to quantify the concentration of SO_2 present. Finally, a newly developed microwave resonant cavity (C1) and heating equipment are used to remove water from a MOF sample. This equipment can be used in future experiments to ensure samples contain no water before beginning gas sorption NPD experiments.

5.1 Ammonia Absorption in MOFs

Metal-Organic Frameworks are highly porous materials often suggested as gas storage materials [52, 56, 61, 62, 64]. This makes them possible candidates for ammonia storage. As ammonia is a highly corrosive gas, it is possible that ammonia absorption will lead to degradation of the MOF host material. Thus for any MOF to be recommended as an eligible storage material, its ammonia absorption and desorption characteristics and interactions with the host must first be well studied. To do this, simultaneous NPD and MCR techniques are used to give unique insight into these characteristics, not possible using other techniques applied individually. This section describes simultaneous neutron powder diffraction with dielectric measurements designed to shown the viability of three MOFs to store ammonia. The MOF materials selected were HKUST-1, UIO-66 and CPO-27-Co. HKUST-1 had been shown to be stable to ammonia absorption, but likely to decompose if water is also present [41, 69]. UIO-66 and CPO-27-Co have been shown to be viable candidates for ammonia storage due to their stability to ammonia in [40, 61, 112]. The combination of these techniques can give a unique insight into the properties of these storage materials during the absorption and desorption processes.

5.1.1 Experimental Setup

These measurements are carried out on the Polaris time-of-flight NPD instrument at the ISIS pulsed neutron and muon spallation source in the Rutherford Appleton Laboratory. The Polaris instrument is used as it is a high intensity, medium resolution powder diffractometer, optimised for rapid characterisation of structures [113–115]. The sample rested on a gas permeable silica frit inside a quartz tube which was inserted through the microwave cavity. The cavity used for this experiment will be referred to as the C2 cavity. Quartz is used for the sample containment tube as it has a relatively minimal effect on the microwave field compared to other suitably stable sample tube materials, as well as being a weak neutron scatterer. A modified version of a standard microwave cavity [27] is used. The cavity and quartz tube are supported using a custom built rig which locates the sample inside the microwave cavity and in line with the neutron beam. This cavity was designed with geometry to allow it to operate at 2.5 GHz for the TM_{010} mode with a 46 mm radius and 65 mm height. These cavity dimensions were chosen to ensure a high Q factor and also to prevent interference from other resonant modes. Sample holes of 10.5 mm radius are included to accommodate the sample tube and microwave chokes are used to ensure minimum radiative losses of the microwave field. A 20 mm high section of the cavity, coincident with where the neutron beam intercepts the resonator, was milled to a thickness of 1 mm to minimise neutron scattering from the sample environment. The three pieces of aluminium used for the cavity are secured using nylon bolts, again to reduce scattering from the structure in line with the scattering angles of the neutron beam.

The microwave field is excited using two panel mounted SMA connector jacks with extended centre conductor, providing capacitive coupling to the electric field. This microwave cavity setup including the rig used to secure the cavity during NPD measurements can be seen in Figure 5.1. Radio frequency (RF) cables were used to connect the SMA connectors on the microwave cavity to a FieldFox N9912A VNA. The power transmission coefficient $|S_{21}|^2$ was measured in the frequency domain and non-linear, least-squares curve fitting to a Lorentzian response was used to determine resonant frequencies, Q factors and resonant bandwidths. Microwave data were recorded every 6 seconds. NPD data were collected every 2 minutes - the fastest possible rate. This ensured reaction dynamics were captured while still maintaining a appropriately high resolution.

The gas supply was regulated by a custom-built gas panel. Outgasses were measured by a mass flow meter (Chell CCD100) before passing into a mass spectrometer (HPR-20 QIC R&D Plus from Hiden Analytical). This mass spectrometer was used to monitor deuterated ammonia (ND_3), hydrogen, deuterium, argon, nitrogen, oxygen and water. This setup is shown in Figure 5.2. All measurements were taken at room temperature and pressure. Details on the synthesis and preparations of the MOF samples can be found in [116].

The experimental rig was loaded into the vacuum chamber of Polaris and then the sample loaded into the quartz tube. Argon was then flowed through the sample to remove anything

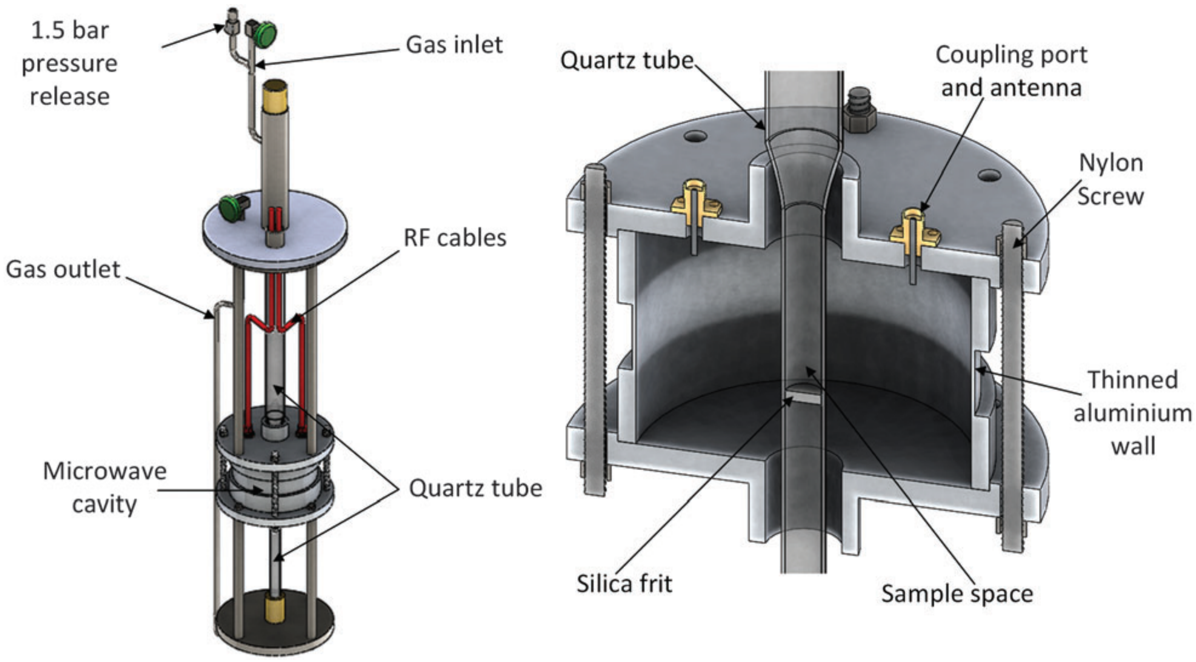

Figure 5.1: Schematic diagram of the experimental housing for the C2 cavity in the Polaris neutron diffractometer (left) and the MCR alone, showing internal position of components (right). [9]

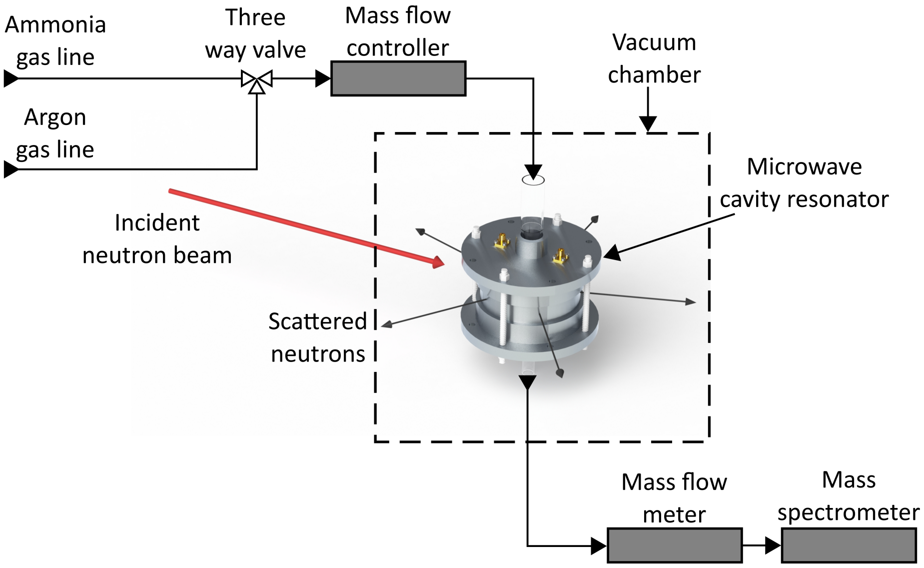

Figure 5.2: Schematic diagram of the simultaneous neutron diffraction and microwave measurement setup for ammonia absorption experiments, showing neutron beam, gas lines and measurement apparatus.[116]

possible absorbed by the MOF during the loading process (most commonly water). Argon was used as it is an inert gas that would not react with the sample. Deuterated ammonia (ND_3) is then flowed through the sample until a plateau was observed in the microwave data, NPD data showed no further change in structure and mass spectrometer began to show ammonia in the outgas. Argon is flowed again in order to flush the ammonia from the sample. Due to the relatively slow rate of neutron diffraction data collection, the flow rate of gases was set to be very low (5 sccm) so that all the structural changes induced by gas absorption could be captured.

5.1.2 Results

The dielectric response for a substance absorbing ammonia is expected to show a drop in both resonant frequency and Q factor. The absorption of a highly polar material both physisorbed to the surface and coordinated within the material causes a drop in resonant frequency. The Q factor of the system is also expected to drop from the absorption of ammonia due to its associated high dielectric loss. This response would be consistent with the absorption of a polar molecule with dielectric loss into a solid state sample [103].

5.1.2.1 Dielectric response of HKUST-1

The dielectric response of HKUST-1 under gas flow is shown in Figure 5.3. The lag between a gas glow being switched on and it reaching the sample is due to the gas taking time to travel along the length of pipe at a slow flow rate. The change in fractional frequency shift (relating to the change in polarisation of the sample) and inverse Q factor shift (relating to the change in dielectric loss of the sample) are measured as ammonia is absorbed, and desorbed by passing argon through the sample, as described in Section 2.8. As ammonia is absorbed by the sample, polarity and dielectric loss of the sample increases. This is consistent with the expected response upon absorption of ammonia, as demonstrated in Figure 2.21. After approximately 1.8 hours, these changes reversed direction with fractional frequency shift beginning to rise

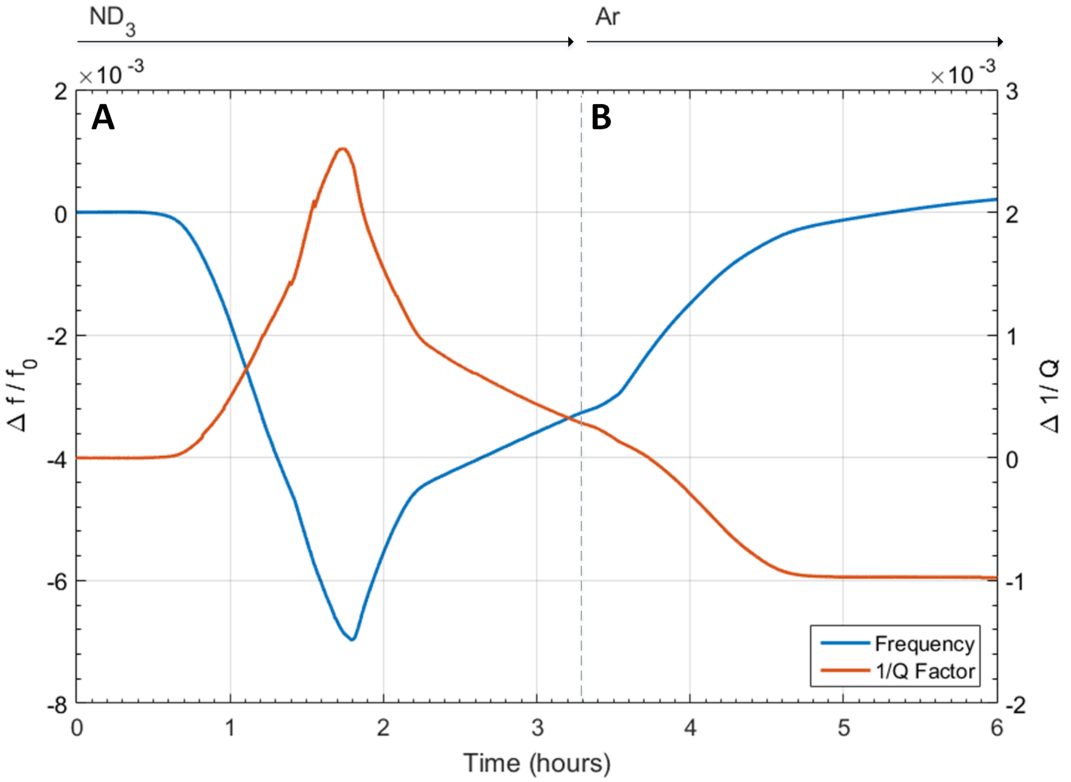

Figure 5.3: Fractional frequency shift and inverse Q factor shift for ammonia absorption and desorption in HKUST-1 under ammonia (ND_3) and argon (Ar) flows. Section A is the first ammonia flow and section B is the system flushed with argon.[116]

and inverse Q factor shift dropping with similar rate as before the inflection, but with opposite sign. This behaviour would be consistent with the loss of ammonia. However when considered alongside the NPD data shown in Figure 5.6, this behaviour is consistent with a structural change and indicates the decomposition of the MOF under ammonia, as reported previously [41, 69]. From 2.2 hours to 3.5 hours the rise in fractional frequency shift and drop in inverse Q factor continued, but with a lower rate of change. Ammonia gas flow was then replaced with argon flow and the rate of change increased until saturation at approximately 5 hours, where polarity of the sample returned to its original value but with considerably lower dielectric loss.

5.1.2.2 Dielectric response of UiO-67

The microwave dielectric response of UiO-67 is shown in Figure 5.4. As ammonia is absorbed the fractional frequency shift was observed to decrease as the inverse Q factor shift increased, which is consistent with the absorption of a polar material with associated dielectric loss. These changes continue until approximately 2.2 hours where the sample became saturated with ammonia and the dielectric response plateaued. This response can be seen in section A of Figure 5.4 and was also observed in previous studies [9, 27]. After dielectric saturation ammonia flow was maintained, during which the dielectric loss remained approximately constant and the polarisation decreased slightly. Changes in dielectric loss, and therefore inverse Q factor shift, are most closely associated with physisorbed ammonia [27]. This is because the dielectric loss relates to the strength of dipolar bonds and the rotational freedom of the molecule. Changes in polarity, and therefore resonant frequency are more closely associated with chemisorbed ammonia. These observations suggest a saturation of the host surfaces with ammonia as there is very little change in inverse Q factor, but a small amount of loss of ammonia from tightly bound sites as a small change in fractional frequency was observed.

Once ammonia gas flow is replaced by argon gas flow in section B, polarisation and dielectric loss of the sample decreases. The gradient of these changes reduce in section B with much slower change in polarisation and dielectric loss. This is due to the gas flow being interrupted meaning loss of ammonia from the sample slows considerably. When the argon gas flow is re-introduced, changes in fractional frequency shift and inverse Q factor shift continue at their original rate. This is consistent with the loss of ammonia, both physisorbed and chemisorbed, from the sample. Once this desorption process has completed, dielectric loss returns largely to its original value however polarisation is significantly lower than before the first ammonia flow. This suggests that some tightly bound ammonia (influencing the sample polarisation to a greater degree than its dielectric loss) was retained within the UiO-67 sample. The ammonia absorption process was repeated in section C with similar results; except that when the sample was held under static ammonia (around 10.5 hours to 12.5 hours) the changes in dielectric properties were smaller than when the sample was held under static argon. This small decrease

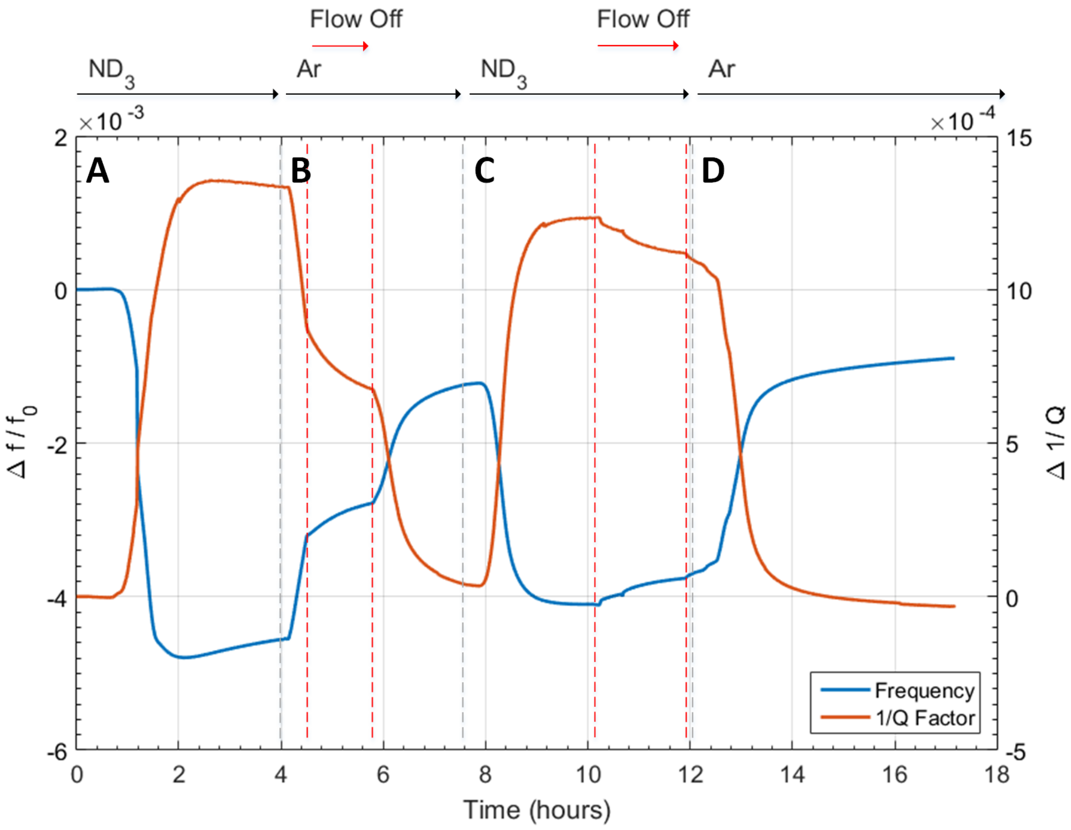

Figure 5.4: Fractional frequency shift and inverse Q factor shift for ammonia absorption and desorption in UiO-67 under ammonia (ND_3) and argon (Ar) flows. Section A is the first ammonia flow, section B is the system flushed with argon, section C is the second ammonia flow and D is the second flush with argon. [116]

in polarity and dielectric loss is consistent with the dielectric properties arising from the natural loss of ammonia due to equilibrium processes. In the final stage (section D) ammonia is lost under argon flow and it is apparent that the dielectric loss recovers to only very slightly less than its original value. The fractional frequency shift, however, still demonstrates a significant negative shift, consistent with the production of a more polar material as described above. This shows that some tightly bound ammonia remains within the MOF even after flushing with argon gas.

5.1.2.3 Dielectric response of CPO-27-Co

The changes in dielectric properties of CPO-27-Co on exposure to ammonia are shown in Figure 5.5. A sudden decrease in fractional frequency shift and increase in inverse Q factor shift were observed on ammonia absorption. The initial dielectric behaviour for CPO-27-Co was similar to that observed for UiO-67 and HKUST-1, and again was consistent with the absorption of ammonia. After approximately 1.5 hours this behaviour was reversed, with a slower decrease in dielectric loss and polarisation observed, normally consistent with the loss of ammonia. Dielectric properties appear to saturate after around 2.5 hours, where the gas flow was replaced by argon. Under argon flow both fractional frequency shift and inverse Q factor shift increase until a plateau was observed at around 5 hours. Argon was replaced with ammonia and flow almost immediately stopped due to experimental difficulties between 5 hours and 7 hours. During this period of no gas flow, no changes in dielectric response were observed. When the ammonia flow was restarted at around 7 hours, an immediate decrease in fractional frequency shift and inverse Q factor shift were observed. This was followed by a general decrease in dielectric loss and approximately stable polarisation. This behaviour was not monotonic. On replacing the ammonia flow with argon at around 9.5 hours, the dielectric loss was observed to return to its original value whereas the polarisation of the sample decreased almost linearly until the completion of the experiment.

Examination of the dielectric properties of CPO-27-Co initially suggested the presence of a structural transition or decomposition reaction. However, inspection of the diffraction data, shown in Figure 5.10 indicates no new Bragg peaks and therefore no change in the CPO-27-Co structure. The observed initial rise and then decrease of fractional frequency shift and inverse Q factor shift is therefore anomalous and not easily explained. The subsequent behaviour of the material under argon and ammonia flow was inconsistent with previous results showing how ammonia interacts with solids. The addition of ammonia caused a decrease in dielectric loss and relatively small, but complex, changes in polarisation. It has previously been observed [9, 27] that when ammonia binds to a solid it produces a decrease in the fractional frequency shift, due to increased polarisation of the sample, and an increase in the inverse Q factor shift

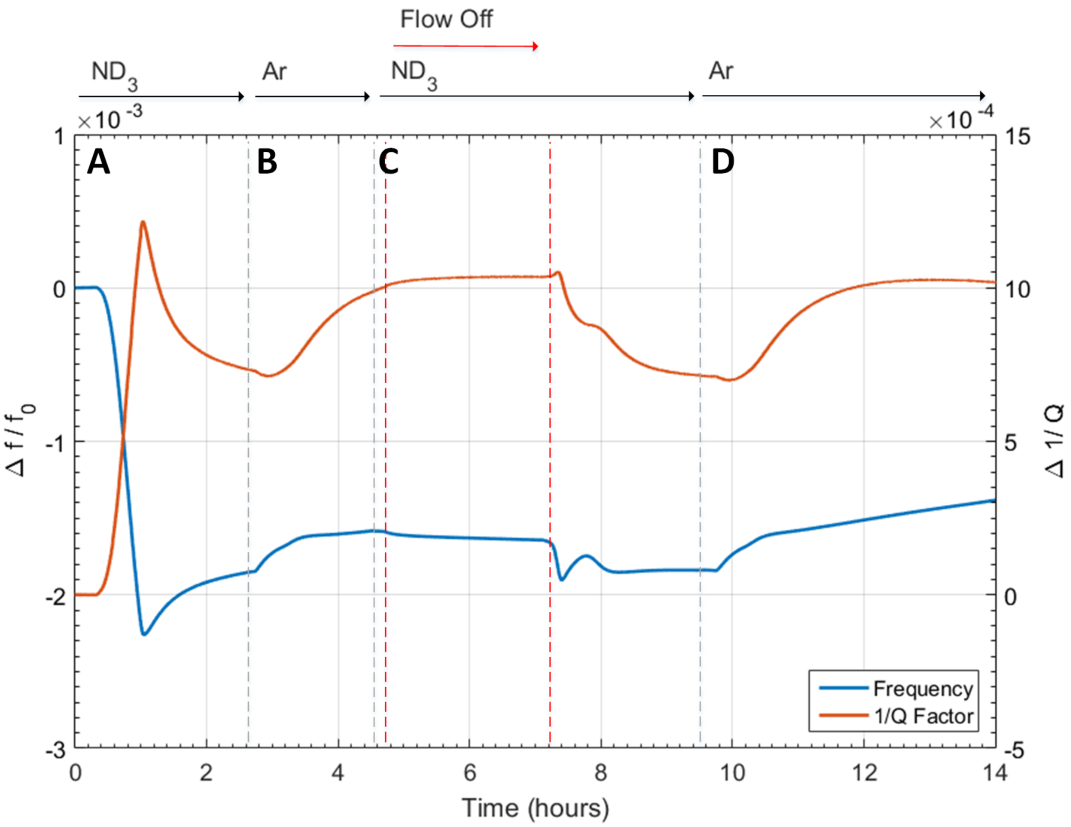

Figure 5.5: Fractional frequency shift and inverse Q factor shift for ammonia absorption and desorption in CPO-27-Co under ammonia (ND_3) and argon (Ar) flows. Section A is the first ammonia flow, section B is the system flushed with argon, section C is the second ammonia flow and section D is the second flush with argon. [116]

due to greater dielectric loss. Here, the behaviour seems to be the opposite and indicates that, after its initial exposure to ammonia and flushing with argon, further exposure to ammonia causes CPO-27-Co to reduce the amount of weakly bound ammonia. This is associated with increases in inverse Q factor. Whilst very slightly increasing the amount of more strongly bound ammonia - associated with decreases in frequency. Mass spectroscopy indicated no ammonia in the outgas and therefore showed no ammonia was not lost from the sample during this time.

5.1.2.4 Structural properties of HKUST-1

A surface plot of the Bragg diffraction from the absorption and desorption of ammonia (ND_3) by HKUST-1 is shown in Figure 5.6. The gaps in the Bragg information correspond to interruptions in time resolved data collection. These data may be used to help us understand the ammonia absorption and desorption processes observed in HKUST-1. The Bragg peaks observed at the beginning of the experiment were consistent with the structure of HKUST-1. A clear structural transformation from the original HKUST-1 structure to a new phase or phases was observed after the ammonia reaches the sample. There are two small changes in gradient in the inverse Q factor shift at approximately 1.4 and 1.6 hours that hint at complex behaviour within this structural transformation. After 1.8 hours the new phase had become the dominant phase. It is therefore likely that this transformation was the origin of the unusual change in dielectric properties observed in Figure 5.3. On exposure to argon gas, some of the Bragg peaks of this new phase or phases weaken in intensity and broaden in resolution where others remain strong. As argon flow is thought to remove weakly bound ammonia molecules, the change in intensity of these Bragg peaks suggests the presence of multiple phases, some associated with ammonia and others not. These changes in structure indicate the degradation of HKUST-1 during the course of this experiment.

Initially ammonia is absorbed by HKUST-1, resulting in the expected increase in dielectric loss and polarisation. At some point in this absorption process by HKUST-1, decomposition occurs resulting in the production of materials with vastly differing dielectric properties. This is clearly seen within the diffraction data, where a clear phase transformation to a poorly crystalline (as evidenced by broad Bragg peaks) new phase or phases was observed. When dielectric data is superimposed onto structural data as seen in Figure 5.7, the first inflection point in the inverse Q factor shift data (around 1.4 hours) occurs at or close to the onset of phase change, with the decrease in inverse Q factor shift occurring as this phase becomes dominant. The subsequent decrease in gradient for the rate of change of dielectric properties at approximately 2.2 hours is less easily explained. However, close inspection of the diffraction data identifies a number of Bragg peaks that appear and disappear throughout the duration of

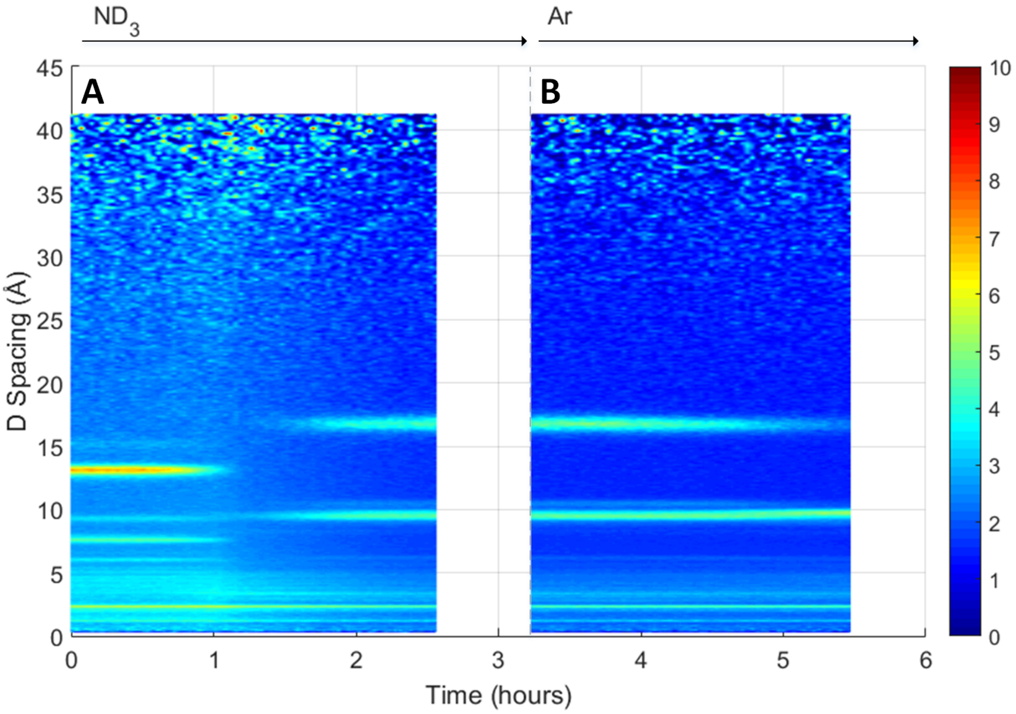

Figure 5.6: A surface plot of Bragg diffraction collected from bank 1 of POLARIS during ammonia absorption and desorption within HKUST-1 under ammonia (ND_3) and argon (Ar) flows. The intensity of the Bragg lines is represented by the colour scale on the right. The white spaces represent the periods when time resolved data collection was stopped to collect high resolution diffraction data. Section A is the first ammonia flow and section B is the system flushed with argon. [116]

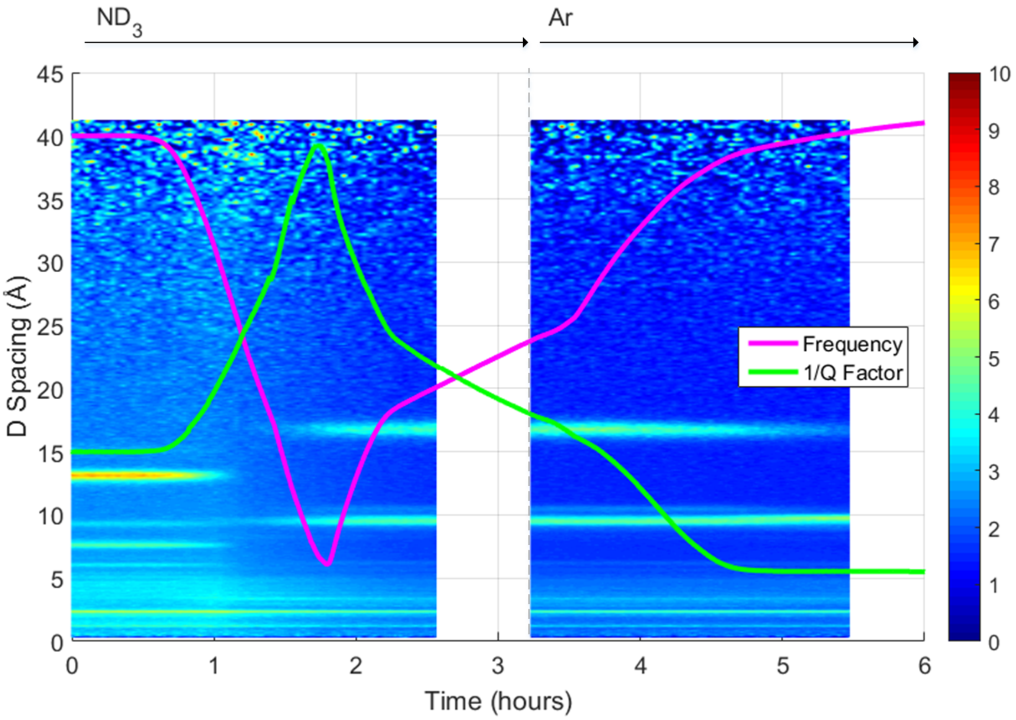

Figure 5.7: Superimposition of the surface plot of Bragg diffraction and dielectric data during ammonia absorption and desorption within HKUST-1 under ammonia (ND_3) and argon (Ar) flows. [116]

the experiment, and this change in gradient appears to be coincidental with the appearance of a Bragg peak at approximately 10 Å. This suggests complex phase change behaviour. On exposure to argon flow, the poorly crystalline phase with its main peak at approximately 18 Å begins to disappear (from 2.5 to 5.5 hours) with a simultaneous decrease in inverse Q factor shift and increase in fractional frequency shift.

5.1.2.5 Structural properties of UiO-67

A surface plot of the Bragg diffraction for the absorption and desorption of ammonia (ND_3) by UiO-67 is shown in Figure 5.8. As the ammonia flow reaches the sample, new Bragg peaks corresponding to a structural modification induced by ammonia binding were observed. In section B, the sample has been flushed with argon gas and the sample isolated from the flow. Here, the Bragg peaks corresponding to the new ammonia containing structure remain at approximately constant intensity. This indicates that ammonia molecules remained tightly bound within the structure, which was consistent with the dielectric data discussed in section 5.1.2.2. Once the ammonia flow is resumed, the Bragg peaks for the ammonia coordinated UiO-67 material decrease in intensity. During this time the full width half max peak intensity increases with background intensity remaining constant. These changes can be attributed to many sources including loss of crystallinity, variable stoichiometry, increased stress/strain and smaller particles. It is not possible to attribute these changes to one or more of these causes without considerable further study. The strengthening and weakening of the intensity of the Bragg peaks on exposure to ammonia or flushing with argon, suggests that further structural changes are created in the MOF host beyond the structure observed on first exposure to ammonia. Although further detailed structural analyses would have to be performed to fully identify these. The final sample polarisation, as indicated by the change in fractional frequency shift, was lower than that of the original sample, whereas a final inverse Q factor shift of approximately zero was recorded. These observations are consistent with both the presence of an ammonia coordinated material or more polar decomposition product. However if decomposition products were produced which were crystalline, new Bragg peaks would be observed. If these products were amorphous an increase in background would be expected. As neither of these seem present, this suggests UiO-67 is able to reversibly bind and release ammonia at room temperature and pressure without significant degradation.

When overlaying the dielectric properties on the Bragg surface plot in Figure 5.9 there is a high degree of correlation between the Bragg diffraction intensity and the dielectric properties. In particular between 4 and 6 hours when the sample was not under gas flow, the fractional frequency shift and inverse Q factor shift both tend to fixed values with the intensity of the main Bragg peak (15 Å) remaining at constant intensity. When ammonia is passed over the sample again (8–11 hours) the Bragg intensity of the new phase decreases noticeably as the polarisation and dielectric loss of the sample increases. All of these factors are consistent with the uptake of ammonia as seen previously.

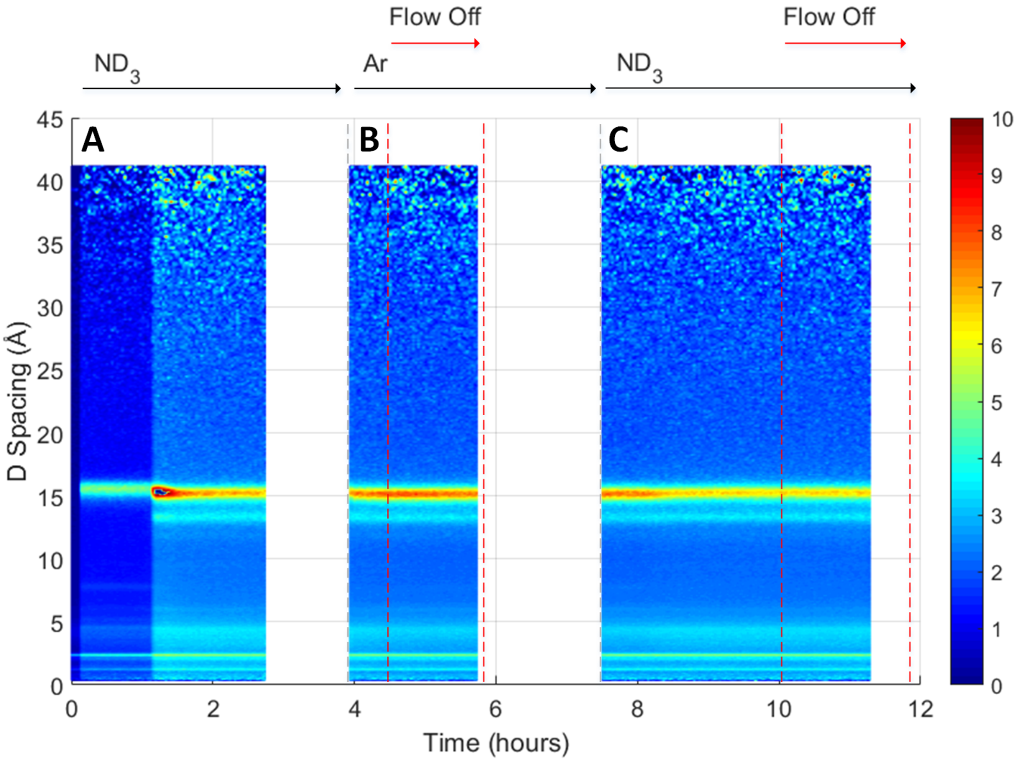

Figure 5.8: A surface plot of Bragg diffraction collected from bank 1 of POLARIS during ammonia absorption and desorption within UiO-67 under ammonia (ND_3) and argon (Ar) flows. The intensity of the Bragg lines is represented by the colour scale on the right. The white spaces represent the periods when time resolved data collection was stopped to collect high resolution diffraction data. Section A is the first ammonia flow, section B is the system flushed with argon and section C is the second ammonia flow. [116]

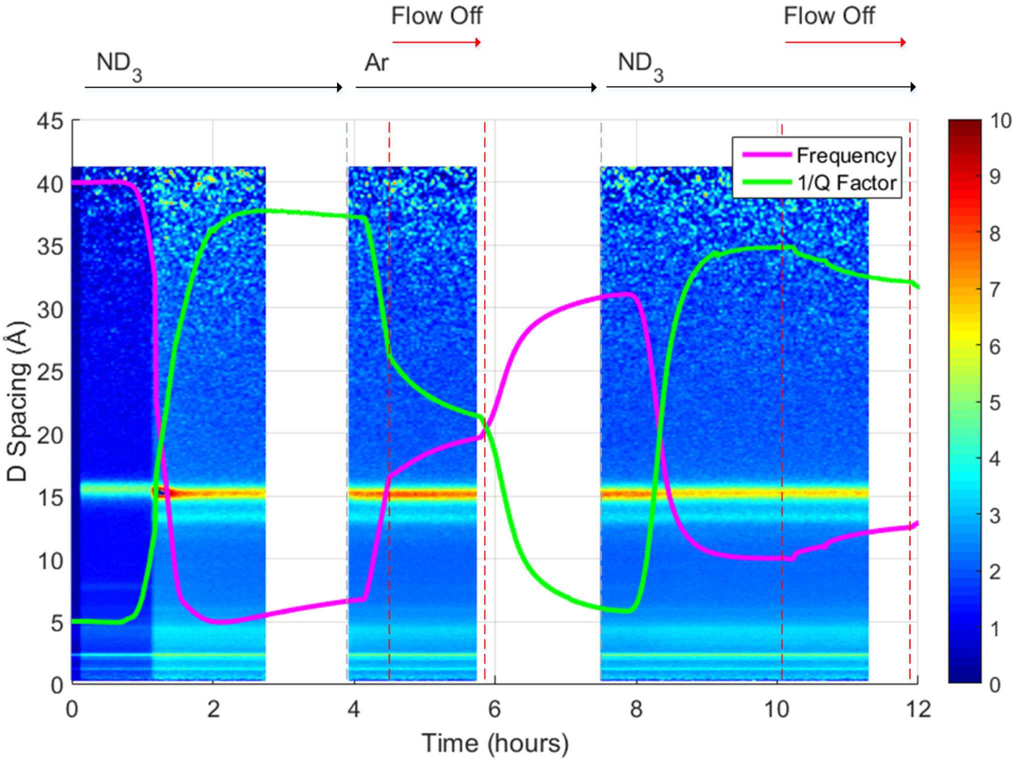

Figure 5.9: Superimposition of the surface plot of Bragg diffraction and dielectric data during ammonia absorption and desorption within UiO-67 under ammonia (ND_3) and argon (Ar) flows. [116]

5.1.2.6 Structural properties of CPO-27-Co

A surface plot of the Bragg diffraction from the absorption and desorption of ammonia (ND_3) by CPO-27-Co is shown in Figure 5.10. The Bragg peaks observed at the beginning of the experiment were consistent with the structure of CPO-27-Co. There appears to be no clear structural transformation in the sample during the ammonia absorption and desorption processes. This may be unexpected given the variety of dielectric properties observed, but likely corresponds to retention of the framework structure upon binding of ammonia. Binding of gases by CPO-27-Co usually occurs through chemisorption at open metal sites, followed by physisorption within the pores. While all the Bragg peaks are relatively weak (the Bragg peak at 2.5 Å is due to diffraction from the sample environment) there does appear to be a change in the intensity of the Bragg peaks arising from CPO-27-Co. Although there is a general variation in scattering intensity across all the data (as evidenced by the variation in background intensity) and therefore it is difficult to conclude much useful information from these data.

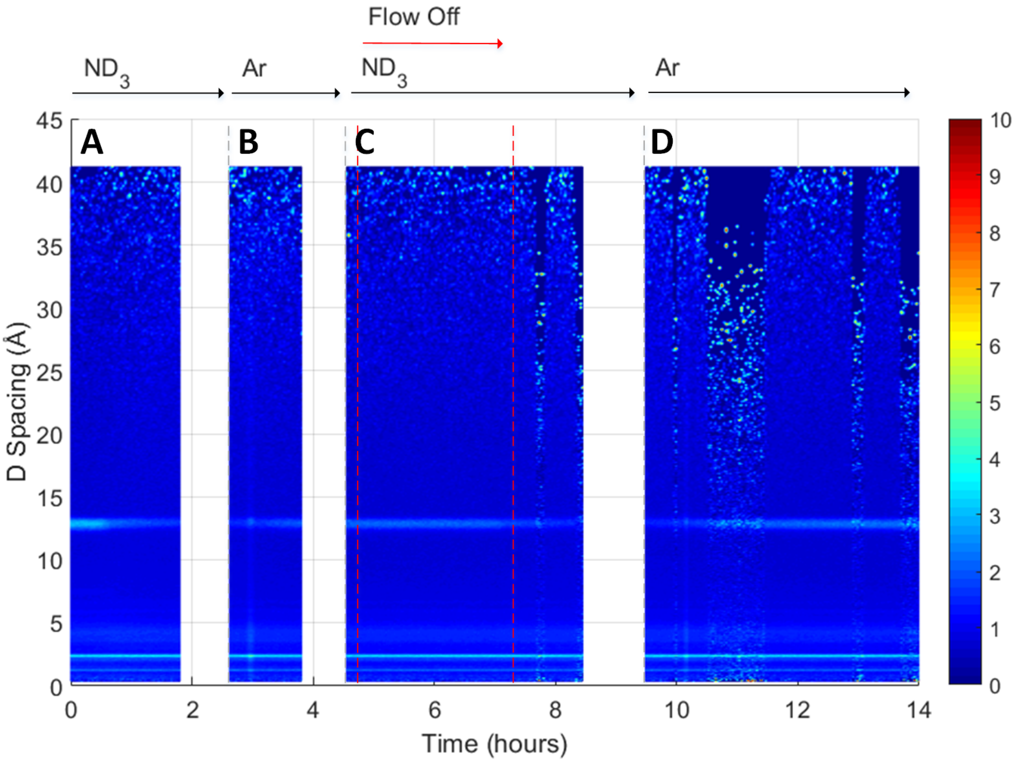

Figure 5.10: A surface plot of Bragg diffraction collected from bank 1 of POLARIS during ammonia absorption and desorption within CPO-27-Co under ammonia (ND_3) and argon (Ar) flows. The intensity of the Bragg lines is represented by the colour scale on the right. The white spaces represent the periods when time resolved data collection was stopped to collect high resolution diffraction data. Section A is the first ammonia flow, section B is the system flushed with argon, section C is the second ammonia flow and section D is the second flush with argon. [116]

The dielectric data is overlaid on top of the Bragg data in Figure 5.11. This shows the decrease in intensity of Bragg peak at around 13 Å aligns with the decrease in fractional frequency shift and increase in inverse Q factor shift from the dielectric data. After this point it is difficult to conclude much information from this overlaid graph.

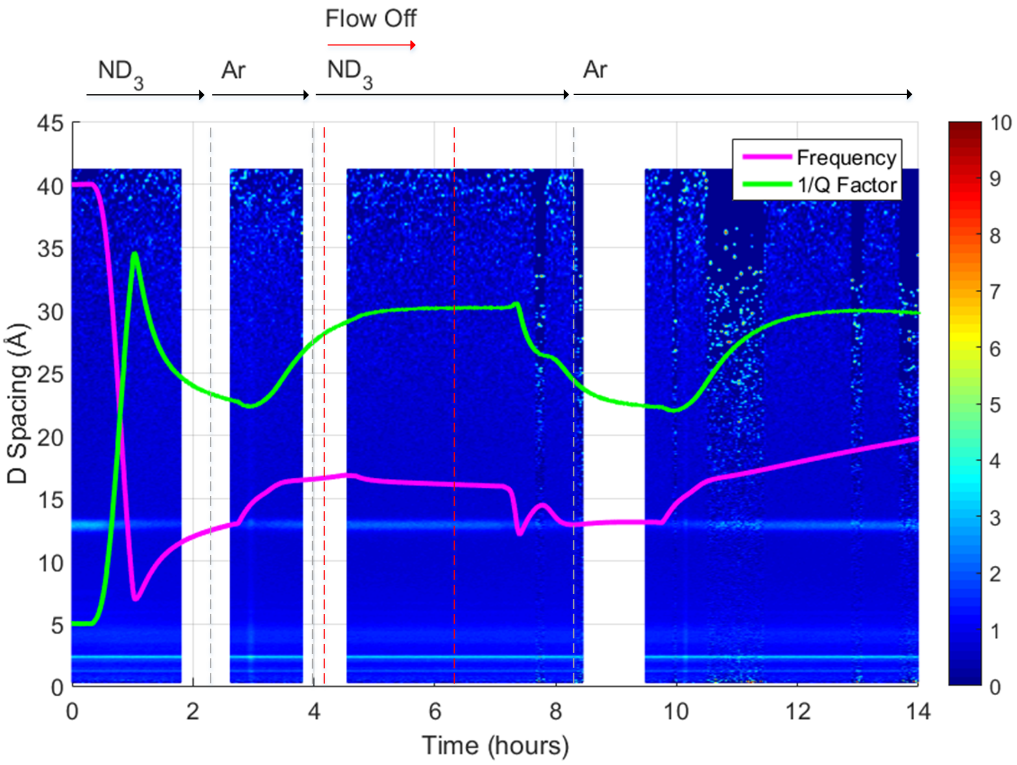

Figure 5.11: Superimposition of the surface plot of Bragg diffraction and dielectric data during ammonia absorption and desorption within CPO-27-Co under ammonia (ND_3) and argon (Ar) flows. [116]

5.1.3 Conclusions on Ammonia Absorption in MOFs

HKUST-1 decomposed under ammonia flow although it was not possible to identify the decomposition products. This decomposition explains the unusual dielectric response shown in Figure 5.3 during ammonia absorption. The structural response shown in Figure 5.6 shows this complex interaction with ammonia where the sample decomposes, producing a number of new phases as ammonia is absorbed by the sample. Due to this decomposition, ammonia storage in HKUST-1 warrants no further investigation.

UiO-67 displayed dielectric properties expected during the absorption and desorption of a lossy, polar molecule such as ammonia, as shown in Figure 5.4. After argon has been flowed through the sample the inverse Q factor shift is seen to return to almost its original value, whereas the fractional frequency shift does not. This indicates the retention of tightly bound, chemisorbed ammonia to the metal centres of the MOF. The structural data shows a change in structure as ammonia is absorbed by the sample, however there is no decomposition of the sample, as seen in Figure 5.8.

Dielectric results for CPO-27-Co, shown in Figure 5.5 suggest either decomposition of the sample or a change in structure due to its unusual dielectric behaviour. The diffraction data shows no additional Bragg peaks forming and therefore no change in the CPO-27-Co structure in Figure 5.10. The observed initial change and then relaxation of fractional frequency shift and inverse Q factor shift is therefore anomalous with our understanding of how ammonia interacts with solid materials. Potentially, this unexpected decrease in polarity and dielectric loss during ammonia flow could be due to the formation of ammonia networks. These networks would decrease dielectric loss and polarisation as hydrogen bonds form between ammonia molecules.

Such behaviour is difficult to interpret, but it may be that on exposure to additional ammonia, the weakly bound ammonia begins to form coordinated (hydrogen bonded) networks. This has been seen in other MOFs,[117] where the hydrogen-bonded ammonia molecules have fewer degrees of freedom than weakly absorbed individual molecules and therefore contribute less to dielectric loss. This behaviour could explain the sharp rise and then relaxation of dielectric properties observed on first exposure to ammonia. When the ammonia flow is replaced with argon, ammonia is removed, disrupting the coordination networks and restoring their ability to contribute to increased inverse Q factor shift. Such networks might also affect the polarisation of the system, with multiple hydrogen bonded layers of ammonia acting to dampen polarisation effects. This would cause smaller overall changes to sample polarisation with respect to dielectric loss. Further studies are required to confirm the presence of coordinated ammonia networks and to validate this hypothesis. These conclusions are consistent with the observed data and, if confirmed, highlight the ability of CPO-27-Co to stably store considerable quantities of ammonia.

The combined methodology of diffraction and dielectric spectroscopy provides a valuable tool to interpret complex ammonia absorption and desorption behaviour, providing insights not available from the use of these techniques individually. The literature has previously demonstrated its utility in examining simple molecular species such as metal salts [9, 27]. These experiments have now shown that it is equally applicable to study much more complex materials such as MOFs, and that the methodology provides information on subtle adsorption processes and structural features that may be missed by other techniques applied individually. The MOF materials investigated show a variety of properties, ranging from decomposition, through structural modification to structural inviolability, with the potential for ammonia filtering and/or storage highlighted for the UiO-67 and CPO-27-Co materials. These materials show strong binding and significant uptake. Furthermore, an understanding of the interaction of these materials with ammonia provides significant insight, that may be used to design a new generation of materials with enhanced resistance to ammonia.

5.2 SO_2 Absorption in MOFs

The MOF MFM-170 has been shown to be stable to SO_2 and absorb SO_2 repeatedly in large volumes. Characterisation of MFM-170 is necessary during absorption and desorption of SO_2 to understand the mechanisms involved in these processes. This section documents the characterisation of MFM-170 using simultaneous NPD and dielectric characterisation. Bragg diffraction data was used to show structural changes in the MOF as SO_2 is absorbed and desorbed from the sample. Dielectric characterisation is used as a complementary technique to acquire additional information on the changes in polarity and dielectric loss of the sample during this process. Previous studies using these combined techniques in Section 4.1 and in [9, 27] have been used to determine considerable information on mechanism and kinetics of absorption processes and this information is crucial in evaluating this material as a SO_2 absorber.

5.2.1 Experimental Setup

These measurements are also carried out on the Polaris time-of-flight NPD instrument at the ISIS pulsed neutron and muon spallation source in the Rutherford Appleton Laboratory. The experimental setup used for this experiment was similar to that used in Section 5.1. The experimental rig shown in Figure 5.1 is used with the C2 microwave cavity and the same quartz tube setup. The FieldFox used for experiments in Section 5.1 is replaced by a Copper Mountain S5085 VNA. As with the ammonia absorption experiments, the power transmission coefficient $|S_{21}|^2$ was measured in the frequency domain and non-linear, least-squares curve fitting to a Lorentzian response was used to determine resonant frequencies, Q factors and resonant bandwidths. Microwave data were recorded every 6 seconds. NPD data were collected every 2 minutes - the fastest possible rate. This again ensured reaction dynamics were captured while still maintaining an appropriately high resolution.

Gas flows for this experiment were provided by the ISIS toxic gas panel. It was not possible to use a mass flow meter for these experiments as no SO_2 compatible meters were available. All measurements were taken at room temperature and pressure. The schematic diagram of this setup is shown in Figure 5.12. As the MFM-170 MOF readily absorbs water from the air, the activated sample was loaded into the sample tube inside a glove bag in an argon atmosphere. This minimised the amount of water present in the sample at the beginning of the experiment. Argon was used as an inert gas that would not react with the sample. Sulphur Dioxide (SO_2) was then flowed through the sample until the microwave data plateaued, and NPD data showed no further change in structure. Argon is flowed again in order to flush SO_2 from the sample. Due to the relatively slow rate of neutron diffraction data collection, the flow rate of gases was set at a slow rate so that all the structural changes induced by gas absorption could be captured.

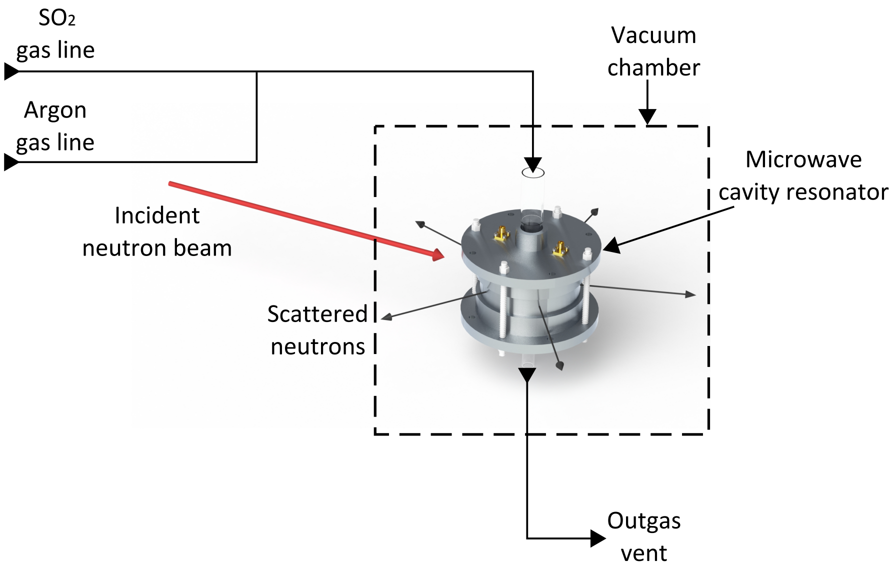

Figure 5.12: Schematic diagram of the simultaneous neutron diffraction and microwave measurement setup for sulphur dioxide absorption experiments, showing neutron beam, gas lines and measurement apparatus.

5.2.2 Results

5.2.2.1 Dielectric Response

Sulphur dioxide is a polar molecule with a high dielectric loss. This is expected to have the effect of reducing the resonant frequency and Q factor of the cavity as SO_2 is absorbed by the sample. Figure 5.13 shows the dielectric response of the sample as it absorbs SO_2. The beginning of the graph is under argon flow. Gas flow of SO_2 was introduced at a slow flow rate at 1.8 hours and took approximately 5 minutes to reach the sample. At this point the fractional frequency shift increased slightly before beginning to decrease. It is difficult to be certain of the reason for the slight rise in frequency, but this may be due to the change in pressure introduced by changing the gas. As sulphur dioxide is polar, the drop in fractional frequency shift is the expected behaviour. At approximately 2.3 hours a change in gradient of the fractional frequency shift is observed. The cause of the gradient change is unclear but may be due to SO_2 leaving one binding site in the MOF and re-binding at another site - causing a

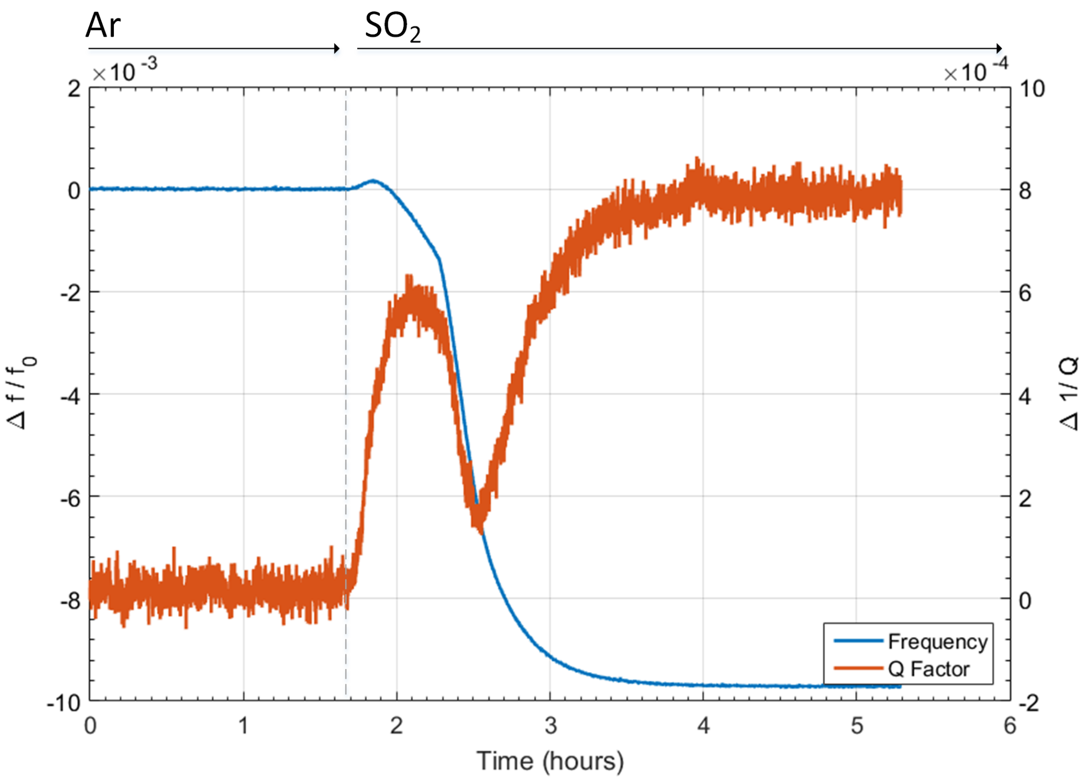

Figure 5.13: Fractional frequency shift and inverse Q factor shift for SO_2 absorption in MFM-170 under SO_2 flow.

change in the polarity of the system. Polarisation then continued to rise before tailing off to a plateau where the sample was saturated with SO_2.

Changes in inverse Q factor shift showed a somewhat complex behaviour. As SO_2 was absorbed by the sample, the inverse Q factor shift began to rise, as expected, for the absorption of a material with high dielectric loss. At approximately 120 minutes however, dielectric loss began to drop whilst SO_2 is still being absorbed. This is not the expected behaviour for this system and the reason for this unexpected behaviour is not yet understood. At around 2.7 hours, inverse Q factor shift began to increase again before tailing off to a plateau.

Once the sample was fully saturated with SO_2, the gas flow was switched to argon at the same flow rate. The dielectric response is shown in Figure 5.14. Due to a crash in the drivers used to control the VNA, a large section of the dielectric data for this section was lost. As the argon flushes the SO_2 from the sample, the polarisation of the sample begins to decrease.

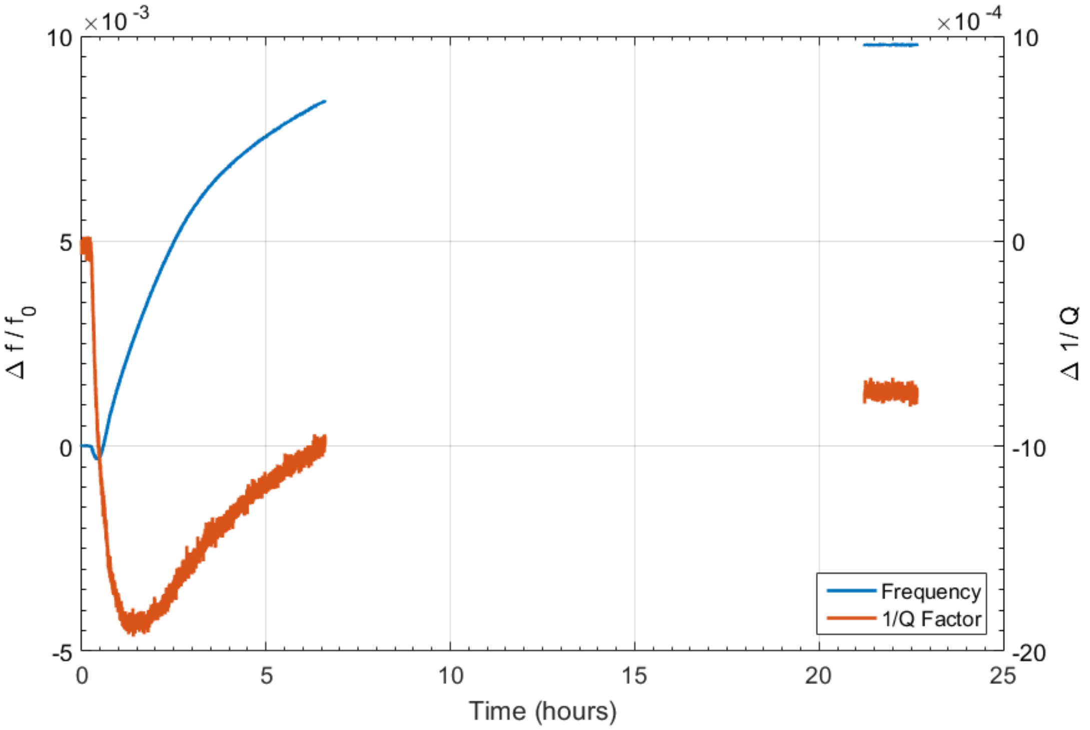

Figure 5.14: Fractional frequency shift and inverse Q factor shift for SO_2 desorption in MFM-170 under Argon (Ar) flow.

From the data present, it is assumed the frequency response continues in one curve to the final value seen at the end of this graph. Dielectric loss decreases as SO_2 is remove from the system. At approximately 100 minutes however, dielectric loss begins to increase. Again, this behaviour is unexpected and warrants further investigation. The curve for inverse Q factor shift is assumed to continue until it reaches its final value.

Figure 5.15 shows the dielectric response during a second SO_2 absorption process, but this time at a much faster flow rate. This faster flow rate causes full saturation with SO_2 in under 2.5 hours, as opposed to the 4 hours in the first absorption in Figure 5.13. Other than the change in rate of absorption, the behaviour of resonant frequency and Q factor match the same pattern as the first SO_2 absorption. This shows that the unusual behaviour seen in inverse Q factor shift is a repeatable process.

Once the sample was saturated with SO_2, the gas flow was switched to argon at the same elevated flow rate. The dielectric response for this is shown in Figure 5.16. This response

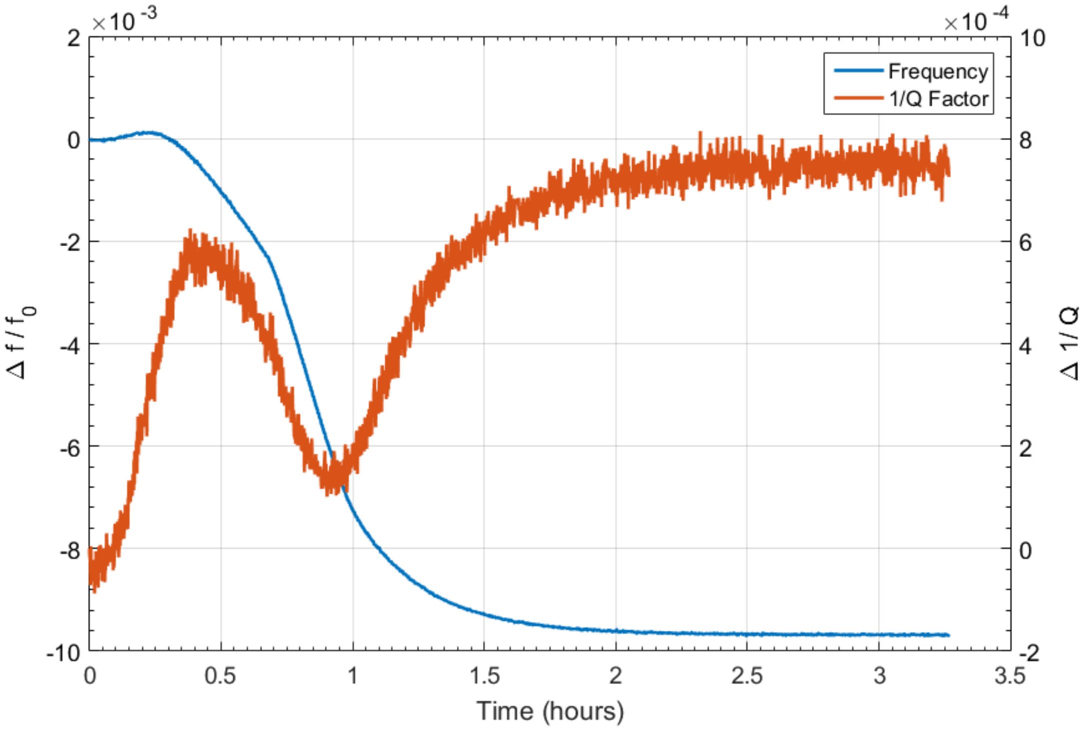

Figure 5.15: Fractional frequency shift and inverse Q factor shift for SO_2 absorption in MFM-170 under SO_2 flow.

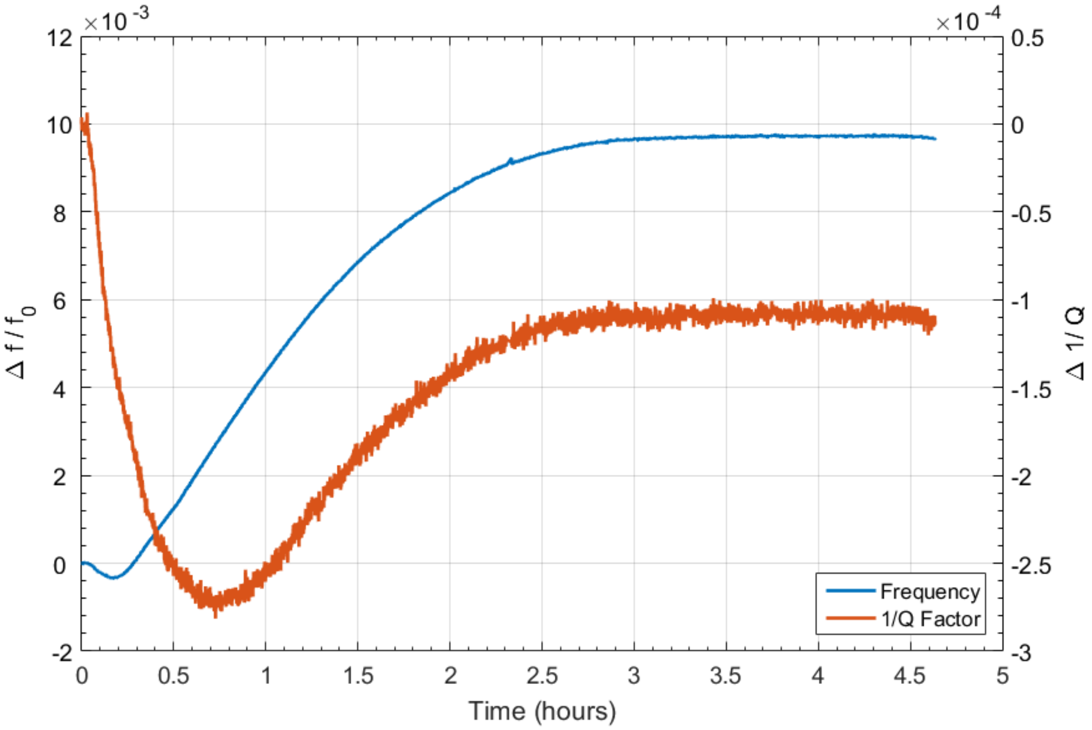

Figure 5.16: Fractional frequency shift and inverse Q factor shift for SO_2 desorption in MFM-170 under Argon (Ar) flow.

confirms the assumption that fractional frequency shift and inverse Q factor shift continue their curve, while dielectric data is lost. Once again, other than the change in rate of SO_2 desorption, the behaviour of resonant frequency and Q factor match the same pattern as the first desorption. Again, this shows that the unusual behaviour in dielectric loss where inverse Q factor shift starts to increase, then begins to decrease before increasing again during SO_2 absorption is a repeatable process.

5.2.2.2 Structural Properties

The Bragg data of MFM-170 as it absorbs SO_2 is shown in Figure 5.17. Structural changes can be seen after approximately 1.75 hours. The Bragg peak at 17 Å greatly reduces, as do peaks at 12 Å and 9 Å. Other Bragg peaks at lower D-spacings also reduce. The Bragg peak at 24 Å exhibits more unusual behaviour. This Bragg peak grows in intensity to a maximum

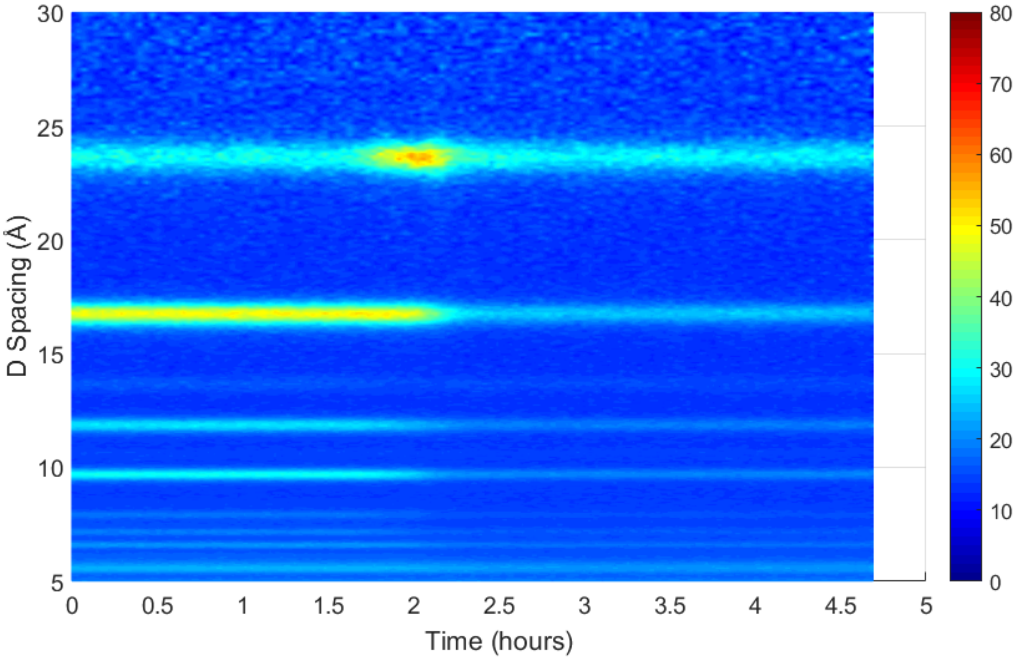

Figure 5.17: A surface plot of Bragg diffraction collected from bank 1 of POLARIS during SO_2 absorption within MFM-170. The intensity of the Bragg lines is represented by the colour scale on the right.

at 2 hours and quickly reduces. The reason for this behaviour is still unknown. Overall, the structure of MFM-170 during SO_2 absorption does not change.

Structural changes during the desorption of SO_2 by flowing argon through the sample can be seen in Figure 5.18. As with the absorption of SO_2, there are no changes in structure during the desorption process. Bragg peaks at 17 Å, 12 Å and 9 Å that reduce during absorption, recover to their original intensity during desorption. Again, the Bragg peak at 24 Å exhibits unusual behaviour. As argon begins to visibly desorb at 0.75 hours, the peak at 24 Å increases in intensity and becomes broader. This broadening is associated with a mixture of stoichiometries, where several Bragg peaks are present at very similar *d*-spacings. These nearby Bragg peaks combine to be observed as a single, broad Bragg peak with high intensity. As the desorption continues, the peak reduces in intensity and narrows to its original width. Again the reason for this behaviour is unknown. As the Bragg peaks show the same structure during SO_2 ab-

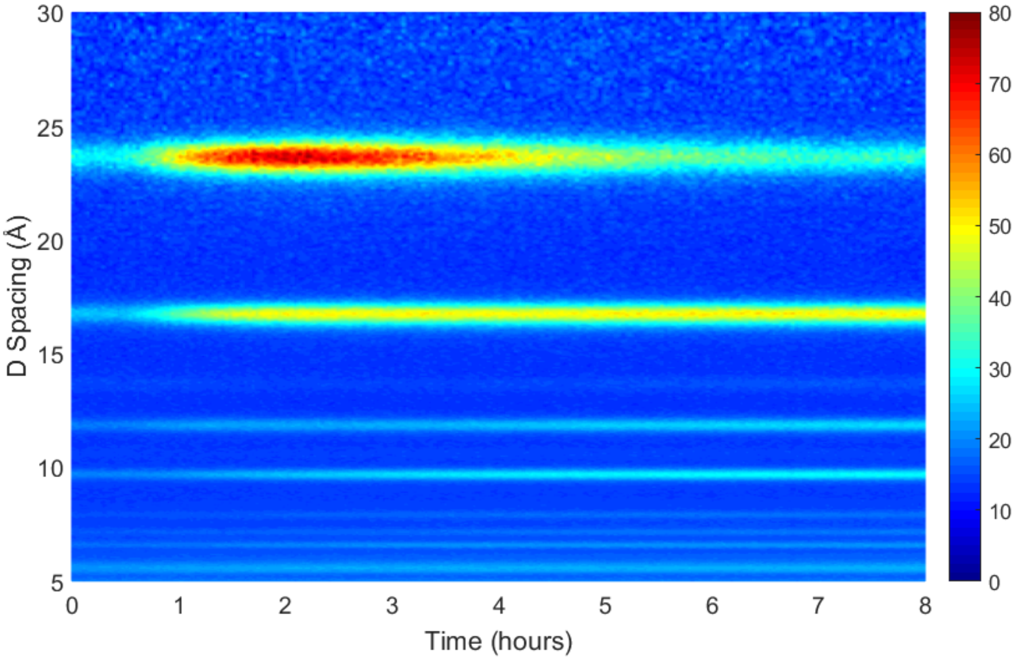

Figure 5.18: A surface plot of Bragg diffraction collected from bank 1 of POLARIS during SO_2 desorption within MFM-170 under Ar flow. The intensity of the Bragg lines is represented by the colour scale on the right.

sorption and desorption, this shows the stability of MFM-170 under these conditions and its ability to store SO_2 without decomposing.

In order to check the repeatability of the behaviours seen above, these experiments were repeated. For this absorption/desorption cycle, the flow rates were increased due to time constraints. The structural data for the absorption and desorption of SO_2 are shown in Figure 5.19 and Figure 5.20 respectively. The time bases for this second cycle are shorter due to the increased flow rate. The Bragg data in Figure 5.20 is incomplete as the neutron beam was shut down before the full desorption profile could be captured. Other than these changes, the patterns observed match those present in the first cycle of SO_2 absorption and desorption. As the structure is the same at the end of the second cycle as at the beginning of these experiments, this shown the ability of MFM-170 to repeatedly store SO_2.

When overlaying dielectric data on top of structural data for SO_2 absorption in Figure 5.21,

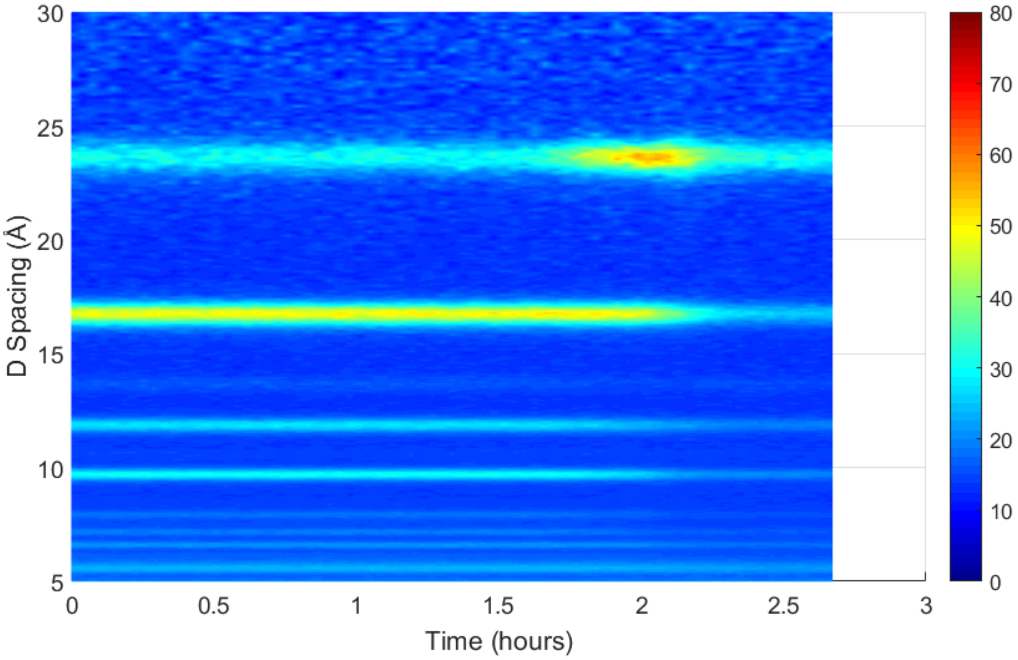

Figure 5.19: A surface plot of Bragg diffraction collected from bank 1 of POLARIS during the second SO_2 absorption within MFM-170. The intensity of the Bragg lines is represented by the colour scale on the right.

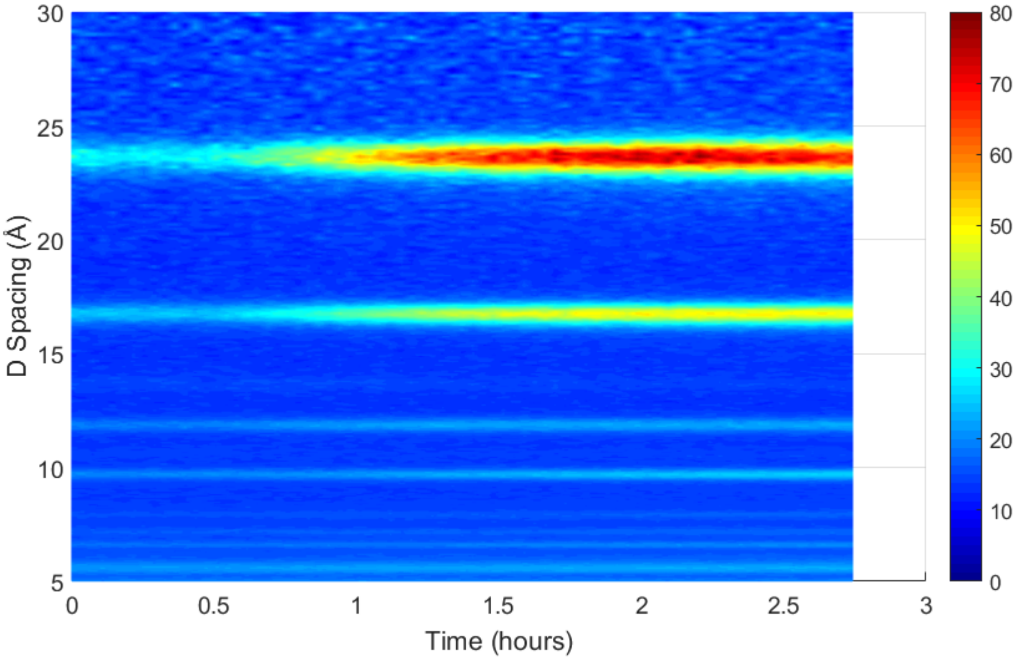

Figure 5.20: A surface plot of Bragg diffraction collected from bank 1 of POLARIS during the second SO_2 desorption within MFM-170 under Ar flow. The intensity of the Bragg lines is represented by the colour scale on the right.

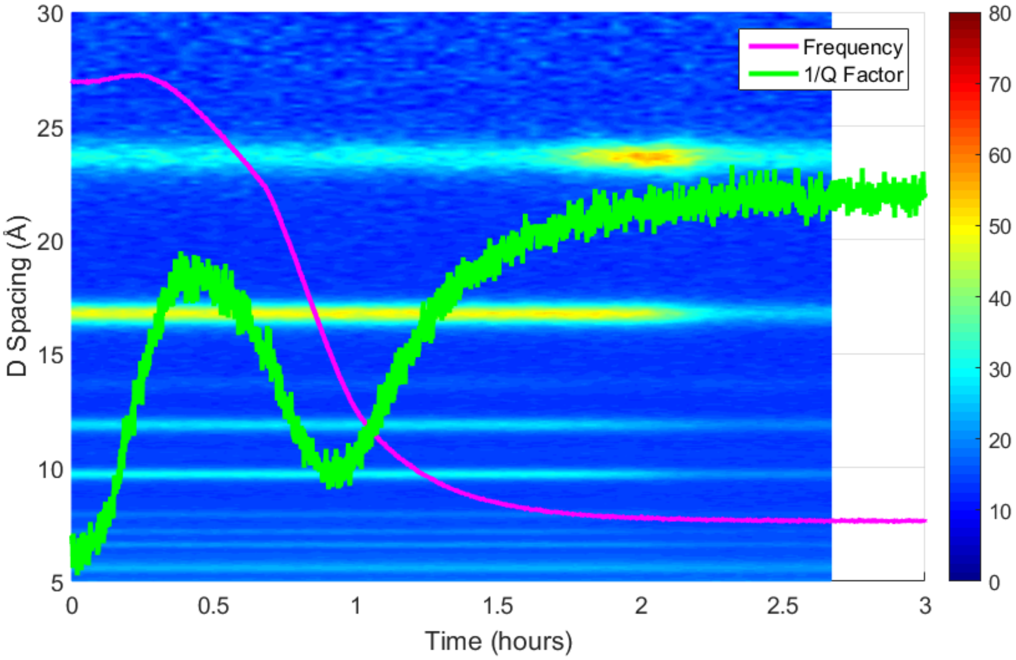

Figure 5.21: Superimposition of the surface plot of Bragg diffraction and dielectric data during SO_2 absorption within MFM-170 under sulphur dioxide (SO_2) flow.

no additional information is provided to explain the unusual behaviours seen in both sets of data. The unexpected drop in dielectric loss from 0.5 hours to 1 hour, is not coincident with the increase and decrease of intensity of the Bragg peak at 24 Å at around 2 hours. This suggests these two behaviours may have two different causes or, giving the sequence, that one influences or is reliant on the other as a domino effect.

For SO_2 desorption, dielectric data overlaid onto structural data is shown in Figure 5.22. As inverse Q factor shift increases, so does the intensity and width of the peak at 24 Å. The structural data for this is cut short so the decrease in intensity of this Bragg peak cannot be seen. Despite this, it can be seen that the inverse Q factor shift increases and reaches its steady final value before this drop in intensity occurs. Again, the combination of dielectric data and structural data does not help to identify causes of unexpected behaviours for this study.

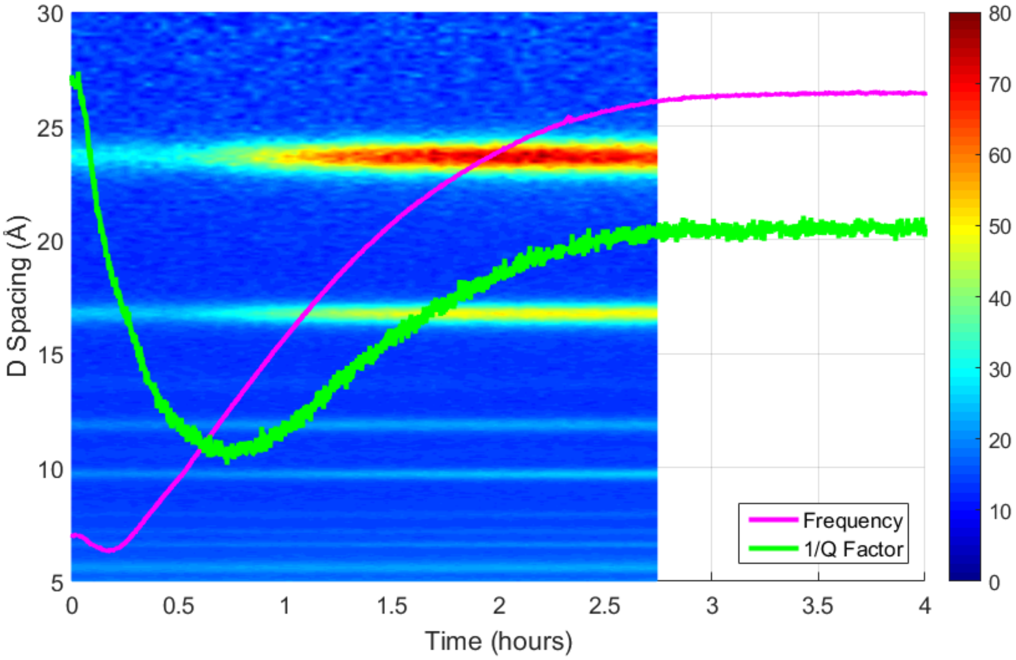

Figure 5.22: Superimposition of the surface plot of Bragg diffraction and dielectric data during SO_2 desorption within MFM-170 under argon (Ar) flow.

5.2.3 Conclusions on SO_2 Absorption in MOFs

In these experiments, the SO_2 absorption and desorption characteristics of MFM-170 were investigated using simultaneous dielectric characterisation and neutron diffraction. The frequency results for these processes behaved as expected where, as the polar molecule was absorbed by the sample, the frequency dropped. As SO_2 was removed from the sample, fractional frequency shift then recovered to its original value. Q factor however, exhibits more unusual behaviour. An initial drop in inverse Q factor shift occurs, as a molecule with associated dielectric loss is absorbed, as expected. The subsequent decrease and increase seen in the dielectric loss is not expected and cannot easily be explained. The structural data shown by the Bragg peaks also shows some unusual behaviours. The Bragg peak at 17 Å and the peak at 24 Å increases in intensity and quickly decreases in intensity during SO_2 absorption. The same Bragg peaks also increases in intensity and decreases again during removal of SO_2 from the sample, with a broadening of the Bragg peak during this time.

With the current data available it is not possible to find a conclusive reason for these unexpected changes in Q factor and Bragg data. One possible cause is due to the temperature change of the sample which is caused by the exothermic nature of the SO2 absorption process. This temperature change may lead to a change in the dielectric properties of the MOF, SO2 or both. Another possible reason for this behaviour is water in the MOF. Care was taken to ensure as little water was present in the sample during the experiment, but some water in the pores of the MOF is inevitable. Interaction between the MOF, water, and SO2 is another possible cause for the complex behaviour. It should also be mentioned that the Q factor for this cavity is approximately 1500 when empty. Once the sample is loaded into the cavity, the Q factor drops to a mere 40. This Q factor is far lower than ideal for these experiments, but should be adequate and robust enough to be confident in the trends seen in Q factor. Further experiments are required in order to discover the cause of the unexpected behaviour of the inverse Q factor shift during the dielectric measurements, and the Bragg peak at 24 Å. These experiments are detailed in Chapter 7.

5.3 High Temperature MOF Activation

Section 4.1.1 documents the design of equipment intended for use with simultaneous NPD and MCR measurement at elevated temperatures. This setup can be used to activate MOFs to ensure no substances are stored within the pores of theses materials. As MOFs readily absorb water from the air, keeping MOFs activated whilst placing them into the sample environment is not possible. MOFs can be loaded with minimal exposure to air by loading into the sample tube in a glove box or glove bag however, while the sample tube is loaded into the rig, some air exposure is inevitable. In order to ensure the MOF is activated at the beginning of the experiment, the sample must be activated in-situ. This can be done by flowing an inert gas through the sample that has been heated to an adequate temperature. For this experiment the MOF MFM-170 is used, which can be activated using a gas heated to 150 °C.

5.3.1 Experimental Setup

This experiment also uses the POLARIS instrument at ISIS neutron spallation source. The heating equipment and C1 cavity design used can be seen in Section 4.1.1. This setup is mounted into a custom built experimental rig, designed to house the cavity, gas handling, thermocouples, and heating coils. This rig is constructed to be placed in the sample chamber of POLARIS to locate the thinned section of the microwave cavity in line with the neutron beam - to minimise the amount of scattering from the cavity. The microwave cavity was connected via RF cables, capable of operating under vacuum and at temperatures up to 200 °C, to a Copper Mountain S5085 VNA. The power transmission coefficient $|S_{21}|^2$ was measured against frequency and non-linear, least-squares curve fitting to a Lorentzian response was used to determine resonant frequencies, Q factors and resonant bandwidths. Microwave data were recorded every 2 seconds. NPD data were collected every 2 minutes - the fastest possible rate. This ensured any changes in structure during the hydration/dehydrated process are captured and still allows adequate NPD resolution.

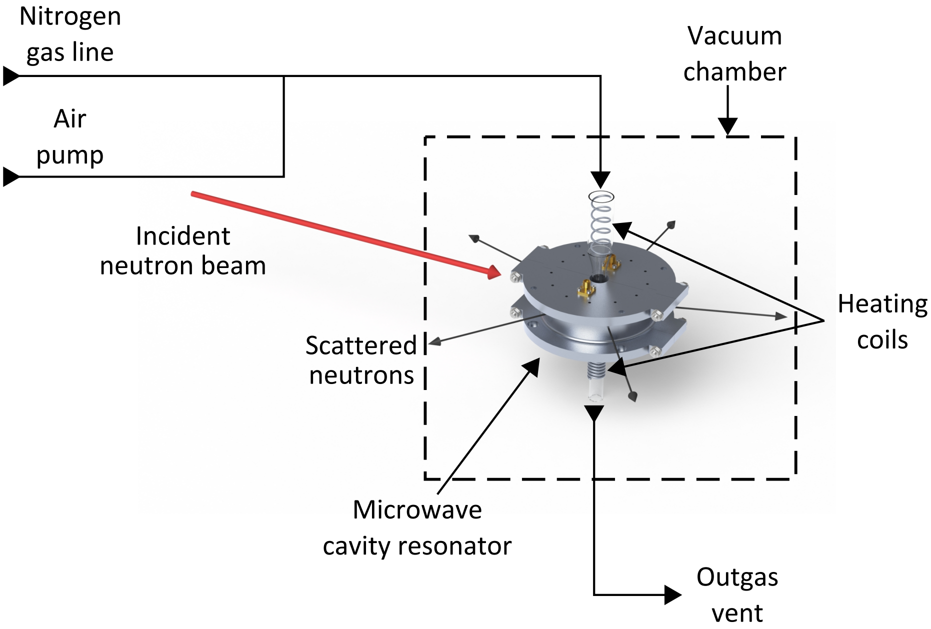

Figure 5.23: Schematic diagram of the simultaneous neutron diffraction and microwave measurement setup with variable temperature, showing neutron beam, gas lines and measurement apparatus.

Gas flow was provided by the ISIS toxic gas panel, which supplied the inert gas nitrogen. Unfortunately, the gas panel provided was not equipped with mass flow meters. Without the use of a mass flow controller, gas flows were estimated. Gas flow was estimated using an upturned volumetric cylinder filled with water, with the opening submerged in water. The outgas tube was inserted into the volumetric flask and the pressure on the gas valve was adjusted until 10 cm^3 of gas entered the flask in 1 minute. This pressure was recorded and, during the experiment, the pressure gauge was set to this reading to match this flow rate. Once the MOF was activated using high temperature nitrogen, an air pump was used to flow air though the sample and re-hydrate the MOF. The schematic diagram showing the experimental setup is shown in Figure 5.23.

The experimental rig, shown in Figure 5.24, was lowered into the POLARIS sample chamber and the MFM-170 sample is loaded into the quartz tube. This sample was as synthesised with

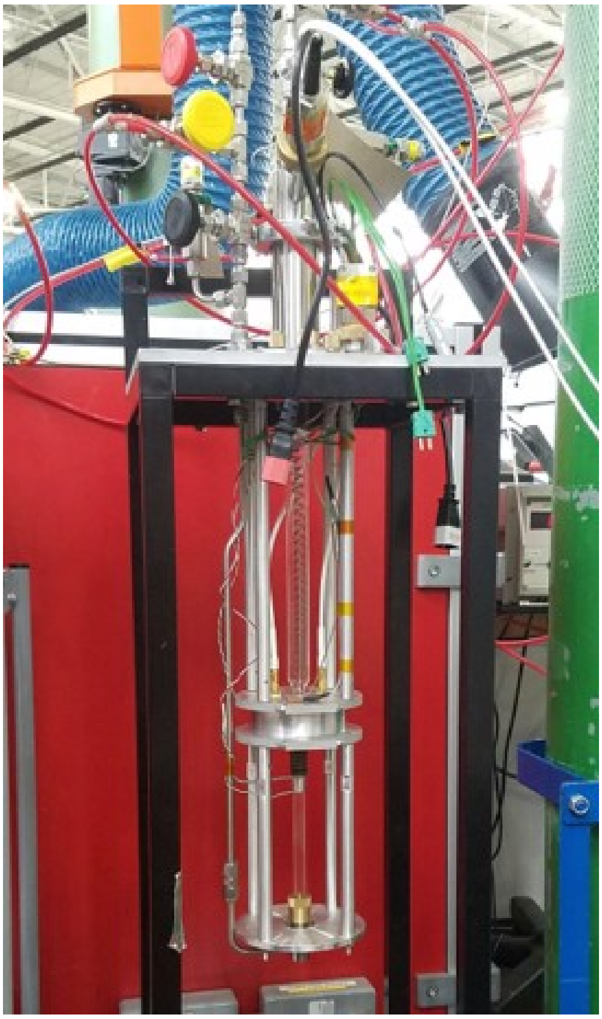

Figure 5.24: Microwave cavity built into experimental rig with quartz tube, heating coils, RF cables, thermocouples, and gas line attachments.

pores saturated with water, acetone and possibly other solvents. Nitrogen was then flowed through the sample for MOF activation. Heating coils were set to heat the flowing nitrogen gas to 150 °C until the sample became fully activated. The air pump was then used to flow air through the sample. The water content in the air is used as a way to fully re-hydrate the MOF - indicated by a plateau in the microwave data. Nitrogen is then flowed again over the sample and heated to dehydrate the sample, but this time at an accelerated flow rate.

5.3.2 Results

For clarity, this experiment will be described in five sections. Section A is the setup of gas flow rate and temperature. The experiment began with the sample under vacuum, then nitrogen was flowed through the sample at an approximate flow rate of 10 sccm. As mass flow meters were not available for this experiment, gas flow rates were estimated by flowing argon into an upturned volumetric cylinder of water and recording the volume of gas in one minute. The gas pressure required to achieve the desired flow rate was recorded and used to set flow rates for this experiment. Heating coils were set initially to 60 °C to observe their heating characteristics during this experiment. During the testing carried out on the experimental equipment described in Section 4.1.3, PID values were chosen to control the heating coils. However, presence of the sample had effected the heating characteristics and therefore the PID values were tuned to make them more appropriate.

Section B is the activation of the MOF sample. The temperature was raised to 150 °C to activate the MOF. This nitrogen flow at 150 °C continued until the MOF was fully activated (dehydrated), as indicated by a plateau in dielectric response.

To ensure the MOF was fully activated, the sample was exposed to a vacuum in section C with some additional heating. The vacuum pump was connected to the gas line at the bottom of the sample, so as to cause as little disturbance of the sample as possible. This also protected against the sample being pulled into the gas lines, which was a concern for a bottom up direction of evacuation. The sample was also allowed to cool naturally during this time.

Section D is the rehydration of the MOF. The MOF was rehydrated by using an air pump to flow air from the experiment hall through the sample. This atmospheric air had a high enough moisture content that the MOF readily hydrated, without the need to saturate the air with water by bubbling it through a water bath. The vacuum pump was not used for this section of the experiment and the sample was not heated during section D.

The final section of the experiment, section E, is the second activation of the sample. This activation again used 150 °C heating from the coils, but this time used a much faster nitrogen flow, approximately 40 sccm. While this flow rate was considerably faster than the previous testing, heating of 150 °C was still achieved.

5.3.2.1 Temperatures

Three temperatures were recorded during the experiment:

- Thermocouple placed through the centre of the top heating coil, inside the quartz tube, and placed as close to the sample as possible without disturbing the electromagnetic field inside the resonator.
- Thermocouple attached to the side of the quartz tube below the cavity but above the bottom coil, and placed as close to the sample as possible without disturbing the electromagnetic field inside the resonator.
- Resistance temperature detector (RTD) secured to the top face of the microwave cavity.

The temperatures recorded by the thermocouples and RTD are shown in Figure 5.25. During section A, the heating coils were raised to 60 °C. The top coil reached this temperature and stabilised within 15 minutes, however the bottom coil fluctuated ±20 °C. This required a change in the PID values of the coils temperature controller. After this, the temperature reached stability in an acceptable amount of time.

In section B, temperature set points of both coils were then raised to 150 °C and reached stability at this temperature within a few minutes. Resonator temperature during this stage increased to approximately 53 °C after approximately 12 hours. This resonator temperature was slightly higher than during the testing in Section 4.1.1. This increased resonator temperature, when compared to testing, still lies within the acceptable operating temperatures for this cavity resonator of up to 100 °C.

During section C, the sample was under dynamic vacuum and there was no heating of the top coil. This is because there may not have been enough thermal load to stop the coil burning out. As the bottom coil had sufficient thermal contact with the quartz tube, this was set at 100 °C to ensure the sample is fully activated. As no change was observed in both fractional frequency shift and inverse Q factor shift, indicating no further water could be removed from the MOF under these conditions, both coils were switched off. The small rise in temperature measured by the top coil thermocouple was caused by the rise in the temperature of the apparatus. Once activation was compete, the coils, cavity and sample were then left to cool.

There is no heating provided by the heating coils in section D. Air was flowed through the sample which had a high enough water content to hydrate the sample. The temperatures of all three measurement locations show temperatures of 20-25 °C during this time.

In Section E the coils are heated to 150 °C to reactivate the sample. This required coils to be heated to 150 °C. Despite the increase in flow rate of nitrogen gas to approximately 40 sccm during this period, the coils were still able to reach a stable 150 °C within 15 minutes. Here, the heating duration at 150 °C was much when shorter compared to the first activation, as the activation process completed many times faster. This was due to the increased argon flow rate. Resonator temperature reached a maximum of 44 °C due to this shorter heating time. After the MOF was fully activated, the heating coils were switched off and the whole sample environment allowed to cool.

5.3.2.2 Dielectric Response

The dielectric response of a substance releasing water is expected to show an increase in fractional frequency shift and decrease in inverse Q factor shift. Water is a highly polar molecule which, when removed from the system, will cause a rise in frequency. As water also has a very high dielectric loss, this will cause a decrease in inverse Q factor shift as water is removed from the system.

Figure 5.26 shows the dielectric response of the sample during the experiment. At the start of section A the sample is under vacuum and no heating. As the sample is loaded “as synthesised” the pores in the MOF will contain acetone as well as other solvents and water. These solvents are not bound to the MOF and readily evaporate at room temperature. This is the

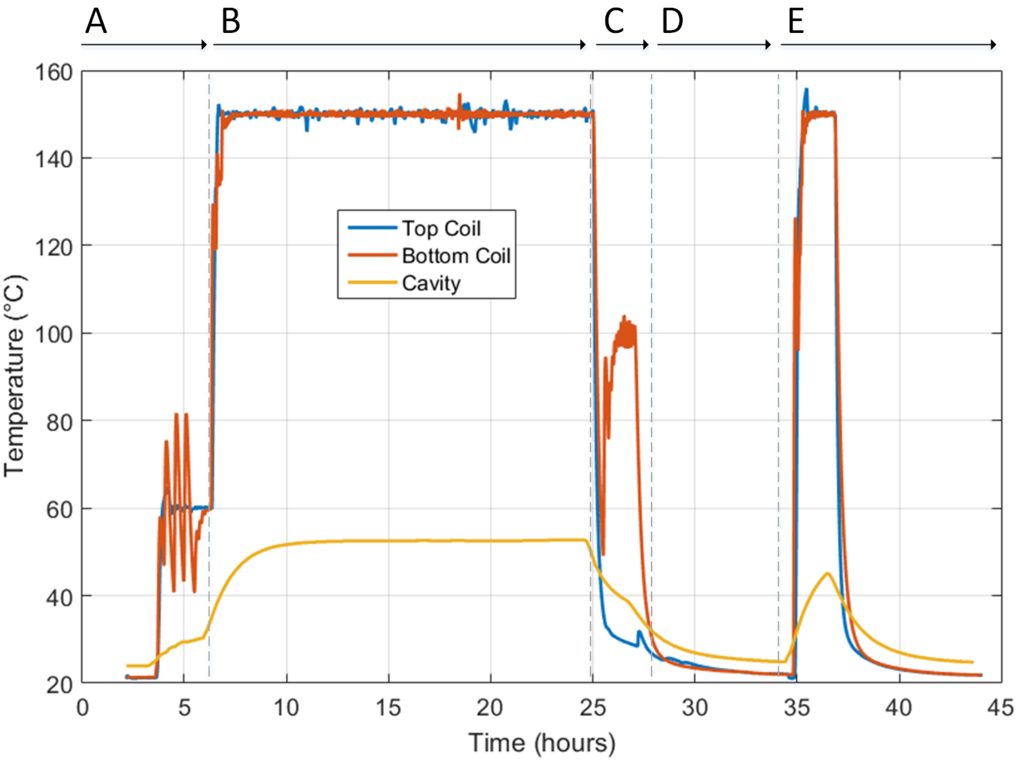

Figure 5.25: Temperature measurements from the centre of the top heating coil (inside the quartz tube), directly above the bottom heating coil (outside the quartz tube), and the cavity (affixed to the top plate).

cause for the decrease in polarisation and dielectric loss of the sample at the beginning of the experiment. Once the heating coils are set to 60 °C between approximately 4 and 6 hours, more of these solvents are removed from the system. This caused further decrease in polarisation and dielectric loss. Some of the weakly bound, physisorbed water is likely also removed during this time, contributing to these changes.

At the start of Section B, the heating coils at set to 150 °C and maintained at that temperature for 6 hours. During this time, the rise in fractional frequency shift accelerates considerably. The increase in temperature accelerated the rate at which any remaining solvents are flushed from the system. It also increased the loss of physisorbed water from the system, as well as removing water strongly bound to the MOFs metal centres. The change in gradient of frequency at around 7 hours is likely caused by the different rates of loss of the solvents, physisorbed water, and strongly bound water. As the temperature increased to 150 °C at around 6 hours, the dielectric loss began to increase. This is not the expected response when a lossy substance, such as water, is removed from the sample. As the system is not yet under thermal equilibrium, and there are multiple solvents present in the sample, it is not possible to pinpoint the reason for this increase in dielectric loss. At 7.5 hours inverse Q factor began to decrease, as expected when substances with dielectric loss are removed from the sample.

At the start of section C, there is a step change in fractional frequency shift. This change is not associated with a sudden change in dielectric properties, and is likely due to the movement of the sample as the vacuum pump is switched on. When the pump is switched off there is another step change, back to the frequency value at the start of section C. Again, this is likely due to the sample returning to its previous position. Dielectric loss also shows some small changes in both directions in this time. This is again caused by small movements in the sample. There is no change in inherent sample dielectric properties during this section. Placing the sample under vacuum had no further effect on its dielectric properties and thus sample was fully activated during section B. This proves the effectiveness of the equipment to be used for in-situ MOF activation.

In section D the MOF is rehydrated with water. This caused the polarisation and dielectric loss of the sample to increase. The rehydration of the MOF by passing air through the sample took approximately 6 hours. The final values of frequency and Q factor did not return to the values seen at the start of the experiment. At the beginning of the experiment the MOF sample was “as synthesised” meaning it was not only fully saturated with absorbed water, but also non-bound, free water was present i.e. the sample was wet. This sample also likely contained additional acetone and other solvents not bound to the MOF. The values of frequency and Q factor not returning to values at the beginning of the experiment was expected. This is because additional liquids present at the start of the experiment caused increases in polarity and dielectric loss of the sample that were not present in section D.

Section E shows the second activation of the sample. As the 150 °C nitrogen flow caused water to be desorbed from the MOF, the polarisation and dielectric loss of the sample began to decrease. Due to the increase in nitrogen flow rate to approximately 40 sccm, this desorption process was considerably faster than the first activation. The activation of the MOF takes place in the first hour of section E. At this point, the fractional frequency shift and inverse Q factor shift values match that of the first activation. This showed the sample was fully activated with no water remaining in the MOF. After this, the dielectric loss continued to decrease, from 37 hours onwards. This is due to the cooling of the microwave cavity. The frequency response is not effected by this, as the frequency response plotted in Figure 5.26 has been temperature corrected using the method shown in Section 2.7.7. As discussed in Section 2.7.7, this method cannot reliably be used to correct for changes in Q factor due to temperature.

5.3.2.3 Structural Properties

A surface plot of Bragg diffraction patterns of the MFM-170 sample during the experiment are shown in Figure 5.27. The Bragg peaks observed, stay of mostly constant intensity with no changes in structure. This behaviour is to be expected for this experiment as the MOF is stable to water and pore sizes for this MOF do not expand. The gaps in Bragg data represent when changes to gas lines were made to the sample environment, meaning the neutron beam must be stopped during this time. The main change observed in this surface plot is the change in

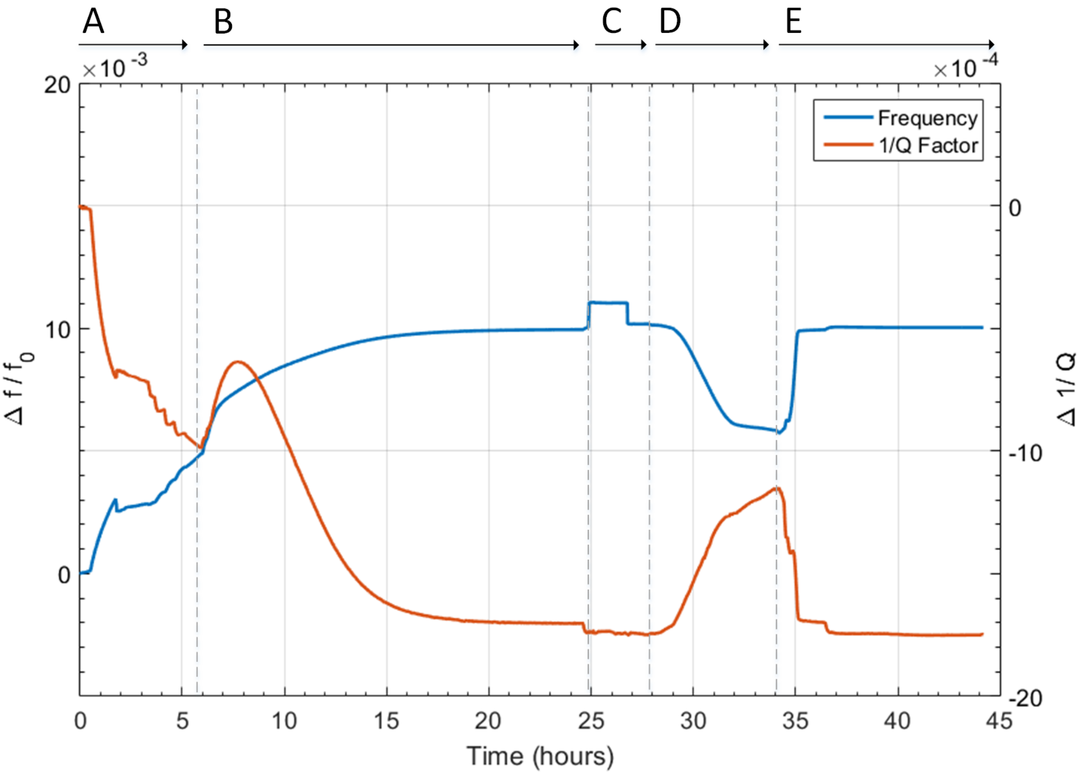

Figure 5.26: Fractional frequency shift and inverse Q factor shift during activation through heating, and rehydrating a MFM-170 sample under argon (Ar) flow. Where A is the setup of eating coils and gas flow, B is the first activation of the MOF, C is under vacuum and cooling, D is the rehydration of the MOF, and E is the second activation.

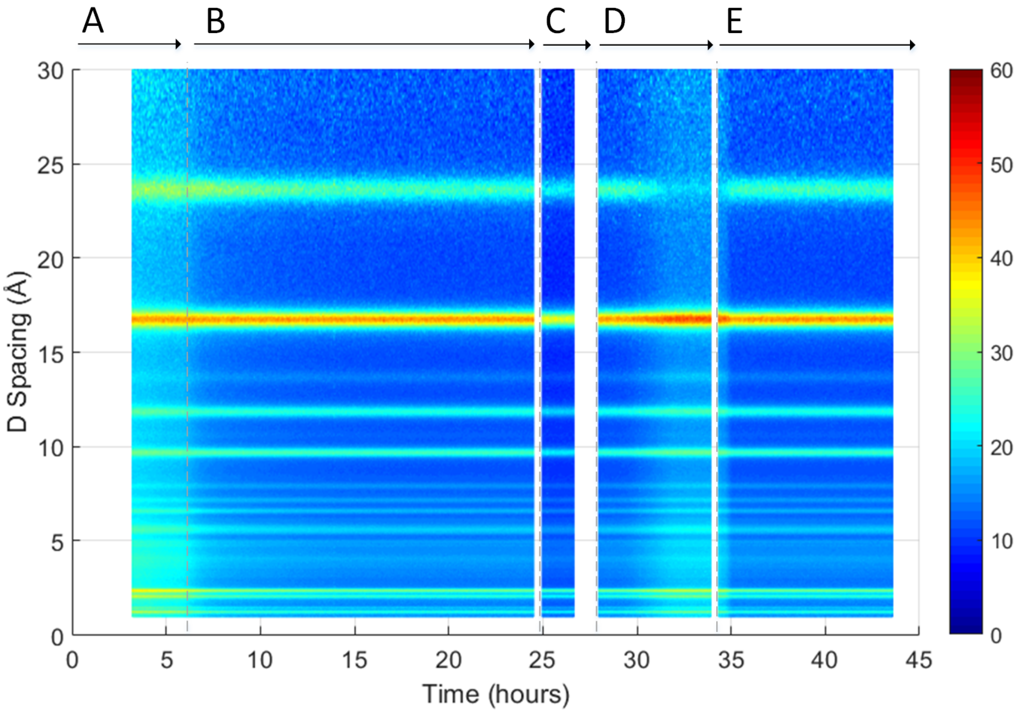

Figure 5.27: A surface plot of Bragg diffraction collected from bank 1 of POLARIS during activation through heating, and rehydrating a MFM-170 sample under argon (Ar) flow. The intensity of the Bragg lines is represented by the colour scale on the right. The white spaces represent the periods when NPD data recording was stopped to allow changes in setup. Where A is the setup of heating coils and gas flow, B is the first activation of the MOF, C is under vacuum and cooling, D is the rehydration of the MOF, and E is the second activation.

background scattering. This is mostly due to the hydrogen present in the water. Hydrogen has a high incoherent scattering, resulting in an increase in background scattering. As the water, and therefore hydrogen, is removed from the sample this background scattering decreases.

The change in background scattering can be seen clearly from section A to section B of the NPD data. Figure 5.28 shows these sections in more detail. The background scattering at the start of section A is very high due to the large amounts of water and solvents present in the sample. As the nitrogen is heated and passed over the sample in section B, the background scattering reduces as the water and solvents leave the MOF. The Bragg diffraction in Figure 5.28 seems to suggest the MOF is fully activated in under 4 hours. The dielectric data in Figure 5.26 shows the MOF is not fully activated for at least 12 hours after the nitrogen is

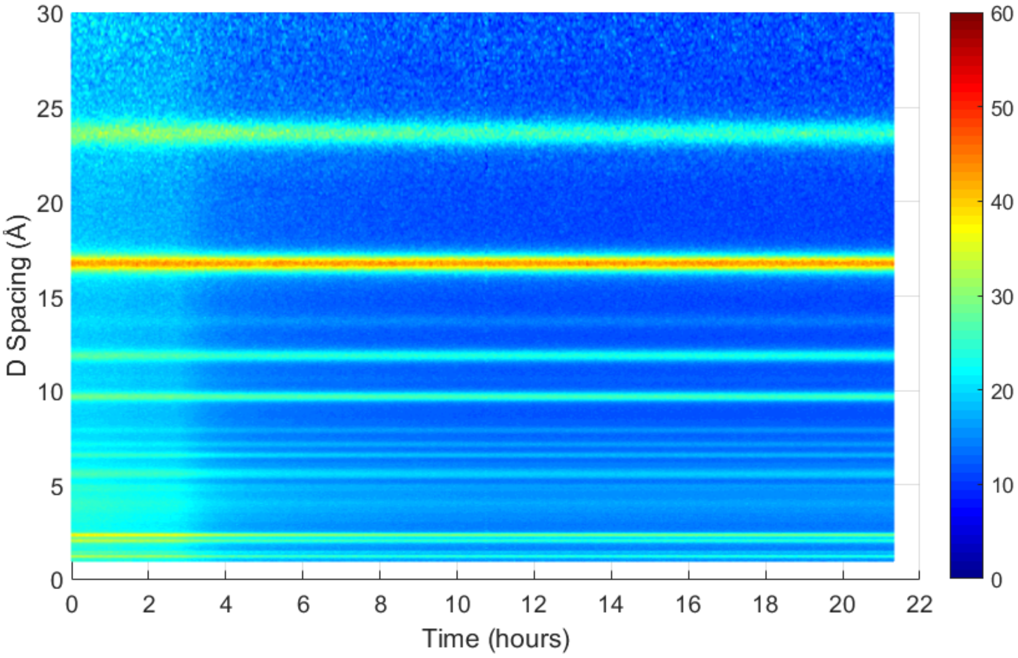

Figure 5.28: A surface plot of Bragg diffraction of section A and B of the experiment, collected from bank 1 of POLARIS during activation through heating of an MFM-170 sample under argon (Ar) flow. The intensity of the Bragg lines is represented by the colour scale on the right.

heated to 150 °C. This shows the sensitivity of microwaves to polar and lossy materials such as water.

The dielectric data for section C suggested little change in dielectric properties of the sample, however possible movement of the sample may have masked subtle behaviours. Section C of the NPD data can be seen in Figure 5.29. These Bragg data supports the previous statement that there is no change during this period as there is no recognisable change in structure or background scattering. This, in turn, shows that the MOF was fully activated before the vacuum was applied.

Section D is the rehydration of the MOF and Bragg data for this is shown in Figure 5.30. The MOF was rehydrated by passing air from the experiment hall through the sample using an air pump. As water is absorbed by the sample, the increased amounts of hydrogen present caused

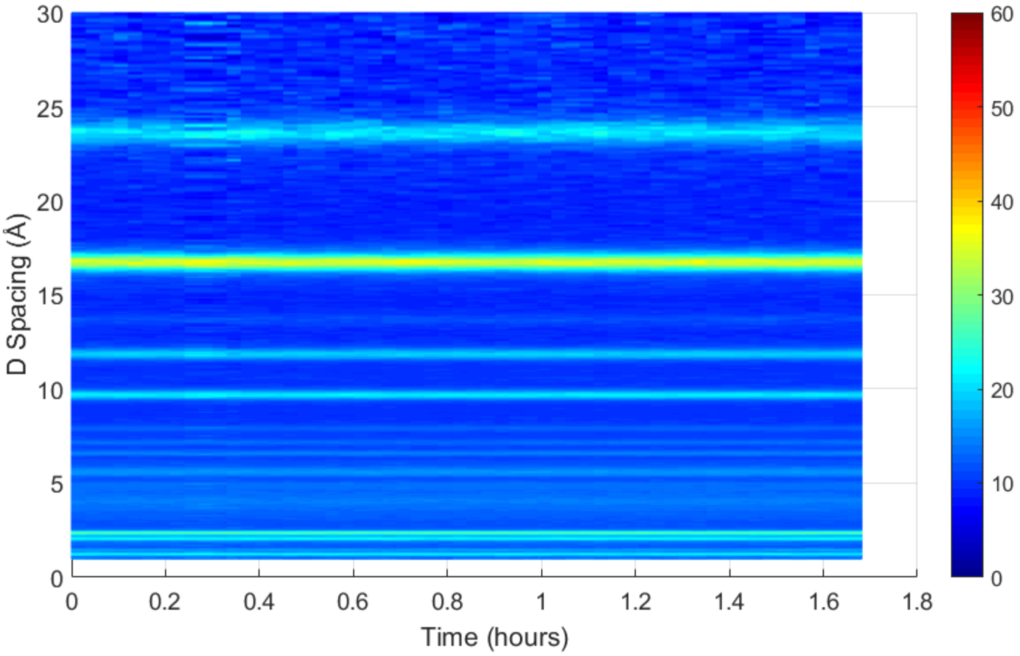

Figure 5.29: A surface plot of Bragg diffraction of section C of the experiment,collected from bank 1 of POLARIS of an MFM-170 sample under vacuum. The intensity of the Bragg lines is represented by the colour scale on the right.

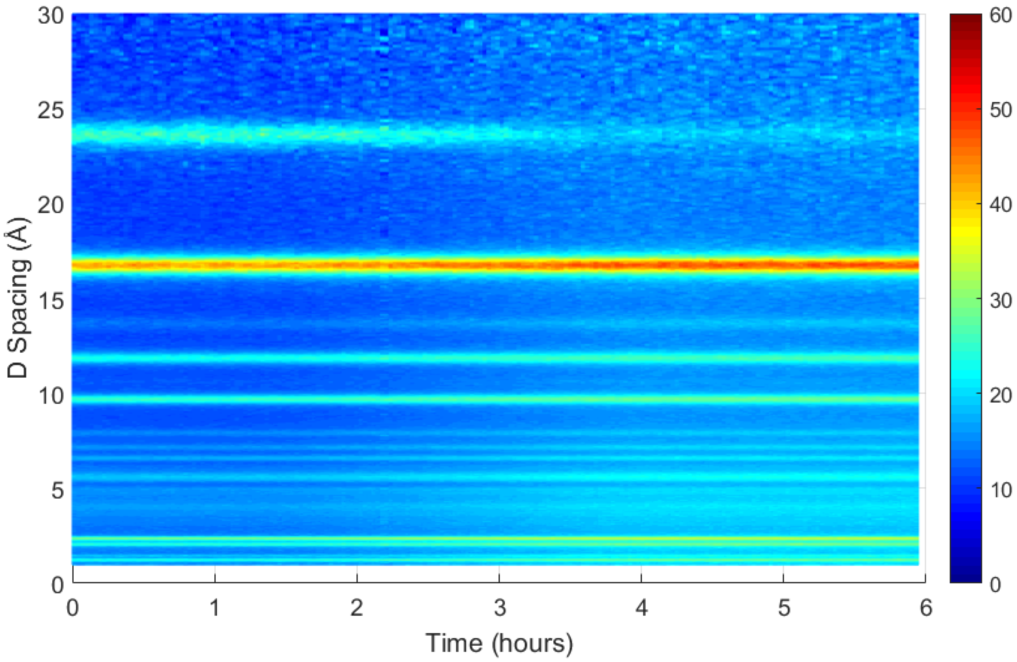

Figure 5.30: A surface plot of Bragg diffraction of section D of the experiment, collected from bank 1 of POLARIS during rehydration of an MFM-170 sample under atmospheric air flow. The intensity of the Bragg lines is represented by the colour scale on the right.

background scattering to increase. The amount of background scattering observed at the end of section D is visibly less than the level at the beginning of section A, as seen in Figure 5.28. This is due to the fact that there was water present in the starting sample not absorbed by the MOF as well as solvents present, contributing to the levels of background scattering.

The Bragg data for the second dehydration of the MFM-170 sample, in section E, is shown in Figure 5.31. The background scattering reduces very quickly for this activation of the sample, due to the increased flow rate of 150 °C nitrogen gas through the sample. This increased rate can clearly be seen when comparing the rate of decrease in background scattering from section A, in Figure 5.28, to section E, in Figure 5.31. After the dehydration of the sample, no further changes are observed via NPD data.

Figure 5.32 shows the dielectric data superimposed on top of the structural data. In section A, it can be seen that there are considerable changes in dielectric data, especially fre-

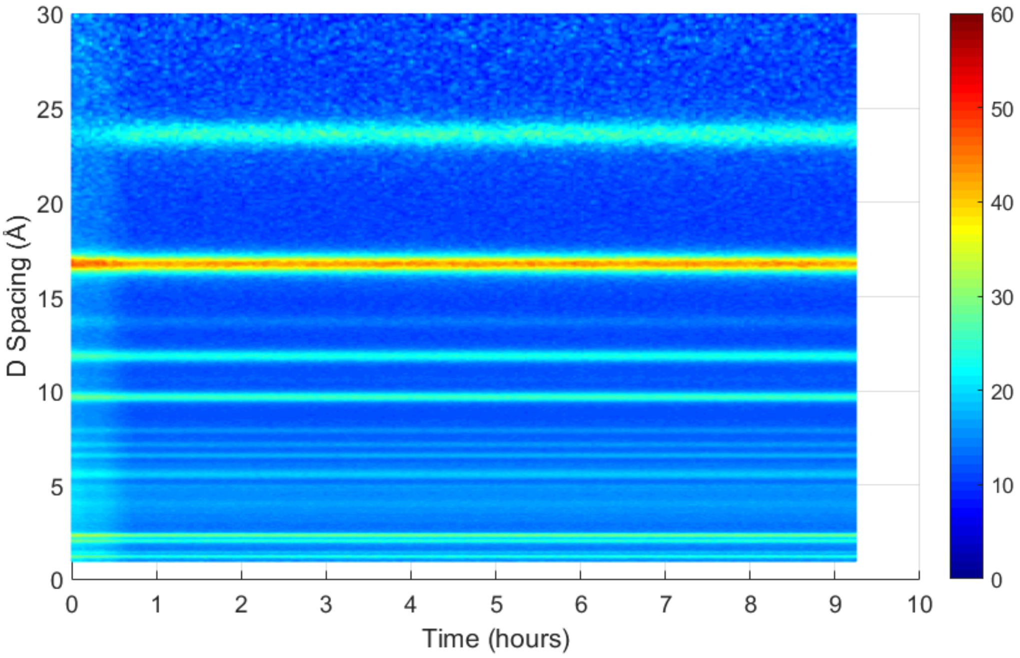

Figure 5.31: A surface plot of Bragg diffraction of section E of the experiment, collected from bank 1 of POLARIS during the second activation through heating of an MFM-170 sample under argon (Ar) flow. The intensity of the Bragg lines is represented by the colour scale on the right.

quency response, before the sample is exposed to neutrons and high temperature nitrogen is flowed through the sample. This is likely due to the solvents with low boiling points being flushed from the sample. As the sample is heated in section B, and water begins to leave the sample, the background scattering reduces significantly and seems to show full activation within around 4 hours. The dielectric data however, shows the MOF is not fully activated for at least 12 hours after the nitrogen is heated to 150 °C. This shows the sensitivity of microwaves to polar and lossy materials such as water. This is one of the reasons that simultaneous MCR measurements can be a vital complimentary measurement technique to be used alongside NPD. Section C shows no change in structure or dielectric properties.

In section D, the dielectric response shows the presence of water before there is a change in the background scattering. Both the dielectric data and Bragg data confirm there is less water present after hydration than when the experiment began. The dielectric data shows less water is present as frequency and Q factor values do not return to their original value at the start of the experiment. The background scattering in the Bragg data shows less water is present as there is less background scattering at the end of section D than at the beginning of the experiment. The second dehydration, in section E, occurred several times faster than the first. This is shown by both the changes in dielectric data and the fast reduction in background scattering. The changes in Q factor from 37 hours onwards are likely due to changes in the cavity temperature alone. This is backed up by no visible changes in the Bragg data during this period.

5.3.3 Conclusions of High Temperature MOF Activation

This experiment was carried out using the equipment designed in Section 4.1. The equipment was designed to be able to heat a inert gas flowing at 10 sccm to 150 °C during simultaneous NPD and MCR experiments. This high temperature equipment has been used to activate the MOF MFM-170. With the 10 sccm flow rate specified, the activation process completed in approximately 12 hours. When the flow rate was considerably increased, this activation

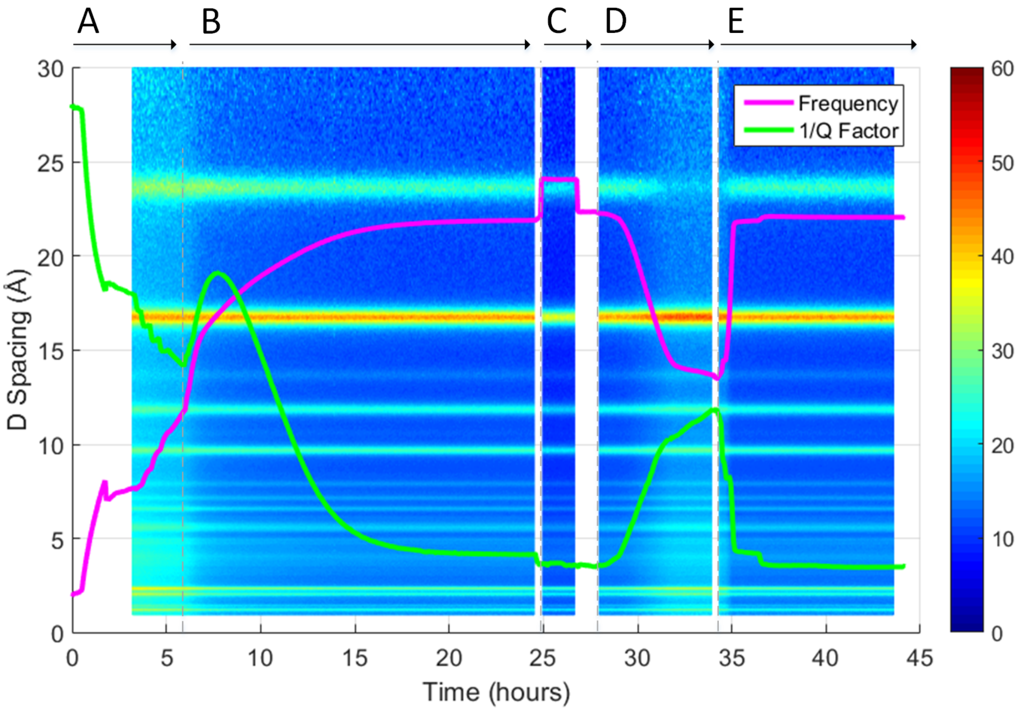

Figure 5.32: Superimposition of the surface plot of Bragg diffraction and dielectric data during activation through heating, and rehydrating a MFM-170 sample under argon (Ar) flow.

process took place in under 1 hour. This shows the equipment is capable of performing the required experiments far better than the initial specification.

Dielectric results show fractional frequency shift increased and inverse Q factor shift decreased as water left the sample. This was the expected result for the loss of a lossy, polar molecule. The combination of dielectric and NPD results show that after the first activation, where the sample was exposed to a vacuum, there was no more water removed from the MOF. This reinforces the idea that the MOF is fully activated. Upon rehydration of the sample, both dielectric results and Bragg data show there is not as much water present as there was when the experiment began with a wet sample. This is expected as at the start of the experiment the sample contained more water than could be absorbed by the MOF, as well as additional solvents.

The final activation of the MOF occurred at a much faster rate due to the increased nitrogen flow rate. This shows the potential to use this equipment as a fast way to ensure activation of a sample for in-situ NPD experiments. Temperature correction methods used on the frequency results ensure the changes observed in frequency are all from changes in the sample, not changes in cavity temperature.

Chapter 6

Simultaneous X-ray Diffraction and Microwave Measurement

The absorption of ammonia by halide salts is investigated using simultaneous X-ray diffraction and the microwave characterisation technique. These experiments were carried out on the I15-1 beam-line at Diamond Light Source using the hairpin resonator designed in Section 4.2. As these experiments were the first of their kind, this X-ray beam-time was allocated as development time, intended for testing of equipment and development of techniques. Due to this the experiments carried out, and conclusions drawn, in this section are designed to show the effectiveness of simultaneous X-ray diffraction with dielectric measurement. These experiments should give a broad picture of the absorption of ammonia in halide salts, but the focus is on the use and effectiveness of the setup. This beam-line can be used for X-ray Pair Distribution Function (XPDF) measurements as well as Bragg diffraction. Only Bragg data are described in this chapter as XPDF data from these measurements did not provide any additional information.

6.1 Ammonia Absorption in Halide Salts

Halide salts have been shown to be able to store ammonia [35, 78], and this absorption process has previously been recorded by simultaneous NPD and MCR measurements [9, 27]. This section describes the simultaneous X-ray diffraction and dielectric measurement of two halide salts under ammonia absorption conditions. The samples chosen for investigation are $MgCl_2$ and $CaBr_2$. These samples have been selected as they have previously been shown to store ammonia [6, 31]. The combination of techniques chosen can give information on phase transformations in salts and differentiate between weakly and strongly bound ammonia. Phase transformations can be seen in the Bragg data by changes in the structure of the sample as ammonia is absorbed. Strongly and weakly bound ammonia can be differentiated by their effect on the dielectric response of the system. Weakly bound, physisorbed ammonia has stronger dipolar bonds than coordinated ammonia. This leads to an increased dielectric loss and so contributes to a greater change in Q factor of the system.

6.2 Experimental Setup

These experiments were carried out at Diamond Light Source using the XPDF beamline I15-1. Although this beam-line is capable of providing XPDF data along with Bragg peak data, only Bragg data is discussed in this chapter as XPDF data did not provide any additional information. The H1 hairpin style microwave resonator, custom made for these experiments, was designed using COMSOL Multiphysiscs, to simulate the structure and its electromagnetic behaviour. The design and simulation of the H1 resonator is shown in Section 4.2.

The sample was loaded into a quartz tube with inner diameter of 3.8 mm and outer diameter of 4.0 mm. This quartz tube was as thin as possible to decrease the amount of X-ray scattering from the tube, and increase the resolution of the XPDF measurements. Quartz wool was used to support the sample. The quartz tube was glued into metal extensions to increase mechanical strength and allow gas lines to be connected. This quartz tube was held in place

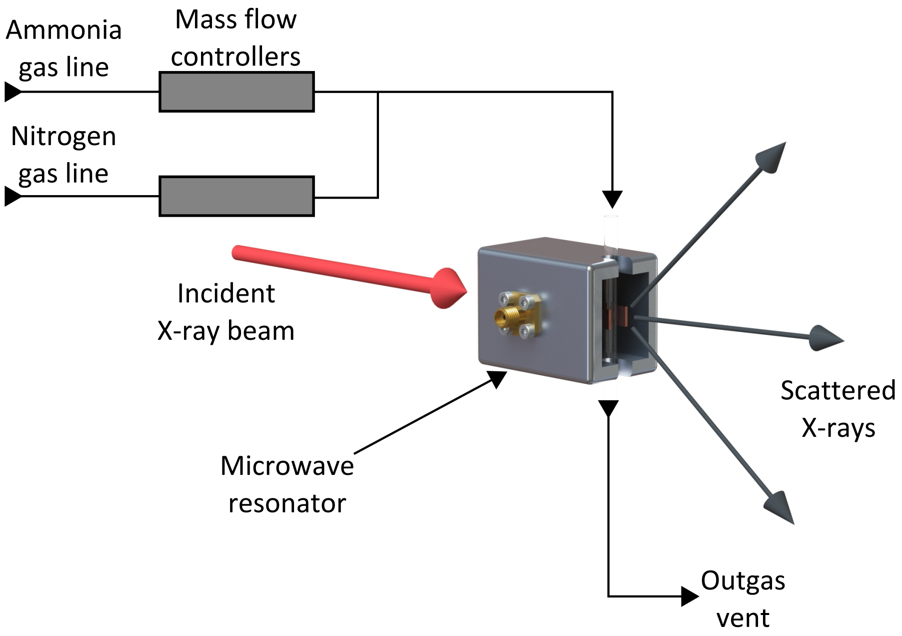

Figure 6.1: Schematic diagram of the simultaneous X-ray diffraction and microwave measurement setup, showing X-ray beam, gas lines and measurement apparatus.

using a custom-built fitting which was secured to the metal tube extensions. Ammonia and nitrogen gas flows were provided via the Diamond gas rig. Gas flow rates were set to 5 sccm - to ensure reaction dynamics are controlled at an appropriate rate. All measurements were taken at room temperature and pressure.

The resonator was connected via the SMA connectors and RF cables to a Copper Mountain S5085 VNA. The power transmission coefficient $|S_{21}|^2$ was measured against frequency and non-linear, least-squares curve fitting to a Lorentzian response was used to determine resonant frequencies, Q factors and resonant bandwidths. Microwave data were recorded every 2 seconds. X-ray diffraction data were collected at 1 minute intervals to ensure reaction dynamics are captured while still allowing sufficient resolution. The schematic diagram showing the experimental setup is shown in Figure 6.1.

The resonator was aligned so the X-ray beam passed through the hole at the bottom of the resonator shielding and through the sample location. The sample was then loaded in the quartz

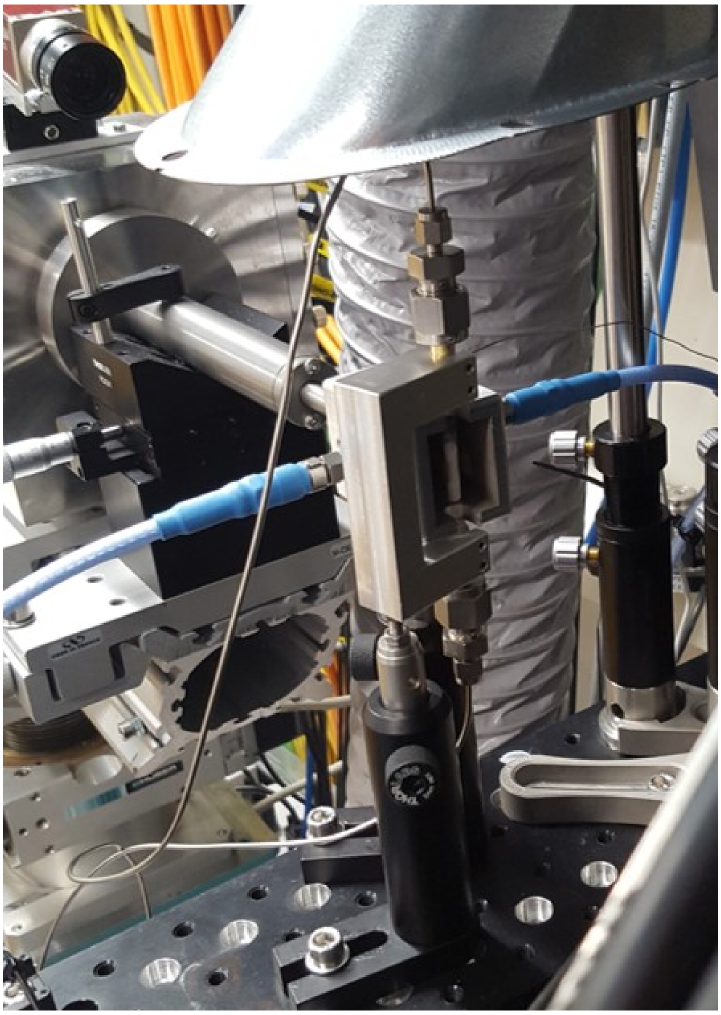

Figure 6.2: Hairpin resonator in experimental position with quartz tube, $MgCl_2$ sample, RF cables, and gas line attachments.

tube and secured in the custom fitting. The curve in the slot out of the resonator shielding allowed repeatable positioning of the sample tube. The resonator in position for the experiment and loaded with the $MgCl_2$ sample is shown in Figure 6.2. Nitrogen was then passed through the sample at 5 sccm to obtain a base measurement for both X-ray diffraction and dielectric response. Ammonia (NH_3) is then flowed through the sample until the microwave data plateaued and X-ray principal component analysis (PCA) showed no further change in structure. Nitrogen flow was reintroduced in order to flush ammonia from the sample.

6.3 Results

6.3.1 Dielectric response of $MgCl_2$

As shown in Figure 6.3, at the beginning of this experiment nitrogen is passed through the sample at 5 sccm to ensure a constant background. Once it was established there would be no change in frequency and Q factor under these conditions, the nitrogen flow was stopped and ammonia flow at 5 sccm began. There was a small lag of under 5 minutes after ammonia flow was started before its effect was observed in the dielectric data. This was due to the slow flow rate and length of gas piping leading to the sample. Some delay was also caused as the sample extended beyond the width of the hairpin resonator, allowing ammonia to be absorbed by part of the sample not present in the sample area.

Once ammonia reaches the measurement area, fractional frequency shift began to decrease, and inverse Q factor shift began to increase. This is the expected behaviour when a polar material with associated dielectric loss is absorbed by the sample. Fractional frequency shift continued to drop with the rate of change reducing until approximately 1.1 hours. At that point polarisation increased more rapidly for around 5 minutes, before a brief plateau appeared at approximately 1.2 hours. Polarisation of the sample then increases again and the rate of change reduced, before a final plateau was observed at around 1.5 hours. The plateaus observed in the dielectric data occur during changes in stoichiometry of the sample.

Once ammonia is introduced, inverse Q factor shift began to increase and rate of change reduced until around 0.5 hours. At this point fractional frequency shift dropped at a constant rate. Dielectric loss of the sample then experienced some complex behaviours until 1.1 hours, where polarisation and dielectric loss of the sample increased. Similar to the behaviour in frequency, inverse Q factor shift began to increase again, before a brief plateau at 1.2 hours and then a further increase. Unlike fractional frequency, inverse Q factor did not reach a constant value and started to decrease. This behaviour is likely due to residual physisorbed ammonia becoming bound as a result of the long capillary and unidirectional gas flow reaching

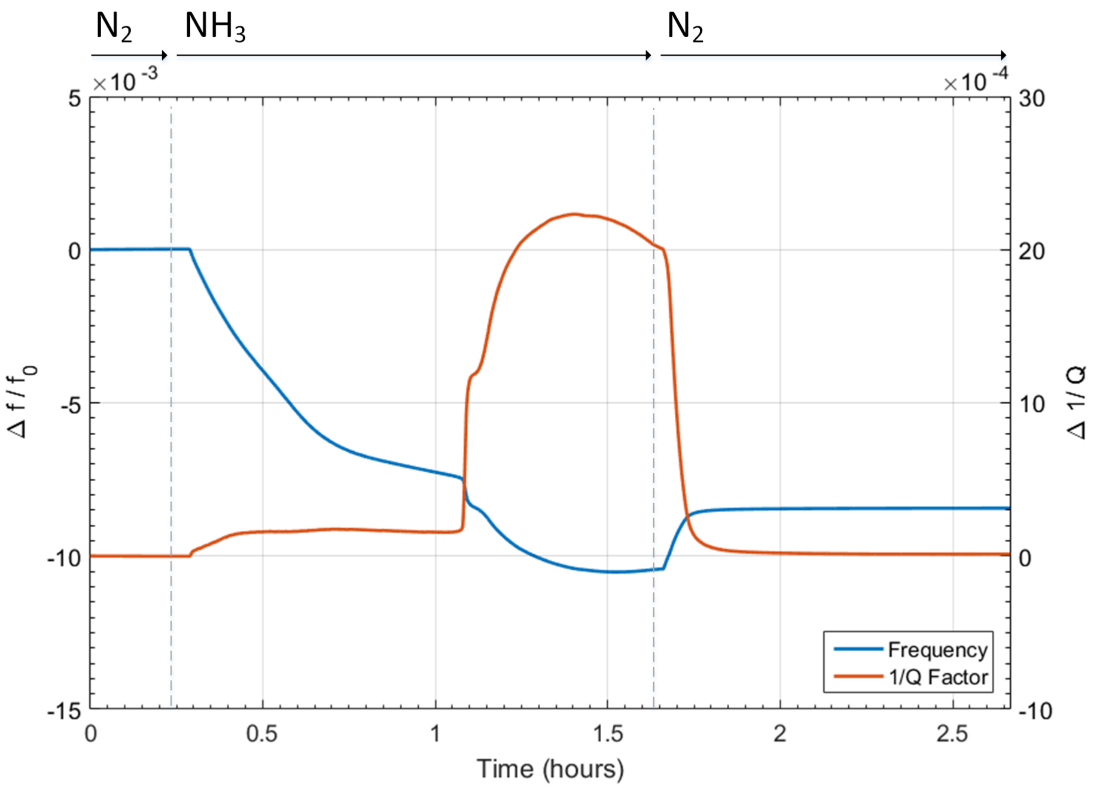

Figure 6.3: Dielectric response for ammonia absorption and desorption in $MgCl_2$ under ammonia (NH_3) and nitrogen (N_2) flows. The starting sample corresponds to $MgCl_2$. The plateau before 1.1 hours corresponds to $Mg(NH_3)Cl_2$. The brief plateau at 1.2 hours corresponds to $Mg(NH_3)_2Cl_2$ and at the final plateau under ammonia flow, the sample had reached the final stage of $Mg(NH_3)_6Cl_2$.

the end of the sample.

As magnesium chloride absorbs ammonia, the stoichiometry of the material changes in stages from $MgCl_2$, to $Mg(NH_3)Cl_2$, then $Mg(NH_3)_2Cl_2$, and finally $Mg(NH_3)_6Cl_2$[31, 77]. The structure of each of these stoichiometries can be seen in Figure 6.4. The space groups and lattice parameters for these materials available on the Inorganic Crystal Structure Database (ICSD) can be found in Table 6.1. These structural changes can be seen in the dielectric response, where the starting sample corresponds to $MgCl_2$. The plateau before 1.1 hours corresponds to $Mg(NH_3)Cl_2$. The brief plateau at 1.2 hours corresponds to $Mg(NH_3)_2Cl_2$ and at the final plateau under ammonia flow, the sample had reached the final stage of $Mg(NH_3)_6Cl_2$.

After the sample had fully saturated with ammonia, the gas flow was switched to nitrogen at

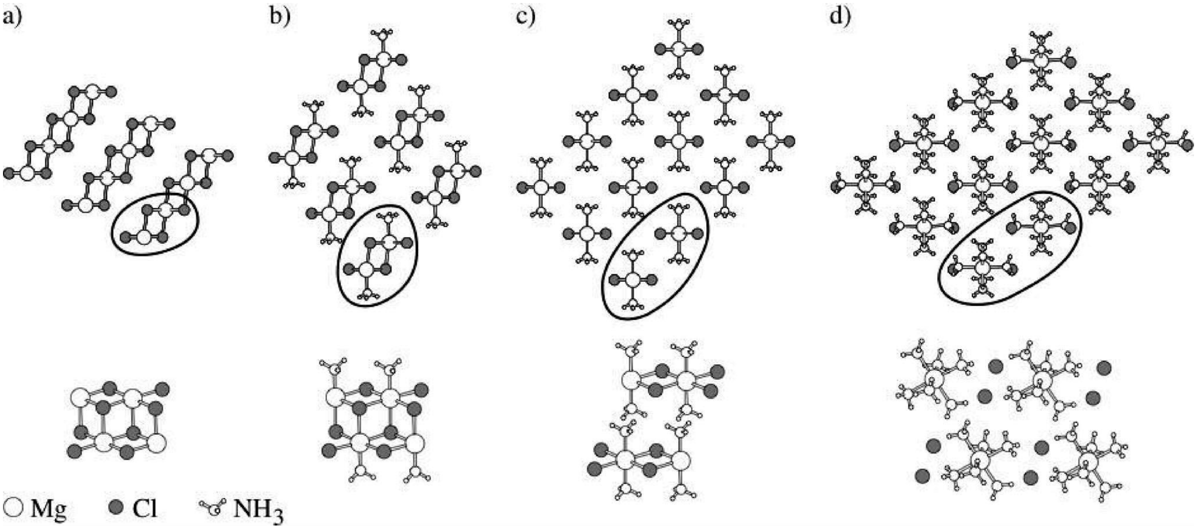

Figure 6.4: Crystal structure of (a) $MgCl_2$, (b) $Mg(NH_3)Cl_2$, (c) $Mg(NH_3)_2Cl_2$, and (d) $Mg(NH_3)_6Cl_2$[31].

Table 6.1: Space groups and lattice parameters for $MgCl_2$ ammoniation products

Chemical Formula	Space Group	Lattice Parameter	Cell Volume
$MgCl_2$ [118]	P -3 m 1 (164)	3.641(3) 3.641(3) 5.927(60) 90. 90. 120.	68.05 [Å^3]
$Mg(NH_3)Cl_2$	Not Available	Not Available	Not Available
$Mg(NH_3)_2Cl_2$ [119]	C m m m (65)	8.1810(2) 8.2067(2) 3.7550(1) 90. 90. 90.	252.11 [Å^3]
$Mg(NH_3)_6Cl_2$ [23]	F m -3 m (225)	10.12258(3) 10.12258(3) 10.12258(3) 90. 90. 90.	1037.23 [Å^3]

a flow rate of 5 sccm. As nitrogen passed through the sample some ammonia was removed, causing a decrease in sample polarisation and in dielectric loss. Dielectric loss decreased at a constant rate before levelling off at slightly below its starting, un-ammoniated Q factor value. Sample polarisation however only partially recovers approximately 25% towards its starting value.

6.3.2 Dielectric Response of $CaBr_2$

As with $MgCl_2$ there was no change in dielectric properties as nitrogen was flowed through the sample. There was a short delay after ammonia flow was started before it was seen in the dielectric response. Polarisation and dielectric loss of the sample began to increase as ammonia was absorbed by the $CaBr_2$ sample. Frequency and Q factor continued to change up until approximately 1 hour. At this point, due to the expansion of the sample, gas was not able to flow through the sample. Flow was quickly swapped to nitrogen, which was able to flow freely, and then swapped back to ammonia within 5 minutes. Ammonia then flowed freely, allowing a small additional amount of ammonia absorption, which continued until 1.5 hours. At this point an ammonia flow was unable to be resumed. This meant full saturation of ammonia within the sample was not possible for this experiment. For the $CaBr_2$ sample there are no clear plateaus observed for changes in stoichiometry partly due to the interruptions in flow rate and since saturation with ammonia was not possible.

Nitrogen gas was able to flow thought the sample. This caused a removal of ammonia and a decrease in polarisation and dielectric loss. This trend continued until approximately 2 hours where the data plateaued. Both fractional frequency shift and inverse Q factor shift only partially recovered. Again, as the sample expanded under ammonia absorption, comparing starting and ending values is not possible.

Ammonia absorption in $CaBr_2$ was investigated in [27] using simultaneous dielectric characterisation and NPD. During the experiment by Jones et al. it was observed that frequency decreased as ammonia was absorbed. The rate of change of frequency changes as the $x = 8$

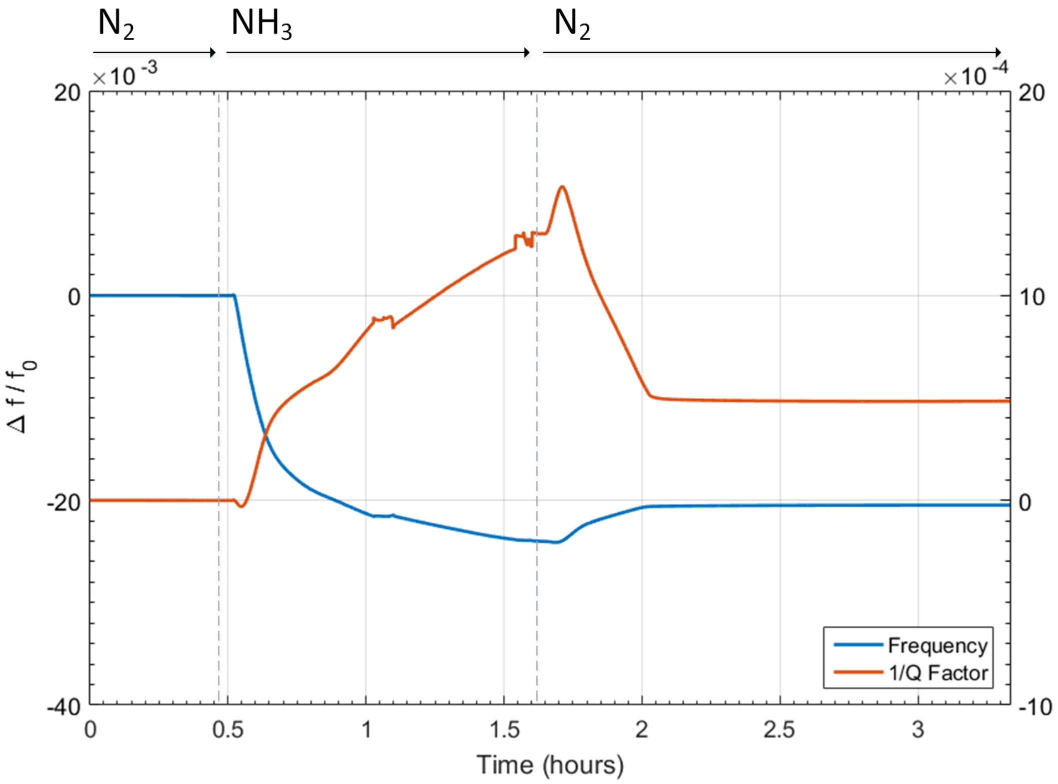

Figure 6.5: Dielectric response for ammonia absorption and desorption in $CaBr_2$ under ammonia (NH_3) and nitrogen (N_2) flows.

phase becomes dominant. Bandwidth increased as ammonia was absorbed. As the $x = 8$ phase became dominant, bandwidth decreased before continuing to increase until fully saturated with ammonia. The dip in bandwidth during the experiment was due to the increase in the unit cell size of the material and the longer dipolar bonds. The dipole interaction between the ammonia molecule and the binding site reduces as the bond length increases contributing to a lower dielectric loss. Conversely, in Figure 6.5, fractional frequency change does not show a change in gradient. Inverse Q factor does have a change in gradient at 0.8 hours but does not reduce at any point during the experiment. The reason for the difference in findings for in these experiments is the sample geometry. In the NPD experiment by Jones et al. the sample was a thin layer of salt in a wide sample tube. The findings in Figure 6.5 are using a sample in a capillary tube. This change in geometry can affect the dynamics of the ammonia gas flow, changing how it interacts with the sample and leading to the difference in findings.

6.3.3 Structural Properties of $MgCl_2$

Figure 6.6 shows the Bragg X-ray diffraction data exhibits no change in structure during nitrogen flow, as expected. As ammonia is absorbed by the sample, structural changes can be seen within the salt. Peaks at around 5 Å and 3.5 Å reduced in intensity between 0.4 and 0.6 hours. During this time a peak appeared and grew in intensity at around 2.5 Å. This change in structure was due to the change in stoichiometry from $MgCl_2$ to $Mg(NH_3)Cl_2$. After 60 minutes the peak at 3 Å grew in intensity, along with slight changes in intensity of the peaks at 4.5 Å and 5 Å. This change in structure was due to the change in stoichiometry from $Mg(NH_3)Cl_2$ to $Mg(NH_3)_6Cl_2$. The $Mg(NH_3)_2Cl_2$ phase was not seen in the Bragg data as the change in stoichiometry, and therefore structure, was too fast to be observed. Although the $Mg(NH_3)_2Cl_2$ phase was present on a local scale in the sample, the Bragg data showed the average structure over the whole sample - where the $Mg(NH_3)_2Cl_2$ phase cannot be observed. Once nitrogen was reintroduced there were no further changes in structure.

Overlaying the dielectric data on top of the Bragg data shows the relation between structure and dielectric properties of $MgCl_2$ and can be seen in Figure 6.7. As ammonia is absorbed by the sample, and the stoichiometry moves to the $Mg(NH_3)Cl_2$ phase, both the dielectric data and the structural data showed changes beginning at 0.3 hours. The change in stoichiometry to $Mg(NH_3)_2Cl_2$ can be seen briefly in the dielectric data at 1.1 hours. After a brief plateau in dielectric data, further change occurs as the sample moves to the $Mg(NH_3)_6Cl_2$ phase. The structural data does show changes in this time-frame, however the change to the $Mg(NH_3)_2Cl_2$ phase is indistinguishable from the change to the $Mg(NH_3)_6Cl_2$ phase. This demonstrates the sensitivity of the microwave characterisation technique during absorption of a polar and lossy material such as ammonia. Once a nitrogen flow was reintroduced, dielectric data showed changes in polarity and loss of the sample. No change was observed in the structure during this time. This suggests removal of some ammonia from the sample, but no change in average structure.

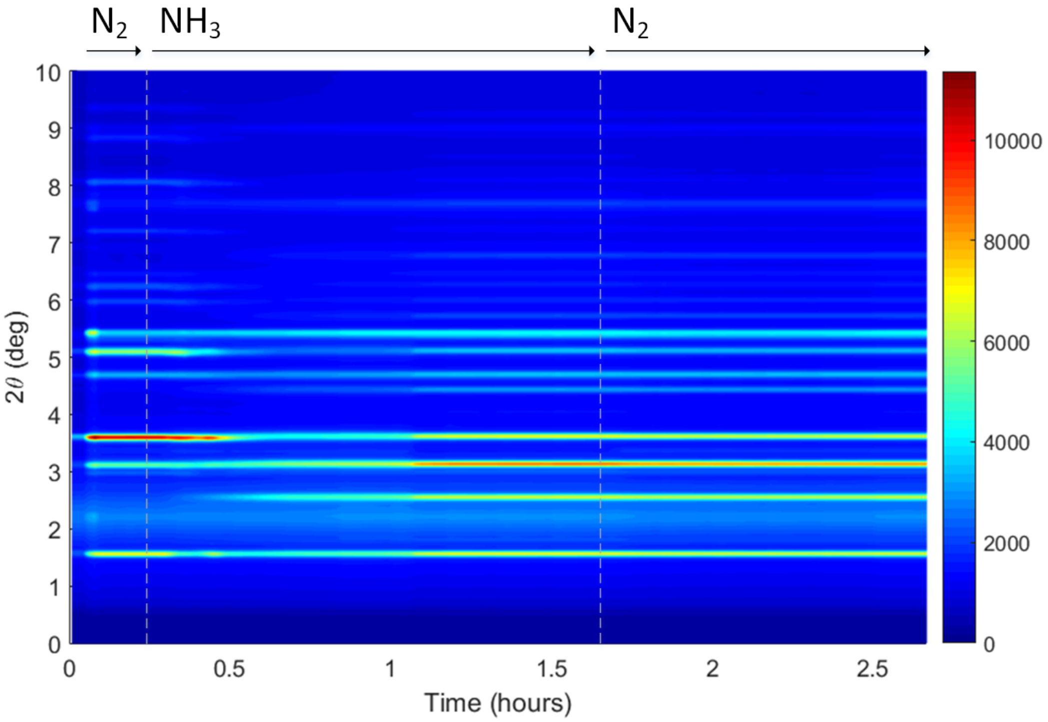

Figure 6.6: A surface plot of Bragg diffraction collected from I15-1 during ammonia absorption and desorption within $MgCl_2$ under ammonia (NH_3) and nitrogen (N_2) flows. The intensity of the Bragg lines is represented by the colour scale on the right.

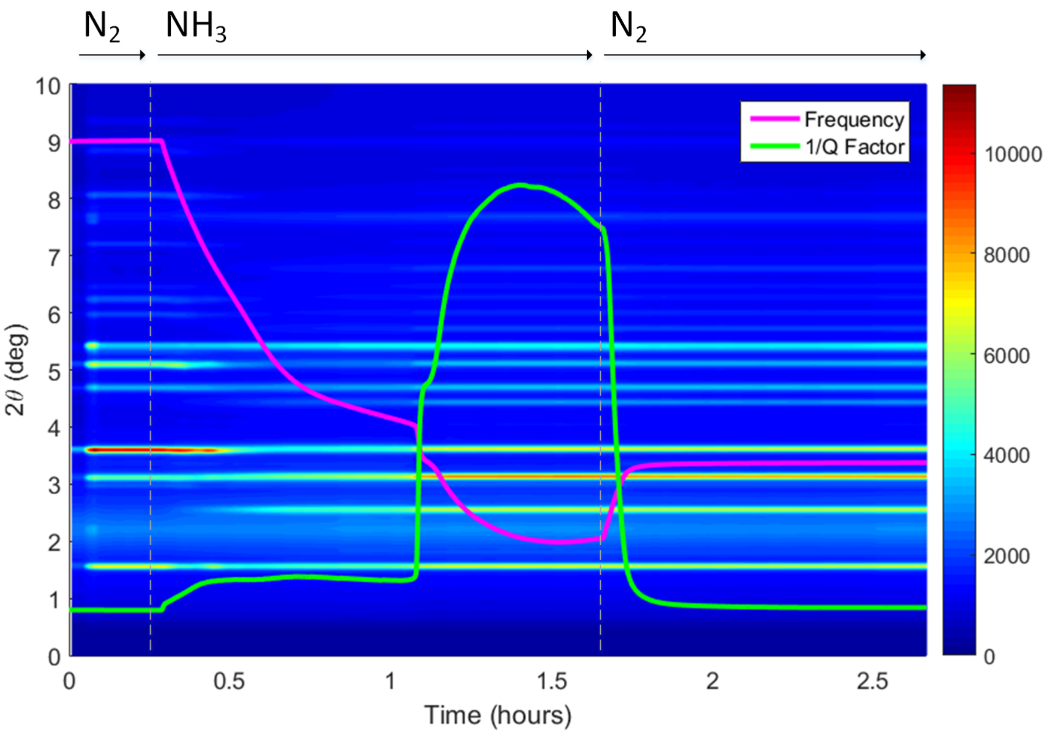

Figure 6.7: Superimposition of the surface plot of Bragg diffraction and dielectric data during ammonia absorption and desorption within $MgCl_2$ under ammonia (NH_3) and nitrogen (N_2) flows.

Table 6.2: Space groups and lattice parameters for $CaBr_2$ ammoniation products

Chemical Formula	Space Group	Lattice Parameter	Cell Volume
$CaBr_2$ [120]	P n n m (58)	6.584(6) 6.871(6) 4.342(4) 90. 90. 90.	196.43 [Å³]
$Ca(NH_3)_1Br_2$	Not Available	Not Available	Not Available
$Ca(NH_3)_2Br_2$	Not Available	Not Available	Not Available
$Ca(NH_3)_6Br_2$	Not Available	Not Available	Not Available
$Ca(NH_3)_8Br_2$ [121]	P n m a (62)	12.0478(3) 7.4406(2) 15.7216(4) 90. 90. 90.	1409.32 [Å³]

6.3.4 Structural Properties of $CaBr_2$

The Bragg data for ammonia absorption in $CaBr_2$ can be seen in Figure 6.8. There are no structural changes observed during the nitrogen flow though the $CaBr_2$ sample. As ammonia was absorbed by the sample, structural changes can be seen, with Bragg peaks at approximately 2 Å, 3Å , 3.8 Å, and 4.6 Å being replaced with peaks at 2.5 Å, 3.5 Å, and 4.2 Å. This occurs between 0.5 and 0.7 hours. This change in structure corresponds to the change in stoichiometry from $CaBr_2$ to $Ca(NH_3)_8Br_2$. Literature suggests changes in stoichiometry of $Ca(NH_3)_x$ Br_2 where $x = 0, 1, 2, 6, 8$ [77]. The space groups and lattice parameters for these materials available on the ICSD can be found in Table 6.2. These suggested changes in structure are not visible in the Bragg data, where the stoichiometry jumped to the $x = 8$ state. For the $CaBr_2$ sample, no structural changes can be seen when the nitrogen flow was reintroduced.

When ammonia absorption in $CaBr_2$ was investigated in [27], seen in Figure 2.26, under neutron diffraction, the $x = 2$ phase was observed first followed by the $x = 8$ phase. In Figure 6.8, only the change in stoichiometry from the starting material to the $x = 8$ phase is observed.

Overlaying the dielectric data on top of the Bragg data shows the relation between structure and dielectric properties of $CaBr_2$, and can be seen in Figure 6.9. This shows dielectric changes occurred simultaneously with structural data, as the $CaBr_2$ sample absorbs ammonia to become $Ca(NH_3)_8Br_2$. Due to the gas flow problems experienced it was difficult to asses if this was the only stoichiometric change observed in the dielectric data. However, structurally, only one change in stoichiometry occurs. Once a nitrogen flow was reintroduced, dielectric

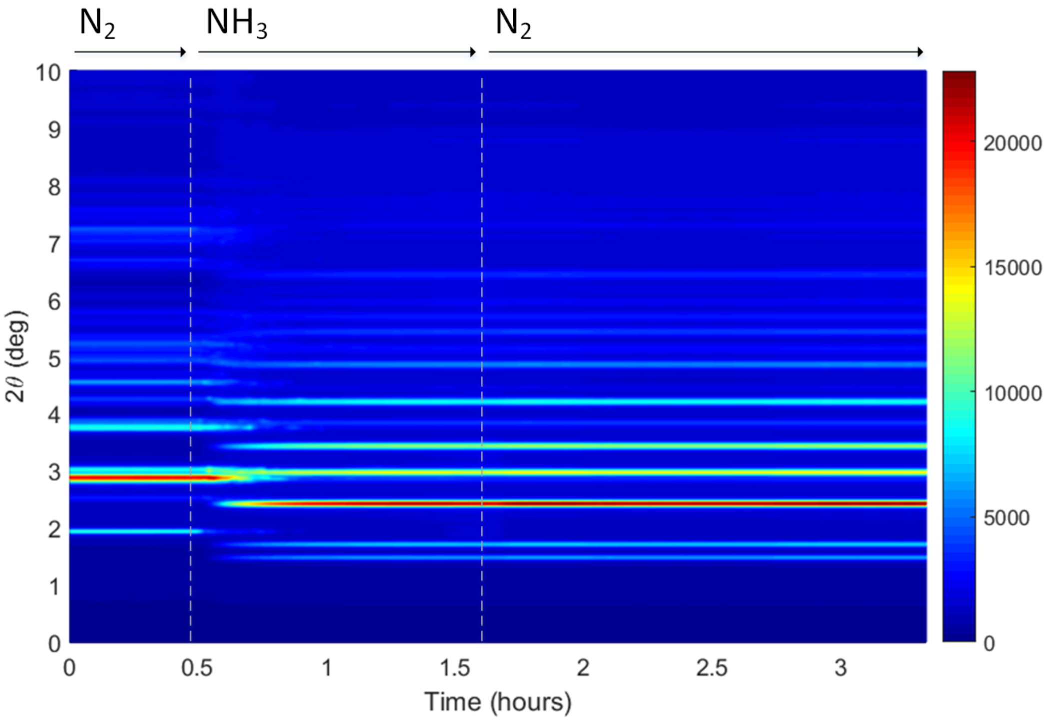

Figure 6.8: A surface plot of Bragg diffraction collected from I15-1 during ammonia absorption and desorption within $CaBr_2$ under ammonia (NH_3) and nitrogen (N_2) flows. The intensity of the Bragg lines is represented by the colour scale on the right.

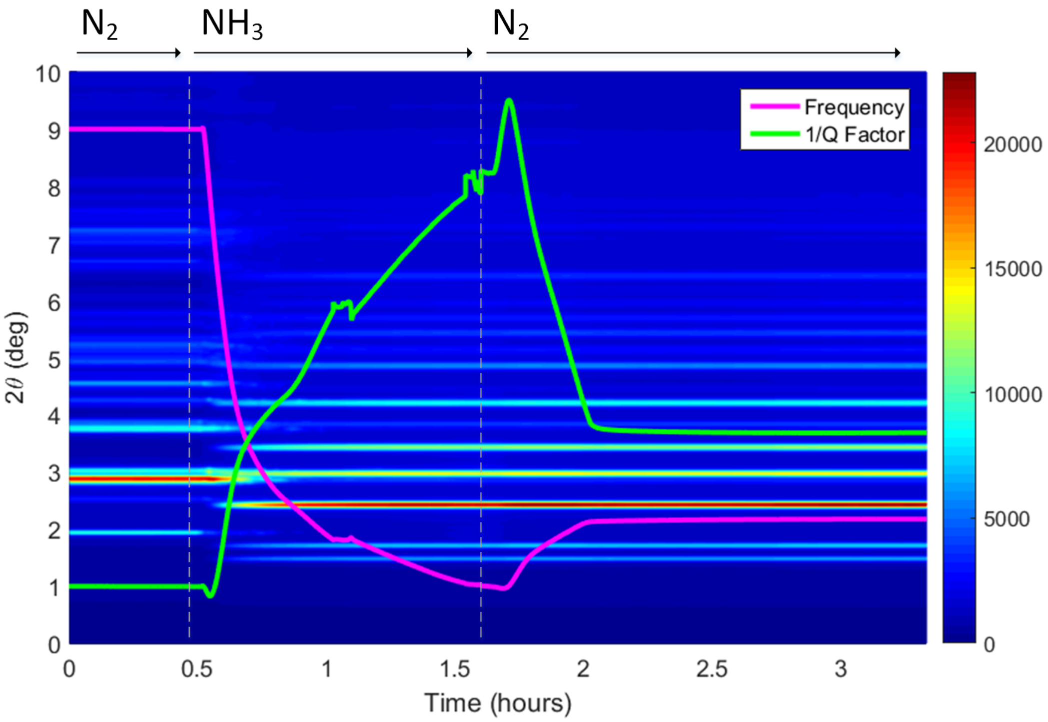

Figure 6.9: Superimposition of the surface plot of Bragg diffraction and dielectric data during ammonia absorption and desorption within $CaBr_2$ under ammonia (NH_3) and nitrogen (N_2) flows.

data showed changes in polarity and loss of the sample. No change was observed in the structure during this time. As with the $MgCl_2$ sample, this suggests removal of some ammonia from the sample, but no change in average structure.

6.4 Conclusion

This chapter has shown the use of a hairpin geometry resonator with simultaneous X-ray diffraction, to monitor the absorption of ammonia in halide salts. This geometry of resonator has allowed the X-ray path to be unobstructed by the resonator allowing high resolution X-ray data. Dielectric data with this geometry resonator, a lossy sample, and a high filling factor has maintained a high enough Q factor to reliably measure dielectric response of the system.

As $MgCl_2$ absorbed ammonia the dielectric data showed a plateau in both frequency and Q factor as the stoichiometry changed. All changes in stoichiometry expected for $Mg(NH_3)_xCl_2$ are observed, where $x = 0, 1, 2, 6$. Where $x = 2$ there is a very short but defined plateau. These plateaus correspond to the changes in stoichiometry experienced during ammonia absorption. Comparing the size of the fractional frequency shifts, or relating the shift to the amount of ammonia stored, is not possible as the sample expands to over twice its original volume when ammonia is absorbed. This expansion changed the proportion of the sample present in the measurement area. The sample expands under absorption of ammonia, however sample volume did not visibly reduce during the following nitrogen flow. This change in sample volume means it is not possible to compare starting and ending values of frequency and Q factor for this experiment. Structural Bragg data for $MgCl_2$ shows the $x = 0, 1, 6$ changes, however the $x = 2$ stage does not last long enough to be visible structurally. The $x = 2$ phase may also be difficult to observe in structural data due to its similarity in structure to the $x = 6$ phase.

As $CaBr_2$ absorbed ammonia the literature states the stoichiometric changes should follow the pattern $Ca(NH_3)_xBr_2$ where $x = 0, 1, 2, 6, 8$. The structural changes observed in this experiment showed only a transition directly to the $x = 8$ state. Dielectric data is slightly unclear due to the interruptions in gas flow, however this does not seem to show any additional transitions.

These experiments show the strength of the microwave characterisation technique to monitor these systems, as changes in dielectric response of the system has been show to closely correlate to changes in Bragg peak intensity. Microwave characterisation has also been shown to observe changes in stoichiometry not visible by X-ray diffraction. It also shows the success of the hairpin geometry resonator for use with simultaneous X-ray diffraction.

Chapter 7

SO_2 Absorption in MFM-170

Here the absorption and desorption characteristics of the MOF MFM-170 are investigated using the microwave characterisation technique. These experiments were carried out under varying conditions, including with an activated MOF, fully hydrated MOF and partially hydrated MOF. Dielectric properties were also recorded while measuring the temperature of the sample to observe the exothermic and exothermic natures of the absorption and desorption of SO_2 respectively. This experiment uses a hairpin geometry of microwave resonator to allow a thermal camera to monitor the temperature of the sample tube during dielectric measurements under SO_2 and nitrogen flows.

7.1 Method

The first series of experiments in this chapter were conducted using the C1 microwave cavity, the design of which is discussed in Section 4.1. The C1 cavity was used instead of the C2 cavity (which was used for the initial SO_2 NPD experiments in Section 5.2) as it has a much higher Q factor - approximately 7000 versus the 1500 for the cavity used for the NPD experiments. The quartz tube for these experiments had an outer diameter of 6 mm with an inner diameter of 4 mm. The sample was held in place using quartz wool at both ends of the

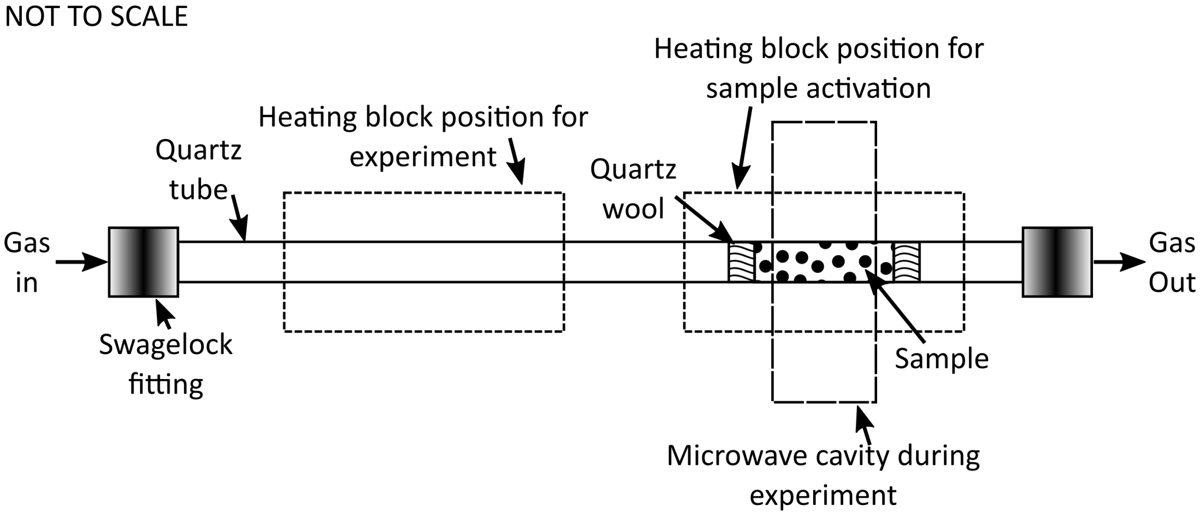

Figure 7.1: Setup of equipment for SO$_2$ absorption experiments showing; sample held in place by quartz wool inside the sample tube, Swagelock fittings connecting quartz tube to gas lines, microwave cavity location, gas flow direction, and heating block position both during dielectric measurement and during sample activation.

sample. The quartz tube had a length of 600 mm. The tube length was selected to allow the use of an aluminium heating block to be used to activate the sample. The 40 mm long powdered sample was loaded near the end of the tube furthest from the gas flow. Once the sample had been activated the excess section of tube was used to slide the heating block onto allowing the microwave cavity to be secured around the sample. This allowed dielectric measurements to be conducted without needing to disconnect gas connections which would have exposed the sample to air.

Swagelok fittings were used to connect gas lines to the quartz tube. A hot plate was used to heat a cuboid aluminium heating block with a cylindrical hole to 160 °C. The heating block was placed around the sample and heated to 160 °C. This heated the sample to the appropriate temperature for activation and nitrogen gas was flowed through the MOF for sample activation. After activation the block was allowed to cool and removed from the sample. A valve was used to allow selection of either a flow of nitrogen or SO$_2$ gas. These gas flow rates were not controlled as no flow controllers were available for SO$_2$ gas. Instead the flow was set by adjusting the pressure on the gas regulators. This setup is shown in Figure 7.1.

The final experiment in this chapter uses the hairpin geometry resonator H1 to investigate the exothermic nature of SO_2 absorption, and endothermic nature of SO_2 desorption. The open structure of the hairpin resonator allows the use of a thermal camera to monitor the temperature of the sample during the SO_2 absorption and desorption processes. The quartz tube and gas line setup used in this experiment is the same as all other experiments in this chapter.

7.2 Results

7.2.1 Activated MFM-170 SO_2 Absorption

In order to explain the unusual behaviours seen in Section 5.2, a control experiment must first be conducted to show the dielectric response of MFM-170 under SO_2 absorption and desorption. To do this the MFM-170 sample was activated for 8 hours at 160 °C. A flow of SO_2 was then passed through the sample until dielectric response plateaued. Nitrogen was then flowed through the sample to remove the SO_2 until the dielectric response again plateaued. This cycle of absorption and desorption of SO_2 was then repeated.

Figure 7.2 shows the change in fractional frequency shift and inverse of Q factor shift during SO_2 absorption and desorption. As SO_2 was absorbed by the sample the fractional frequency decreased rapidly and inverse Q factor shift increased rapidly which is consistent with the absorption of a polar molecule with associated dielectric loss. The dielectric response became fully saturated in under 15 minutes. Nitrogen was then flowed through the sample to remove the SO_2. As the SO_2 was desorbed by the sample the fractional frequency and inverse Q factor shift begin to return to their original values. Frequency continued to increase until it reached its original value at 3.5 hours with changes in gradient seen at approximately 1.25 and 2 hours. Inverse Q factor shows a more complex behaviour and began to increase again at approximately 1.25 hours before decreasing again at 1.75 hours until reaching a plateau. The exact reason for the change in frequency gradients and points of inflection of inverse Q factor sift are not known although one explanation is that the SO_2 is leaving one binding site in the

MOF, causing the initial decrease in inverse Q factor shift, before re-binding at a different binding site, causing the rise in inverse Q factor shift. SO_2 is then finally removed from the MOF, where the inverse Q factor shift decreases once again. Fractional frequency recovers to very close to its original value however inverse Q factor does not fully recover. This strongly suggests some SO_2 is still present within the sample, likely strongly bound to the metal centres [27].

When the SO_2 absorption and desorption behaviour was repeated the same patterns in frequency and Q factor were observed. The second cycle of SO_2 absorption and desorption in Figure 7.2 shows the repeatability of the results. After this second cycle was complete, nitrogen was left to flow for around 8 hours. During this time very little change in frequency was observed but Q factor very slowly recovered to very close to its starting value at the beginning of this experiment. This shows that, if left for an extended period of time, a flow of nitrogen gas is likely to remove all absorbed SO_2 from the sample even at room temperature.

7.2.2 Hydrated MFM-170 SO_2 Absorption

The cycle of SO_2 absorption and desorption was then repeated after hydrating the MOF. The dielectric response during hydration and SO_2 cycle is shown in Figure 7.3. In order to hydrate the sample, nitrogen gas was bubbled through water before passing through the MOF. MFM-170 readily absorbs water from the air and has a very strong binding with water at the metal centres . Water absorption is accompanied by a colour change in the MOF from deep blue/purple to light blue/green. When loosely piled in open air the MOF absorbs water in a matter of seconds. When tightly packed in a quartz tube however, the absorption process was observed to take longer. When in air, the whole sample rapidly changed colour in a gradient. In a quartz tube however, the sample changes colour at the end exposed to hydrated nitrogen with a distinct line between hydrated and activated MOF. The line was observed to slowly move through the MOF as more of the sample became hydrated. The vast increase in amount of time is due to the reduces surface area of the MOF in contact with the hydrated nitrogen

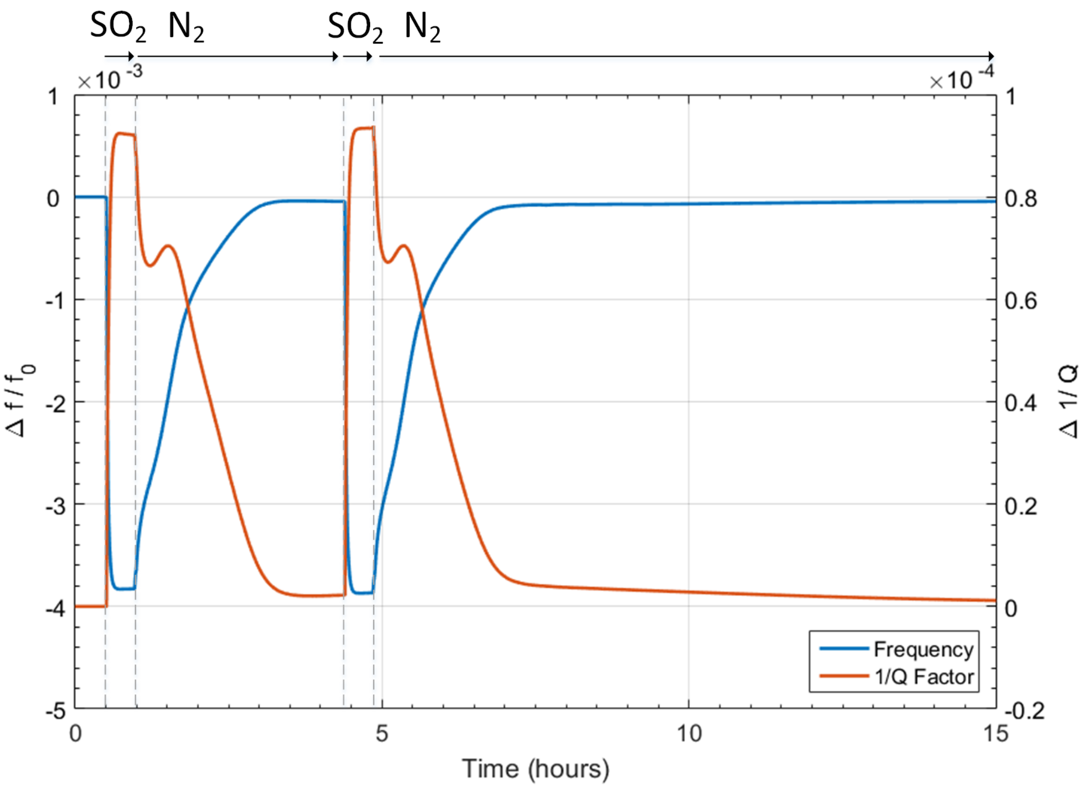

Figure 7.2: Dielectric response during SO_2 absorption then desorption under nitrogen flow for an activated MFM-170 sample.

and the increased packing density impeding the movement of hydrated nitrogen through the sample.

The slow absorption of water by the sample can be seen in the first section of Figure 7.3. Here, the water absorption process took approximately 7 hours. As water was absorbed, the fractional frequency shift decreased and inverse Q factor shift increased, as expected. Once the dielectric response had plateaued and the sample is saturated with water the gas flow is switched to pure SO_2. At this point the fractional frequency shift was observed to decrease and inverse Q factor shift increased at a much faster rate than observed during hydration, presumably due to the higher concentration of SO_2 in the gas stream than water in the air. Once the dielectric data was observed to plateau the gas flow was switched back to dry nitrogen.

With water and SO_2 both present in the sample in considerable amounts a direct analysis of the dielectric response is not possible as there are many possible complex sorbent behaviours occurring simultaneously. The absorbed SO_2 may displace the water bound to the MOF, bind to the water bound in the MOF, or dissolve in the water present if liquid water in present within the MOF cavities. Furthermore, different dielectric responses may be expected for SO_2 bound to the MOF when surrounded by water molecules, surrounded by more SO_2 molecules, or surrounded by any combination of water and SO_2 molecules. The same is true when water is bound to the MOF when surrounded by SO_2, and so on.

Under the dry nitrogen flow dielectric properties recovered a significant portion towards their starting values before this process slowed considerably. After the recovery slowed, inverse Q factor shift increased slightly before decreasing to its original value. Again exact analysis of this feature is not possible but is likely caused by changes in relative water and SO_2 concentrations changing the prevalent interactions present in the MOF.

The microwave characterisation technique highlights many dynamic and complex behaviours that are not easy to observe by other analytical techniques such as X-ray or neutron diffraction. The dielectric measurement technique allows measurement during the dynamic changes in this experiment. This shows the strength of the technique for observing gas absorption and

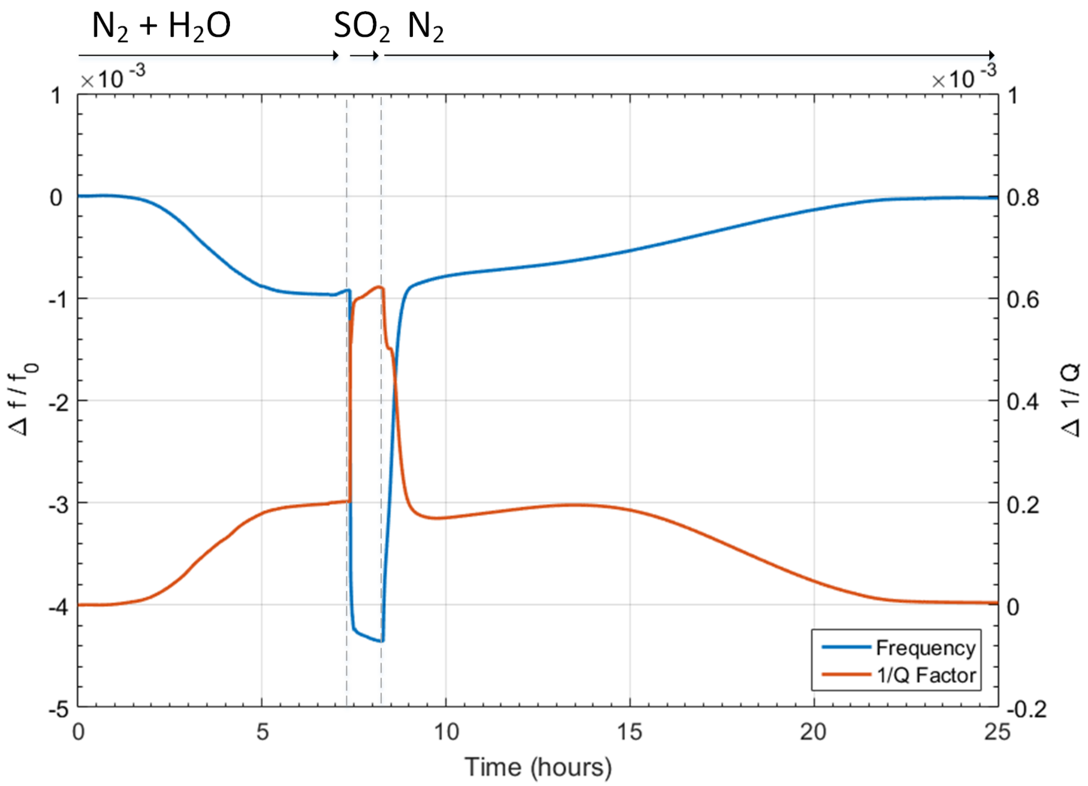

Figure 7.3: Dielectric response during the hydration using hydrated nitrogen then SO_2 absorption then desorption under nitrogen flow for a MFM-170 sample.

desorption due to its high sensitivity, however further experiments would be required to fully understand the complex behaviours observed.

7.2.3 Partially Hydrated MFM-170 SO_2 Absorption

After the hydrated MFM-170 experiment was conducted in Section 7.2.2 all SO_2 had been removed from the sample but some water was likely still present in the sample due to the high binding energy of water to the MOF. The state of the sample is similar to that in Section 5.2 where some water is likely to be present in the MOF. SO_2 was then flowed through the sample and after 0.8 hours the gas flow was switched to nitrogen to desorb the newly absorbed SO_2 from the sample. The dielectric response for this is shown in Figure 7.4 and closely matches the response observed for the activated sample in Figure 7.2 with a small difference seen in the change in fractional frequency shift and inverse Q factor shift. For the partially hydrated sample, frequency and Q factor showed a smaller change. This may be due to the water already present in the sample taking up space that could otherwise be taken by SO_2.

Although the experimental conditions for this sample closely match those of the sample during the simultaneous dielectric and NPD measurements, the results do not match the unusual behaviour observed in Section 5.2. During SO_2 absorption for the NPD experiments inverse Q factor experiences two points of inflection similar to during SO_2 desorption in Figure 7.4. This behaviour is not seen during SO_2 absorption in Figure 7.4. During SO_2 desorption for the NPD experiments inverse Q factor decreases sharply before reducing to its final value. Again this behaviour is not seen in Figure 7.4. As the conditions of the MOF are similar in these two experiments it is expected the dielectric response would be similar. In order to discover the reason for the difference in response further investigation is required. Possible experiments include; repeating the experiment offline with the C2 cavity and the same sample size as the NPD experiment to see if the results are repeatable offline, and repeating the experiment with the same sample size in the C1 cavity to see if the results can be replicated with a cavity with higher Q factor.

7.2.4 Dielectric with Thermal Measurement of Activated MFM-170 SO_2 Absorption

Another possible cause for the unusual behaviour seen in Section 5.2 may be changes in temperature. Changes in temperature may effect dielectric measurements in two ways; either by causing changes in cavity dimensions, described in Section 2.7.7, or by changing the dielectric properties of the material. To test this hypothesis the temperature of the sample must be monitored during microwave measurements. To do this the C1 microwave cavity described in Section 7.1 cannot be used as there is no line of sight to the sample and no thermocouple can be placed within the cavity without vastly changing the results. Consequently a hairpin resonator is used. The design of the H1 resonator used is discussed in Section 4.2. Using a

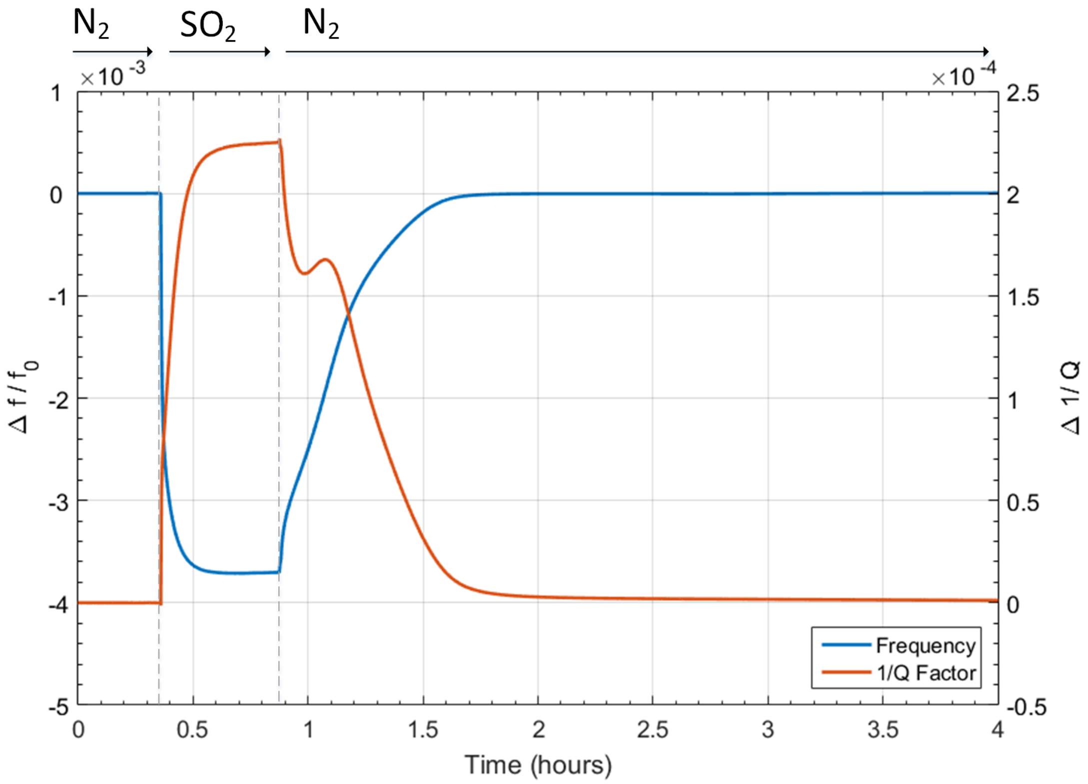

Figure 7.4: Dielectric response during SO_2 absorption then desorption under nitrogen flow for a partially hydrated MFM-170 sample.

hairpin geometry of resonator allows dielectric measurement with an open structure allowing for a thermal camera to be used to monitor the temperature of the quartz tube surrounding the sample during dielectric measurements. This method still does not give the perfect temperature measurement as the temperature recorded will be for the quartz tube itself and the sample is likely to be a higher temperature. This method does however, give a very good estimate of sample temperature during SO_2 absorption and desorption. The same gas flow equipment as described in Section 7.1 was used for this experiment.

The temperature of the quartz tube surrounding the sample during SO_2 absorption and desorption is shown in Figure 7.5. As SO_2 was absorbed by the sample the temperature of the sample rose. This was expected as SO_2 absorption is an exothermic process [19]. The temperature was observed to rise from 19 °C to 38 °C in around 2 minutes. The sample then cooled, returning to its original value less than 8 minutes later while SO_2 was still flowing through the sample. The temperature of the sample then remains constant until nitrogen gas was introduced. Under nitrogen flow the temperature of the sample was observed to decrease, which was expected as SO_2 desorption is an endothermic reaction. Sample temperature drops from 19 °C down to almost 10 °C during SO_2 desorption in around 5 minutes. The temperature then returned to its original value in under 12 minutes. As the temperature of the flowing gas is at room temperature, it is likely that the flow of gas will have a cooling effect on the sample and surrounding quartz tube at elevated temperatures. As the gas flow rates are not known and are likely to be different for SO_2 and nitrogen, calculating time constants for these temperature changes would not be valid.

The dielectric response of the hairpin resonator during SO_2 absorption and desorption can be seen in Figure 7.6. As SO_2 is absorbed by the sample the fractional frequency shift decreased and inverse Q factor shift increased, as observed previously. The resonant frequency of the resonator would also be affected by the heating effect from the sample observed alone. For this resonator the hairpin ends were separated by 6 mm with the sample occupying the central 5 mm. This leaves only 0.5 mm between the sample tube outer wall and the copper hairpin resonator which should allow heat to be transferred to the hairpin resonator via convection and

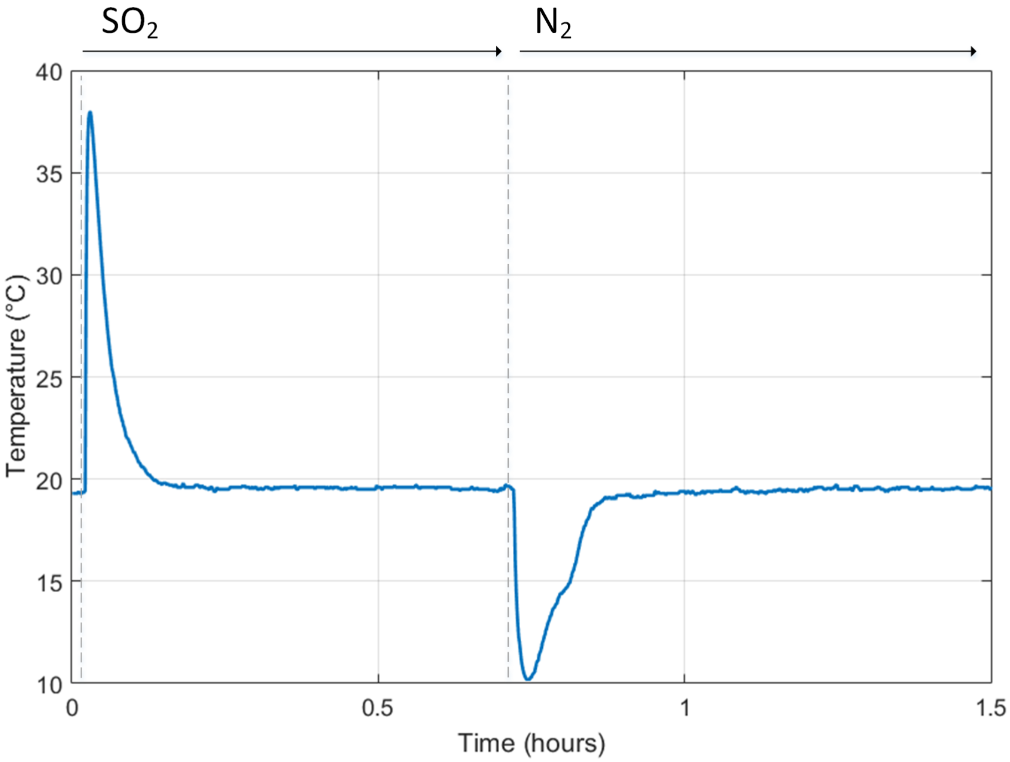

Figure 7.5: Temperature measurement from the sample area inside the quartz tube between the hairpin ends during SO_2 absorption then desorption under nitrogen flow for a activated MFM-170 sample.

radiation. The heating of the hairpin resonator during the exothermic absorption of SO_2 would cause the resonating structure to expand, resulting in a decrease in the resonant frequency that occurs in addition to that expected from the introduction of SO_2. It is difficult to separate the two effects as they occur simultaneously and both evolved from a single cause, the binding of SO_2. For a hairpin cavity there are no recorded methods of correcting for changes in temperature as there are for cavity resonators. It could be possible to find a resonant mode where frequency was only effected by temperature and not by the sample but for this resonator this was not possible. The effect of temperature on Q factor is considerably smaller than its effect of frequency. This is because temperatures effect on Q factor is a second order effect whereas with frequency this effect is first order.

As nitrogen flow is introduced, SO_2 is removed from the sample. The fractional frequency shift then returned to its original value with one or more changes in gradient. The inverse Q factor shift initially decreased before exhibiting the same points of inflection observed in Figure 7.2 but at an earlier point of the absorption. This change in the timing of the feature is likely due to the different flow rates in these experiments. The late change in inverse Q factor shift after 0.9 hours can be attributed to the loss of strongly bound SO_2 in the MOF as the strongly bound SO_2 will be removed from the sample last due to its higher bonding energy.

7.3 Conclusions

In this chapter the dielectric properties of the MOF MFM-170 have been investigated under SO_2 absorption and desorption. These characteristics have been explored through a series of experiments under different conditions. The experiment with the fully activated MOF showed the reaction of the sample under SO_2 absorption and desorption in ideal conditions with no other absorbed species bound to the metal centres or in the pores of the MOF. In these conditions absorption of SO_2 is very rapid causing a decrease in fractional frequency shift and increase in inverse Q factor shift. When SO_2 is removed, more complex behaviour is seen with change in frequency gradient and inflections in inverse Q factor. These are likely due to

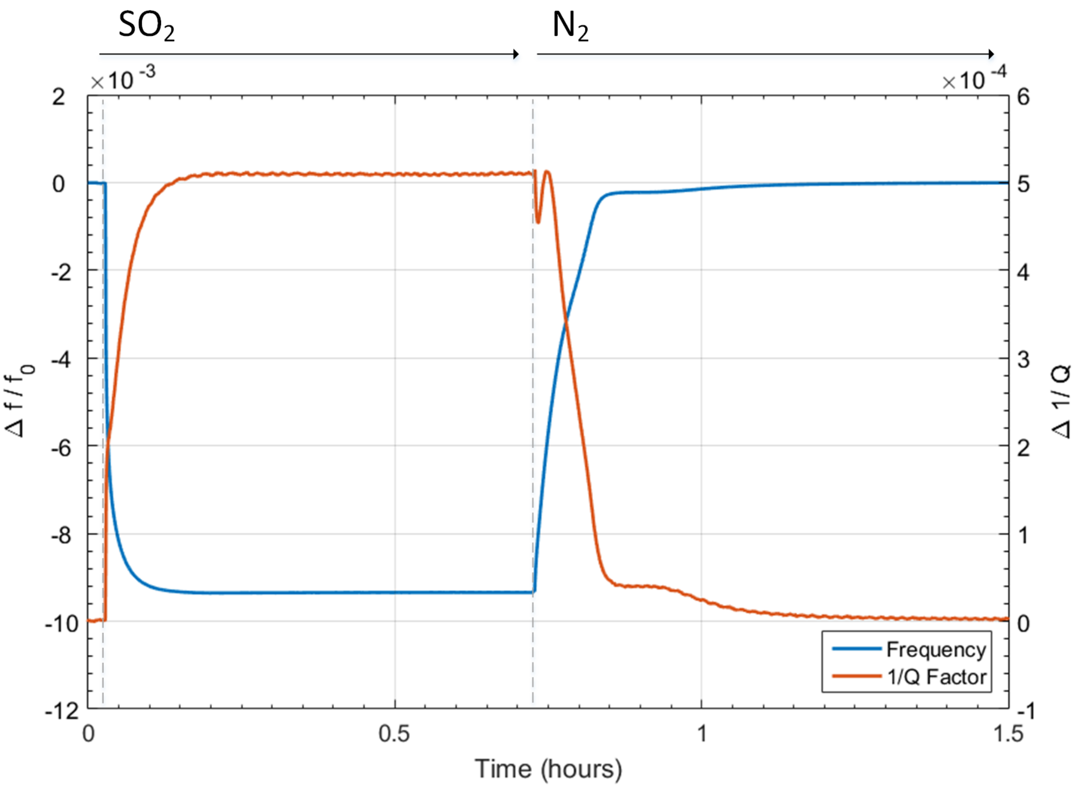

Figure 7.6: Dielectric response during SO_2 absorption then desorption under nitrogen flow for a partially hydrated MFM-170 sample during temperature measurements

SO_2 moving between binding sites in the MOF. When this experiment was repeated with a partially hydrated MOF, very similar dielectric behaviour was observed.

When the MFM-170 sample is fully hydrated a different behaviour is observed. Water is introduced to the MOF which exhibits simple dielectric changes seen by a decrease in fractional frequency shift and increase in inverse Q factor. Absorption of SO_2 into the hydrated MOF shows a similar absorption response in the dielectric measurements as with the activated MOF. The desorption of SO_2 from the sample however exhibits a much more complex behaviour. As nitrogen is flowed through the sample and removes SO_2 and water, there is an initial fast process similar to that observed in the activated sample. There is then a longer term process showing a much slower removal of lossy, polar material from the sample. Pinpointing the precise cause of the dielectric response during this experiment has not been possible due to the number of possible processes causing the response.

The final SO_2 absorption experiment was used to investigate the thermal effects of the exothermic nature of SO_2 absorption and endothermic nature of SO_2 desorption. The thermal camera used allowed analysis of the temperature changes experienced by the sample as SO_2 was absorbed and desorbed from the sample. Temperature measurements showed an increase of almost 20 °C during SO_2 absorption and decrease of almost 10 °C during SO_2 desorption. The use of a hairpin geometry resonator allowed the monitoring of temperature during dielectric measurements. The dielectric response observed during this experiment were similar to the previous activated sample with changes in the timings of features, due to the likely difference in flow rates.

Chapter 8

Final Conclusions

8.1 Materials Conclusions

In this thesis, gas sorption in metal-organic frameworks has been investigated. The absorption of both ammonia and sulphur dioxide have been observed. The absorption and storage of ammonia has been studied to find a material suitable for solid state storage of ammonia for use as an energy vector. Ammonia absorption and desorption using simultaneous microwave dielectric and structural characterisation was measured for HKUST-1, UiO-67, and CPO-27-Co. In these experiments, HKUST-1 decomposed during ammonia absorption. This was seen in the dielectric response as an unexpected decrease in polarisation and dielectric loss as ammonia was absorbed, indicating the decomposition of the sample into a compound with very different dielectric properties. The structural data showed new phases being produced as ammonia was absorbed with a different overall structure at the end of the experiment than the starting material. Due to this, HKUST-1 has been deemed unsuitable for use as an ammonia storage material. UiO-67 showed changes in dielectric properties consistent with absorption of a lossy, polar molecule during ammonia absorption, with sample dielectric loss and polarity increasing during the sorption process. After the desorption of ammonia, frequency shift was seen to return to its starting value but Q factor did not. This is likely to be due to some tightly bound ammonia still bound to the metal centres of the MOF. Structural data showed little change during ammonia absorption and desorption, showing the sample was stable to ammonia absorption. The structural data for CPO-27-Co showed no changes in structure during the absorption and desorption of ammonia. Dielectric data showed a more complex behaviour, suggesting the possible presence of coordinated ammonia networks however, further investigation is required to prove this hypothesis. This set of experiments have shown the capability of UiO-67 and CPO-27-Co to store considerable amounts of ammonia and may be considered as ammonia absorption and storage materials.

Sulphur dioxide absorption in the metal-organic framework MFM-170 has also been investigated in this thesis. The chemical structure of MFM-170 has not yet been published, but initial studies have shown its stability during SO_2 absorption and its exceptional SO_2 storage capacity. Work in this thesis has been performed to investigate the absorption and desorption processes in this MOF and to study the possibility of using this MOF as a selective SO_2 absorber for desulphurisation or for an SO_2 sensor. Simultaneous microwave dielectric and structural characterisation studies were performed on the absorption and desorption of SO_2 in MFM-170. The dielectric results showed the polarity of the sample increased as SO_2 was introduced and the polarity then decreased as SO_2 is flushed from the sample, as expected. The dielectric loss of the sample and Bragg data showed more unusual behaviours. Dielectric loss during ammonia absorption appears to begin to increase, before decreasing, and increasing again until reaching its final value, all during the absorption of SO_2. The structural data showed a Bragg peak increasing in intensity and width before returning to its starting intensity and width, all during the absorption of SO_2. With the data available from this experiment it has not been possible to explain these behaviours.

To attempt to explain the unusual behaviours in Q factor and structural data during NPD experiments, further investigation of SO_2 in MFM-170 was conducted without structural characterisation. These experiments included cycling SO_2 absorption and desorption when the MOF was; fully activated, fully saturated with water, and partially saturated with water. Temperature effects due to the exothermic nature of SO_2 absorption and endothermic nature of SO_2

desorption were also investigated using a hairpin type resonator and thermal camera. During these experiments, it was not possible to re-create the pattern observed in dielectric loss data observed in the in-situ NPD experiments. Further experimentation is required to find the reason for the unusual behaviours observed in the SO_2 NPD experiments.

The absorption of ammonia by halide salts was also investigated in this thesis. This experiment consisted of simultaneous X-ray diffraction and dielectric characterisation. For the $CaBr_2$ sample, the structural data shows a jump in stoichiometry from the starting sample to fully saturated with ammonia ($Ca(NH_3)_8Br_2$), while dielectric data did not show any additional stoichiometric changes. For the $MgCl_2$ sample, the structural data also showed a jump in stoichiometry from the starting sample to fully saturated with ammonia ($Mg(NH_3)_6Cl_2$). This time however, the dielectric results showed clear changes from the starting sample to $Mg(NH_3)_1Cl_2$, to $Mg(NH_3)_2Cl_2$, before reaching the fully saturated $Mg(NH_3)_6Cl_2$state. Observing the changes in stoichiometry not visible in the Bragg diffraction data shows the strength and sensitivity of microwave dielectric characterisation to monitor polar gas sorption systems.

8.2 Techniques Conclusions

A cavity style resonator and heating equipment have been designed, simulated, constructed, tested and used for simultaneous NPD and MCR measurements. This resonator uses a thinned section of cavity wall to minimise neutron scattering from the resonator. A reduced cavity height allows heating coils to be placed as close to the sample as possible to maintain a more constant temperature across the sample. A heating coil is placed inside the top of the sample tube such that a gas can be flowed through the coil and heated before passing through the sample. The heated gas then, in turn, heats the sample. The second heating coil, below the microwave cavity, minimises and temperature gradient across the sample. This method of heating means no additional material is placed in the path of the neutron beam and no heating equipment is effecting the electromagnetic fields inside the microwave cavity. The effectiveness of this equipment was used to activate a MOF sample during simultaneous structural and dielectric characterisation. The heating coils were able to heat a gas flow, and subsequently the sample, to the appropriate 150 ℃ at an appropriate flow rate to activate the sample. During this heating, the microwave cavity remained at a low enough temperature such that temperature effects were minimal. The microwave cavity maintained a high Q factor throughout the experiment, even when presented with a fully water saturated sample with high dielectric loss.

A hairpin style resonator has been designed, simulated, constructed, tested and used for simultaneous X-ray diffraction and dielectric characterisation. Incorporating a hole through the bottom plate of the hairpin, supporting structure and shielding allowed the incident X-ray beam to be unimpeded by the resonator before reaching the sample. This hairpin geometry makes use of the open end of the resonating structure to allow X-rays scattered by the sample to be unimpeded before reaching the measurement plane. This maximises the possible resolution of these measurements which is especially important for XPDF experiments. The resonator allowed sufficient sensitivity to observe changes in dielectric properties, as well as a high enough Q factor to measure samples with high dielectric loss. The equipment was used on i15-1 at Diamond for XPDF measurements of ammonia absorption of halide salts. These experiments showed the close correlation between Bragg data and microwave dielectric results and showed the ability to observe changes in stoichiometry not visible in X-ray data. This experiment proved the concept of using a hairpin style resonator for simultaneous structural and dielectric characterisation of materials.

This thesis has also presented a new method for temperature correction in cylindrical cavity perturbation measurements using degenerate modes. The temperature correction method developed uses split degenerate modes to correct for changes in resonant frequency caused by changes in resonator temperature. The validity of this technique was proven by heating the microwave cavity and water sample from 20 ℃ to 60 ℃, calculating the permittivity of the water during this temperature sweep and comparing to literature values. This experiment showed the temperature correction technique used was incredibly accurate as the results were well within the possible errors of the system, mostly relating to sample volume. It has also shown how a strategically placed, off-axis perturbation can be used to suppress the lower frequency degenerate mode such that a single clean Lorentzian frequency response is observed.

Microwave characterisation has proved to be a robust and sensitive measurement technique throughout this thesis. The effectiveness of this instrumentation relies on the design and construction of the microwave resonator used, two of which have been designed as part of this thesis; a cavity resonator (C1) for simultaneous neutron diffraction, and a hairpin resonator (H1) for simultaneous X-ray measurements and simultaneous thermal measurement. Microwave dielectric measurements have been used to characterise heterogeneous gas sorption processes as an individual technique, as well as for simultaneous measurements alongside; neutron diffraction, X-ray diffraction, and thermal measurement. Using microwave characterisation provides information on the polarity and dielectric loss of a sample however, information on more complex chemical processes can also be extracted from this data. For example, this technique has been used to differentiate between physisorbed and strongly bound polar gasses within a solid state host. Dielectric characterisation has also shown changes in stoichiometry not observed in structural data from X-ray diffraction.

8.3 Future Work

During the simultaneous neutron diffraction and microwave measurement of SO_2 absorption in MFM-170 experiments carried out in Section 5.2, some unusual results were seen in both Q factor and Bragg data. Upon absorption of the polar gas, inverse Q factor shift increased at first, then began to decrease, before increasing again until reaching its final value. Bragg data for this absorption showed one peak increasing in intensity and broadening before decreasing in intensity and returning to its original width, all during SO_2 absorption. This behaviour was unexpected and is yet to be fully explained. There are three ways in which this experiment could be improved upon if repeated. These improvements may either help explain the cause of these unexplained behaviours or, if the experimental procedure is improved, these unexplained results may not occur. The problems faced and possible improvements are shown below:

Unknown gas flow rate: This experiment was carried out without the use of mass flow meters for argon and SO_2 flows. Flow rates were estimated but may not be accurate. Repeating the experiments with mass flow meters to set gas flow rates would allow control of absorption and desorption rates.

Low Q factor: The Q factor for the duration of this experiment was below 50. This low Q factor value adds some uncertainty in the validity of the results. The trends in Q factor data observed seem robust, even if the high levels of noise are not ideal. Repeating this experiment using a cavity resonator with a higher Q factor, once the sample is inserted, would give more confidence in the dielectric results.

Starting sample conditions: Although every effort was made to ensure the starting sample was as close to activated as possible for this experiment, some water was inevitably present in the starting sample. The sample was activated and loaded in a glove bag to minimise exposure to the water vapour in the air. During the sample loading into the experimental rig, the sample was exposed to air for a approximately one minute. As the sample readily absorbs water from the air, some water was inevitably absorbed by the sample. It is possible the unexplained behaviours in Q factor and Bragg data relate to the water present in the sample. Using the heating equipment designed in Section 4.1 would allow the in-situ activation of the sample, ensuring no water was present in the sample when SO_2 is introduced.

The equipment developed in Section 4.1 and used in Section 5.3 was used to activate a MOF sample in-situ for simultaneous NPD and dielectric characterisation. In future, the use of this equipment will allow the user to ensure the sample is free from water and other solvents before carrying out the experiment. This is especially important when measuring air sensitive samples such as MOFs, which absorb water from the air. This equipment will also allow other experiments requiring heating to be carried out, such as catalytic processes.

The hairpin type resonator developed in Section 4.2 and used in Chapter 6 was used to perform simultaneous XPDF and dielectric characterisation. This equipment was used to observe the absorption of ammonia in halide salts. Further experiments to evaluate ammonia absorption in a greater selection of halide salts can be used to observe and compare their absorption behaviours. This equipment may also be used to characterise a variety of samples and sample conditions, not limited to those discussed in this thesis.

References

[1] M. P. Suh, H. J. Park, T. K. Prasad, and D. Lim. Hydrogen storage in metal-organic frameworks. *Chem. Rev.*, 112(20):782–835, 2011.

[2] R. Lan, J. T. S. Irvine, and S. Tao. Ammonia and related chemicals as potential indirect hydrogen storage materials. *Int. J. Hydrogen Energy*, 37(2):1482–1494, 2012.

[3] J. A. Turner. Sustainable hydrogen production. *Science*, 305(5686):972–974, 2004.

[4] A. Zuttel. Materials for hydrogen storage. *Mater. Today*, 6(9):24–33, 2003.

[5] C. H. Christensen, T. Johannessen, R. Z. Sørensen, and J. K. Nørskov. Towards an ammonia-mediated hydrogen economy? *Catal. Today*, 111(1-2):140–144, 2006.

[6] A. Klerke, C. H. Christensen, J. K. Nørskov, and T. Vegge. Ammonia for hydrogen storage: challenges and opportunities. *J. Mater. Chem.*, 18(20):2304, 2008.

[7] S. Niaz, T. Manzoor, and A. H. Pandith. Hydrogen storage: Materials, methods and perspectives. *Renew. and Sust. Energ. Rev.*, 50:457–469, 2015.

[8] W. I. F. David, J. W. Makepeace, S. K. Callear, H. M. A. Hunter, J. D. Taylor, T. J. Wood, and M. O. Jones. Hydrogen Production from Ammonia Using Sodium Amide. *J. Am. Chem. Soc.*, 136(38):13082–13085, 2014.

[9] J. Hartley, A. Porch, and M. O. Jones. A non-invasive microwave method for assessing solid-state ammonia storage. *Sensor. Actuat. B-Chem.*, 210:726–730, 2015.

[10] A. J. Rieth, Y. Tulchinsky, and M. Dinc. High and Reversible Ammonia Uptake in Mesoporous Azolate Metal-Organic Frameworks with Open Mn , Co , and Ni Sites. *J. Am. Chem. Soc.*, 138(30):9401–9404, 2016.

[11] P. L. Piirilä, H. Nordman, O. S. Korhonen, and I. Winblad. A thirteen-year follow-up of respiratory effects of acute exposure to sulfur dioxide. *Scand. J. Work, Env. Hea.*, 22(3):191–196, 1996.

[12] R. E. Stoiber and A. Jepsen. Sulfur Dioxide Contributions to the Atmosphere by Volcanoes. *Science*, 182(4112):577–578, 1973.

[13] D. P. Rall. Review of the health effects of sulfur oxides. *Environ. Health Persp.*, Vol 8:97–121, 1974.

[14] J. H. Carter, X. Han, F. Y. Moreau, I. Da Silva, A. Nevin, H. G.W. Godfrey, C. C. Tang, S. Yang, and M. Schröder. Exceptional Adsorption and Binding of Sulfur Dioxide in a Robust Zirconium-Based Metal-Organic Framework. *J. Am Chem Soc.*, 140(46):12–15, 2018.

[15] X. Han, S. Yang, and M. Schröder. Porous metal-organic frameworks as emerging sorbents for clean air. *Nat. Rev. Chem.*, 3, 2019.

[16] Zhen Zhen Yang, Liang Nian He, Ya Nan Zhao, and Bing Yu. Highly efficient SO2 absorption and its subsequent utilization by weak base/polyethylene glycol binary system. *Env. Sci. Tech.*, 47(3):1598–1605, 2013.

[17] M. Zidar, J. Golob, M. Veber, and V. Vlachy. Absorption of SO_2 into Aqueous Solutions. 2. Gas-Liquid Equilibrium of the MgO-SO_2 -H_2O System and Graphical Presentation of Operation Lines in an Equilibrium Diagram. *Ind. Eng. Chem. Res.*, 36(10):4342–4346, 2002.

[18] F. P. Terraglio and R. M. Manganelli. The absorption of atmospheric sulfur dioxide by water solutions. *J. Air Pollut. Contr. Assoc.*, 17(6):403–406, 1967.

[19] X. Li, L. Zhang, Y. Zheng, and C. Zheng. SO_2 Absorption Performance Enhancement by Ionic Liquid Supported on Mesoporous Molecular Sieve. *Energ. Fuel.*, 29(2):942–953, 2015.

[20] K. Tan, P. Canepa, Q. Gong, J. Liu, D. H. Johnson, A. Dyevoich, P. K. Thallapally, T. Thonhauser, J. Li, and Y. J. Chabal. Mechanism of preferential adsorption of SO_2 into two microporous paddle wheel frameworks M(bdc)(ted)$_{0.5}$. *Chem. of Mater.*, 25(23):4653–4662, 2013.

[21] M. Savage, Y. Cheng, T. L. Easun, J. E. Eyley, S. P. Argent, M. R. Warren, W. Lewis, C. Murray, C. C. Tang, M. D. Frogley, G. Cinque, J. Sun, S. Rudić, R. T. Murden, M. J.

Benham, A. N. Fitch, Al. J. Blake, A. J. Ramirez-Cuesta, S. Yang, and M. Schröder. Selective Adsorption of Sulfur Dioxide in a Robust Metal-Organic Framework Material. *Adv. Mater.*, 28(39):8705–8711, 2016.

[22] S. Yang, J. Sun, A. J. Ramirez-Cuesta, S. K. Callear, W. I. F. David, D. P. Anderson, R. Newby, A. J. Blake, J. E. Parker, C. C. Tang, and M. Schröder. Selectivity and direct visualization of carbon dioxide and sulfur dioxide in a decorated porous host. *Nat. Chem.*, 4(11):887–894, 2012.

[23] M. O. Jones, D. M. Royse, P. P. Edwards, and W. I. F. David. The structure and desorption properties of the ammines of the group II halides. *Chem. Phys.*, 427:38–43, 2013.

[24] C. Petit and T. J. Bandosz. Enhanced adsorption of ammonia on metal-organic framework/graphite oxide composites: Analysis of surface interactions. *Adv. Funct. Mater.*, 20(1):111–118, 2010.

[25] C. Petit and T. J. Bandosz. Synthesis, characterization, and ammonia adsorption properties of mesoporous metal-organic framework (MIL(Fe))-graphite oxide composites: Exploring the limits of materials fabrication. *Adv. Funct. Mater.*, 21(11):2108–2117, 2011.

[26] D. Saha and S. Deng. Ammonia adsorption and its effects on framework stability of MOF-5 and MOF-177. *J. Colloid Interf. Sci.*, 348(2):615–620, 2010.

[27] M. O. Jones, J. Hartley, and A. Porch. Simultaneous neutron diffraction and microwave dielectric characterisation of ammine materials - a non-destructive, non-contact characterisation tool for determining ammonia content in solids. *Phys. Chem. Chem. Phys.*, 18(33):23340–23347, 2016.

[28] D. Pontiroli, D. D'Alessio, M. Gaboardi, C. Milanese, S. G. Duyker, V. K. Peterson, N. Sharma, and M. Riccò. Ammonia-storage in lithium intercalated fullerides. *J. Mater. Chem. A*, (42):21099–21105, 2015.

[29] C. H. Christensen, R. Z. Sørensen, T. Johannessen, U. J. Quaade, K. Honkala, T. D. Elmøe, R. Køhler, and J. K. Nørskov. Metal ammine complexes for hydrogen storage. *J. Mater. Chem.*, 15(38):4106–4108, 2005.

[30] T. D. Elmøe, R. Z. Sørensen, U. Quaade, C. H. Christensen, J. K. Nørskov, and T. Johannessen. A high-density ammonia storage/delivery system based on $Mg(NH_3)_6Cl_2$ for SCR-DeNO$_x$ in vehicles. *Chem. Eng. Sci.*, 61(8):2618–2625, 2006.

[31] R. Z. Sørensen, J. S. Hummelshøj, A. Klerke, J. B. Reves, T. Vegge, J. K. Nørskov, and C. H. Christensen. Indirect, reversible high-density hydrogen storage in compact metal ammine salts. *J. Am. Chem. Soc.*, 130(27):8660–8668, 2008.

[32] W. I. F. David. Effective hydrogen storage: a strategic chemistry challenge. *Faraday Discuss.*, 151:399, 2011.

[33] M. Colombo, G. Koltsakis, I. Nova, and E. Tronconi. Modelling the ammonia adsorption-desorption process over an Fe-zeolite catalyst for SCR automotive applications. *Catal. Today*, 188(1):42–52, 2012.

[34] M. Dietrich, D. Rauch, U. Simon, A. Porch, and R. Moos. Ammonia storage studies on H-ZSM-5 zeolites by microwave cavity perturbation: correlation of dielectric properties with ammonia storage. *J. Sens. Sens. Syst.*, 4(2):263–269, 2015.

[35] M. Kubota, K. Matsuo, R. Yamanouchi, and H. Matsuda. Absorption and desorption characteristics of NH3 with metal chlorides for ammonia storage. *J. Chem. Eng. JPN*, 47(7 SPECIAL ISSUE):542–548, 2014.

[36] A. Leineweber, M. W. Friedriszik, and H. Jacobs. Preparation and Crystal Structures of $Mg(NH_3)_2Cl_2$, $Mg(NH_3)_2Br_2$, and $Mg(NH_3)_2I_2$. *Journal of Solid State Chemistry*, 147(1):229–234, 1999.

[37] D. Rauch, G. Albrecht, D. Kubinski, and R. Moos. A microwave-based method to monitor the ammonia loading of a vanadia-based SCR catalyst. *Appl. Catal. B-Environ.*, 165(2):36–42, 2015.

[38] D. Rauch, M. Dietrich, T. Simons, U. Simon, A. Porch, and R. Moos. Microwave Cavity Perturbation Studies on H-form and Cu Ion-Exchanged SCR Catalyst Materials: Correlation of Ammonia Storage and Dielectric Properties. *Top. Catal.*, 60(3-5):243–249, 2017.

[39] T. Hügle, M. Hartl, and D. Lentz. The Route to a Feasible Hydrogen-Storage Material: MOFs versus Ammonia Borane. *Chem. Eur. J.*, 17(37):10184–10207, 2011.

[40] M. J. Katz, A. J. Howarth, P. Z. Moghadam, J. B. DeCoste, R. Q. Snurr, J. T. Hupp, and O. K. Farha. High volumetric uptake of ammonia using Cu-MOF-74/Cu-CPO-27. *Dalton T.*, 45(10):4150–3, 2016.

[41] E. Borfecchia, S. Maurelli, D. Gianolio, E. Groppo, M. Chiesa, F. Bonino, and C. Lamberti. Insights into adsorption of NH_3 on HKUST-1 metal-organic framework: A multitechnique approach. *J. Phys. Chem. C*, 116(37):19839–19850, 2012.

[42] T. Kajiwara, M. Higuchi, D. Watanabe, H. Higashimura, T. Yamada, and H. Kitagawa. A systematic study on the stability of porous coordination polymers against ammonia. *Chem. Eur. J.*, 20(47):15611–15617, 2014.

[43] A. Vale. Sulphur dioxide. *Medicine*, 40(3):158, 2012.

[44] European Environment Agency. Sulphur Dioxide (SO_2). Technical report, 2015.

[45] S. Satyapal, J. Petrovic, C. Read, G. Thomas, and G. Ordaz. The U.S. Department of Energy's National Hydrogen Storage Project: Progress towards meeting hydrogen-powered vehicle requirements. *Catal. Today*, 120(3-4 SPEC. ISS.):246–256, 2007.

[46] D. K. Ross. Hydrogen storage: The major technological barrier to the development of hydrogen fuel cell cars. *Vacuum*, 80(10):1084–1089, 2006.

[47] G. Thomas and G. Parks. Potential Roles of Ammonia in a Hydrogen Economy. pages 1–23, 2006.

[48] K. Huang, Y. L. Chen, X. M. Zhang, S. Xia, Y. T. Wu, and X. B. Hu. SO_2 absorption in acid salt ionic liquids/sulfolane binary mixtures: Experimental study and thermodynamic analysis. *Chem. Eng. J.*, 237:478–486, 2014.

[49] S. Darake, A. Rahimi, M. S. Hatamipour, and P. Hamzeloui. SO_2 Removal by Seawater in a Packed-Bed Tower: Experimental Study and Mathematical Modeling. *Sep. Sci. Technol.*, 49(7):988–998, 2014.

[50] A. Andreasen and S. Mayer. Use of seawater scrubbing for SO_2 removal from marine engine exhaust gas. *Energ. Fuel.*, 21(6):3274–3279, 2007.

[51] G. Caiazzo, A. Di Nardo, G. Langella, and F. Scala. Seawater scrubbing desulfurization: A model for SO_2 absorption in fall-down droplets. *Environ. Prog. Sustain. Energ.*, 31(2):277–287, 2012.

[52] D. Britt, D. Tranchemontagne, and O. M. Yaghi. Metal-organic frameworks with high capacity and selectivity for harmful gases. *P. Natl. Acad. Sci. USA.*, 105(33):11623–11627, 2008.

[53] H. C. Zhou, J. R. Long, and O. M. Yaghi. Introduction to metal-organic frameworks. *Chem. Rev.*, 112(2):673–674, 2012.

[54] L. Li, I. Da Silva, D. I. Kolokolov, X. Han, J. Li, G. Smith, Y. Cheng, L. L. Daemen, C. G. Morris, H. G. W. Godfrey, N. M. Jacques, X. Zhang, P. Manuel, M. D. Frogley, C. A. Murray, A. J. Ramirez-Cuesta, G. Cinque, C. C. Tang, A. G. Stepanov, S. Yang, and M. Schroder. Post-synthetic modulation of the charge distribution in a metal-organic framework for optimal binding of carbon dioxide and sulfur dioxide. *Chem. Sci.*, 10(5):1472–1482, 2019.

[55] J. R. Long and O. M. Yaghi. The pervasive chemistry of metal-organic frameworks. *Chem. Soc. Rev.*, 38(5):1213–1214, 2009.

[56] H. Furukawa, K. E. Cordova, M. O'Keeffe, and O. M. Yaghi. The chemistry and applications of metal-organic frameworks. *Science*, 341(6149):1230444, 2013.

[57] L. E. Kreno, K. Leong, O. K. Farha, M. Allendorf, D. Van Richard P., and J. T. Hupp. Metal-Organic Framework Materials as Chemical Sensors. *Chem. Rev.*, 112:1105–1125, 2012.

[58] H. Oh and M. Hirscher. Quantum Sieving for Separation of Hydrogen Isotopes Using MOFs. *Eur. J. Inorg. Chem.*, 2016(27):4278–4289, 2016.

[59] Y. S. Bae and R. Q. Snurr. Development and evaluation of porous materials for carbon dioxide separation and capture. *Angew. Chem. Int. Edit.*, 50(49):11586–11596, 2011.

[60] J. Lee, O. K. Farha, J. Roberts, K. A. Scheidt, S. T. Nguyen, and J. T. Hupp. Metal-organic framework materials as catalysts. *Chem. Soc. Rev.*, 38(5):1450, 2009.

[61] T. Grant Glover, G. W. Peterson, B. J. Schindler, D. Britt, and O. Yaghi. MOF-74 building unit has a direct impact on toxic gas adsorption. *Chem. Eng. Sci.*, 66(2):163–170, 2011.

[62] J. Sculley, D. Yuan, and H. Zhou. The current status of hydrogen storage in metal-organic frameworks-updated. *Energ. Environ. Sci.*, 4(8):2721, 2011.

[63] G. Sastre. Hydrogen physisorption in metal-organic frameworks: Concepts and quantum chemical calculations. *Theor. Chem. Acc.*, 127(4):259–270, 2010.

[64] Y. He, W. Zhou, G. Qian, and B. Chen. Methane storage in metal-organic frameworks. *Chem. Soc. Rev.*, 43(16):5657–78, 2014.

[65] W. L. Queen, M. R. Hudson, E. D. Bloch, J. A. Mason, M. I. Gonzalez, J. S. Lee, D. Gygi, J. D. Howe, K. Lee, T. A. Darwish, M. James, V. K. Peterson, S. J. Teat,

B. Smit, J. B. Neaton, J. R. Long, and C. M. Brown. Comprehensive study of carbon dioxide adsorption in the metal-organic frameworks M_2(dobdc) (M = Mg, Mn, Fe, Co, Ni, Cu, Zn). *Chem. Sci.*, 5(12):4569–4581, 2014.

[66] K. Sumida, D. L. Rogow, J. A. Mason, T. M. McDonald, E. D. Bloch, Z. R. Herm, T. H. Bae, and J. R. Long. Carbon dioxide capture in metal-organic frameworks. *Chem. Rev.*, 112(2):724–781, 2012.

[67] I. Spanopoulos, P. Xydias, C. D. Malliakas, and P. N. Trikalitis. A Straight Forward Route for the Development of Metal-Organic Frameworks Functionalized with Aromatic -OH Groups: Synthesis, Characterization, and Gas (N_2 , Ar, H_2 , CO_2 , CH_4 , NH_3) Sorption Properties. *Inorg. Chem.*, 52(2):855–862, 2013.

[68] N. B. Shustova, A. F. Cozzolino, S. Reineke, M. Baldo, and M. Dinca. Selective Turn-On Ammonia Sensing Enabled by High-Temperature Fluorescence in Metal-Organic Frameworks with Open Metal Sites. *J. Am. Chem. Soc.*, 135(36):13326–13329, 2013.

[69] G. W. Peterson, G. W. Wagner, A. Balboa, J. Mahle, T. Sewell, and C. J. Karwacki. Ammonia Vapor Removal by $Cu_3(BTC)_2$ and Its Characterization by MAS NMR. *J. Phys. Chem. C*, 113(31):13906–13917, 2009.

[70] C. H. Hendon and A. Walsh. Chemical principles underpinning the performance of the metal-organic framework HKUST-1. *Chem. Sci.*, 6(7):3674–3683, 2015.

[71] M. J. Katz, Z. J. Brown, Y. J. Colón, P. W. Siu, K. A. Scheidt, R. Q. Snurr, J. T. Hupp, and O. K. Farha. A facile synthesis of UiO-66, UiO-67 and their derivatives. *Chem. Commun.*, 49(82):9449, 2013.

[72] S. Hindocha and S. Poulston. Study of the scale-up, formulation, ageing and ammonia adsorption capacity of MIL-100(Fe), Cu-BTC and CPO-27(Ni) for use in respiratory protection filters. *Faraday Discuss.*, 201:113–125, 2017.

[73] P. D. C. Dietzel, P. A. Georgiev, J. Eckert, R. Blom, T. Strässle, and T. Unruh. Interaction of hydrogen with accessible metal sites in the metal-organic frameworks M_2(dhtp) (CPO-27-M; M = Ni, Co, Mg). *Chem. Commun.*, 46(27):4962–4964, 2010.

[74] N. Ko, J. Hong, S. Sung, K. E. Cordova, H. J. Park, J. K. Yang, and J. Kim. A significant enhancement of water vapour uptake at low pressure by amine-functionalization of UiO-67. *Dalton Trans.*, 44(5):2047–2051, 2015.

[75] J. H. Cavka, S. Jakobsen, U. Olsbye, N. Guillou, C. Lamberti, S. Bordiga, and K. P. Lillerud. A New Zirconium Inorganic Building Brick Forming Metal Organic Frameworks with Exceptional Stability. *J. Am. Chem. Soc.*, 130(42):13850–13851, 2008.

[76] S. R. Johnson, W. I. F. David, D. M. Royse, M. Sommariva, C. Y. Tang, F. P. A. Fabbiani, M. O. Jones, and P. P. Edwards. The Monoammoniate of Lithium Borohydride, $Li(NH_3)BH_4$: An Effective Ammonia Storage Compound. *Chem. Asian J.*, 4(6):849–854, 2009.

[77] S. Westman, P. Werner, T. Schuler, and W. Raldow. X-ray investigations of ammines of alkaline earth metal halides. I. The structures of $CaCl_2$ $(NH_3)_8$, $CaCl_2(NH_3)_2$ and the decomposition product CaClOH. *Acta Chem. Scand.*, 35:467–472, 1981.

[78] H. Zhu, X. Gu, K. Yao, L. Gao, and J. Chen. Large-Scale Synthesis of $MgCl_2 \cdot 6NH_3$ as an Ammonia Storage Material. *Ind. Eng. Chem. Res.*, 48(11):5317–5320, 2009.

[79] I. C. Hwang, T. Drews, and K. Seppelt. $Mg(NH_3)_6Hg_{22}$, a mercury intercalation compound. *J. Am. Chem. Soc.*, 122(35):8486–8489, 2000.

[80] W. L. Bragg. The Diffraction of Short Electromagnetic Waves by a Crystal. *P. Camb. Philos. Soc.*, 17:43–57, 1913.

[81] R. Pynn. Neutron Scattering- A Non-destructive Microscope for Seeing Inside Matter. Neutron Scattering Applications and Techniques. Springer US, Boston, MA, 2009.

[82] G. E. Bacon. *X-ray and Neutron Diffraction.* Pergamon Press, Oxford, first edition, 1966.

[83] B. Fultz and J. M. Howe. *Transmission Electron Microscopy and Diffractometry of Materials (Third Edition).* 2007.

[84] L. B. McCusker and C. Baerlocher. Using electron microscopy to complement X-ray powder diffraction data to solve complex crystal structures. *Chem. Commun.*, (12):14391439–1451, 2009.

[85] C. Randau, U. Garbe, and H. G. Brokmeier. StressTextureCalculator : a software tool to extract texture, strain and microstructure information from area-detector measurements. *J. App. Crystallogr.*, 44(3):641–646, 2011.

[86] D. Pozar. *Microwave Engineering Fourth Edition.* John Wiley & Sons, Inc., 2005.

[87] Ralph D. Nelson Jr. Electric Dipole the Gas Phase. *National Standard Reference Data Series*, 1970.

[88] R. A. Waldron. Perturbation theory of resonant cavities. *P. IEE Part C: Monographs*, 107(12):272, 1960.

[89] R.G. Carter. Accuracy of microwave cavity perturbation measurements. *IEEE T. Microw. Theory*, 49(5):918–923, 2001.

[90] M. Lin, Y. Wang, and M. N. Afsar. Precision Measurement Of Complex Permittivity And Permeability By Microwave Cavity Perturbation Technique. *Infrared and Millimeter Waves and 13th International Conference on Terahertz Electronics*, 1:62–63, 2005.

[91] K.T. Mathew and U. Raveendranath. Cavity Perturbation Techniques for Measuring Dielectric Parameters of Water and Other Allied Liquids. *Sensors Update*, 7(1):185–210, 2000.

[92] D. Kajfez, S. Chebolu, M. R. Abdul-Gaffoor, and A. A. Kishk. Uncertainty analysis of the transmission-type measurement of Q-factor. *IEEE T. Microw. Theory*, 47(3):367–371, 1999.

[93] X. F. Wang, Z. G. Shi, and K. S. Chen. Research of coupling coefficient extraction of a cavity resonator. *2011 China-Japan Joint Microw. Conf.*, (May 2011):1–4, 2011.

[94] https://uk.comsol.com/products.

[95] M. S. Yildiz and M. Celik. Numerical investigation of the electric field distribution and the power deposition in the resonant cavity of a microwave electrothermal thruster. *AIP Adv.*, 7(4):1–11, 2017.

[96] E. H. Ooi and E. Y. K. Ng. Simulation of aqueous humor hydrodynamics in human eye heat transfer. *Comput. Biol. Med.*, 38(2):252–262, 2008.

[97] J. A. Cuenca, D. R. Slocombe, and A. Porch. Temperature Correction for Cylindrical Cavity Perturbation Measurements. *IEEE T. Microw. Theory*, 65(6):2153–2161, 2017.

[98] J. Molla, A. Ibarra, J. Margineda, J. M. Zamarro, and A. Hernandez. Dielectric property measurement system at cryogenic temperature and microwave frequencies. *IEEE T. Instrum. Meas.*, 42(4):817–821, 1993.

[99] A. Porch, D. Slocombe, J. Beutler, P. Edwards, A. Aldawsari, T. Xiao, V. Kuznetsov, H. Almegren, S. Aldrees, and N. Almaqati. Microwave treatment in oil refining. *Appl. Petrochem. Res.*, 2(1-2):37–44, 2012.

[100] U. Kaatze. Complex permittivity of water as a function of frequency and temperature. *J. Chem. Eng. Data*, 34(4):371–374, 1989.

[101] C. Zou, J. C. Fothergill, and S. W. Rowe. The effect of water absorption on the dielectric properties of epoxy nanocomposites. *IEEE T. Dielect. El. In.*, 15(1):106–117, 2008.

[102] Markus Dietrich, Dieter Rauch, Adrian Porch, and Ralf Moos. A Laboratory Test Setup for in situ Measurements of the Dielectric Properties of Catalyst Powder Samples under Reaction Conditions by Microwave Cavity Perturbation: Set up and Initial Tests. *Sensors*, 14(9):16856–16868, 2014.

[103] D. Cannell and I. Youngs. *A Guide to characterisation of dielectric materials at RF and microwave frequencies*. National Physical Laboratory, 2003.

[104] N. Clark, N. Jones, and A. Porch. Measurement of average particle size in metal powders by microwave cavity perturbation in the magnetic field. *Sensor. Actuator. A Phys.*, 259:137–143, 2017.

[105] T. Hanaguri, K. Takaki, Y. Tsuchiya, and A. Maeda. An instrument for low- and variable-temperature millimeter-wave surface impedance measurements under magnetic fields. *Rev. Sci. Instrum.*, 74(10):4436–4441, 2003.

[106] M. Barter, S. Partridge, D. R. Slocombe, and A. Porch. Temperature Correction Using Degenerate Modes for Cylindrical Cavity Perturbation Measurements. *IEEE T. Microw. Theory*, 65(6):800–805, 2018.

[107] A. E. Atia and A. E. Williams. General TE_{011}-Mode Waveguide Bandpass Filters. *IEEE T. Microw. Theory*, 24(10):640–648, 1976.

[108] W. J. Ellison. Permittivity of pure water, at standard atmospheric pressure, over the frequency range 0-25 THz and the temperature range 0-100 °C. *J. Phys. Chem. Ref. Data*, 36(1):1–18, 2007.

[109] M. Merabet and T. K. Bose. Dielectric measurements of water in the radio and microwave frequencies by time domain reflectometry. *J. of Phys. Chem.*, 92(21):6149–6150, 1988.

[110] A. Porch, D. I. Odili, and P. A. Childs. Microwave characterisation of carbon nanotube powders. *Nanoscale Res. Lett.*, 7(1):429, 2012.

[111] A. Porch. Private Communication, 2019.

[112] D. Kajfez, S. Chebolu, A. A. Kishk, and M. R. Abdul-Gaffoor. Temperature dependence of composite microwave cavities. *IEEE T. Microw. Theory.*, 49(1):80–85, 2001.

[113] S. Hull, R. I. Smith, W. I. F. David, A. C. Hannon, J. Mayers, and R. Cywinski. The Polaris powder diffractometer at ISIS. *Physica B*, 180-181:1000–1002, 1992.

[114] R.I. Smith and S. Hull. User Guide for the Polaris Powder Diffractometer at ISIS. Technical report.

[115] www.isis.stfc.ac.uk/pages/polaris.aspx, date accessed: 29-03-2019.

[116] M. Barter, J. Hartley, F. Yazigi, R. J. Marshall, R. S. Forgan, A. Porch, and M. O. Jones. Simultaneous neutron powder diffraction and microwave dielectric studies of ammonia absorption in metal-organic framework systems. *Phys. Chem. Chem. Phys.*, 20(15):10460–10469, 2018.

[117] P. D. C. Dietzel, R. E. Johnsen, R. Blom, and H. Fjellvåg. Structural changes and coordinatively unsaturated metal atoms on dehydration of honeycomb analogous microporous metal-organic frameworks. *Chem. Eur. J.*, 14(8):2389–2397, 2008.

[118] I. W. Bassi, F. Polato, M. Calcaterra, and J. C. J. Bart. A new layer structure of $MgCl_2$ with hexagonal close packing of the chlorine atoms. *Z. Krist.-Cryst. Mater. Z.*, 159(1-4):297–302, 1982.

[119] A. Leineweber, M. W. Friedriszik, and H. Jacobs. Preparation and Crystal Structures of $Mg(NH_3)_2Cl_2$, $Mg(NH_3)_2Br_2$, and $Mg(NH_3)_2I_2$. *J. Solid State Chem.*, 147(1):229–234, 1999.

[120] E. B. Brackett, T. E. Brackett, and R. L. Sass. The crystal structure of calcium bromide. *J. Inorg. Nucl. Chem.*, 25(10):1295–1296, 1963.

[121] P. Woidy, A. J. Karttunen, T. G. Müller, and F. Kraus. The Unusual Coordination Sphere in the Octaammine Calcium(II) Ions of $[Ca(NH_3)_8]Br_2$ and $[Ca(NH_3)_8]I_2$ and the Thermal Decomposition of the Iodide to $[Ca(NH_3)_6]I_2$. *Z. Naturforsch. B*, 69(11-12):1141–1148, 2014.

Appendix A

Derivations

A.1 Q factor for cavity height derivation for microwave cavity TM$_{010}$ mode

Q factor derivation for a cylindrical cavity in the TM$_{010}$ mode.

$$Q = \omega_0 \frac{< U >}{< P >} \tag{A.1}$$

Where:

$$E_z = E_0 J_0(kr) e^{j\omega t} \tag{A.2}$$

$$H_\phi = \frac{E_0}{\eta_0} J_1(kr) e^{j\omega t} \tag{A.3}$$

Stored energy:

$$< U >= \frac{1}{2}\mu_0 \int H_\phi^2 dv = \frac{1}{2}\mu_0 H_0^2 d \int\limits_0^a 2\pi r J_1^2(kr) dr \tag{A.4}$$

Total energy dissipated from the cavity wall as well as top and bottom plates:

$$<P>=<P_1>+<P_2> \tag{A.5}$$

Energy dissipated in the cavity wall:

$$<P_1>=\frac{1}{2}R_S H_0^2 J_1^2(ka)2\pi ad \tag{A.6}$$

Energy dissipated in the cavity top and bottom plates combined:

$$<P_2>=R_S H_0^2 \int_0^a 2\pi r J_1^2(kr)dr \tag{A.7}$$

Subbing into A.1:

$$Q=\omega_0\frac{<U>}{<P>}=\frac{\frac{1}{2}\omega_0\mu_0 H_0^2 d\int_0^a 2\pi r J_1^2(kr)dr}{R_S H_0^2 J_1^2(ka)\pi ad+R_S H_0^2\int_0^a 2\pi r J_1^2(kr)dr} \tag{A.8}$$

Using Bessel function identities:

$$\int_0^a J_1^2(kr)rdr=\frac{a^2}{2}\left[J_1'^2(ka)+\left(1-\frac{1}{k^2a^2}\right)J_1^2(ka)\right] \tag{A.9}$$

$$J_1'(ka)=-\frac{1}{ka}J_1(ka)-J_0(ka) \tag{A.10}$$

$$2\pi\int_0^a rJ_1^2(kr)\,dr=\pi a^2 J_1^2(ka) \tag{A.11}$$

Subbing back into A.8 and simplifying:

$$Q=\frac{\frac{1}{2}\omega_0\mu_0 d\pi a^2 J_1^2(ka)}{R_S J_1^2(ka)\pi ad+R_S\pi a^2 J_1^2(ka)}=\frac{1}{2}\frac{\omega_0\mu_0}{R_S}\frac{da}{d+a}=\frac{1}{2}\frac{\omega_0\mu_0}{R_S}\frac{a}{1+a/d} \tag{A.12}$$

To express in terms of skin depth(δ):

$$\frac{\omega_0\mu_0}{2R_S} = \frac{\omega_0\mu_0}{2\sqrt{\frac{\omega_0\mu_0\rho}{2}}} = \sqrt{\frac{\omega_0\mu_0}{2\rho}} = \frac{1}{\delta} \tag{A.13}$$

Finally subbing into A.12 gives:

$$Q = \frac{a/\delta}{1 + a/d} \tag{A.14}$$

A.2 Electric Field Pattern in Cylindrical Cavities

Maxwell's curl equations in phasor form are the following, assuming $e^{j\omega t}$ time dependence of the field amplitudes:

$$\nabla \times \bar{E} = -j\omega\mu\bar{H} \tag{A.15}$$

$$\nabla \times \bar{H} = j\omega\varepsilon\bar{E} \tag{A.16}$$

Taking the curl of equation A.15 and using equation A.16:

$$\nabla \times \nabla \times \bar{E} = -j\omega\mu\nabla \times \bar{H} = \omega^2\mu\varepsilon\bar{E} \tag{A.17}$$

Using vector identities:

$$\nabla^2\bar{E} + \omega^2\mu\varepsilon\bar{E} = 0 \tag{A.18}$$

E_z can be defined as:

$$E_z(r,\phi,z) = R(r)\Phi(\phi)Z(z) \tag{A.19}$$

where R, Φ, and Z are functions of radius, angle, and height respectively. Let:

$$k^2 = \omega^2\mu\varepsilon \tag{A.20}$$

Using the identity of the Laplace operator in cylindrical coordinates for $\nabla^2\bar{E}$:

$$\frac{1}{r}\frac{\partial}{\partial r}\left(r\frac{\partial E_z}{\partial r}\right) + \frac{1}{r^2}\frac{\partial^2 E_z}{\partial\phi^2} + \frac{\partial E_z}{\partial z^2} + k^2E_z = 0 \tag{A.21}$$

Subbing A.19 intoA.21:

$$\frac{1}{r}\frac{\partial}{\partial r}\left(r\frac{\partial R(r)\Phi(\phi)Z(z)}{\partial r}\right)+\frac{1}{r^2}\left(\frac{\partial^2 R(r)\Phi(\phi)Z(z)}{\partial \phi}\right)+\left(\frac{\partial^2 R(r)\Phi(\phi)Z(z)}{\partial z^2}\right)+k^2 R(r)\Phi(\phi)Z(z)=0 \tag{A.22}$$

Simplifying and dividing by $R(r)\Phi(\phi)Z(z)$:

$$\frac{\frac{1}{r}\frac{d}{dr}\left(\frac{rdR(r)}{dr}\right)}{R(r)}+\frac{\frac{1}{r^2}\left(\frac{d^2\Phi(\phi)}{d\phi^2}\right)}{\Phi(\phi)}+\frac{\frac{\left(d^2 Z(z)\right)}{dz^2}}{Z(z)}+k^2 \tag{A.23}$$

Then separating by parts. Let:

$$\frac{\frac{d^2 Z(z)}{dz^2}}{Z(z)}=-k_z^2 \tag{A.24}$$

$$\frac{d^2 Z(z)}{dz^2}+k_z^2 Z(z)=0 \tag{A.25}$$

Solving the second order linear equation:

$$Z(z)=C_1 e^{jk_z z}+C_2 e^{-jk_z z} \tag{A.26}$$

where C_n is an arbitrary constant. Using Euler's Formula and simplifying:

$$Z(z)=(C_1+C_2)\cos(k_z z)+j(C_1-C_2)\sin(k_z z) \tag{A.27}$$

Applying boundary conditions for the cavity $|Z(0)|=C_3$ and $|Z(h)|=C_3$, where h is the cavity height:

$$Z(z)=C_3 cos(k_z z) \tag{A.28}$$

$$Z(z)=C_3\cos\left(\frac{z\pi p}{h}\right) \tag{A.29}$$

where p is from the mode TM_{mnp}. Subbing equationA.23 into equation A.25 gives:

$$\frac{\frac{1}{r}\frac{d}{dr}\left(r\frac{dR(r)}{dr}\right)}{R(r)}+\frac{\frac{1}{r^2}\left(\frac{d^2\Phi(\phi)}{d\phi^2}\right)}{\Phi(\phi)}+k^2-k_z^2=0 \tag{A.30}$$

Let $k_r^2 = k^2 - k_z^2$ and multiply by r^2:

$$\frac{r\frac{d}{dr}\left(\frac{rd(R(r))}{dr}\right)}{R(r)} + \frac{\frac{d^2\Phi(\phi)}{d\phi^2}}{\Phi(\phi)} + r^2k_r^2 = 0 \tag{A.31}$$

Let:

$$\frac{\frac{d^2\Phi(\phi)}{d\phi^2}}{\Phi(\phi)} = -m^2 \tag{A.32}$$

Then rearrange to get:

$$\frac{d^2\Phi(\phi)}{d\phi^2} + m^2\Phi(\phi) = 0 \tag{A.33}$$

Solving the second order linear equation, using Euler's Formula then simplifying gives:

$$\Phi(\phi) = (C_4 + C_5)\cos(m\phi) + j(C_4 - C_5)\sin(m\phi) \tag{A.34}$$

Let $C_6 = C_4 + C_5$ and$C_7 = j(C_4 - C_5)$ then:

$$\Phi(\phi) = C_6\cos(m\phi) + C_7\sin(m\phi) \tag{A.35}$$

Then using trigonometric identities:

$$\Phi(\phi) = C_8\cos(m\phi + \theta) \tag{A.36}$$

Subbing equation A.32 into equation A.31:

$$\frac{r\frac{d}{dr}\left(\frac{rdR(r)}{dr}\right)}{R(r)} + r^2k_r^2 - m^2 = 0 \tag{A.37}$$

Multiplying by $R(r)$:

$$r\frac{d}{dr}\left(\frac{rdR(r)}{dr}\right) + R(r)\left(r^2k_r^2 - m^2\right) = 0 \tag{A.38}$$

This expands to become:

$$r^2\frac{d^2R(r)}{dr^2} + r\frac{dR(r)}{dr} + R(r)\left(r^2k_r^2 - m^2\right) = 0 \tag{A.39}$$

Using Bessel function identities:

$$R(r) = C_9 J_m(r k_r) \tag{A.40}$$

Boundary conditions show $R(a) = 0$ where a is the cavity radius. Let α_{mn}be the n^{th} root of J_m. Then:

$$R(r) = C_9 J_m \left(\frac{r}{a} \alpha_{mn} \right) \tag{A.41}$$

Finally sub $R(r)$, $\Phi(\phi)$, and $Z(z)$ into equation A.19 where $E_0 = C_3 C_8 C_9$:

$$E_z \left(r, \phi, z \right) = E_0 J_m \left(\frac{\alpha_{mn} r}{a} \right) \cos \left(m \left(\phi + \theta \right) \right) \cos \left(\frac{p \pi z}{h} \right) \tag{A.42}$$